Gunther Weirum

Structural investigation of zinc-palladium and zinc oxide-palladium model catalyst surfaces

DISSERTATION

zur Erlangung des akademischen Grades
Doktor der technischen Wissenschaften

Doktoratsstudium der technischen Wissenschaften
Technische Physik

Technische Universität Graz

Betreuer:

Univ.-Prof. Dr.rer.nat. Svetlozar Surnev

Institut für Physik, Karl-Franzens Universität Graz

in Zusammenarbeit mit

Univ.-Prof. Dr.rer.nat. Robert Schennach

Institut für Festkörperphysik, Technische Universität Graz

Graz, Juni 2010

Abstract

In this thesis a low energy electron diffraction- and scanning tunnelling microscopy-study of PdZn(111) surface alloys and of pure and Co-doped ZnO-films on a Pd(111)-substrate is presented. The formation of a 1:1 stoichiometric PdZn surface alloy at room-temperature is reported after Zn-deposition onto a Pd(111) surface. For this alloy the formation of a bilayer with p(2×1)-structure, consisting of alternating zinc- and palladium- rows, can be confirmed. In the case of pure ZnO-films on a Pd(111)-substrate two different structures emerge at submonolayer coverage. One forms a p(4×4)-superstructure, consisting of an open, honeycomb-like mesh, which could be identified as a polar $Zn_6(OH)_5$-structure. The second one, with 1:1 Zn-O stoichiometry, forms a 5/6-coincidence structure with a planar h-BN geometry, displaying a distinct moiré pattern with p(6×6)-periodicity. Variation of the oxygen chemical potential during film-preparation leads to formation of oxygen vacancies in the 6×6-structure for low values and formation of 6×6-bilayers at high values. At coverages above 1 ML only the planar h-BN structure is thermodynamically stable. The ZnO grows in layer-by-layer fashion up to 3 monolayers coverage. For thicker films a transition to island-growth takes place accompanied by an increase in surface roughness. For a low oxygen chemical potential during the film growth, the emergence of metallic Zn-adlayers on top of ZnO has been proposed in the DFT-analysis. These Zn- adlayers expose a slightly compressed 6×6-structure and a higher surface roughness. The ZnO-films remain stable until an annealing temperature of 600 K - then thermal decomposition sets in. In this process the formation of a PdZn-surface alloy with 1:1 stoichiometry can be confirmed. The ZnO-films however show a certain resistance against reduction by hydrogen. Doping the ZnO-films with Co leads in most cases to completely intermixed Zn(1-x)Co(x)O-films. Yet with an appropriate preparation method it becomes possible to form distinct ferromagnetic CoO-islands within a nonmagnetic ZnO-matrix, an important result for the field of spintronic devices.

Diese Doktorarbeit beschäftigt sich mit der strukturellen Erforschung von PdZn(111)-Oberflächenlegierungen sowie von reinen und Co-dotierten ZnO-Schichten auf einem Pd(111)-Substrat, anhand von Beugung niederenergetischer Elektronen und Rastertunnelmikroskopie. In diesem Zusammenhang wurde beobachtet, dass die Beschichtung einer Pd(111)-Oberfläche mit Zinkschon bei Raumtemperatur zur Bildung einer stöchiometrischen 1:1 PdZn Oberflächenlegierung führt. Für diese Legierung konnte die Ausbildung einer Doppellage mit p(2×1)-Struktur bestätigt werden, die aus abwechselnden Zink- und Palladium-Reihen besteht. Für reine ZnO-Schichten auf einer Pd(111)-Oberfläche konnten zwei verschiedene Strukturen beobachtet werden, wenn die Bedeckung im submonolagigen Bereich liegt. Die erste bildete ein p(4×4)-Überstruktur, bestehend aus einem Honigwabengitter, dessen Struktur aus polaren $Zn_6(OH)_5$-Einheiten gebildet wird. Die zweite Struktur, mit einer 1:1 Zn-O Stöchiometrie, bildete eine 5/6-Koinzidenzstruktur mit

planarer h-BN Geometrie. Dadurch entstand ein Moiré-Raster mit p(6×6)-Periodizität. Änderung des chemischen Sauerstoffpotentials während der Schichtherstellung führten bei Absenkung zu Sauerstoff-Fehlstellen in der 6×6-Struktur und bei entsprechender Erhöhung zur Bildung von 6×6-Bilagen. Bei Bedeckungen größer als eine Monolage war nur noch die planare h-BN Struktur thermodynamisch stabil. Bis zu einer Schichtdicke von 3 ML zeigte ZnO Lagenwachstum, bei dickeren Schichten erfolgte ein Übergang zu Inselwachstum begleitet von einer Aufrauhung der Oberfläche. Bei niedrigem chemischen Sauerstoffpotential während der Schichtherstellung kam es zur Ausbildung von metallischen Zink-Lagen auf dem schon bestehenden ZnO-Film, gleichzusetzen mit einer Zn-Terminierung der gesamten Schicht. Diese Zn-Lagen wiesen eine leicht komprimierte 6×6-Struktur und eine erhöhte Oberflächen-Rauheit auf. Die ZnO-Schichten zeigten sich stabil bis zu einer Temperatur von 600 K - weiteres Erhitzen führte zu thermischer Zersetzung. Die Bildung einer PdZn-Oberflächenlegierung mit 1:1 Stöchiometrie im Laufe dieses Prozesses konnte bestätigt werden. Die ZnO-Schichten zeigten ebenfalls eine gewisse Resistenz gegen eine Reduktion mit Wasserstoff. Das dotieren der ZnO-Schichten mit Cobalt führte in den meisten Fällen zu völlig gemischten Zn(1-x)Co(x)O-Filmen. Jedoch konnten mit einer geschickten Präparation auch magnetische CoO-Inseln inmitten einer nichtmagnetischen ZnO-Matrix erzeugt werden, ein Resultat, das für das Gebiet der Spintronik von Interesse ist.

Table of contents

Introduction

Zinc-oxide (ZnO) is a very interesting material for a variety of technical and every-day applications. It is, for example, used in electronic devices, in gas-sensing elements, as an additive in chemical processes, as a pigment, in sun-blockers or even as a dietary supplement. The scientific investigation of ZnO has been enforced in the 1970s and 1980s but the interest subsided when it has not been possible to produce p-doped ZnO. In the recent years this has changed again, as new ways of applications evolved: P-doping of ZnO has become possible by the use of elements like nitrogen, phosphor or arsenic. Moreover, ZnO provides a variety of different nanostructures, which can be p-doped apart from the thermodynamic equilibrium, thus opening up new possibilities. By n-doping ZnO with aluminium, indium or gallium, transparent conductive oxides (TCO) for electrooptical devices can be created, thus providing an alternative for the currently used indium-tin-oxide. Also the replacement of gallium-nitride in blue light emitting diodes by ZnO is researched intensively. The nonlinear optical characteristics of the material also provide interesting opportunities for optics, like rectification of laser beams or optical amplification in laser-diodes. A completely new field in spintronics evolves with the mixing of zinc-oxide and transition metals – the diluted magnetic semiconductors (DMS). Last but not least ZnO has also been discovered as a useful material in the field of catalysis. [kp06, kn04, nn04, pa03, zp05, ls05, öj05, ds05, ks05, ws04, ws98, kz71, mz69]

The last point – catalysis – is of special interest for this thesis because it provides the major part of the underlying motivation for the presented research. The larger technological and scientific framework is formed by the desire to construct commercially efficient fuel-cells for the replacement of combustion engines. This would provide a variety of advantages, including a higher efficiency and the reduction of pollutant-emission. Yet one of the problems at hand is the mobile supply with hydrogen. The storage of molecular hydrogen itself poses severe difficulties due to high diffusion rates and the easy inflammability of the substance. One of the approaches to solve this problem is the mobile production of hydrogen by catalytic dissociation of methanol. In contrast to hydrogen, methanol can be stored much more easily and safer. The extraction of hydrogen can be accomplished by steam reforming according to the reaction

$$CH_3OH+H_2O \rightarrow CO_2+3H_2$$

This methanol steam reforming (MSR)-reaction can be catalysed at temperatures as low as 473 K. This method avoids the formation of sulphur, which is harmful for the fuel cells, and ensures low concentrations of carbon-monoxide, due to the low reaction temperatures. Currently used catalysts are based on copper like e.g. $Cu/ZnO/Al_2O_3$. These catalysts however exhibit several disadvantages, like sintering at temperatures above 543 K, pyrophoric behavior or rapid deactivation. Another suitable material-class for the catalysis of

the MSR-reaction is provided by transition-metals, especially the platinum-group. Yet these metals alone tend to form a large amount of carbon-monoxide, instead of carbon-dioxide. [np07, tc01, hc04, kj06, bi01, ia95, cc02, pa99]

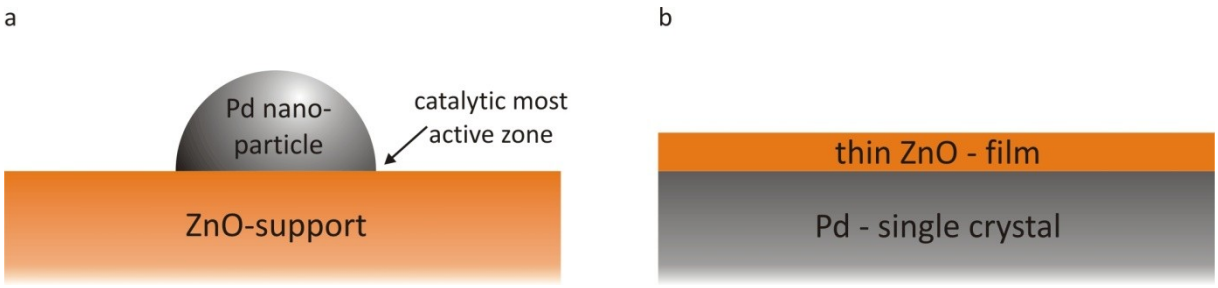

Fig. 0. 1: Schematic representations of a technological catalyst (a) and a model catalyst (b), consisting of palladium and zinc-oxide.

One way out of the dilemma is the combination of palladium and zinc-oxide. A technological catalyst, made of these two materials, is composed, like shown in figure 0.1a: Pd-nanoparticles are dispersed on a zinc-oxide support. The result is that the properties of the catalytic active metal are altered by the support, especially in the interface region at the base of the nanoparticles, where the catalytic most active zone is assumed to be at the rim. In the case of Pd/ZnO the modification causes a high selectivity for the formation of carbon-dioxide, reducing the amount of carbon-monoxide to a minimum. Moreover the catalyst shows good activity and a high thermal stability. Complete reformation of methanol can already be obtained at 573 K. [cc02, ia95, ij91, ic93]

The reason for the change in selectivity from carbon-monoxide to carbon-dioxide is thought to stem from the formation of a bimetallic interface-alloy, since reduction of ZnO at higher temperatures increased activity as well as selectivity of Pd/ZnO-catalysts. This PdZn alloy phase and its influence on the catalytic performance have been investigated minutely. It could be shown, that a 1:1 surface-alloy of these two materials is one of the active components in MSR-process over Pd/ZnO. This alloy can already be formed at 350K and proved a high stability up to a temperature of 873 K. Investigations showed, that the electronic structure of the alloy differs strongly from the one of pure palladium. Indeed a shift of the Pd 4d-band to higher energies could be observed in the alloy phase, like shown in figure 0.2. At the same time, the density of states (DOS) at the Fermi-level is strongly reduced. Theoretical investigation revealed that a charge transfer from zinc to palladium in the alloy is responsible for these changes. The resulting DOS exhibits a strong resemblance to the one of metallic copper, thus explaining the comparable catalytic activity and selectivity for CO_2-formation. [np07, nj04, bs06, rj94, wj09, ia95, ij91, ic93, kj06, tc97, it03, ib98, ir00, fp82, rj94, cp03]

Apart from the electronic configuration, the surface structure itself is important for the catalytic performance. Information about adsorption- and catalytic active sites is crucial for the technical realization and improvement of catalytic systems. This data can be provided by surface-science. Technical catalysts however present poor specimens for surface science

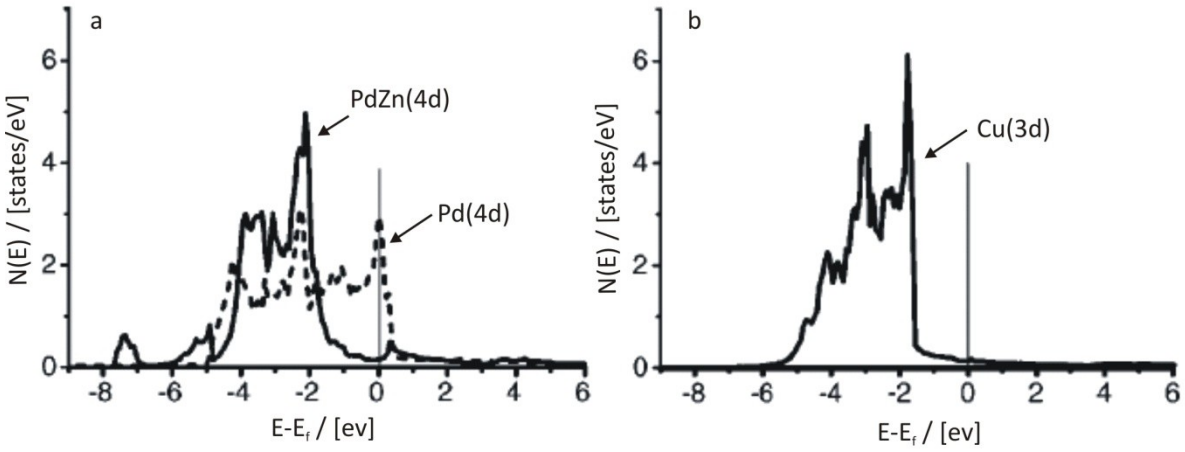

Fig. 0. 2: Calculated local density of states (LDOS) of Pd-, PdZn- and Cu- surfaces with (111)-orientation. (a) 4d-bands of Pd (dashed line) and a PdZn(1:1)-alloy (solid line). (b) 3d-band of metallic copper. Note the resemblance of the PdZn-DOS and the one of Cu. Legend: N(E) - number of states for a given energy E, E_f – Fermi-energy. Original pictures from [cp03].

techniques – they are often polycrystalline, badly ordered and operated in a "dirty" environment. To overcome this problem, model-systems are created, consisting of thin films on well defined surfaces of single crystals. Since the surfaces of metals have been explored more thoroughly in the past, the positions of substrate and coating are often reversed. In the case of Pd/ZnO such a "reversed model catalyst" looks like depicted in figure 0.1b: Thin ZnO-films are grown on top of a Pd-substrate and investigated in an ultrahigh-vacuum (UHV) environment. The obvious differences between technical and model-catalysts, which arise due to their different composition and environment, are generally known as "pressure-gap" and "materials gap". In spite of these differences, model catalysts provide valuable information about the metal-oxide interface, i.e. its physical and chemical properties. This information can be further processed by theoretical models and finally be applied to improve the effectiveness of technical catalysts.

In previous studies it could be shown, that the (111)-surfaces of Pd and PdZn are of special interest, since this orientation shows a high probability to appear on surfaces of technical Pd/ZnO-catalysts. Thus a Pd single crystal, cut along the (111)-surface provides the ideal substrate for surface-science investigations. It does not only allow formation of an appropriate Pd/ZnO-interface by the growth of thin ZnO-films, but also renders an easy creation of PdZn(111) surface-alloys possible. There already exists a variety of corresponding studies on the latter, but the definite surface-structure could not yet be determined with certainty (as discussed in section 3.2.2). For thin ZnO-films on a Pd(111) surface theoretical predictions of a graphite-like structure exist, which could be confirmed for a Ag(111)-substrate, but experimental affirmation for ZnO on Pd(111) was missing. In both cases (Pd/ZnO and PdZn) surface-analysis with the means of scanning-probe-microscopy presents a unique opportunity to gain insight into the structural compositions and to extend the knowledge about these surfaces. This is accomplished in the thesis at hand with help of scanning-tunnelling-microscopy (STM) supported by low energy electron diffraction (LEED). [wj09, ka09, ks10, cp03, bs06, rj94, ss09, cj05, cp06, tp07, zp04, sp08]

In addition to the importance for catalytic applications, thin ZnO-films also play a major role in the field of diluted magnetic semiconductors (DMS). In these systems, magnetic species are added to a non-magnetic, semiconducting host-material. For proper substance combinations and stoichiometries, functional materials with novel properties can be created. In DMS the combination of semiconductivity and magnetic orientation are of special interest. In particular for semiconductors with a large bandgap, like ZnO, the intermixing with transition-metals has been predicted to result in ferromagnetic behaviour at room-temperature. In this context, ZnO forms the host-material - typical additives are iron, manganese, nickel, cobalt and vanadium. Especially cobalt has received increasing attention due to the ability of the resulting $Zn_{1-x}Co_xO$-mixtures, to maintain a ferromagnetic hysteresis at room-temperature [kp06]. The underlying processes for this behaviour are not yet fully understood. The proposed mechanisms include indirect carrier-mediated exchange, alloy-formation, percolation of polarons, influence of the substrate and the formation of uncompensated spins at the surfaces of nano-inclusions. The last point has attracted the interest of several groups in the recent past. Indeed it could be shown that a segregation of Co-rich and Co-poor regions occurs, thus creating magnetic CoO-islands within a nonmagnetic ZnO-matrix. This is of special interest for further miniaturisation of data storage devices. The effect could be observed particularly for thin Co-doped ZnO-films on Ag(111). Since ZnO-films on Pd(111) are investigated in this thesis, it is an obvious opportunity to investigate mixed ZnCoO-films too. This analysis provides the answers to 2 questions: 1^{st} – if it is possible to observe such a segregation also on a Pd(111)-substrate and 2^{nd} – if it is possible to identify regions with different composition with STM. [oe08, ds00, dp07, dp06, cn05, dn06, mp09]

Thus three research topics are covered within this thesis: the structure of PdZn(111)-surface alloys and adjacent Zn-layers, the structure of ZnO-films on a Pd(111) substrate and the structure of mixed ZnCoO-films on Pd(111). The applied techniques were scanning tunnelling microscopy (STM) and low energy electron diffraction (LEED). The results from these experiments have been supplemented by density-functional-theory (DFT) calculations, performed by co-workers. The thesis itself is divided into two parts: The first – introductory - part includes the first three chapters. In chapter 1 information about principles in surface science are provided. Chapter 2 deals with the theory and instrumentation of the applied experimental techniques. In chapter 3 relevant data of the used materials Pd, Zn, ZnO and CoO can be found. In the second part of the thesis, the results of the corresponding experiment are presented: Chapter 4 covers the topic of PdZn(111) surface alloys and adjacent Zn-layers, chapter 5 deals with structure and properties of ZnO-films on Pd(111) and in chapter 6 mixed ZnCoO-films on Pd(111) are discussed. Subsequent to these chapters a general summary of the results is given, followed by the appendices, which contain the lists of abbreviations, figures, tables and the references.

Chapter 1: Concepts of surface science

In this chapter some basic concepts of surface science will be presented. The selection of themes is limited to those, which are relevant for the understanding of the results, presented in the chapters 4-6. They contain an introduction to the surface free energy, terms of surface geometry, a passage about polar surfaces, some concepts of film-growth and a brief description of some electronic effects on surfaces.

1.1 The surface free energy

Like any other system, the behaviour of solid surfaces is governed by two tendencies: the maximisation of entropy and the simultaneous minimisation of the total energy. Concerning the latter point, the free energy and the corresponding Gibbs-free-energy are the relevant parameters in surface science. A change in the Gibbs-free-energy of the surface G^s can be described in the following way for a constant pressure p:

$$G^s = -S^s dT + V^s dp - A d\gamma + \sum_i \mu_i dn_i \qquad (1.1)$$

S^s is the surface entropy, T the temperature, V^s is the volume of the surface region and p the pressure in this volume, n is the number of atoms with the chemical potential μ. The important term in this formula is –Adγ, where A denotes the surface area and γ is the surface tension. [Is93]

To understand the significance of this term, the surface tension must be explained more detailed. γ corresponds to the energy, which is necessary to create a new surface area. The physical background of this extra energy is the breaking of bonds, when a new surface is formed. γ strongly depends on the composition and the orientation of the emerging surface. A minimisation of G^s comes hand in hand with a minimisation of the product γA. This means that a solid tends to minimize surface areas with a large surface tension and to maximize areas with a small surface tension. Thus γ is a major driving force in surface science. [Is93]

A direct consequence of this behaviour is the reconstruction of surfaces. When, for example, a single-crystal is cut and the newly formed surface has a surface tension which is too high, the surface is reconstructed. In this process micro-facets with smaller γ-values are formed. A surface reconstruction is, of course, also influenced by other parameters. In most cases an activation-energy for bond-breaking and material movement is necessary, which is often provided by heating the surface. But the important point is that the surface tension is the driving force behind the process of reconstruction. [Is93]

1.2 Surface geometry

Surfaces can be regarded on different scales. On a macroscopic level the form and (crystallographic) orientation of a surface are regarded. On a microscopic scale, the atomic arrangement is the point of interest. This arrangement is called “surface-structure”. In between these two extremes is the mesoscopic area. On this level the form and orientation of islands, the surface roughness and likewise parameters are investigated. They are summarized with the term “surface-morphology”. [ls93, ue96]

1.2.1 Surface lattices in real and reciprocal space

In surface science typically highly ordered surfaces of single crystals are regarded. The positions of atoms on these surfaces can be described by long-ranging grids, the surface lattices. Like in crystallography, those grids consist of point- and space-groups. Allowed operations are the identity, 2-,3-,4- and 6-fold rotation, reflection and the glide-reflection. As a consequence 5 surface-Bravais-lattices emerge. Their unit cells are shown in figure 1.1. [ue96]

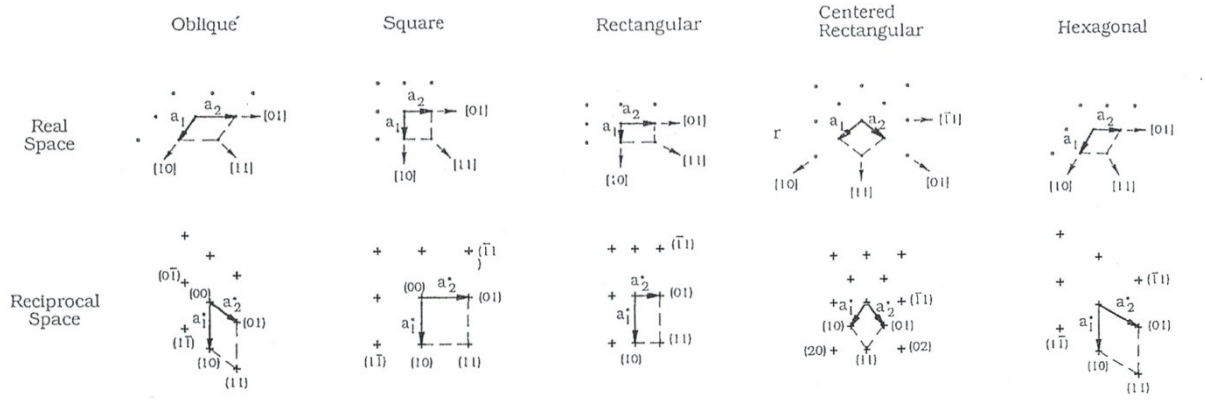

Fig. 1. 1: Surface Bravais-lattices in real and reciprocal space. a_1 and a_2 denote the unit cell vectors in real space. a_1^* and a_2^* are their corresponding vectors in reciprocal space. Figures taken from [ue96].

The base vectors of the Bravais lattice are typically denoted as $\vec{a}_1$ and $\vec{a}_2$. Directions on the surface are either given as functions of $\vec{a}_1$ and $\vec{a}_2$, $\vec{T}_{h,k}=h\vec{a}_1+k\vec{a}_2 \rightarrow [h,k]$, or they are noted [uvw] according to the directions of the 3d-unit cell of the crystal. Directions which are equivalent on the surface (undistinguishable due to the surface geometry) are marked by pointed breaks <uvw>. The surface itself is named according to its miller indices in the crystal (hkl). As an example the surfaces of an fcc-crystal are shown in figure 1.2, together with the main directions on these surfaces. [ue96]

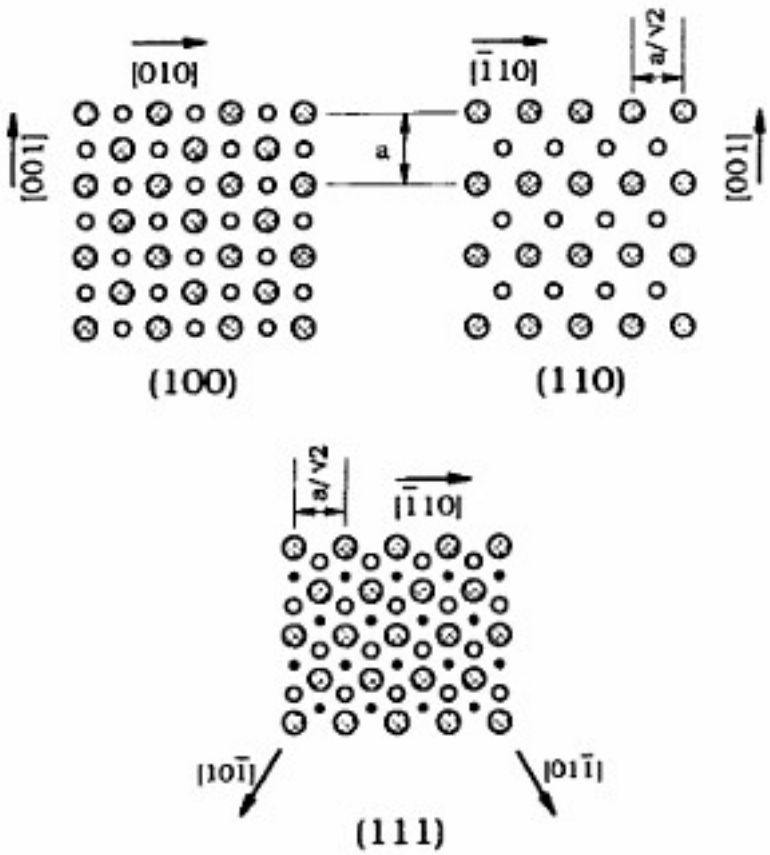

Fig. 1. 2: (100)-, (110)- and (111)-surfaces of a face-centred-cubic crystal. Cross-hatched circles represent atoms in the topmost layer, open circles are atoms one layer below the surface and black dots stand for atoms two layers below the surface. Picture taken from [ue96].

A surface can also be described in reciprocal space. The transformation equations for the unit cell vectors of the Bravais-lattices are:

$$\vec{a}_1^* = 2\pi \frac{\vec{a}_2 \times \vec{n}}{|\vec{a}_1 \times \vec{a}_2|}, \vec{a}_2^* = 2\pi \frac{\vec{a}_1 \times \vec{n}}{|\vec{a}_1 \times \vec{a}_2|} \quad (1.2)$$

with $$\vec{a}_i^* \cdot \vec{a}_j = 2\pi\delta_{ij} \quad (1.3)$$

$\vec{n}$ denotes the unit vector normal to the surface.

A general direction in reciprocal space is given by $\vec{G}_{h,k}=h\vec{a}_1^*+k\vec{a}_2^*$, with h and k being the corresponding Miller-indices. The unit cells of the individual Bravais-lattices in reciprocal space are also shown in figure 1.1. [ls93, ue96]

1.2.2 Defects

At temperatures larger than 0 K, defects become probable on every surface. Typical defects are adatoms, vacancies in the surface, surface impurities and dopants, stepedges, kinks, ledge adatoms, domain boundaries and dislocations. Examples of such defects are shown in figure 1.3. [ue96]

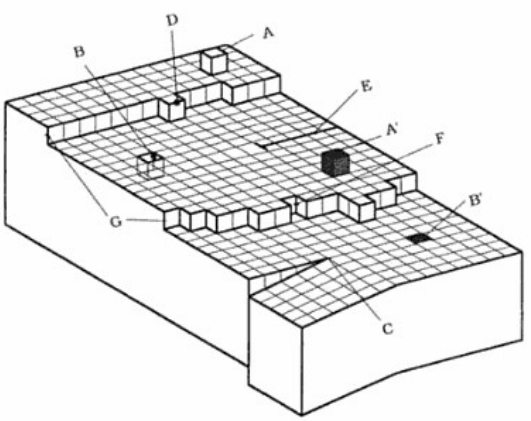

Fig. 1. 3: Different types of surface defects. A: adatom, A': adatom of different species, B: vacancy, B': Inclusion of a foreign atom in the surface, C: twist dislocation, D: ledge-adatom, E: edge-dislocation, F: kink, G: step-edges. Picture copied from [ue96].

A quantitative description of defects can be achieved by using an autocorrelation function:

$$P(\vec{R}) = \int \rho(\vec{r})\, \rho(\vec{r}+\vec{R})\, d\vec{r} \tag{1.4}$$

$\rho(\vec{r})$ is the probability of finding a defect at position $\vec{r}$, within the radius $d\vec{r}$. With the autocorrelation function it is possible to calculate the probability $P(\vec{R})$ to find another defect within the radius R around $\vec{r}$. Defects can be divided into two different sorts according to their autocorrelation values: Defect structures with long-range order show high $P(\vec{R})$-values for large distances R. Defects without long-range order have $P(\vec{R})$-values close to zero for large R-values. [ls93, ue96]

Dislocations and domain boundaries are special kinds of defects. Dislocations are volume defects by definition but they produce line- or point defects when they reach a surface, like shown in figure 1.4. They are characterized by the dislocation axis $\vec{\xi}$ and the burgers vector $\vec{b}$, which marks the difference between disturbed and undisturbed surface lattice. For screw dislocations $\vec{b}$ and $\vec{\xi}$ are parallel, resulting in a value equal to $\vec{b}$ for the product $\vec{\xi}\cdot\vec{b}$. In the case of an edge dislocation $\vec{b}$ stands normal to $\vec{\xi}$, giving a product equal to $\vec{\xi}$ or zero. A quantitative description is reached by the dislocation density ρ_d, which is calculated by

$$\rho_d = \frac{l_d}{V} \tag{1.5}$$

l_d is the length of the dislocation and V is the unity volume. The resulting value ρ_d corresponds to the number of dislocations going through a defined surface. [ls93, ue96]

Domain boundaries are often observed in adsorbate-layers. They separate areas with different orientation or structure, like shown in figure 1.5. Domain boundaries are formed by the merging of growing islands with different crystallographic parameters. [ls93, ue96]

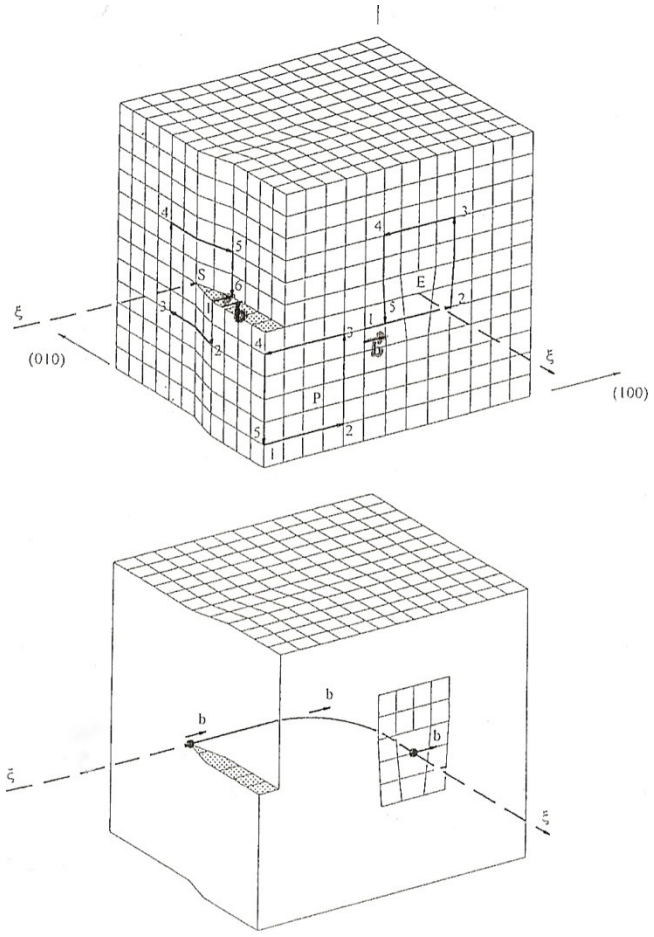

Fig. 1. 4: Mixed dislocation appearing as edge dislocation at the $(0\bar{1}0)$-surface and as screw dislocation at the $(\bar{1}00)$-surface. ξ denotes the dislocation axis, b is the Burgers vector. b is determined by comparison of closed loops of the undisturbed lattice (P) and the areas around the dislocations (E and S). Picture copied from [ue96].

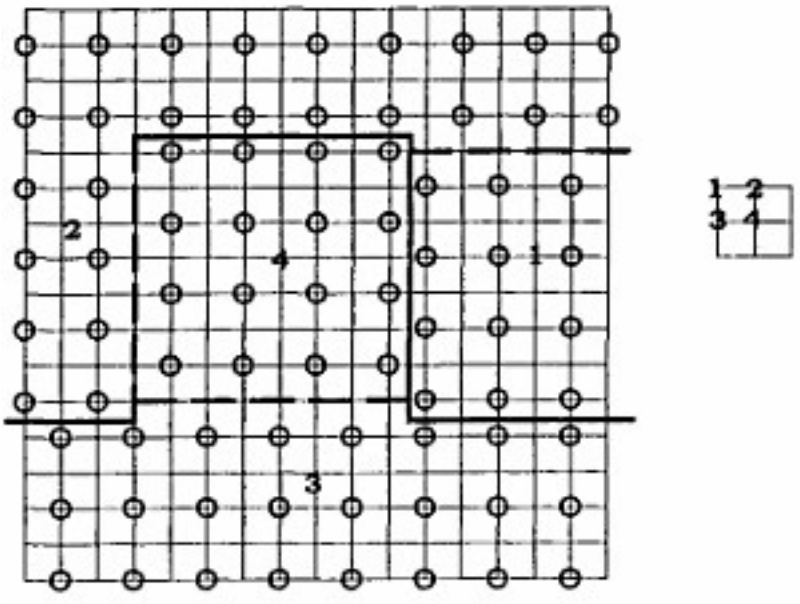

Fig. 1. 5: Domain boundaries for a (2×2)-superstructure on a square surface lattice. Four different domains (1-4) are shown in the image. Original picture from [ue96].

1.2.3 Superstructures

Superstructures can be formed either by reconstruction of a surface or by the growth of adsorbate-films. In the context of this thesis, the latter will be described in this section. When an adsorbate-film is grown on a crystalline surface it may either be amorphous or crystalline (epitaxial growth) itself. The emerging interface between substrate and adsorbate can be either abrupt, governed by interdiffusion or a new compound is formed at the interface. Sketches of these possibilities are shown in figure 1.6. [ls93]

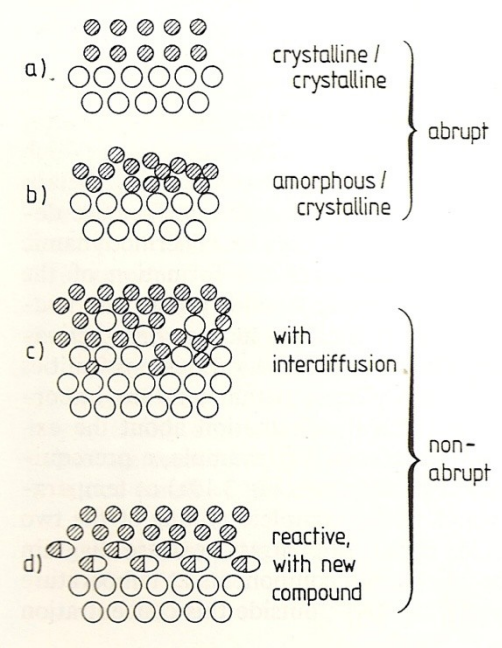

Fig. 1. 6: Different forms of solid-solid interfaces. Open and shaded circles represent different materials. Semi-shaded symbols depict compounds of these materials. Picture taken from [ls93].

If the adsorbate film or the newly formed compound has an ordered structure, a relation between the substrate lattice and the adsorbate lattice (newly formed compounds will also be addressed as adsorbates in the following discussion) can be formed. [ls93]

In the general case the unit cells of substrate and adsorbate will not be identical. The substrate surface lattice with the unit cell vectors $\vec{b}_1$ and $\vec{b}_2$ is described as a function of the undisturbed surface lattice of the substrate with the unit cell vectors $\vec{a}_1$ and $\vec{a}_2$. The most general form to describe the relation between the two lattices is the matrix notation

$$\begin{pmatrix} b_1 \\ b_2 \end{pmatrix} = \begin{bmatrix} s_{11} & s_{12} \\ s_{21} & s_{22} \end{bmatrix} \begin{pmatrix} a_1 \\ a_2 \end{pmatrix} \tag{1.6}$$

A classification of adsorbate structures can be achieved, by forming the determinant of the transformation matrix $\bar{S}$. Since the following relation is valid

$$\det \bar{S} = \frac{|\vec{b}_1 \times \vec{b}_2|}{|\vec{a}_1 \times \vec{a}_2|} \tag{1.7}$$

the determinant represents the ratio between the unit cell areas of substrate and adsorbate. If det $\bar{S}$ gives an integer number, the adsorbate forms a “simple superstructure”, if det $\bar{S}$ is a rational number, then the superstructure is called a “coincidence structure”. If det $\bar{S}$ results in an irrational number, then the adsorbate structure is called “incoherent” or “incommensurate”. Examples for these superstructure types are shown in figure 1.7. [ls93]

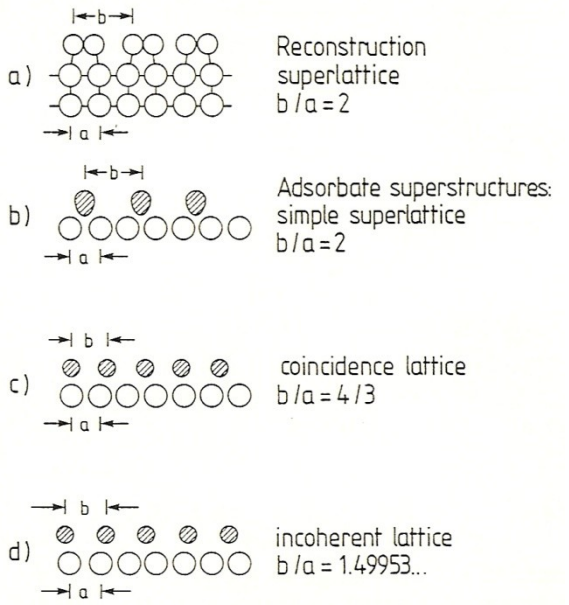

Fig. 1. 7: Different types of superstructures. Open and shaded circles represent different materials, with lattice constants a and b. In (a) the case of a pairing-row reconstruction of a crystal surface is shown. (b)-(d) depict different situations for adsorbate-layers on a substrate surface. Original picture from [ls93].

If the basic symmetries of the two lattices are the same (e.g. hexagonal on hexagonal) a more intuitive notation is used, called Wood’s notation. In this relation the lengths of the adsorbate-unit cell vectors are given as functions of the substrate unit cell vector lengths. Differences in the directions of the unit cell vectors are marked by a rotation-term:

$$b_1 = m a_1,\ b_2 = n a_1$$

$$\Rightarrow i(m \times n)R\ Z° \qquad (1.8)$$

i is an indicator for the type of the adsorbate unit cell: p stands for primitive and c for centred. If a primitive unit cell is present, the indicator is often omitted instead of writing p. Z is the degree of rotation of the adsorbate-lattice with respect to the substrate lattice in degrees. If the unit cell vectors of substrate and film have the same directions, then the rotation-term is left out. A few examples are shown in figure 1.8. Wood’s notation will be used throughout this thesis. [ls93]

Another important parameter is the lattice mismatch ε of the two lattices. It is calculated according to the following formula [ls93]:

$$\epsilon = \frac{b-a}{a} \qquad (1.9)$$

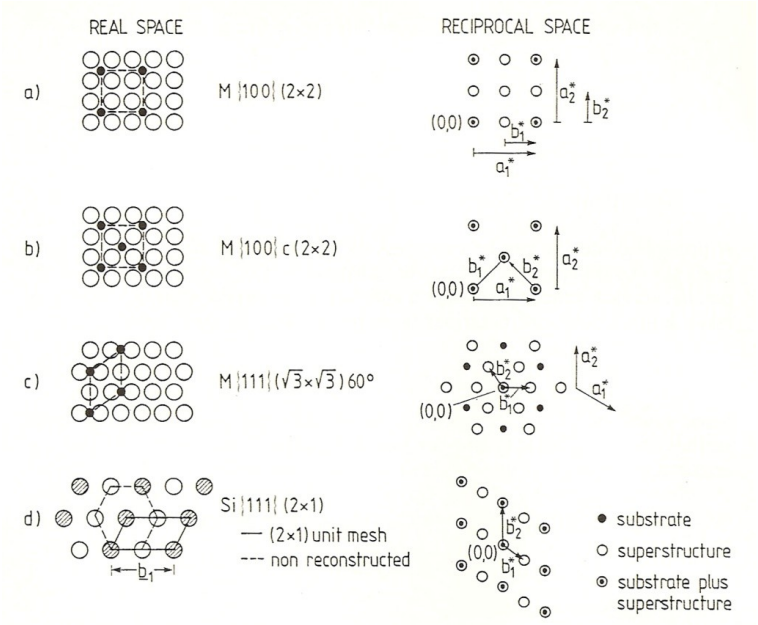

Fig. 1. 8: A few examples for Wood´s notation. In (a) to (c) adsorbate structures on different surfaces of a metal M are shown. (d) depicts the (2×1) reconstruction of a Si(111)-surface, which can be obtained by cutting the crystal in UHV. For all cases the corresponding structures are shown in real and reciprocal space. The c(2×2)-structure in (b) can also be written as primitive $(\sqrt{2}\times\sqrt{2})$R(45°). Picture taken from [Is93].

The mismatch between the two lattices can be compensated in two ways: either by straining the adsorbate film or by forming edge dislocations in it. Which type of compensation is applied, depends on the lattice mismatch ε itself and on the thickness h of the grown film. In figure 1.9 the total energy per unit area is plotted over ε and h for strain- and dislocation-

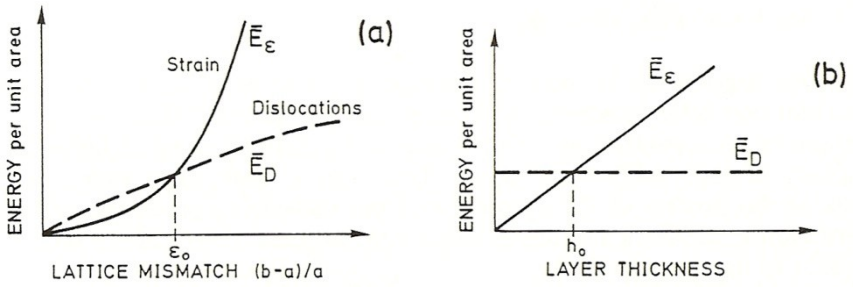

Fig. 1. 9: Dependence of the surface energy on the lattice mismatch ε (a) and the layer thickness h (b) of adsorbate layers. Solid lines represent the energy curves for strained films, broken lines show the energy curves for strain compensation by dislocation-formation. An adsorbate-film can only sustain the imposed strain if both, ε and h, stay below the critical values ε_0 and h_0. Otherwise the formation of dislocations becomes energetically more favourable. Original picture from [Is93].

compensation. For both parameters critical values, ε_0 and h_0, exist. If one of those critical values is exceeded, then the formation of dislocations becomes energetically more favourable than straining the film. The number of formed dislocations depends on the lattice mismatch and can be calculated by [Is93]

$$n_d = \frac{b}{\epsilon} = \frac{b^2}{b\text{-}a} \qquad (1.10)$$

1.2.4 Moiré effect

The moiré effect can best be described by an analogy from wave-mechanics: The superposition of two or more waves, with similar amplitude but slightly different wavelengths, leads to a modulation of the amplitude in the resulting signal – a beat.

A similar effect can be observed if two or more, slightly different, lattices are superimposed. The two basic operations to create a suitable difference are rotation of identical lattices against each other or superposition of lattices with slightly different periodicities. Also combinations of the basic operations are possible. In these cases a modulation of the amplitude or intensity of the resulting pattern can be observed, which shows a larger periodicity than the individual lattices. This is the moiré pattern. In figure 1.10 examples for the superposition of two lattices are given. [ak00]

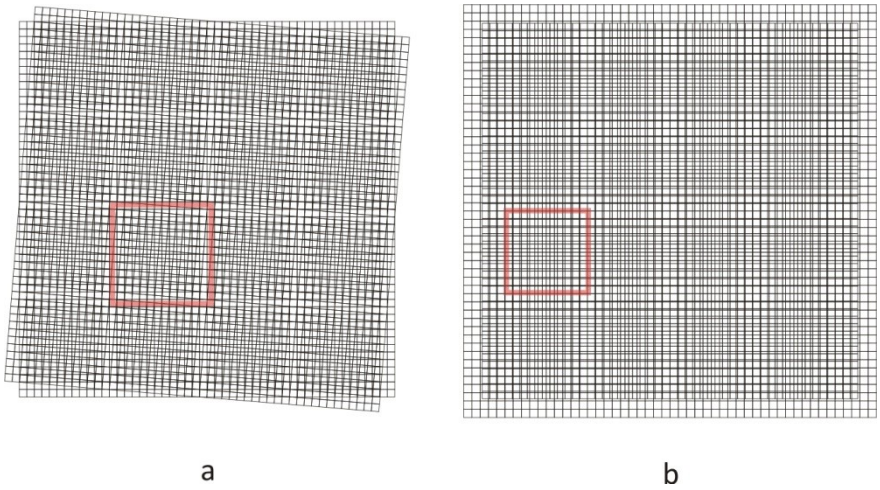

Fig. 1. 10: The moiré-effect, produced by rotation of identical square-lattices against each other (a) and by superposition of two square-lattices with different lattice constants. In both cases the unit cells of the resulting moiré-structures are marked with red lines.

The formation of moiré-patterns can also be observed in surface science, when the lattice constants of substrate and superstructure show small differences. This is typically the case for coincidence structures but can also be observed in the cases of defect structures or films with short ranged order. The moiré-effect creates a buckling of the surface like shown schematically in figure 1.11 for the case of different periodicities. [ak00]

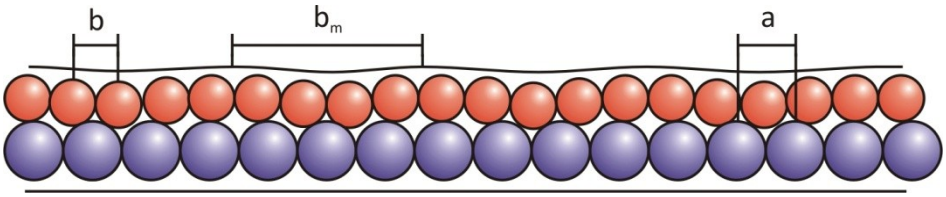

Fig. 1. 11: Origin of the moiré effect on crystal surfaces. On an even substrate, with lattice constant a (blue spheres), an adsorbate film, with lattice constant b (red spheres), forms a coincidence structure. Due to the lattice mismatch a buckling of the surface emerges, which gives rise to the moiré structure with periodicity b_m.

The periodicity of the moiré-pattern depends on the lattice constants of the superimposed structures and the angles, which they include. Since in surface science just two different structures are superimposed in most cases, the periodicity of the moiré-structure can be calculated by using the formula:

$$b_m = \frac{a \cdot b}{\sqrt{a^2+b^2-2ab \cdot \cos\alpha}} \tag{1.11}$$

where b_m is the periodicity of the moiré-pattern, a and b are the lattice constants of the superimposed structures and α is the angle, included by the base-vectors of these two structures. [ak00]

1.3 Electronic surface effects

The electronic structure of a surface differs from the one inside the bulk. The reason for this difference is the surface itself, which forces the electron density to decrease to zero rapidly. The consequences of this rapid drop can be analyzed with the help of the jellium-model [bd05, lp70].In this model the positive charges are not bound to the atomic cores, but smeared out evenly over the whole volume of the solid, with a sharp cutoff at the surface. [bd05]

As shown in figure 1.12, the electron-density cannot follow the sharp edge of the positive charge density but decreases within a certain distance, which is called the screening length. The reason for this effect is the finite wavelength of the electron-wavefunction, which is shortest for electrons at the Fermi-level with

$$\lambda_f = \frac{2\pi}{3\pi^2 n^{1/2}} \tag{1.12}$$

λ_f is the wavelength at the Fermi level and n is the electron density. With the Fermi-wavelength the smallest possible screening length can be calculated:

$$r_{sf} = \sqrt{a_0 \cdot \lambda_f} \tag{1.13}$$

with a_0 being the Bohr-radius. As a result of (1.12) and (1.13) the screening length depends on the electron density in the solid. This is also shown for two examples in figure 1.12. [bd05, lp70]

The damped oscillation of the electron density near the surface (Friedel-ocillation) is also a result of the finite electron-wavelength. It ends with an exponential decay of the electron density at the surface of the solid. Due to this exponential decay a dipole is formed at the surface, which has some strong influence on the electronic and structural properties of the surface. [bd05]

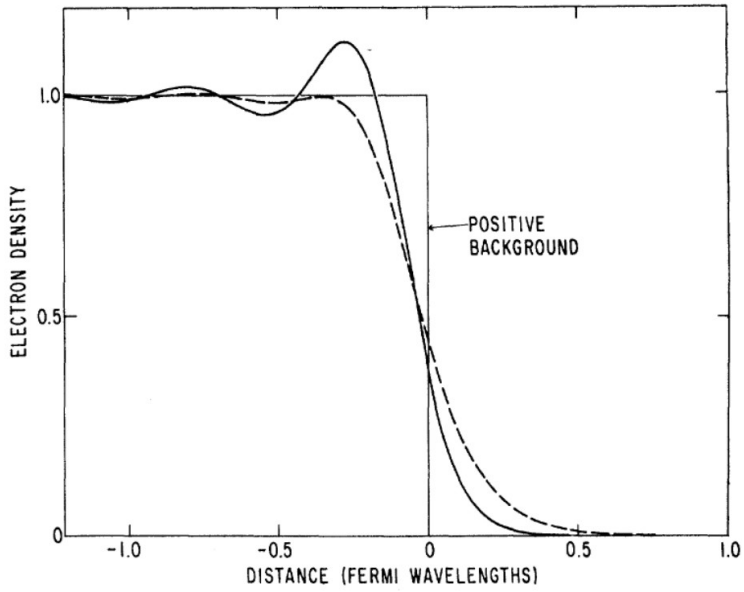

Fig. 1. 12: The Jellium model of a surface. At the abrupt cutoff of the positive charge density at the surface, the electrons can only react within the screening length, which is given by (1.13). The screening length itself depends on the overal electron density, which is shown by the dashed (2.02×10^{23} electrons/cm^3) and the solid line (1.29×10^{23} electrons/cm^3). Picture taken from [lp70]

Results of the formation of a surface dipole are e.g. relaxation (reduction of the interlayer-spacing near the surface) of some surfaces due to Coulomb-repulsion, the Smoluchowski-effect (smearing out of the electron charge density at step edges) and a change of the workfunction of the material [bd05, Ls93]. The influence of the surface dipole in the last point has the effect, that different surfaces of a material show different workfunctions, since the value of the dipole-moment depends on the surface-structure: open or rough structures have lower workfunctions, than close-packed ones. [bd05]

Structure and composition of the surface also have some other influences on the wavefunction of the electrons, which have become known under the name “quantum size effects”. Thin adsorbate-films, step edges, islands or adatom-structures may pose boundary conditions which result in oszillations of the electron density at the surface, which may form standing waves under suitable conditions. A famous example for such a case, the quantum coral [cs93], is shown in figure 1.13. These oszillations of the electron density do not only change the overall energy of adsorbate films, but they can also lead to electronic repulsion of adatoms. Thus they play an important role for nucleation and film growth. [bd05]

One prerequisite for the emergence of quantum-size effects is that the concerned electrons are in special surface states. These electronic states are a result of the periodicity of the surface structure (surface-lattice). Due to this periodicity 2-dimensional Bloch waves emerge with wavefunctions $\psi_{(\vec{r})}$:

$$\psi_{(\vec{r})} = u_k(\vec{r}_{\parallel}, z) \cdot \exp(i \cdot \vec{k}_{\parallel} \cdot \vec{r}_{\parallel}) \qquad (1.14)$$

where $\vec{r}_{\parallel}$ and $\vec{k}_{\parallel}$ are wave vectors parallel to the surface in real and reciprocal space, z is the surface position and u_k is the amplitude-function of the Bloch-wave. [bd05]

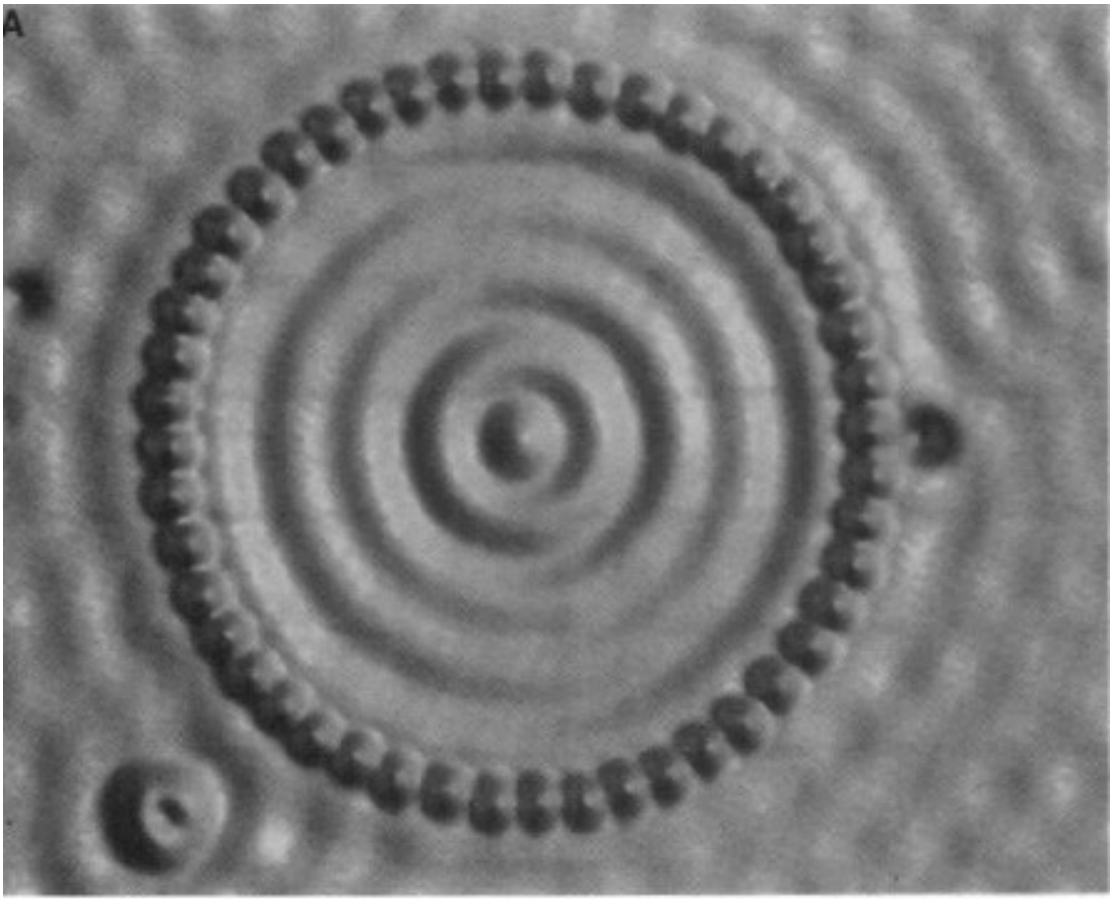

Fig. 1. 13: Standing electron waves within a quantum coral obtained by precise positioning of Fe-atoms on a Cu(111)-surface. Original picture from [cs93].

Real surface states are characterized by u_k-values which diminish in the bulk, or in other words: there exist no bulk states with the same $\vec{k}_{||}$-vectors or the same energy. As a result of this differentiation, surface states can only be found in places of the band structure, where no bulk-states are projected onto the surface. [bd05]

Examples for surface states are shown in figure 1.14 for a metal and a semiconductor. In case of a metal (figure 1.14a) the electrons in a surface state are practically free, because their electron density is located on the outer side of the surface. Thus they are only slightly influenced by the cores in the solid. [kp83]

Surface states of semiconducting materials (figure 1.14b) have their origin in dangling bonds (unsaturated valence states) at the surface. These dangling bonds are highly energetic. Thus they pose a major driving force for surface reconstructions of semiconductors, which aim for their minimization [ls93, ue96]. Yet in most cases total saturation of the valence states is not possible. The remaining unsaturated states form a new band of surface states. Often these surface states are split up into filled and empty bands, depending on the material and the surface, due to asymmetries in the surface structures and thus in the saturated valence states. [bd05]

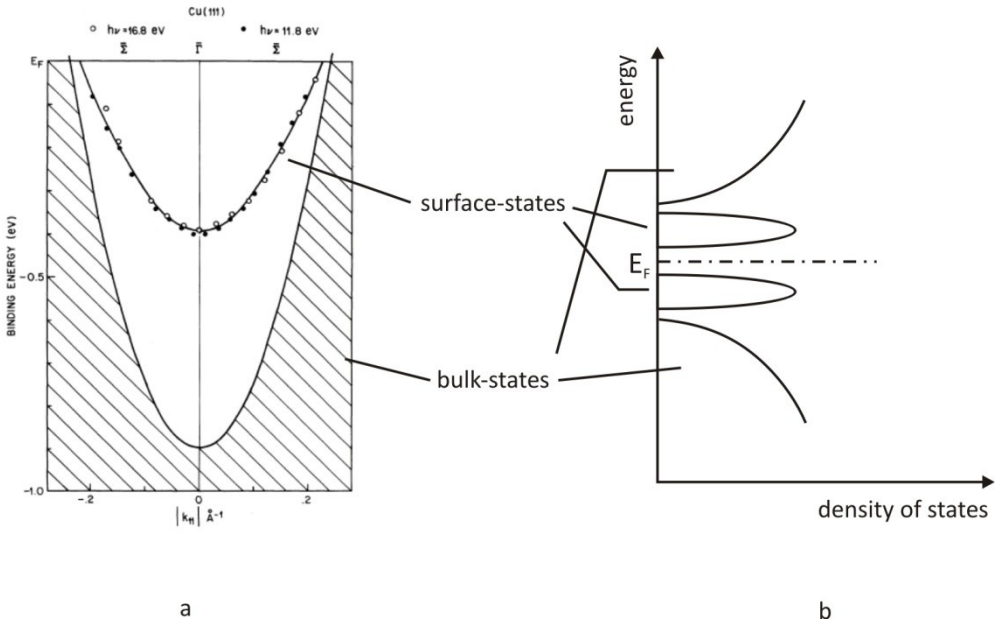

Fig. 1. 14: Surface states in a metal (a) and in a semiconductor (b). In the metal the electrons in the surface state are practically free (visible from the parabolic shape in the energy dispertion relation). In the semiconductor a splitting of the surface state into a filled band (donor) and an empty band (acceptor) takes place. If these surface bands are situated within the band gap, the Fermi level E_F is often situated between them to avoid surface charging. Original pictures from [kp83] (a) and [bd05] (b).

The surface states of semiconductors come to a special meaning when they are located within the bandgap. Charge neutrality of the surface is only given if the Fermi-level at the surface is energetically located above the filled band and below the empty band, like shown in figure 1.14b. If the Fermi-level were situated higher, electrons would be inserted into the empty band resulting in a negative charging of the surface. An according positive surface charging can be obtained by an energetic lowering of the Fermi-level and thus a removal of electrons from the filled band. Due to this mechanism the Fermi-level at the surface is fixed between the bands of the surface states, to avoid charging of the surface, if a corresponding counter-charge cannot be created within the bulk (e.g. by high doping concentrations). This effect is also known as Fermi-level-pinning. [bd05, ls93]

1.4 Polar surfaces

Every surface of a solid has a microscopic dipole moment due to the electrons reaching out of the surface. Yet a special class is formed by polar surfaces. They differ from non-polar surfaces by the presence of an additional macroscopic dipole moment $\vec{P}$ of intrinsic origin across the surface. [gr08, jw75]

For analysis of this intrinsic origin it is helpful to imagine a surface, created by cutting a single crystal at position x along the surface normal $\vec{n}$. No reconstruction or other

adjustment processes shall take place – so the surface represents a "frozen bulk termination" [gr08]. If the bulk unit cell of the crystal has a nonzero dipole moment in the direction of $\vec{n}$, then the planes parallel to the surface act like condensers with a resulting layer dipole moment per unit area

$$\mu_l = \sigma \cdot d \qquad (1.15)$$

where σ is the charge density within a layer and d is the layer spacing [gr08, nj00]. These microscopic dipole moments μ_l add up to a macroscopic dipole moment which can be measured across the surface. The polarity of the surface thus depends on its orientation $\vec{n}$. [gr08]

This insight allows a classification of surfaces. A widely used criterion is the one of Tasker, which is originally formulated for ionic crystals:

> "Type 1 is neutral with equal numbers of anions and cations on each plane and type 2 is charged but there is no dipole moment perpendicular to the surface because of the symmetrical stacking sequence. The type 3 surface is charged and has a dipole moment in the repeat unit perpendicular to the surface." [tj79]

This characterization can be generalized for all kinds of crystals by focussing on the bulk unit cell instead of the sequence of crystallographic planes: In every crystal it is possible to choose a dipole-free bulk unit cell parallel to the surface. This is shown schematically in figure 1.15. Note that the dipole-free unit cell contains incomplete atomic layers in the shown case. [gr08]

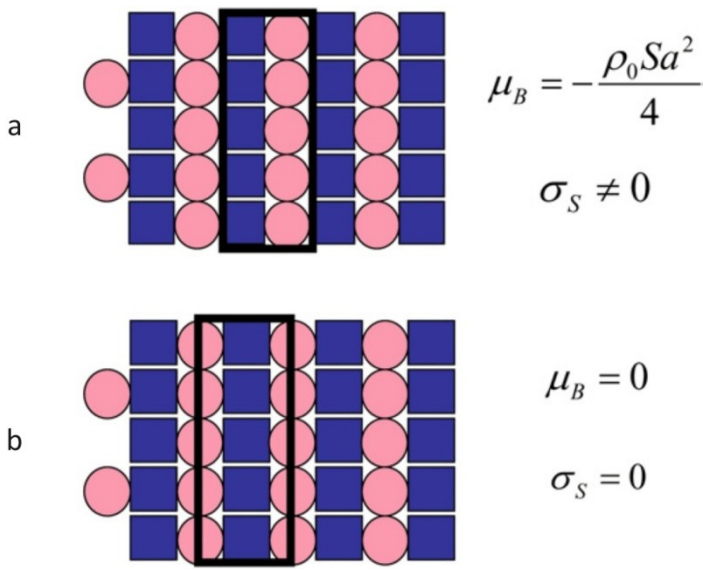

Fig. 1. 15: Choice of a dipole-free unit cell. The crystal is built up by two differently charges species /blue squares and pink circles), which are located in separate planes parallel to the surface (left side). If the surface unit cell is chosen like shown in (a), it has a non-zero bulk dipole moment μ_B and a surface charge σ_s. A dipole-free unit cell of the same structure is shown in (b). Picture taken from [gr08]

From this point of view the characterization of surfaces can be rephrased in the following way:

> "A frozen bulk termination is polar, if it cannot be obtained by piling up dipole-free bulk unit cells exclusively. A frozen bulk termination is non-polar, if there exists (at least) one dipole-free bulk unit cell which leaves the surface region empty, that is, without complete or incomplete atomic layer(s)." [gr08]

This point of view has two direct consequences: By defining a dipole-free bulk unit cell, the origin of the macroscopic dipole moment is shifted into the surface region and it is also shown, that the question of polarity does not only depend on the surface orientation, but also on its termination. If, for example, the dipole-free bulk unit cell includes incomplete atomic layers, like in figure 1.15, it automatically results in a polar bulk termination. [gr08, tj79]

If the bulk termination of a crystal is indeed polar, this has an energetic consequence for the surface, because the macroscopic dipole moment makes a contribution to the surface free energy [gr08, nj00]. With (1.15) this contribution E_p can be calculated to be

$$E_p=2\pi N d\sigma^2 \tag{1.16}$$

where N is the number of crystallographic planes parallel to the surface. Now a single crystal, cut at position x along $\vec{\hat{n}}$, can be viewed as a semi-infinite system and N tends toward infinity. Yet if this is the case, then E_p diverges, what leads to a surface instability. On basis of this conclusion a stability criterion can be phrased, which must be fulfilled by every polar surface:

$$\frac{\mu_b(x)}{\Omega_0}-\sigma_s(x)=0 \tag{1.17}$$

In this formula μ_b is the bulk dipole moment, Ω_0 is the volume of the bulk unit cell and σ_s is the "polarization surface charge density" [gr08, nj00, jw75], which is defined by

$$\sigma_s=\vec{P}\cdot\vec{\hat{n}} \tag{1.18}$$

where $\vec{P}$ denotes the polarization across the surface. As a consequence of this relation $\sigma_s = 0$ for non-polar surfaces and $\sigma_s \neq 0$ for polar surfaces. Since the contribution from the bulk can be eliminated by the choice of a dipole-free bulk unit cell, the stability criterion can only be achieved by changes in the surface electronic structure until $\sigma_s = 0$. These changes create a "compensating field" [gr08, ah76] E_c, which needs to reach a value of

$$E_c = -4\pi \cdot \vec{P} \tag{1.19}$$

to fulfil the stability criterion. [gr08, ah76]

Possible mechanisms for such a surface stabilization include [gr08, nj00]:

- population of surface states
- metallization of the surface
- desorption of atoms or other changes of the stoichiometry
- reconstruction and faceting of the surfaces
- creation and ordering of defects
- adsorption of foreign species
- etc.

The processes which occur on a specific surface strongly depend on the material and on the energetic and kinetic parameters of the surface. Thus in most cases a prediction of the stabilization mechanism is not possible. A consequence of (1.17) is, that frozen bulk termination of crystals cannot be observed experimentally, when the corresponding surface is polar, because some kind of stabilization must take place. [gr08, nj00]

This is however different for thin films with a polar surface. The discussion above is based on the insight that the contribution E_p of the polarization to the surface free energy diverges if the number of atomic planes N parallel to the surface tends towards infinity. In thin films this prerequisite is not given since N is finite. Thus the film can sustain a polarization and the stability criterion (1.17) becomes obsolete. Yet many films show a reaction to the polarization, although compensation is not necessary. Especially in ionic films structural changes and relaxation can be observed as a consequence of the surface polarization. Also with increasing thickness of the film a gradual transition towards the semi-infinite model takes place, which has been discussed above, where a surface stabilization is compellingly necessary. [gr08]

1.5 Growth of thin films

The first steps in the formation of adsorbate-structures are shown in figure 1.16. When some material is deposited onto a surface, the corresponding particles hit the surface, with a rate

$$r_i = \frac{p}{\sqrt{2\pi m_a k T_0}} \tag{1.20}$$

where p is the pressure in the gas phase, m_a is the mass of incoming particles, T_0 is their temperature in the gas phase and k is the Boltzmann-constant. [ls93]

Once the particles have hit the surface, they can either condensate on it or desorb again. In the first case a surface diffusion of the condensed particles sets in. The mean diffusion time on the surface depends on the desorption rate for the condensed particles which is related to the activation energy for desorption E_d and the surface temperature T_s by

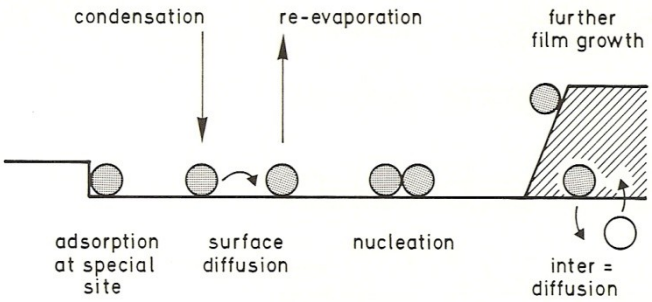

Fig. 1. 16: Microscopic processes during film growth. Particles have a certain probability to desorb from the surface after condensation. They only stay on the surface if they find a suitable adsorption site by surface diffusion. If they coalesce with other adsorbed particles, nucleation centres are formed. Original picture from [ls93].

$$r_d \sim \exp\left(\frac{E_d}{kT_s}\right) \tag{1.21}$$

The particles can only stay longer on the surface if they find suitable adsorption sites. Such sites may be step edges, defects or other adsorbed particles. In the latter case nucleation centres are formed. Yet these nuclei can only then be the origin of larger adsorbate structures, if they reach a critical size within time. Otherwise they disintegrate again and the individual particles desorb or start surface diffusion again. The rate of formation for nuclei with critical size is governed by the surface temperature and the gain in Gibbs free energy ΔG_n due to the formation of the nucleation centre [ls93]:

$$r_n \sim \exp\left(-\frac{\Delta G_n}{kT_s}\right) \tag{1.22}$$

The term ΔG_n can be approximated by a thermodynamic description of the nucleation centres. In this context a differentiation is necessary concerning the form of the individual nuclei. For three-dimensional nuclei the following relation is valid:

$$\Delta G_{3D} = -j \cdot \Delta\mu + j^{2/3} \cdot X \tag{1.23}$$

j is the number of particles in the nucleus and $\Delta\mu$ is the chemical potential with the relation:

$$\Delta\mu = kT \ln \frac{p_0}{p} \tag{1.24}$$

where T is the temperature of the particles in the gas phase, p is the partial pressure of the particles in the gas phase and p_0 is the equilibrium vapour pressure for this species. The ratio of p_0 to p is called “supersaturation”. X is can be calculated by

$$X = \sum_k C_k \gamma_f^{(k)} + C_{s/f}(\gamma_{s/f} - \gamma_s) \tag{1.25}$$

In this context the γ-values stand for the surface tension of the individual facets (k) of the nucleus (f), of the substrate surface (s) and the interface between substrate and nucleus (s/f), as shown in figure 1.17. The corresponding C-values are geometric factors, linking the number of particles j to the area A of the different facets and interfaces by [ls93]

$$C_k = \frac{A_k}{j^{2/3}} \tag{1.26}$$

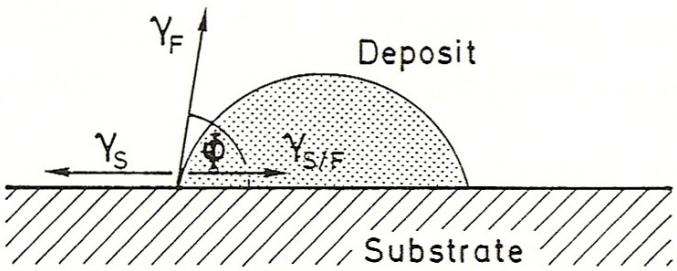

Fig. 1. 17: Surface tensions determining the shape and growth-mode of nucleation centres and adsorbate-films. The individual values represent the surface tension of the substrate surface (γ_s), of the nucleus- or the film-surface (γ_f) and of the interface between substrate and nucleus/film (γ_{sf}). For the surface values a vacuum above the surface is assumed. Original picture from [ls93].

In the case of a two dimensional nucleation centre the change in the Gibbs free energy can be calculated by

$$\Delta G_{2D} = -j \cdot \Delta\bar{\mu} + j^{1/2} \cdot Y \tag{1.27}$$

$\Delta\bar{\mu}$ is an "effective chemical potential" of the nucleus which is defined by

$$\Delta\bar{\mu} = \Delta\mu - (\gamma_f + \gamma_{s/f} - \gamma_s) \cdot \Omega^{2/3} \tag{1.28}$$

with Ω being the area covered by the nucleus. The factor Y can be calculated with

$$Y = \sum_l D_l \gamma_l \tag{1.29}$$

where γ_l denotes the energy of an edge of the nucleus and D links the edge-length e to the number of particles j:

$$D_l = \frac{e_l}{j^{1/2}} \tag{1.30}$$

With help of the ΔG_n-values the critical size of the nucleation centres can be calculated. Since $\Delta G_n < 0$ must apply to let a stable nucleus grow, the critical size can be approximated by setting ΔG_n equal to zero. The resulting values for 2D- and 3D-nuclei are also called "nucleation barriers":

$$j_{cr,2D} = \left(\frac{Y}{2\Delta\bar{\mu}}\right), \; j_{cr,3D} = \left(\frac{2X}{3\Delta\mu}\right) \tag{1.31}$$

The relation of Gibbs free energy, critical size and chemical potential is shown in figure 1.18 for 2D- and 3D-nuclei. Remember, that the chemical potential is a function of the supersaturation in the gas phase. From the graphs it becomes obvious that film growth is only possible if this supersaturation is large enough. It also becomes clear that a nucleus smaller than the critical size will tend to disintegrate again. [ls93]

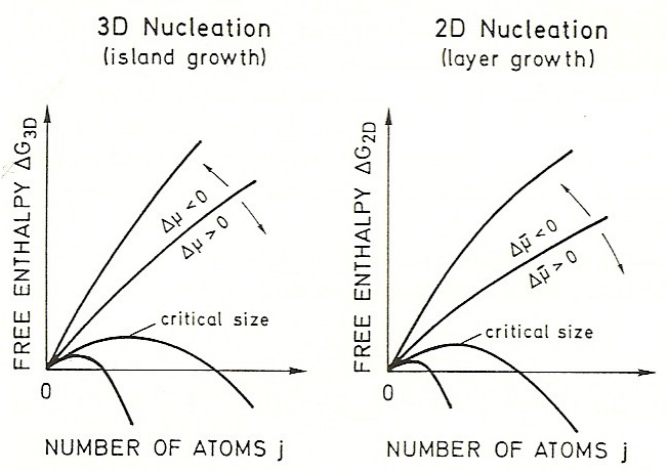

Fig. 1. 18: Relation of the Gibb's free energy (enthalpy) ΔG to the number of atoms j in the nucleation centre. Δμ and $\Delta\bar{\mu}$ are the chemical potential (3D-nucleation) and the effective chemical potential (2D-nucleation). In the graphs they represent the grade of supersaturation in the gas phase. Growth of a film can only occur for a decreasing value of ΔG. This is only the case for supersaturation grades larger than zero and a number of atoms in the nucleus larger than the critical size. Picture taken from [ls93].

Yet if a nucleation centre exceeds the critical size, film growth will set in. Generally three different growth modes can be distinguished, as shown in figure 1.19. For Frank-van der Merve growth (figure 1.19a), the individual layers of the film grow one after another. This is a result of a strong interaction of the film with the substrate and weaker binding-forces within the film. This growth mode is also called layer-by-layer growth. The complementary case is Vollmer-Weber growth (figure 1.19c). In this case the interactions within the film are stronger than those between film and substrate. As a result the adsorbate-film does not cover the entire surface but tends to form individual islands instead. This growth mode is also called island-growth. The third case is a mixture of these two extremes: In the Stranski-Krastanov growth (figure 1.19b) a single adsorbate-layer is formed first, then the film changes to island growth for the successive layers. [ls93]

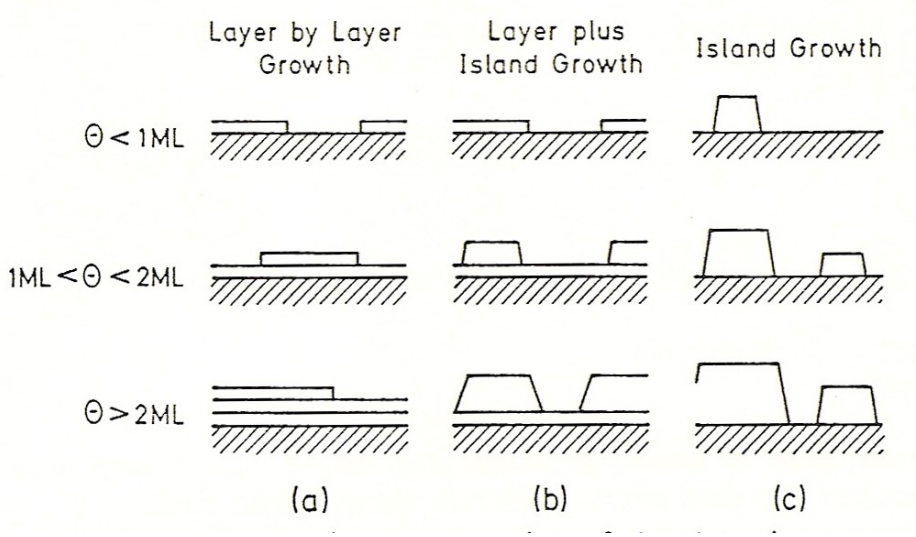

Fig. 1. 19: Different growth modes for adsorbate films - (a) Frank van der Merve-growth, (b) Stranski-Krastanov-growth, (c) Volmer-Weber-growth. Original picture from [ls93].

Which growth mode applies to a certain surface- and material-combination depends on the interaction of the surface tension values, as shown in figure 1.17, and the supersaturation in the gas phase. The following relations apply-

for Frank-van der Merve growth

$$\gamma_s > \gamma_f + \gamma_{s/f} + c \cdot kT \cdot \ln \frac{p_0}{p} \tag{1.32}$$

and for Vollmer-Weber growth

$$\gamma_s < \gamma_f + \gamma_{s/f} + c \cdot kT \cdot \ln \frac{p_0}{p} \tag{1.33}$$

with c being a constant.

Concerning the growth of 2D- and 3D-nucleation centres one more thing should be mentioned in relation with the supersaturation. A 3D-nucleus needs a supersaturation to grow, since the second part in (1.23) is always positive. This means that a gain in the Gibbs free energy can only be obtained if the first term stays negative and that is only the case if $p>p_0$. For a 2D-nucleus however an additional term $(\gamma_f+\gamma_{s/f}-\gamma_s)\cdot\Omega^{2/3}$ comes into play, as shown in (1.27) and (1.28). If γ_s is sufficiently larger than $\gamma_f + \gamma_{s/f}$, then growth of the nucleus also occurs for $p<p_0$. Thus supersaturation is not compellingly necessary for film growth if the right surface- and material combination is chosen. [ls93]

Chapter 2: Experimental techniques

This chapter deals with the techniques, which have been used to prepare and investigate the sample surfaces in this thesis. The experiments have been carried out in an ultra-high-vacuum (UHV) system with a base pressure of 1×10^{-10} mbar. A photograph of the system can be seen in figure 2.1. It basically consists of four chambers in a linear arrangement: one chamber for the preparation of the sample surfaces, one chamber for fast transfer of samples into and out of the UHV-system and two chambers containing the measurement facilities for the surface characterisation – a low energy electron diffraction system (LEED) and a scanning tunnelling microscope (STM). [hr07, kp97, wj09]

For this thesis the preparation chamber has been equipped with a sputtergun, two thermal evaporators for zinc and cobalt, a quartz-microbalance, an indirect sample heating and gas inlets for argon, oxygen and hydrogen. An additional dosing system for pyridine-molecules has been mounted on the transfer chamber.

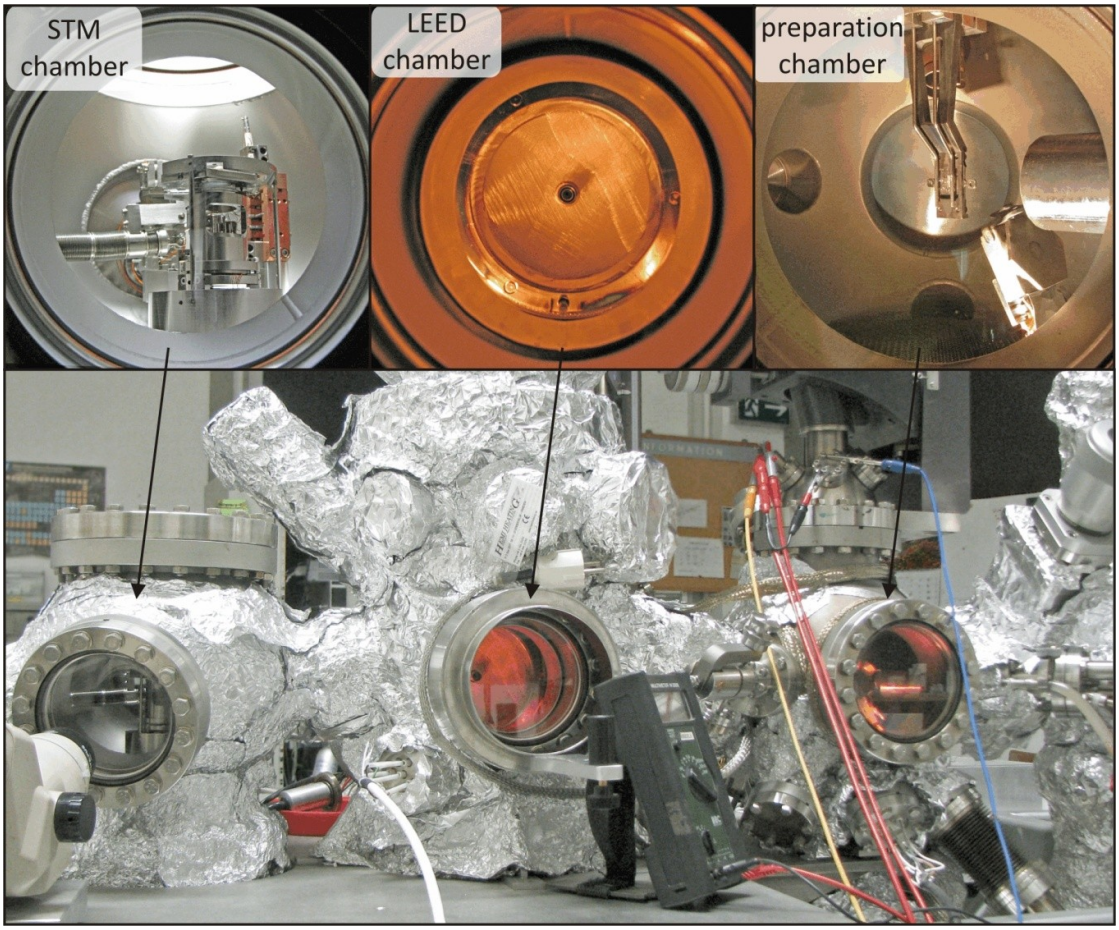

Fig. 2. 1: Photographs of the UHV-system and the three main-chambers, containing STM, LEED and the facilities for the sample preparation. To the right of the preparation chamber a fourth chamber is situated, which is used for fast transfer of samples and STM-tips into and out of the system. Samples and tips can be transferred from one chamber to another by a linear motion transfer-rod, which is mounted to the fast-transfer chamber.

The LEED consists of a 3-grid electrooptical system by VG in combination with a LEG-2 electron gun. The tunnelling-microscope is a 024 µ-STM by Omicron, which is operated at room-temperature. STM-tips have been tailored out of a 0.3 mm tungsten-wire by electrochemical etching with a NaOH-solution or by cutting of a 0.3 mm Pt/Ir-wire. Final tip-cleaning has been performed with an electron bombardment-system situated in the STM-chamber. Data analysis has been carried out by using the WSXM-software. [hr07, kp97, wj09]

The vacuum is created and maintained with a typical pumping system, consisting of a rotary-valve-pump, a turbo-molecular-pump, an ion-pump and a titanium-sublimation-pump. The pressure is monitored by two ion-pressure-gauges, situated in the preparation- and in the LEED-chamber. For vibration isolation the whole UHV system is supported by an active table damping system by Melles-Griot, consisting of three pylons operated with pressured air. [hr07, kp97, wj09]

In the following three sections a short introduction to the surface-characterisation methods, LEED and STM, will be given, followed by an explanation of the applied preparation-procedures for thin adsorbate films on the sample crystal.

2.1 Low energy electron diffraction (LEED)

2.1.1 Basic principle

In LEED, electrons with low energy - typically below 100 eV – are diffracted on a surface. Due to their wave nature, the electrons interfere and a diffraction pattern is formed, depending on the atomic structure of the surface. Because of the low kinetic energy of the electrons, their penetration depth into the crystal is limited to a few atomic layers - thus LEED is highly surface-sensitive. Like in other diffraction methods, the signals obtained by LEED provide information, which is averaged over the whole area illuminated by the incident electron beam. This allows the determination of the periodicity of surface structures with a sufficient long range order with a high degree of precision. Yet due to this averaging-process the phase information is lost, thus LEED can only provide a generalized picture of the investigated surface. [ev85]

2.1.2 Theoretical approach – geometric diffraction

Diffraction on a one-dimensional lattice, as shown in figure 2.2a, can be described using the Bragg-relation. According to this relation, positive interference of the diffracted beams occurs for angles θ, if

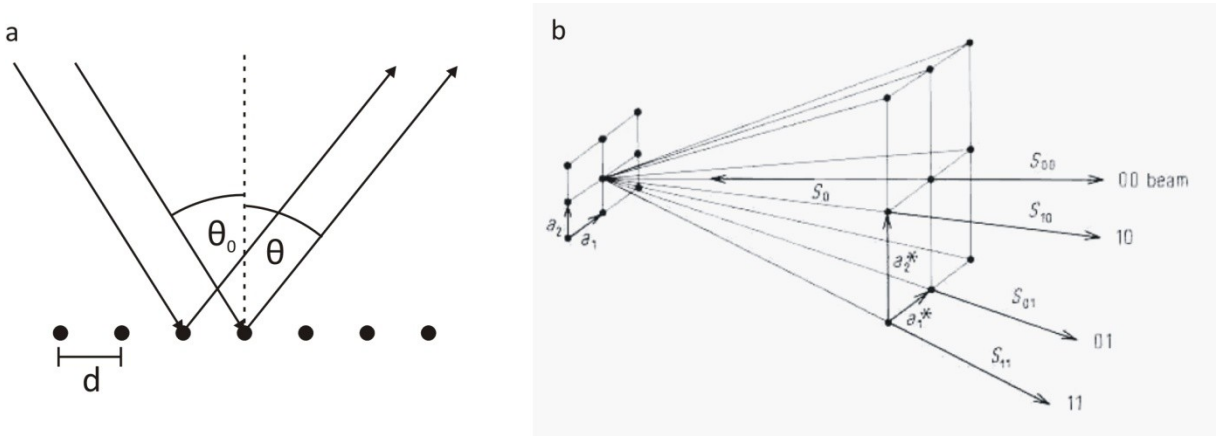

Fig. 2. 2: (a) Diffraction at a one-dimensional lattice. d is the distance between two scatterers, θ_0 is the angle between the incident beam and the surface normal and θ is the corresponding angle of the reflected beam. (b) Diffraction at a two dimensional lattice in vector notation. $a_{1,2}$: unit cell vectors of the surface lattice, s_0: incident beam normal to the surface, s_{xy}: directions for positive interaction of the reflected beams, $a^*_{1,2}$: reciprocal unit cell vectors of the surface lattice. Original pictures from [ev85]

$$d\cdot(\sin\theta - \sin\theta_0)=n\cdot\lambda \qquad (2.1)$$

is fulfilled. In this formula d is the distance between two diffraction centres, θ_0 is the incident angle, θ is the reflection angel, n is the diffraction order and λ is the wavelength of the incident beam. For the electrons in LEED the corresponding de Broglie wavelength is given by

$$\lambda=\frac{h}{m\cdot V_a}\approx\sqrt{\frac{1.5}{V_a}} \qquad (2.2)$$

where h denotes Planck´s constant, m is the mass of an electron and V_a is the acceleration voltage of the electrons. [ev85]

A two-dimensional lattice can be seen as two superimposed one-dimensional lattices including a 90°-angle. Since the incident angle in a typical LEED system is $\theta_0 = 0$, relation (2.1) can be rewritten as

$$d_1\cdot\sin\theta_1 = n_1\cdot\lambda \qquad (2.3)$$

$$d_2\cdot\sin\theta_2 = n_2\cdot\lambda$$

where the indices denote the two different lattices. [ev85]

More insight into this situation can be gained if the diffraction at a two-dimensional lattice is described by using vector notation, like shown in figure 2.2b. If $\vec{s}_0$is the direction of the incident electron beam and $\vec{s}$ are the vectors pointing into the directions of positive interference of the reflected waves, then the following relations are valid:

$$\vec{a}_1(\vec{s}-\vec{s}_0)=h_1\lambda \qquad (2.4)$$

$$\vec{a}_2(\vec{s}-\vec{s}_0)=h_2\lambda$$

where $\vec{a}_1$ and $\vec{a}_2$ are the unit cell vectors of the surface point-lattice and $h_{1,2}$ represent the diffraction order. These are the Laue-equations for diffraction on a two-dimensional lattice, which are equivalent to the Bragg-relations shown in (2.3). The solution for these relations is given by

$$\frac{\vec{s}-\vec{s}_0}{\lambda} = h_1\vec{a}_1^* + h_2\vec{a}_2^* \tag{2.5}$$

where $\vec{a}_1^*$ and $\vec{a}_2^*$ are the reciprocal lattice vectors of the surface point lattice. This means that interference maxima for the reflected beams are determined by the directions of the surface reciprocal lattice. Thus the LEED image of a surface represents its reciprocal lattice. [ev85]

Due to equation (2.5) a graphical solution in reciprocal space becomes possible, which is known as the Ewald-construction. A sketch of this procedure is shown in figure 2.3 for the a_1-direction. The transformation equation for the surface normal into reciprocal space is given by

$$\vec{n}^* = \frac{\vec{a}_1 \times \vec{a}_2}{\vec{n}\cdot(\vec{a}_1 \times \vec{a}_2)} \tag{2.6}$$

In a perfect two-dimensional case, the length $|\vec{n}| = 0$. Consequently the lattice points in reciprocal space are elongated to infinite rods in direction $\vec{n}^*$, as shown in figure 2.3. To perform an Ewald-construction a vector with length $1/\lambda$ is drawn in direction s_0^* of the incident beam, so that its end point coincides with a lattice point on the surface which has

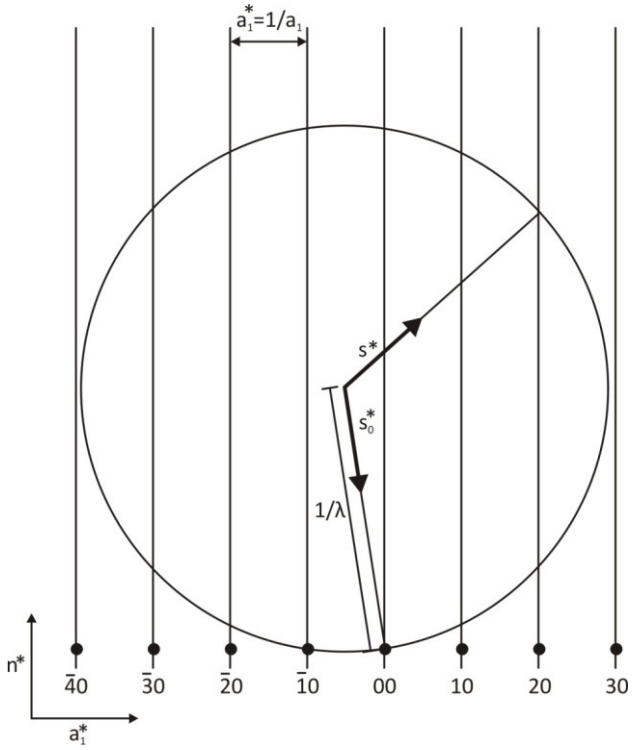

Fig. 2. 3: Ewald-construction in reciprocal space for a row of scatterers in direction of the reciprocal surface unit vector $\vec{a}_1^*$. λ is the wavelength, s_0^* is the incident beam vector, s* represents the direction of a reflected beam and $\vec{n}^*$ is the direction of the surface normal in reciprocal space. The numbers below each scatterer represent the indices of the corresponding LEED-spot. Original picture taken from [ev85].

been chosen as origin. Around the starting point of this vector a sphere with radius 1/λ is formed. The Laue equations are fulfilled for each point, where the sphere crosses a rod. In the corresponding directions interference maxima can be found and LEED spots appear. [ev85]

The Ewald-construction demonstrates nicely what happens if the acceleration voltage V_a of the electrons and thus the beam energy E_b is changed. According to equation (2.2) an increase in V_a leads to a decrease of the corresponding de Broglie wavelength λ. The decrease of λ on the other hand results in an increase of the radius of the Ewald-sphere. The consequences of this expansion are that more interference maxima can be observed, since more rods intersect the sphere and that the directions, in which the maxima appear, change. This change of direction manifests as a decrease of the angles θ_1 and θ_2 in equations (2.3), in other words – the maxima move towards the surface normal with increasing beam energy. [ev85]

If superstructures are present on the surface a superposition of the two lattices occurs in the LEED-image. This is shown for simple superstructures in figure 2.4. (a) represents the LEED-image of a hexagonal substrate lattice with the reciprocal lattice vectors $\vec{a}_1^*$ and $\vec{a}_2^*$. Now it is assumed, that this lattice is overlaid by a p(2×1)-superstructure. The length of the vector $\vec{b}_2$ of this superstructure is twice as large as the one of the substrate vector $\vec{a}_2$. Since the length of a lattice vector in real space is related to the length of the corresponding vector in reciprocal space by

$$\left|\vec{b}_2\right| = \frac{1}{\left|\vec{b}_2^*\right|} \tag{2.7}$$

it follows, that the length of the reciprocal space vector $\vec{b}_2^*$ is equal to half of the length of $\vec{a}_2^*$. As a consequence a LEED-image, as shown in figure 2.4b, is formed. Analogously the p(2×2)-pattern in figure 2.4c can be constructed.

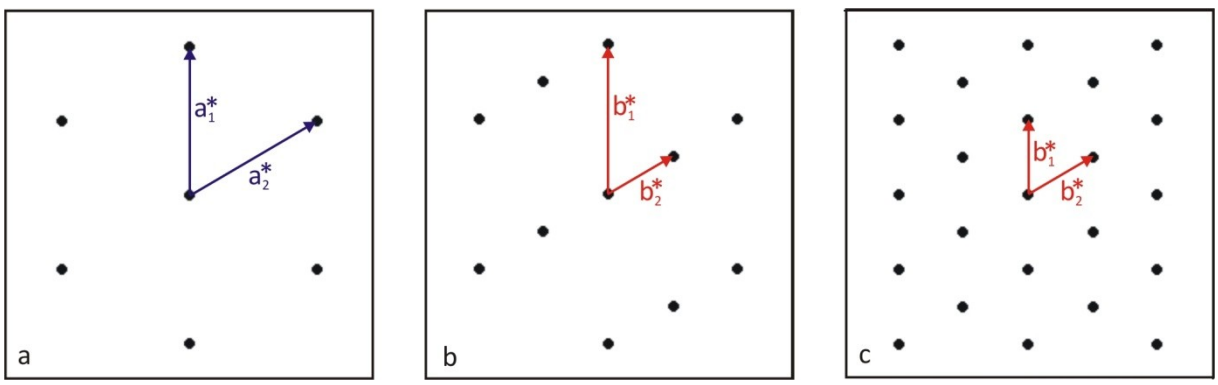

Fig. 2. 4: Theoretical LEED-images of a hexagonal substrate lattice (a) with a p(2×1)-superstructure (b) and a p(2×2)-superstructure (c). a_1^* and a_2^* represent the reciprocal unit cell vectors of the substrate lattice, b_1^* and b_2^* are the reciprocal base vectors of the corresponding superstructures.

The LEED-images in figure 2.4 are constructed for an ideal situation, where only the topmost surface layer contributes to the diffraction-pattern. In reality this is not the case. The penetration depth of the incident beam is not limited to the topmost layer but includes several atomic layers underneath it. This leads to multiple interferences of the reflected beams, in addition to several other dynamic effects which may take place. As a result of these phenomena the diffraction centres can no longer be represented by infinitely long rods in reciprocal space. Instead an intensity modulation along these rods occurs, as sketched by the broken lines in figure 2.5a. A LEED-spot is only created if the Ewald-sphere intersects a rod at a position of an intensity maximum. As a consequence not all the spots, shown in the examples of figure 2.4, are visible in a real LEED-image. An example for this effect is given for a p(2×2)-pattern in figure 2.5b. In this image only the innermost spots of the superstructure appear.

On the other hand the penetration depth of the incident beam also has several advantages. One of them is, that it allows a simultaneous analysis of substrate- and adsorbate-structures, even for closed adsorbate films up to a few monolayers thickness. In these cases the geometrical relation of the substrate- and adsorbate-lattices will still be reflected by the LEED-image. [ev85]

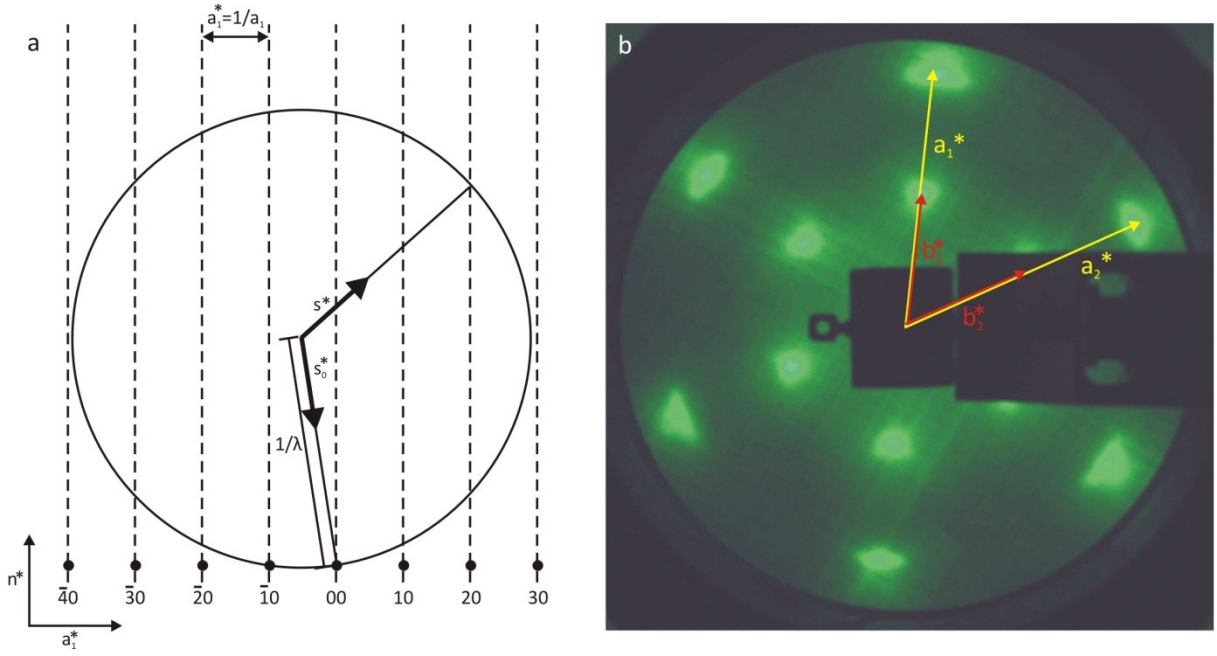

Fig. 2. 5: (a) Schematic Ewald-construction for a non-zero penetration depth of the incident electron beam. The resulting intensity modulation along the surface normal is sketched by the broken lines. Original picture from [ev85]. (b) Experimentally obtained LEED-image of a p(2×2) superstructure at E_b = 58.5 eV. In comparison to the theoretical pattern in figure 2.4c, several spots of the superstructure are missing. Legend: see figures 2.3 and 2.4.

LEED-patterns of simple superstructures can be evaluated quite easily. It becomes more difficult if different domains, coincidence- or incoherent superstructures are involved. In the case of different domains the observable effects depend on the ratio of the domain diameter d_d and the transfer width of the electron beam t_w, which is typically in the range of 5-10 nm [ev85]:

- If $d_d < t_w$, amplitude-superposition of the different reflected beams occurs. This may lead to effects like spot-broadening or –splitting, the appearance of streaks, lines or likewise features.
- If $d_d > t_w$, the signals of the different domains are superimposed in the LEED image. If for example one domain shows a p(2×2) superstructure and another one a p(3×3)-superstructure, then the LEED-image will contain the spots of both diffraction patterns.
- If $d_d >> t_w$, it is possible that the LEED-beam only illuminates areas belonging to one domain. To get information about the other domain(s), the beam must be moved across the surface until the observed pattern changes.

In the case of coincidence- or incoherent superstructures, multiple scattering may occur. In consequence the LEED-pattern does not only show a superposition of the periodicities of substrate and superstructure, but also spots formed by linear combinations of these lattices:

$$\vec{g}=h_1^1\vec{a}_1^*+h_2^1\vec{a}_2^*+h_1^2\vec{b}_1^*+h_2^2\vec{b}_2^* \qquad (2.8)$$

$\vec{a}_1^*$ and $\vec{a}_2^*$ are again the reciprocal lattice vectors of the substrate, $\vec{b}_1^*$ and $\vec{b}_2^*$ those of the superstructure and $\vec{g}$ is the resulting vector in reciprocal space. [ev85]

Coincidence structures pose a special problem. Since the LEED image only shows the geometrical relation of substrate and superstructure, it is not possible to distinguish between simple and coincidence-structures. For example the two structures, shown in figure 2.6, would both result in a similar LEED-pattern. This problem cannot be solved with LEED alone – additional methods, like STM, are necessary to gain more structural information of the surface. [ev85]

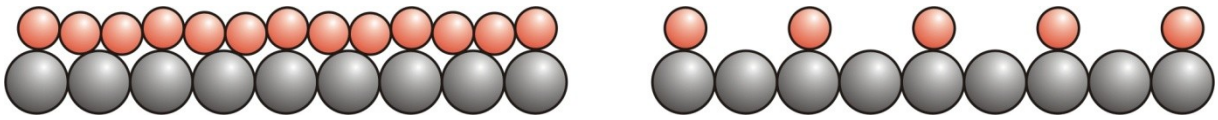

Fig. 2. 6: A coincidence structure (left) and a simple superstructure (right) with similar periodicity. Both structures cause similar LEED-patterns. Grey spheres: substrate atoms, red spheres: adsorbate atoms.

To gain more information with LEED, it is necessary to analyze the intensity profiles of the different diffraction spots. For the proper interpretation of this data more sophisticated theories are needed, including kinetic and dynamic effects. This has not been necessary for this thesis, since the same information could be obtained by using STM. Thus the interested reader is referred to the corresponding literature [ev85] for further information on these theories.

2.1.3 Instrumentation

Figure 2.7 shows the setup of a typical LEED-system schematically. The electron gun consists of a filament in a Wehnelt-cylinder and a focusing system, composed of several deflection plates. At the end of the focusing system the electron beam is guided through the detector system by a "drift-tube" onto the sample surface. The sample itself is situated on a manipulator which allows translation and rotation with respect to the detector. The detector is used to visualize the reflected electron beams. It consists of 3 grids and a fluorescent screen with the form of spherical caps. The first grid is grounded, together with the sample and the drift tube. This guarantees that the space, which is crossed by the electrons, is void of electromagnetic fields. To the second grid a negative potential is applied, which is only slightly smaller than the acceleration voltage. This is used to deflect inelastically diffracted electrons. The third grid is again grounded to shield the remaining elastically scattered electrons from the deflection field. To the fluorescent screen a positive high voltage is applied to finally accelerate the electrons again, so that they have enough energy to stimulate photoemission at the fluorescent screen. The diffraction pattern is recorded by taking photographs of the detector screen. [ev85]

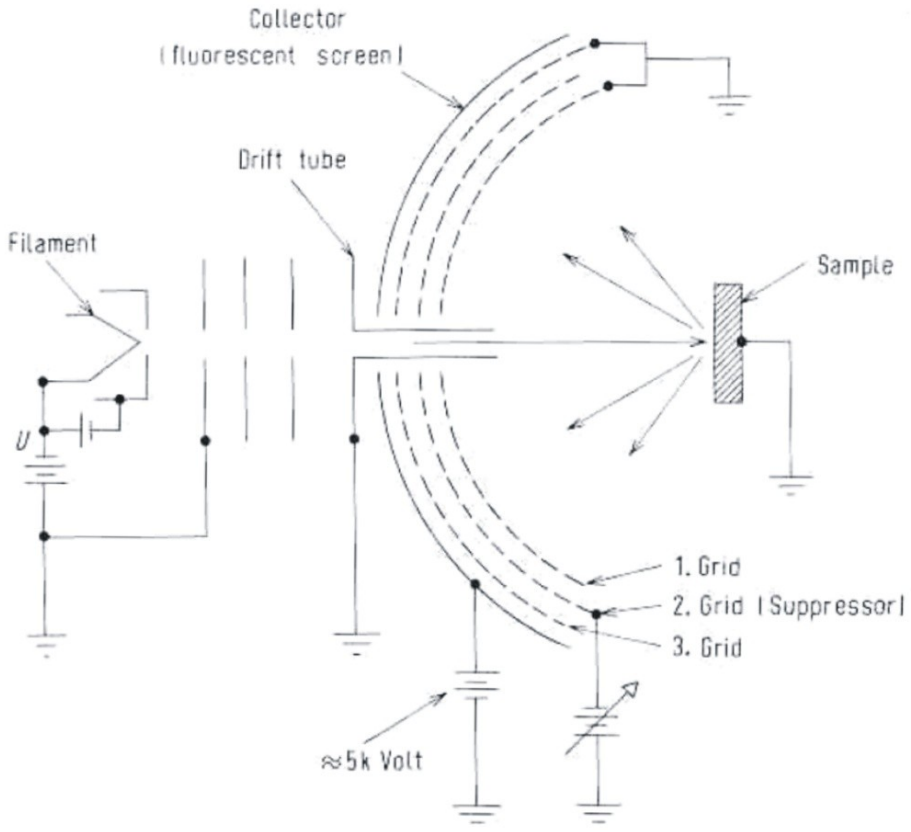

Fig. 2. 7: Schematic representation of a LEED-system. Further explanations are given in the text. Picture copied from [ev85].

Details on the used LEED-apparatus have already been given at the beginning of this chapter. The beam energy can be regulated by the acceleration voltage V_a applied to the Wehnelt-cylinder. In the experiments for the present thesis, typically values between 60 V and 80 V have been used for V_a. The potential applied to the fluorescent screen has been 1 kV. It has also been mentioned that an ion-gauge has been present in the LEED-chamber for pressure control. This device has been switched off during the LEED-measurements to avoid electromagnetic fields within the chamber.

2.2 Scanning tunnelling microscopy (STM)

2.2.1 Basic principles

STM can be described as a local proximal probe technique. Proximal underlines that the sensor or probe is in close proximity to the sample without touching it. Local means, that only a small – in the ideal case point-like - area on a surface is characterized at a time. In STM this is realized by the combination of three independent principles: point-probing, scanning and electron tunnelling. In the experiment the point probe is realized as a very sharp metal tip. To make electron tunnelling possible this tip is brought within a few Å distance from the surface of a conducting sample and a bias is applied between these two electrodes. The resulting tunnelling current I is strongly dependent on the tip-sample separation s_z, as will be shown in section 2.2.1. This fact is used to map a small area on the surface by scanning over it with the tip, as shown in figure 2.8. This is done by piezoelectric drives, which allow precise positioning of the tip. As result an image of the surface structure in real space is obtained. [gs92, wc94]

Apart from the tunnelling effect, the close proximity of tip and sample has some additional advantages. Because of the small separation between electron source and detector, no lens-system is needed for focusing. This also excludes the detriment of the image quality by lens defects. Moreover STM can be treated as a near-field technique, which means that the resolution is independent of the de-Broglie wavelength of the electrons. Due to the low energies of the exchanged electrons, radiation induced damage of the surface does practically not occur. The greatest advantage of STM is, in comparison to diffraction techniques, that non-periodic surface structures, like defects or different phases, can be imaged in real space. [gs92, co93]

Yet STM is also subjected to several restrictions. First of all it is an electronic method. Thus it can only be applied to samples with a sufficient conductivity. The surface maps, obtained by STM, are not only governed by geometrical properties of a surface but to a great extend by its electronic structure. In fact STM allows probing of the distribution in the electronic local density of states (LDOS). [gs92, wc94, co93]

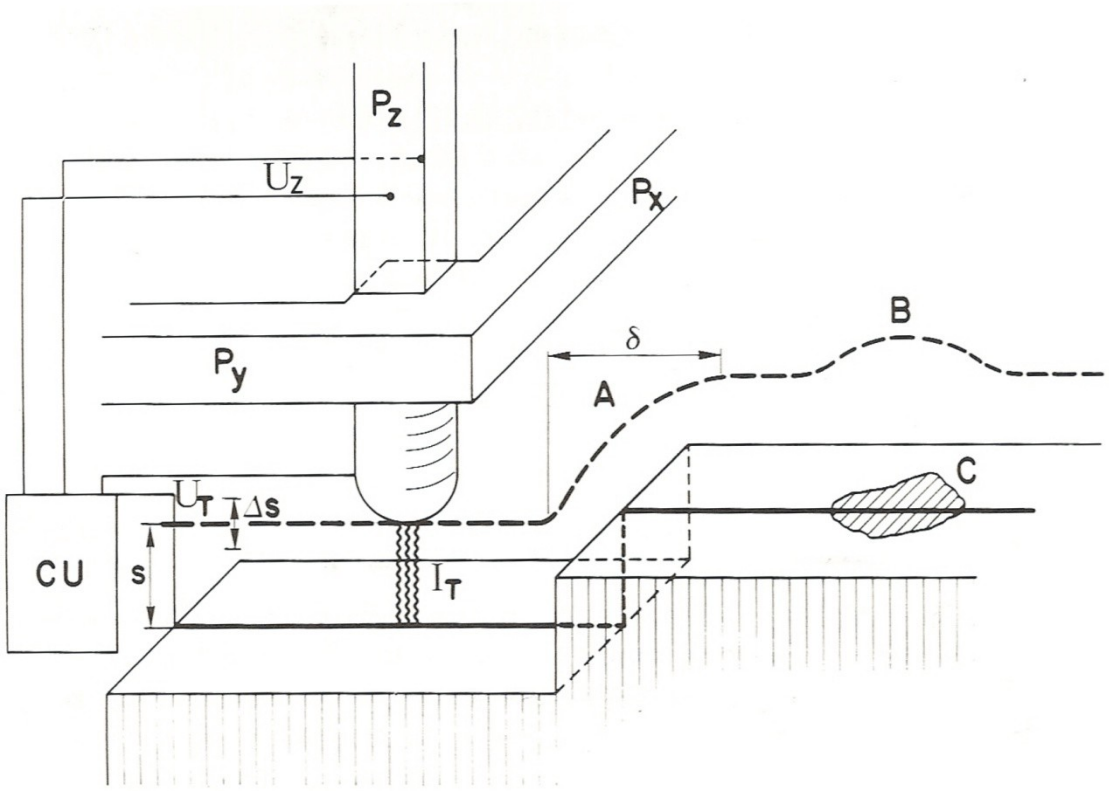

Fig. 2. 8: Basic principle of STM. At the distance s, between tip and surface, a tunnelling current I_T is flowing between those two electrodes, when a bias potential U_T is applied. The tip in then moved across the surface by the three piezoelectric drives P_x, P_y and P_z. During the scan I_T and s are kept constant by an electronic circuit CU. Consequently changes in the surface structure are recorded as movement Δs of the tip in z-direction. This results in a real-space matrix including the values of x, y and z for each measurement point. Since STM probes the electronic structure of the surface, step-edges are imaged with rounded shapes due to the Smoluchovski-effect (A). Also changes in the surface composition (C) may cause contrast in STM-images (B). Picture copied from [wc94].

This is not a disadvantage by itself. On the contrary, it allows deeper insight into the chemical properties of the surface. But as a consequence the contrast in an STM-image is a superposition of structural and electronic (chemical) contrast, as shown in figure 2.8(B). That makes data analysis difficult in many cases. Additionally the gained information does not solely depend on the sample states, but is also influenced by the tip states which are generally unknown and may also change quite often. Generally the tip interacts in several ways with the surface, as will be discussed in section 2.2.3. As mentioned above STM is not restricted by an (electro)optical lens system. Nonetheless image distortions may appear. The reason for that is the piezoelectric drive of the scanner. The precision of the piezos is subjected to several limitations by thermal drift, creepage currents and hysteresis effects, causing unwanted movement of the scanner. Last but not least the limited field of vision poses a problem in STM. The investigated areas are generally very small. Even if several measurement areas are investigated on a surface, the gained information remains local by nature. Thus general statements about the whole surface are often difficult to make by STM-probing alone. So, STM measurements are often combined with averaging methods, like LEED, to gain complementary information about the surface under investigation. [gs92, wc94, co93]

Still, STM remains one of the most powerful tools in surface science. The method is not restricted to vacuum, like many other techniques, but can also be applied in liquid- or gas atmosphere. Nonetheless, the best results are obtained in UHV, since the low residual pressure allows the most effective control of the surface properties. [gs92, wc94]

2.2.2 Theoretical approach

In this section the general relation of tunnelling current and tip-sample-distance are discussed. Electron tunnelling is a quantum-mechanical effect. To establish an equation for the tunnelling current a corresponding ansatz must be made. In the simplest case the tunnelling process can be modelled by a rectangular barrier problem in one dimension, as shown in figure 2.8.

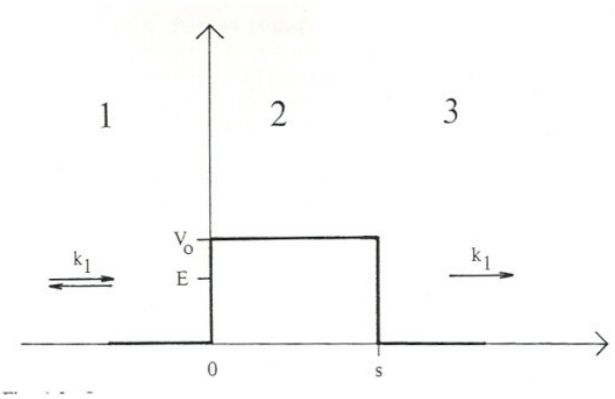

Fig. 2. 9: Rectangular potential barrier in one dimension with width s and height V_0. Picture taken from [wc94].

For a time-independent, elastic approach, a wave running to the right is assumed. The corresponding wave-equation for the region before the potential barrier (region 1 in figure 2.9) is given by

$$-\frac{\hbar^2}{2m}\frac{d^2\psi_1}{dz^2}=E\psi_1 \tag{2.9}$$

with

$$\psi_1=e^{ikz}+Ae^{-ikz} \tag{2.10}$$

and

$$k=\sqrt{\frac{2mE}{\hbar^2}} \tag{2.11}$$

ψ_1 is the wavefunction, E the corresponding energy, z is the position in real space, k is the impulse (corresponding vector to z in reciprocal space), A is a constant, m is the mass of the electron and ħ is the reduced Planck constant. The first term in equation (2.10) denotes the incident wave, the second term is the reflected part of it. [wc94]

Within the barrier (region 2 in figure 2.9) the corresponding equation reads as follows:

$$-\frac{\hbar^2}{2m}\frac{d^2\psi_2}{dz^2}+V_0\psi_2=E\psi_2 \tag{2.12}$$

with

$$\psi_2=B'e^{ik'z}+C'e^{-ik'z} \tag{2.13}$$

where V_0 is the barrier height, k‘ is the impulse in the barrier region and B’ and C’ are constants. Behind the barrier (region 3 in figure 2.9) the electron wave is free-running again:

$$-\frac{\hbar^2}{2m}\frac{d^2\psi_3}{dz^2}=E\psi_3 \tag{2.14}$$

with

$$\psi_3=De^{ikz} \tag{2.15}$$

where D denotes the square root of the fraction of the incident electrons, which have tunnelled through the barrier. Thus the transmission T, which is defined as the ratio of the transmitted current density j_t to the incident current density j_i, can be written as:

$$T=\frac{j_t}{j_i}=|D|^2 \tag{2.16}$$

In the case of a strongly attenuating barrier, T can be approximated by

$$T\approx\frac{16k^2\kappa^2}{(k^2+\kappa^2)^2}\cdot e^{-\kappa s} \tag{2.17}$$

with

$$\kappa=\frac{\sqrt{2m(V_0-E)}}{\hbar} \tag{2.18}$$

The important term in equation (2.17) is $e^{-\kappa s}$. It shows how strongly the tunnelling current depends on the barrier width s, which corresponds to the tip-sample separation in the experiment. A change Δs equal to only 1 Å results in one magnitude change of the corresponding tunnelling current. From this result two conclusions can be drawn: the first one is that STM is indeed extremely sensitive to the surface corrugation. The second one shows, that only the outermost part of the STM-tip contributes to the tunnelling current, since it is closest to the sample. In an ideal case this means that only one atom at the end of the tip is probing the sample surface – thus STM can really be regarded as a point-probe technique. The resulting wavefunction for this calculation is shown in figure 2.10. [wc94]

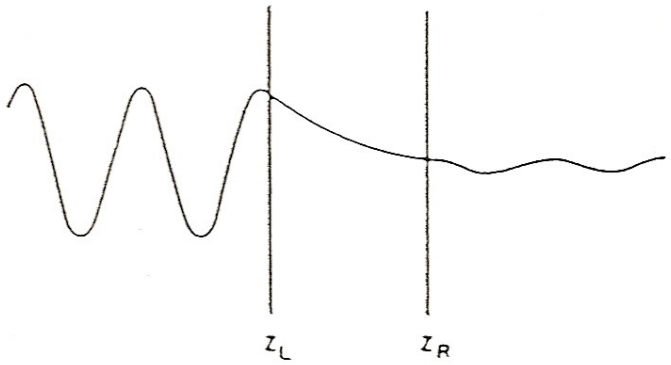

Fig. 2. 10: Resulting wavefunction for the one-dimensional rectangular barrier problem. The incident wave is coming from the left and experiences a strong exponential attenuation within the barrier limits z_L (left barrier-border) and z_R (right barrier border). The transmitted wavefunction shows an explicitly smaller amplitude, what corresponds to a much smaller probability of finding transmitted electrons in this region. Original picture from [wc94].

In a time-dependent, elastic approach for the same barrier-shape, the mathematical procedure is different. In this case the time-dependent Schrödinger equation must be used:

$$H\psi(t)=-i\hbar\frac{d\psi(t)}{dt} \tag{2.19}$$

H is the Hamiltonian operator, ψ(t) is the time-dependent wavefunction and i is the imaginary unit. To solve equation (2.19) the so-called "wave-matching-method" by Bardeen is applied. In this approximation free electron waves are presumed outside the barrier on both sides, as shown in figure 2.11. Within the barrier these wavefunctions are strongly attenuated, according to

$$\psi_1=ae^{ikz} \text{ for } z \geq 0 \text{ and } \psi_2=be^{-ikz} \text{ for } z \leq s \tag{2.20}$$

where a and b are constants and s denotes the barrier width. [wc94]

To solve the Schrödinger equation (2.19), perturbation-theory is used in combination with the corresponding wavefunctions of the two free-electron waves:

$$H=H_0+H_T$$

$$H_0\psi_1=E_1\psi_1 \quad \text{and} \quad H_0\psi_2=E_2\psi_2 \tag{2.21}$$

$$\psi(t)=c(t)\psi_1 e^{-i\frac{E_1 t}{\hbar}}+d(t)\psi_2 e^{-i\frac{E_2 t}{\hbar}}$$

H_0 is the undisturbed Hamiltonian and H_T is the corresponding perturbation term, which is also called "transfer-Hamiltonian". To determine c(t) and d(t), wave-matching of ψ_1 and ψ_2 within the barrier is performed, leading to the "effective tunnelling matrix element"

$$M_{12}=\int \psi_2^*(H-E_1)\psi_1 dz \tag{2.22}$$

with $(H-E_1) = H_T$. [wc94]

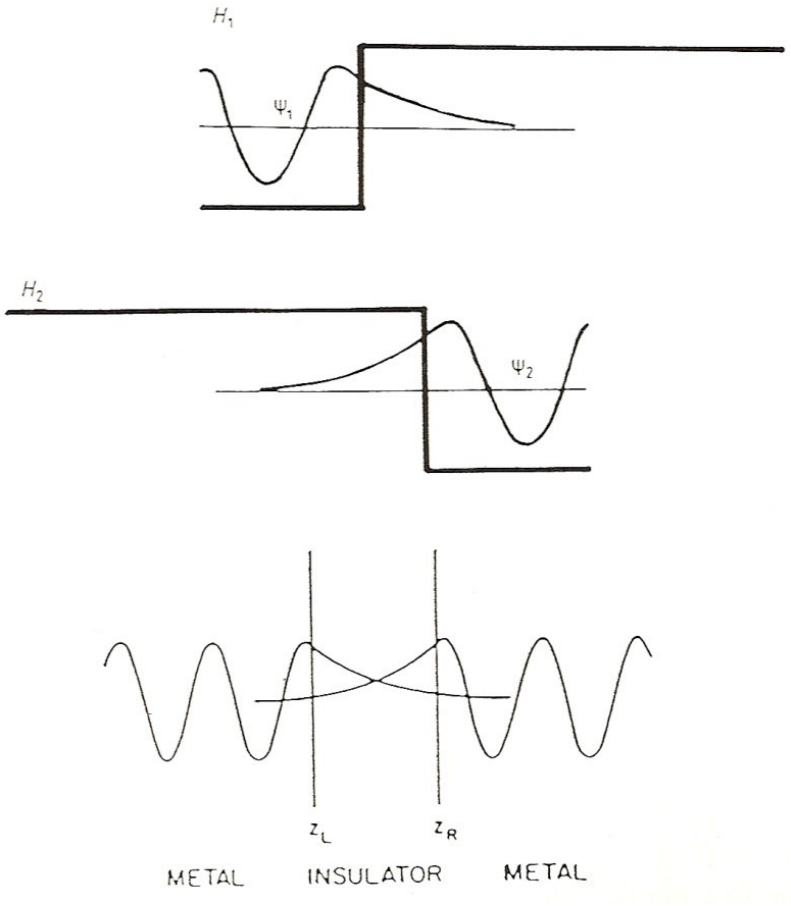

Fig. 2. 11: Wave-matching-method: To the left and the right of the barrier free electron waves are assumed, which are exponentially attenuated within the barrier region. The problem is solved by matching the two waves within the border and by using a perturbation-ansatz to solve the corresponding time-dependent Schrödinger-equation. Picture taken from [wc94].

To calculate the transmitted current density j_t, Fermi's golden rule is applied, what results in

$$j_t = \frac{2\pi}{\hbar} |M_{12}|^2 \frac{dN}{dE_2} \tag{2.23}$$

where N denotes the number of involved states. The final solution of system (2.21) is similar to (2.17). Thus time-dependent and time-independent approaches yield the same result. [wc94]

An even more general theory is the Wenzel-Kramers-Brillouin (WKB) approximation, which treats a one-dimensional barrier of arbitrary form. The result of this theory is given by

$$D(E) = \exp\left(-2 \int_{s1}^{s2} \kappa(z,E) dz\right) \tag{2.24}$$

D(E) is again the square root of the fraction of the incident electrons, which have tunnelled through the barrier, like in (2.15). s1 and s2 are turning points of the barrier-shape. κ is called the "attenuation rate", which is defined by (2.18). The WKB-approximation shows, that the tunnelling current I depends on a variety of parameters, including the applied bias U, the electron energy eU, shape, width and height of the barrier, work functions and electronic states of tip and sample. [wc94, gs92]

Generally the behaviour of the tunnelling current can be divided into two regimes: If the electron energy eU is much smaller than the barrier height V_0, then the following relation applies:

$$I \sim \left(\frac{U}{s}\right) \cdot \exp(-AV_0^{1/2}s) \qquad (2.25)$$

A is a constant with a value of 1.025 $(ev)^{-1/2}Å^{-1}$. (2.25) is valid around the Fermi-level of the sample, where STM-experiments are typically conducted. This is done because higher electron energies pose several disadvantages. First of all the behaviour of the tunnelling current is then governed by

$$I \sim U^2 \exp(-\frac{const}{U}) \qquad (2.26)$$

Thus the high sensibility of I concerning the tip-sample distance s is lost. Moreover oscillations of the tunnelling current arise at these energies. They can be explained by interference of the incident and reflected waves and resonant tunnelling through localized states within the barrier. [wc94, gs92]

Several more theoretical approaches exist, which allow even more detailed analysis by STM-imaging. Theoretically it would even be possible to calculate the involved electronic states and to produce state-maps of individual surfaces. Yet this does not work in the experiment. The problem is that the participating tip-states must be known to make the appropriate calculations and this is generally not the case. Even if the tip states can be estimated, analysis proves unreliable, since the tip is subjected to constant changes by adsorption and desorption of particles, morphological changes, electronic changes due to the close vicinity of the sample surface and so forth. The uncontrollability of the tip states is momentarily the major limit for scanning tunnelling microscopy. Thus in the scientific practice, a consolidation of experimental data and theoretical calculations is achieved by the simulation of STM-images. Reliable data from the STM-measurements is used to construct model surfaces by density functional theory (DFT). These models are used to simulate STM-images for similar tunnelling conditions (I-U combinations). The simulations are then compared with the experimentally obtained images and the models are adjusted if necessary.

2.2.3 Tip-sample interaction

As already mentioned the tiny distance between tip and sample causes physical interaction. At the typical distances of a few Å, both electrodes feel an attractive force. Theoretically the outermost atoms of the tip are already bound weakly to the sample surface. The arising binding energy is composed of a contribution of van der Waals attraction and a resonance-energy which has its origin in the tunnelling matrix element (2.22). The resulting force leads to elastic and also inelastic deformations of the tip towards the surface. As a consequence a change in the tunnelling current is registered. The forces between tip and sample may

become large enough to cause adsorption of surface-particles onto the tip or vice versa. This effect can be utilized to sharpen blunt STM-tips due to rapid approach and retraction to the surface. It also allows to manipulate surface structures by changing the tip-sample distance at chosen positions. On the other hand unevenness of the surface may cause unwanted tip-changes if the separation distance cannot be adjusted quickly enough. [co93 ,gs92]

The close proximity of the tip to the sample may also cause changes in the surface electronic structure. The external field originating from the tip leads to charge redistributions at the surface. The electron density in the gap between the two electrodes rises and electronic states may be created, which cannot be assigned to tip or surface alone. These are the “tip-induced states” (TILS). From a quantum mechanical point of view TILS emerge due to superposition of different Bloch waves from the surface and the tip. As a result also the energy-distribution of the electrons becomes more diffuse, what results in a reduced energy- resolution of the microscope (more states contribute to the tunnelling current and to the contrast in the final image). Also the formation of resonant states in the barrier can be observed at higher electron energies, as already discussed in the last section. [co93, wc94]

2.2.4 Instrumentation

Scanning tunnelling microscopes and their integrated units exist in many different designs. Therefore only the technology of the used 024 µ-STM by Omicron is discussed in this section. A schematic outline of the design is shown in figure 2.12a. In this assembly the sample is fixed in a sample-holder-plate with the surface under investigation facing downwards. The plate can be positioned in x- and y-directions by three piezoelectric steppers. Tip and scanner are situated beneath the sample and can be moved in z-direction by an additional piezoelectric stepper. The piezoelectric elements (steppers and scanner) are made of lead-zirconate-titanate (PZT) ceramics with the chemical formula $Pb[Zr_xTi_{1-x}]O_3$. [co93, wc94, bs00]

The scanner is designed as a tube scanner. In this layout 4 electrodes are placed on the outside of the tube, as shown in figure 2.12b. On the inside of the tube a fifth electrode is mounted. By application of a voltage to electrodes on the outside the scanner can be bent in the corresponding x- or y- direction. Applying a voltage to the inner electrode, results in contraction of the scanner in z-direction. The tube design has the advantages of large displacement, low crosstalk between the different electrodes and a high resonance frequency, which can be estimated by

$$v_r = 1.08 \cdot 10^{-5} l^{-2} \sqrt{r_o^2 + r_i^2} \qquad (2.27)$$

l is the length of the scanner, r_o and r_i are the outer and inner radius of the tube. The drawback of this sort of scanner is that movements in x- and y-direction are not fully planar but also include a component in z-direction. [bs00, co93, wc94]

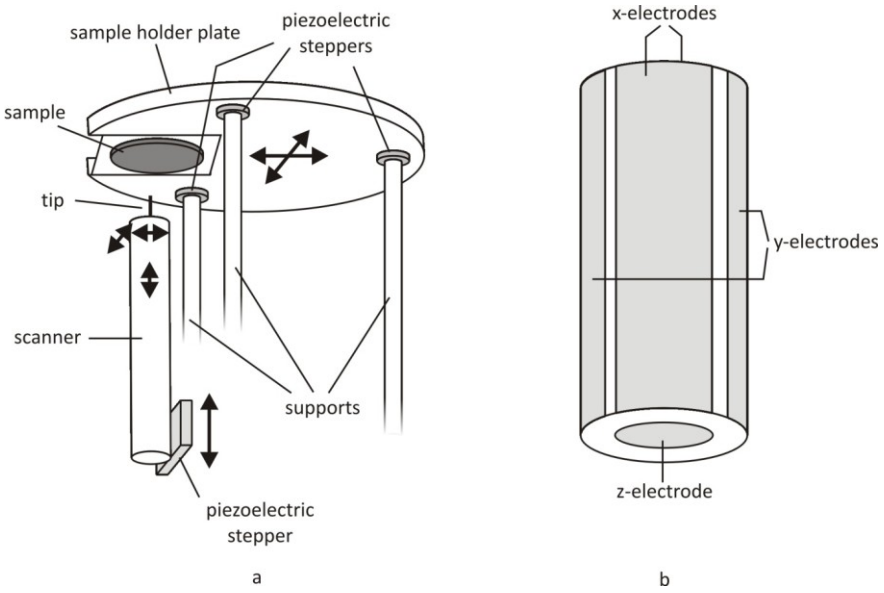

Fig. 2. 12: (a) Basic layout of the used 024 µ-STM by Omicron. The sample is situated in the sample holder plate, facing downwards. The plate can move freely and is positioned by three piezoelectric steppers in x- and y- direction. The tip is fixed on a tube-scanner which is situated beneath the sample. Both can be moved in z-direction by another piezoelectric stepping motor. (b) Layout of a tube-scanner with four electrodes on the outside and one electrode on the inside.

The tip itself is mounted on top of the scanner. As mentioned at the beginning of this chapter, electrochemically etched W-tips and mechanically cut Pt/Ir-tips have been used. Typical shapes of tips, prepared with these methods, are shown in figure 2.13.

The STM-measurements have been conducted with a computer-based control system. First the original Omicron electronics have been used, which have been replaced by a more modern control system by Nanonis (Specs-Zuerich) in the course of this thesis. A schematic block-diagram of such a control system is shown in figure 2.14. In contrast to the shown diagram, the bias U has not been applied to the tip, but to the sample in the configuration used for the experiments.

The STM-images shown in this thesis have all been captured in “constant current” mode. In this operation mode of the STM the tunnelling current and thus the tip-sample distance are kept constant. To achieve this, a special feedback-loop is used within the control cycles of the microscope. Within the feedback loop, the amplified tunnelling current is compared to a preset reference value. [bs00, co93, wc94]

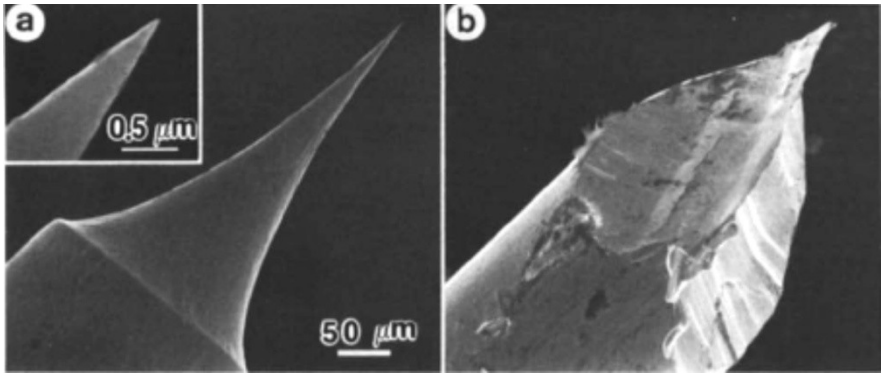

Fig. 2. 13: Microscopic images of STM-tips. (a) Electrochemically etched tip. (b) Clipped tip. Pictures taken from [su89].

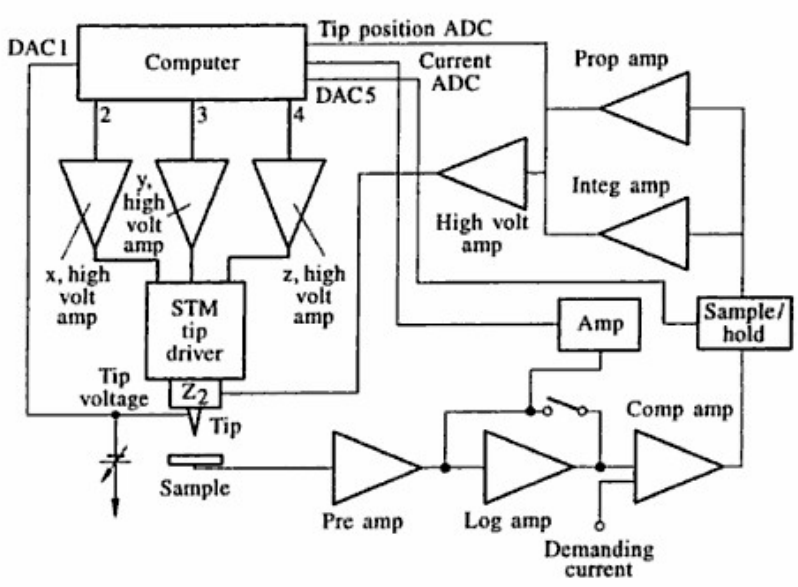

Fig. 2. 14: Block-diagram of a computer-based STM-control. The tunnelling current is amplified in several steps and compared with a preset demanding current. Divergence of these two values leads to an adjustment of the z-position of the tip. The scanning is performed by application of corresponding high-voltages to the scanning unit. Abbreviations: amp – amplifier, ADC – analogue to digital converter, DAC - digital to analogue converter, prop – proportional, integ – integral, volt – voltage, log – logarithmic. Original picture from [bs00].

Deviations from this value lead to an adjustment of the tip position in z-direction. In this mode not the tunnelling current itself is used as measurement signal but the z-position of the tip. Intensity and reaction time of the adjustments can be controlled by proportional and integral devices in the feedback-loop. The corresponding presets depend on scan speed, surface morphology and desired resolution. [bs00, co93, wc94]

To perform high-resolution scans of surfaces it is necessary to shield the STM from vibrations. In the case of the used 024 µ-STM this has been done by a two stage damping. The first damping stage consists of an active table damping system, consisting of three pylons operated with pressured air. The second stage is built by a stack of Viton-buffers, situated directly under the STM. Proper adjustment of this damping system allows to eliminate low- and high-frequency vibrations.

2.2.5 Scanning tunnelling spectroscopy (STS)

STS allows local probing of the density of states (DOS) on a surface by performing bias-spectroscopy. In this operation mode, the STM tip is kept above a chosen site on the surface and the feedback-loop is switched off. Thus the z-position of the tip and consequently the tip-sample separation remain constant. Then the bias U is varied and the corresponding tunnelling current I is recorded. The resulting I/U-curves depend on the material and the LDOS of the surface. For metal-surfaces ohmic behaviour can be found. Semiconductors however display characteristic spectra, depending on the material and the selected surface. [wc94]

Figure 2.15 shows, what happens for STS on a semiconduction surface. Before contact, tip and sample share the same vacuum-level, as shown in (a). When a tunnelling contact is established, the Fermi-levels of the electrodes align (b). Application of a positive bias to the sample results in electrons tunnelling from occupied states of the tip into unoccupied states of the sample (c), for application of a negative bias to the sample electrons are tunnelling from occupied sample states into unoccupied tip states (d). [wc94]

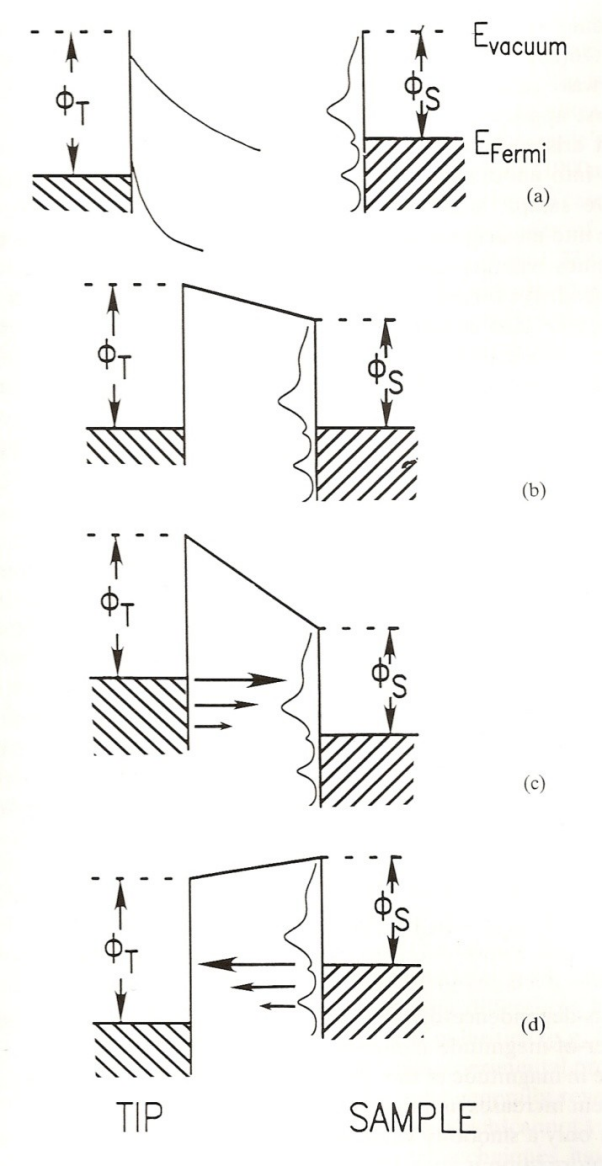

Fig. 2. 15: Principle of bias spectroscopy in STS. (a) Tip and sample share a common vacuum level E_{vacuum} before a tunnelling contact is established. Due to the different workfunctions ϕ_T and ϕ_S, the Fermi-levels E_{Fermi} are different. (b) In the tunnelling contact the Fermi-levels are aligned. (c) For a positive sample-bias, electrons from occupied tip-states around the Fermi-level tunnel into unoccupied sample-states. (d) If a negative sample-bias is applied, electrons tunnel from occupied sample-states around the Fermi-level into unoccupied tip-states. Image taken from [wc94].

Thus, by variation of the bias voltage, it is possible to select the electronic states, contributing to the tunnelling current. The resulting I/U-spectrum represents the LDOS of the surface superimposed onto the transmission background. Since the measured currents are very small (typically in the nA-range) lock-in-technology must be used to reduce the signal to noise ratio. [wc94]

Yet the final spectra do not show the definite LDOS of the surface. The electrons for tunnelling are provided by the Fermi-level of the negative electrode. For a positive bias this does not pose any problem, since the LDOS of the sample is probed and the influence of tip states can be neglected. For negative bias however, mainly the Fermi-level of the sample contributes to the signal and the unoccupied states of the tip are probed. Thus the resulting spectrum is a mixture of unoccupied tip- and sample-states. [wc94]

Bias-spectroscopy has been performed frequently on the sample surfaces under investigation in this thesis. Unfortunately the data analysis revealed that the spectra are not reproducible due to thermal drift and tip-changes at room-temperature. Because of that, the corresponding data is not shown in the chapters 4-6.

2.3 Sample preparation

2.3.1 Substrate and substrate surface cleaning

The substrate is formed by a palladium single crystal, cut along the (111)-surface, which is shown in figure 2.16. The miscut amounts to less than 0.07° what results in large uniform terraces on the substrate surface. Due to long term-cleaning procedures the contamination of the crystal by foreign species, like hydrogen, oxygen or sulphur, has been reduced to a minimum. Thus the sample exhibits a pure, largely defect-free surface. More information about the Pd(111)-surface can be found in chapter 3.1.

To obtain maximum cleanliness of the surface, a special cleaning procedure has been performed before each surface preparation:

- Bombardement of the surface with Ar^+-ions to remove adsorbates
- Flashing the surface to a temperature of 1020 K in UHV to remove zinc-contaminations from the bulk
- Cool-down of the sample in UHV
- Annealing at 800 K and an oxygen pressure of 5×10^{-7} mbar to remove residual zinc- and carbon-contaminations from the surface and the near-surface region
- Cool-down in the same oxygen atmosphere
- Flashing the sample to 1020K to remove subsurface oxygen
- Cool-down in UHV

After this procedure the surface-cleanliness has been checked frequently with LEED and in special cases with STM. In the case of thick adsorbate-films, the first three steps have been repeated several times to obtain a clean substrate surface.

Fig. 2. 16: Photograph of the substrate, made of a palladium single crystal cleaved along the (111)-surface. The crystal is mounted to the sample holder with three tantalum-wires.

2.3.2 Preparation of PdZn-surface alloys and Zn-films

To prepare PdZn(111)-surface alloys, Zn has been deposited onto the substrate surface at room temperature. A well ordered surface-alloy already forms at this temperature, so further annealing has not been necessary. Zn-films have been formed by further deposition of Zn onto the alloy phase.

The deposition of zinc has been performed by physical vapour deposition (PVD) from a custom-built molybdenum-Knudsen cell, which has been resistively heated. The whole evaporator has been water-cooled to avoid evaporation of particles adsorbed on its outer parts. As described in [ka09] in more detail, the precise determination of the deposition rate by the use of a quartz-microbalance has proven difficult, since the sticking coefficient of Zn on the quartz-crystal seems to differ from unity. The procedure, proposed in [ka09], where an approach of the sticking coefficient towards unity can be achieved by formation of a thick zinc-layer on the microbalance, could not be applied, since the geometry of the preparation chamber prohibited a long-term evaporation of zinc without contamination of the sample surface. Instead an alternative procedure has been developed: due to the large thermal inertia of the evaporator, a stable evaporation rate could be achieved by precise heating and cooling cycles. The corresponding deposition rate has been determined by combination of several microbalance- and STM-measurements. For every deposition the same rate has been set by application of this heating-cooling-sequence. The amount of deposited zinc has been controlled by the deposition time. Due to the slow reduction of the zinc-fill in the crucible, adjustments of the procedure had to be made from time to time.

It has been possible to obtain good control of the Zn-coverage by this method although it cannot be as precise as constant measurement of the deposition rate by a microbalance. During the experiments, the only way to check, if the real coverage coincides with the calculated one, has been by STM-measurements. Thus all coverage values given for Zn-containing films should be understood as “apparent coverage”.

2.3.3 Preparation of ZnO-films

For the preparation of ZnO-films two methods have been used: post-oxidation (PO) and reactive evaporation (RE). The PO-procedure has been as follows:

- Substrate cleaning
- Deposition of zinc onto the substrate surface at room-temperature
- Annealing of the sample at 550 K and different oxygen pressures in the range from 5×10^{-8} mbar to 1×10^{-5} mbar
- Cool-down in the same oxygen-atmosphere

Post-oxidation has been primarily used for coverages up to 1 monolayer (ML). For higher coverages the RE-procedure has been used to guarantee full oxidation of the resulting film:

- Substrate cleaning
- Deposition of zinc onto the substrate surface at room-temperature and different oxygen-pressures in the range from 5×10^{-8} mbar to 1×10^{-5} mbar
- Annealing of the sample at 550 K in the same oxygen atmosphere
- Cool-down in the same oxygen-atmosphere

RE has also been used for coverages below 1 ML. In this regime there is not much difference between films grown by PO and RE. PO-grown films exhibited a slightly higher degree of order, but the films tailored by RE have also been of good quality.

2.3.4 Preparation of CoO-films

The preparation of CoO-films has been largely identical to the one of ZnO-films. Also for these films PO and RE have been used according to the procedures, described in the last section. The annealing temperatures have been adjusted a bit, since CoO formed better ordered films between 620 and 650 K. Co has been deposited by PVD, just like Zn. To do so a Co-wire has been placed inside a cage-like heating filament. Evaporation of the Co has been accomplished by resistive heating of this wire. The evaporator has been cooled with liquid nitrogen to avoid unwanted desorption of adsorbed species. In contrast to zinc, the cobalt evaporation rate could be easily determined with the quartz microbalance. Thus Co- and CoO-coverages can be understood as total values.

Chapter 3: Materials

In this chapter information about the materials is given, which have been used for the experiments (Pd, Zn, ZnO and CoO). The sections below contain selected data about the materials basic properties and about relevant surfaces and compounds.

3.1 Palladium

3.1.1 Material data

Palladium is a transition metal from the platinum-group with the atomic number 46, a density of 12.0 g/cm^3 and a relative atomic weight of 106.4. It starts melting at 1825 K and boiling at 3413 K. The electronic configuration of Pd is [Kr]4d^{10}5s^0, it has an electronegativity of 1.4 (after Allred and Rochow) and the valency-numbers 2, 3 and 4. The crystal-system of palladium is face-centred-cubic (fcc) with a lattice constant of 3.89 Å - the unit cell is shown in figure 3.1. Like the other members of the platinum-group, palladium is a good catalyst. For the MSR-process, these elements show a tendency to dissociate the methanol into carbon-monoxide and hydrogen. Concerning hydrogen, palladium shows a very special characteristic: At room-temperature palladium tends to absorb large amounts of hydrogen – the uptake is as high as 900-times the volume of the Pd-host. To remove as much of the hydrogen as possible, the crystal cleaning must be adequately efficient. This is fulfilled by the procedure, presented in section 2.3.1. [wc74, ah76, bd05, kj06]

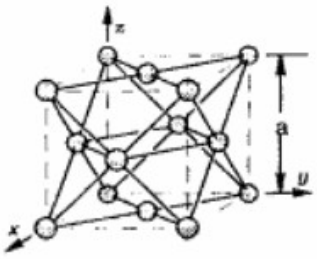

Fig. 3. 1: Unit cell of the face-centred-cubic lattice. a represents the lattice constant. Picture copied from [ue96].

3.1.2 The Pd(111) substrate surface

Throughout all experiments presented in this thesis a Pd(111) surface has been used as substrate. This surface has been chosen for different reasons:

- There are already several studies existent in which similar or comparable surfaces have been used for experiments with PdZn or with ZnO [tp07, gj06, bs06].
- For the PdZn-alloy the (111) surface is predicted to be the most stable one [cp03] thus it is of special interest.
- The Pd(111)-surface can be considered to be stable under the oxidation-conditions used for the experiments in this thesis.

With regard to the last point the interaction of Pd(111) with oxygen needs to be discussed briefly. The reaction parameters for the oxide-preparation are given in chapter 2.3.3. Under these conditions the probability of PdO-formation is extremely low and can be excluded. Yet, as stated in [ls00], oxygen already tends to diffuse into the subsurface region above T = 523 K. To minimize this effect it is necessary to empty the subsurface-oxygen-reservoir before oxidation. Since this is done by the substrate cleaning procedure described in chapter 2.3.1, the diffusion of oxygen into the bulk is slowed down considerably and the amount of subsurface-oxygen can be neglected.

The (111) surface of Palladium displays hexagonal symmetry with the lattice constants $\vec{a}_1 = \vec{a}_2 = 2.75$ Å and thus a surface density of 1.53×10^{15} atoms/cm^2. A graphic representation is shown in figure 3.2a. The three main directions on this surface are $[01\bar{1}]$, $[10\bar{1}]$ and $[\bar{1}10]$. Since the surface is symmetric for six-fold rotation, these directions are equivalent to each other. They are also shown in figure 5.1a, together with the surface unit cell and the main adsorption sites. A (150×150) nm^2 - STM scan of a clean Pd(111) surface with several terraces is presented in figure 3.2b. The inset reveals the according 1x1 LEED-pattern. With a bulk lattice constant of 3.89 Å the step height on the (111) surface can be calculated to be 2.25 Å. This value is in good agreement with the experimental one, obtained by STM measurements: $h_{Pd(111),exp}$ = (2.3 ± 0.3) Å. [ah76]

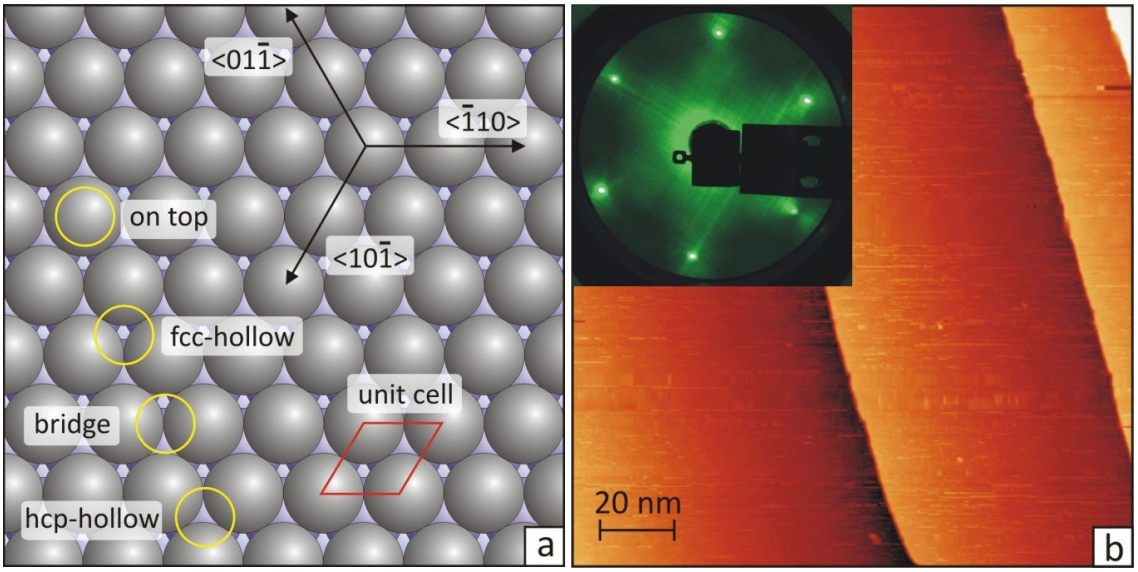

Fig. 3. 2: (a) Model of the Pd(111) surface, showing the unit cell, high symmetry directions and adsorption sites. (b) (150×150) nm^2 scan of the clean Pd surface (U = +1 V, I = 0.4 nA). Inset: Corresponding LEED image (E_e = 68.0 eV).

3.2 Zinc

3.2.1 Material data

Zinc is a transition metal with atomic number 30, a relative mass of 65.38 and a density of 7.14 g/cm^3. It has low melting- and boiling temperatures at T_{melt} = 693 K and T_{boil} = 1180 K. The electronic structure of Zn is [Ar]3d^{10}4s^2, it has an electronegativity of 1.7, according to Allred and Rochow, and a valency number of 2. Zinc crystallizes in a hexagonal structure with close packing (hexagonal-close-packed - hcp) with the space group $P6_3mmc$. The corresponding unit cell is shown in figure 3.3. The lattice constants of Zn are a = 2.66 Å and c = 4.94 Å. [wc74, bd05]

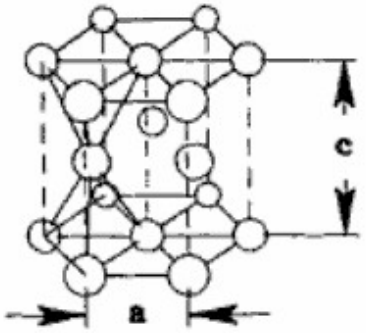

Fig. 3. 3: Unit cell of the hcp-lattice. a and c are the lattice constants. Picture taken from [ue96].

3.2.2 The PdZn(111)-surface alloy

Zinc and palladium are very miscible. As a consequence there exist a variety of alloy-phases with different stoichiometries and structures. Upon these alloys, the thermally most stable one is a 1:1 PdZn-compound with CuAu $L1_0$-structure, which is shown in figure 3.4. [wj09, ls98, hm69]

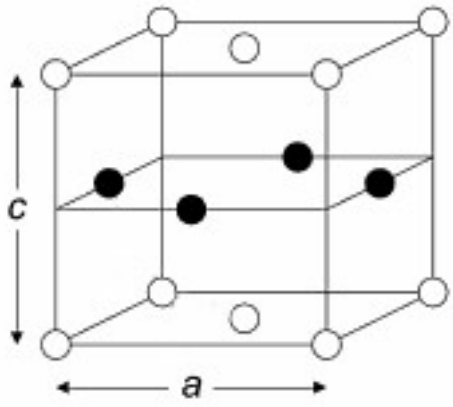

Fig. 3. 4: The unit cell of the CuAu $L1_0$-structure. a and c represent the lattice constants. Original picture from [hs09].

DFT-calculations [cp03, cs04, np07] have shown, that the (111) surface of the 1:1 PdZn-alloy has the lowest surface-energy. Thus this surface, showing alternating rows of palladium- and zinc-atoms, will be preferentially formed and deserves the interest of the scientific community. Indeed several groups have started to investigate the structure of PdZn(111) surface-alloys. These alloys can be tailored easily by Zn-deposition onto a Pd(111) substrate, like described in section 2.3.2. Some groups also performed a heating step after the deposition to enhance the alloy formation. The resulting surface alloys have been investigated with LEED, XPS, TDS and HREELS. Yet the results of these investigations have not been completely consistent. In all cases the formation of a (2×2)-pattern in LEED has been observed, but the interpretation of this pattern diverged. Two different models have been proposed: One favouring the formation of a p(2×1)-structure in different domains, what would be in consistency with the theoretical prediction, and the other one claiming, that a p(2×2)-3 Zn surface adlayer is formed. To clarify this controversial issue by the use of imaging techniques is one of the aims of this thesis. [bs06, fp82, rj94, gj06, js07, ss09]

3.3 Zinc-oxide

3.3.1 Material data

ZnO is a II-VI-compound semiconductor with a large direct bandgap of 3.2 eV at room-temperature. The corresponding band structure can be seen in figure 3.6. It has a relative molecular weight of 81.37, a density of 5.68 g/cm^3 and a melting temperature of 2248 K.

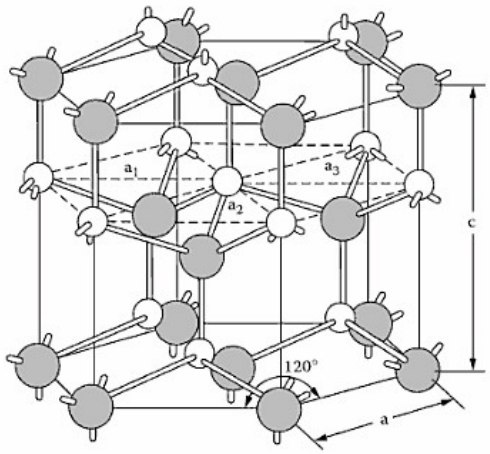

Fig. 3. 5: The wurtzite-structure of ZnO. Grey spheres represent zinc-atoms, white spheres are oxygen-atoms. A and c are the lattice constants. Original picture from [ac07].

The heat of formation ΔH_f^0 is different for zinc in the gas phase (g) and in the solid phase (c):

$$Zn(c)+\frac{1}{2}O_2(g)=ZnO(c) \quad \Rightarrow \quad \Delta H_f^0=-84.67\,\frac{kJ}{mol}$$

$$Zn(g)+\frac{1}{2}O_2(g)=ZnO(c) \quad \Rightarrow \quad \Delta H_f^0=--115.94\,\frac{kJ}{mol}$$

The upper relation is valid in the temperature range from 298 to 693 K and the lower one from 1180 to 2000 K. At normal conditions ZnO in the crystalline phase (c) adopts the wurtzite-structure, shown in figure 3.5, with the lattice parameters a = 3.25 Å and c = 5.21 Å and the space-group $P6_3mc$. [wc74, bc96, kp06]

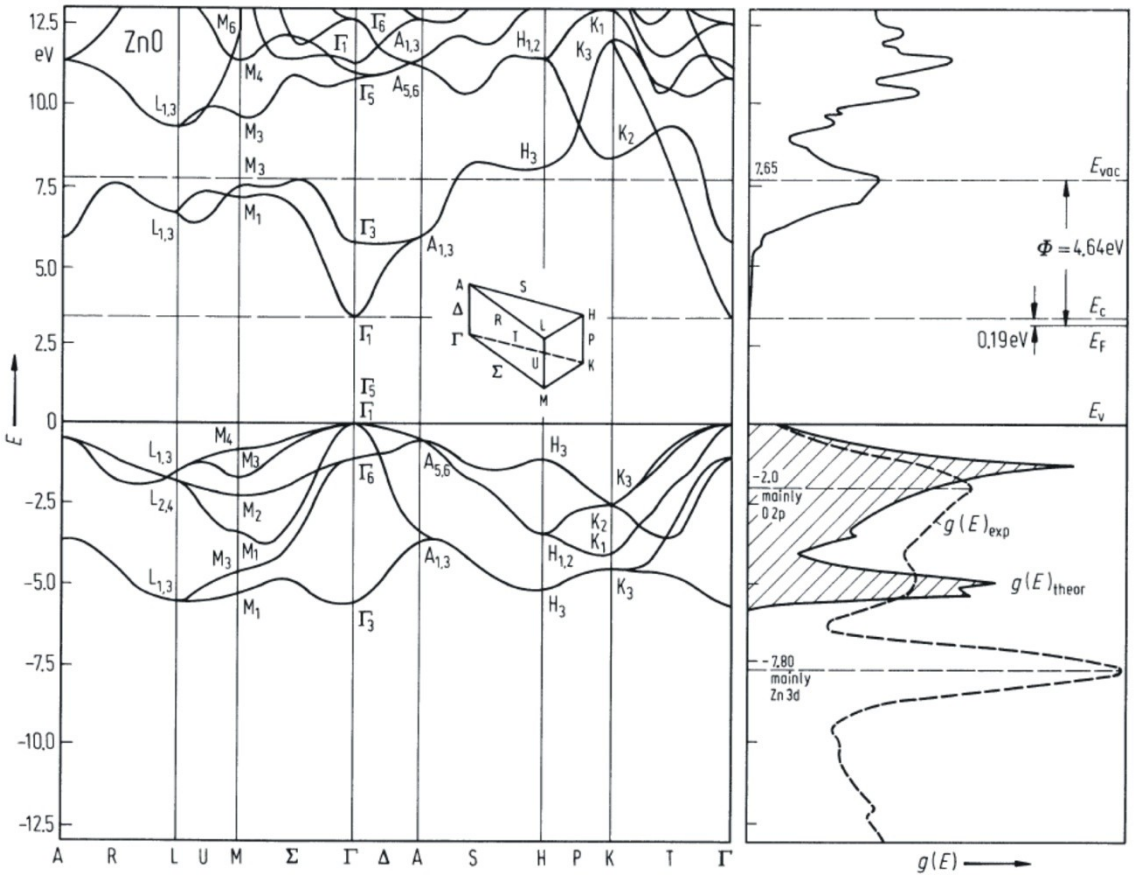

Fig. 3. 6: Band structure of ZnO (left) and calculated density of states (solid line –right) [bs73]. For comparison, a UPS-spectrum is also shown (dashed line – right) [gs80]. Picture taken from [ms82].

3.3.2 Polar surfaces of ZnO

ZnO is an ionic compound which belongs to type 3 – polar materials – of the Tasker classification. The origin of the polarity lies in the wurtzite-structure of ZnO. Zinc-oxide crystals display four low-index surfaces: the $(10\bar{1}0)$- and $(11\bar{2}0)$- surfaces, which are non-polar and the (0001)- and $(000\bar{1})$- surfaces, which are polar. {Remark: surfaces of hexagonal structures are marked by a redundant index (hkil), with i=-h-k, to distinguish them from

surfaces with hexagonal symmetry of cubic structures. [tw06]} The surface dipole-moment arises due to alternating Zn- and O-planes parallel to these surfaces. Thereby each ZnO-layer consists of two separated planes with different species, which display a normal distance of 0.63 Å. The distance between two ZnO –layers (i.e. between planes of similar atomic components, which is equal to the step height on these surfaces) amounts to 2.7 Å. [gr08, nj00, tj79, ds02, wp07, tp07]

Like discussed in chapter 1.4, the surface dipole-moment must be compensated to counteract the polar instability. It has also been mentioned already, that the polarity and the corresponding compensation-mechanisms do not only depend on the surface orientation, but also on the termination of the surface. Thus the behaviour of the two polar surfaces of ZnO differs, as discussed below.

The ZnO(0001)-surface is terminated by a plane containing Zn-atoms. Two mechanisms have been found for the compensation of the surface dipole moment on the clean surface: In one of them, the necessary charge redistribution is achieved by a change in the surface composition. As shown in figure 3.7, triangular terraces with pits of the same shape are formed on this surface. The proposed model reveals that all edges of these “magic triangles” are oxygen-terminated. Thus a deficit in Zn-atoms is created, which corresponds to 25% of the Zn-fraction in a corresponding bulk-plane (shown in figure 3.8a). Theoretical calculations have shown that this mechanism remains stable within a large range of hydrogen- and oxygen chemical potentials. A second, competing process has been found to arise at elevated temperatures, which fulfils the stability criterion (1.17) by the formation of regular step arrays (faceting) on this particular surface. [ds02, dp03, kp03, op08, wj10, wp07]

Alternatively the dipole-compensation can also be achieved by the adsorption of foreign species. For hydrogen- and carbon-monoxide-covered (0001)-surfaces no reconstructions could be detected. Instead (1×1) adlayers are formed by the particles due to their small size in comparison to the ZnO-surface unit-cell, like shown in figure 3.8b for hydrogen. [wp07, sp03, bs01, ps96, wa91, mp06]

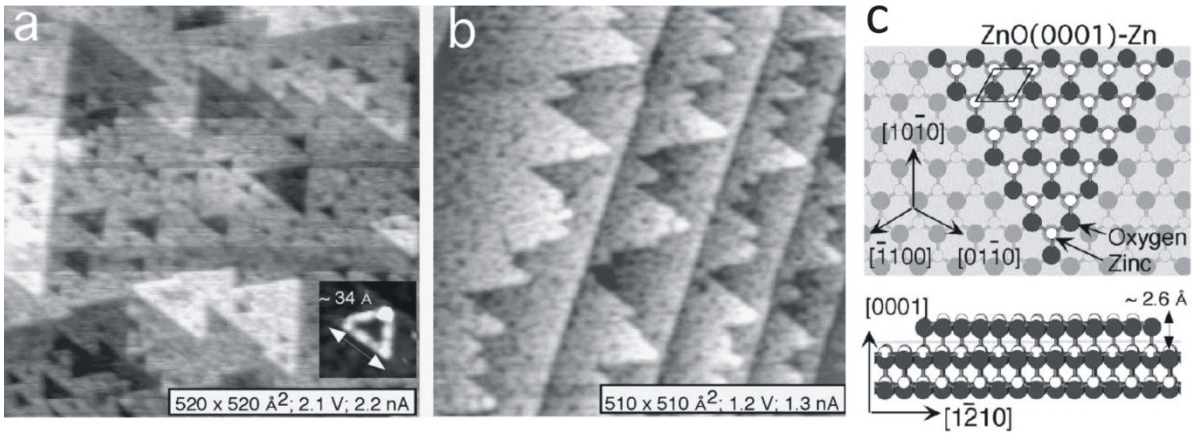

Fig. 3. 7: STM-images of the ZnO(0001)-surface with “magic-islands” on a planar surface site (a) and at a stepped surface site (b). Thereby the shown terraces include one Zn-O double layer, as shown in the model (c). The edges of the terraces are all terminated by oxygen-atoms resulting in an imbalance of Zn- and O-atoms on the surface.) Pictures taken from [ds02].

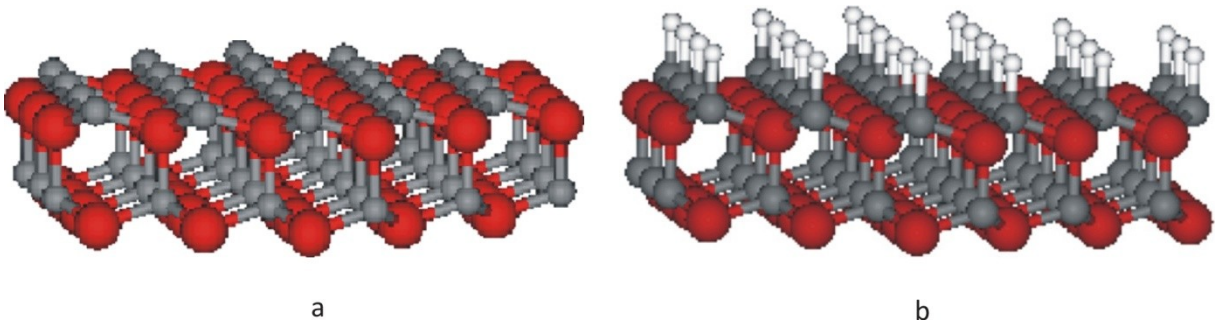

Fig. 3. 8: (a) Model of the unreconstructed ZnO(0001)-surface, reflecting the atom-positions within the bulk. (b) Model of a ZnO(0001)-surface with a H(1×1)-adlayer. Grey spheres represent Zn-atoms, red spheres stand for oxygen atoms and white spheres depict hydrogen. Pictures copied from [wp07].

The ZnO$(000\bar{1})$- surface is terminated by an oxygen-plane. In contrast to the (0001)-surface, the stabilisation mechanisms are not yet fully understood here. Many studies reported on an uncovered unreconstructed (1×1)-surface. Yet experiments with HAS (helium atom scattering) and XPS have revealed information, which suggests that the surface is covered by a hydrogen (1×1) adlayer, like shown in figure 3.9b. Indeed results have been published, where hydrogen-free surfaces have been prepared, which showed a (1×3)-reconstruction (figure 3.9a), created by missing oxygen-rows. It is possible that the reconstruction is also stabilized by residual hydrogen. This very surface appears highly reactive, especially for the dissociation of water, where again a hydroxylated surface (figure 3.9b) is formed. This hydrogen covered surface appears very stable over a wide range of temperatures and pressures, as shown by ab-initio calculations. [wj10, wp07, wp01, kp02, dp03, mp03, kj03, wp06, ba04, bp04, ka05]

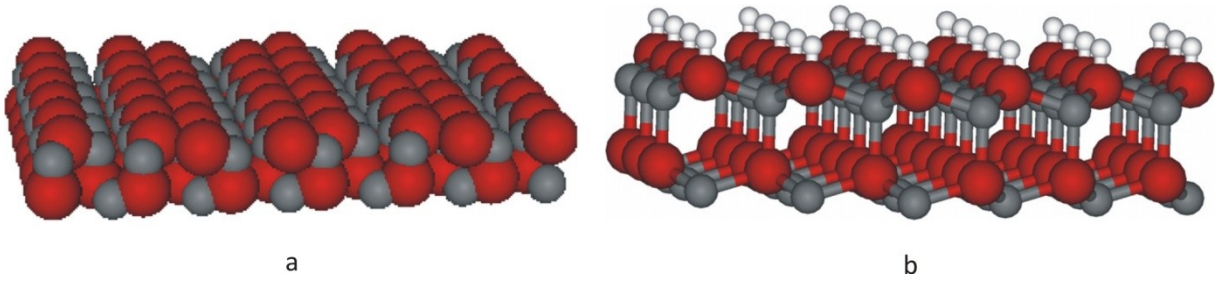

Fig. 3. 9: (a) Model of the (1×3)-reconstruction of the ZnO$(000\bar{1})$- surface. The surface stoichiometry is altered by removal of every third oxygen-row. (b) Model of the unreconstructed, hydroxylated ZnO$(000\bar{1})$- surface. The small dipole momentum of the OH-group allows adsorption of molecules like CO due to van der Waals attraction. Grey spheres represent Zn-atoms, red spheres stand for oxygen atoms and white spheres depict hydrogen. Pictures copied from [wp07].

STM-investigations of a seemingly hydrogen-free $(000\bar{1})$-surface [ds02] however did not show the (1×3)-reconstruction. Instead hexagonal terraces with a step height of 5.3 Å have been observed, like shown in figure 3.10. The corresponding model reveals that the terraces are formed by ZnO-bilayers, but also display an unreconstructed surface. That has also been confirmed by the corresponding LEED-measurements. So the question whether a hydrogen-free unreconstructed $(000\bar{1})$-surface can be formed or not is still subject of intense analysis. [ds02, wp07, wj10]

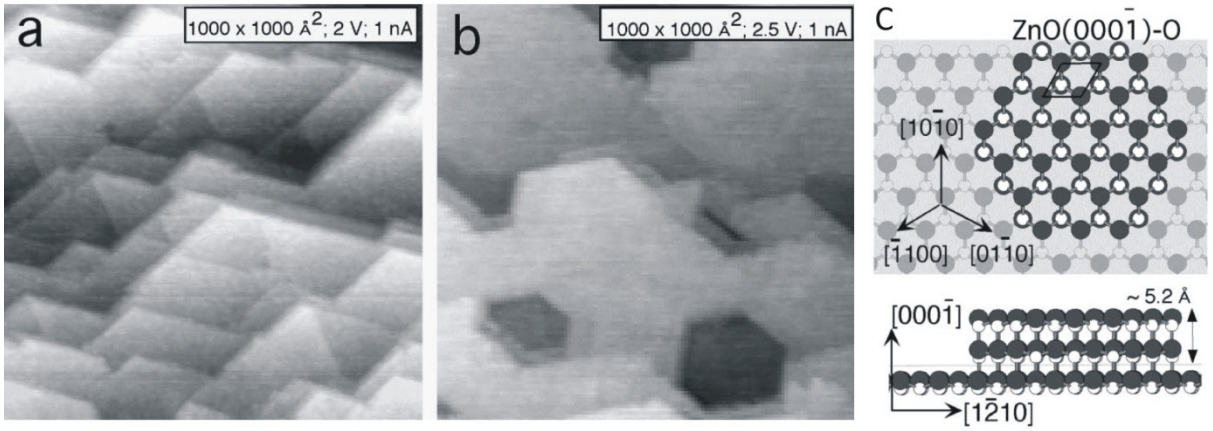

Fig. 3. 10: STM-images of the ZnO$(000\bar{1})$-surface showing double steps on hexagonal terraces at a stepped surface site (a) and on a planar surface site (b). In (c) a corresponding surface model is presented, with grey spheres representing oxygen-atoms and white spheres depicting zinc-atoms. Pictures copied from [ds02].

3.3.3 Thin ZnO-films

The Pd(111) surface, which served as support for the grown ZnO-films in the experiments of this thesis, has a hexagonal structure, like discussed in section 3.1.2. Due to symmetry-matching reasons, it can be assumed, that ZnO-adlayers on this surface, expose either the ZnO(0001)- or the ZnO$(000\bar{1})$-orientation. As discussed in the last section, these surfaces are polar and subjected to certain stabilisation-processes. However, like mentioned in chapter 1.4, the finite size of thin films invokes new stabilisation-pathways and even includes the possibility of the system sustaining a non-zero dipole moment.

A comparable hexagonal surface symmetry, like the one of Pd(111), is also shown by the Ag(111)-surface. There already exists a study of thin ZnO-films on this surface [tp07], which provides useful information about the zinc-oxide structure. The films have been investigated with XPS and STM. In the study it could be demonstrated, that the first two atomic layers of ZnO relaxed from the bulk wurtzite-structure into a planar graphite-like structure (hexagonal boron nitride structure h-BN), like shown in figure 3.11. In the adjacent third and fourth ZnO-layers a transition to the bulk structure could be observed.

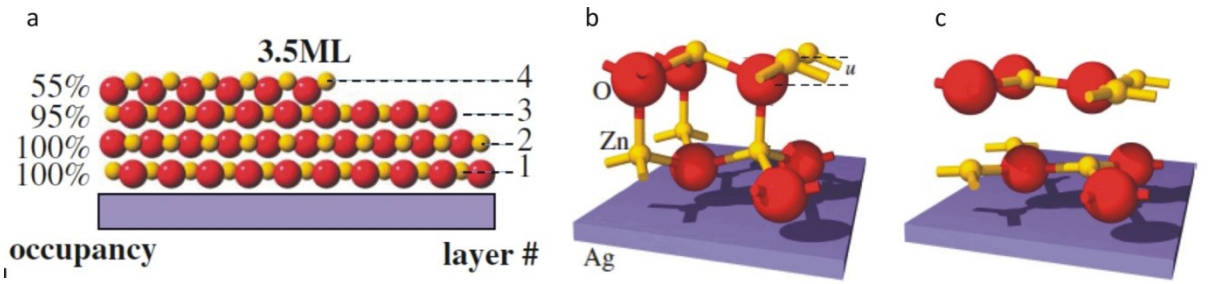

Fig. 3. 11: Models for the ZnO-layers on a Ag(111)-substrate. In (a) the transition of the planar structure (layers 1 and 2) to the bulk structure (layer 4) is illustrated. (b) shows the bulk wurtzite-structure with (0001)-orientation in detail. u denotes the vertical distance of 0.63 Å, between the Zn- and O- sheets of a ZnO-layer. (c) depicts the relaxed h-BN structure, which has been found for the first two ZnO-layers. Original pictures from [tp07].

Theoretical support for this model has also been provided in [gp04] and [fp06]. The ZnO showed a slightly enlarged surface unit cell with b_{ZnO} = 3.3 Å and formed a 7/8-coincidence structure on the Ag(111) substrate ($7 \times b_{ZnO} = 8 \times a_{Ag(111)}$), with the lattice vectors of both lattices being in-line. The observed interlayer-distances are shown in figure 3.12a. The evolution of the vertical distance u of Zn- and O-atoms within a ZnO-layer is presented in figure 3.12b. [tp07, gp04, fp06, wj10]

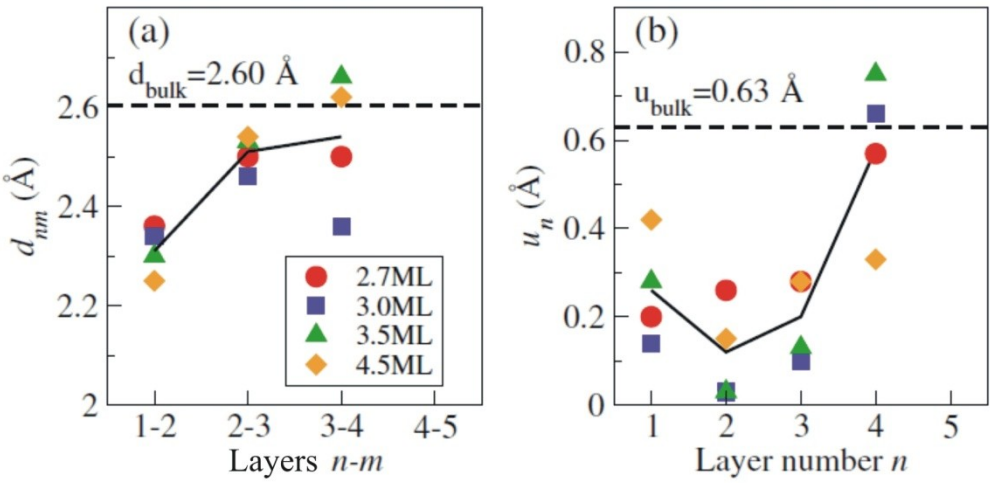

Fig. 3. 12: Evolution of the interlayer-distance d_{nm} (a) and of the vertical Zn-O separation-distance u within a ZnO-layer (b) with increasing film-thickness. A convergence toward the bulk-values can be observed in the 3rd and 4th layer. Pictures taken from [tp07].

3.4 Cobalt-oxide

3.4.1 Material data

CoO is the simplest of several Co-O compounds. It has a relative molecular weight of 74.93, a density of 6.45 g/cm^3 and a melting temperature of 2078 K. Cobalt-oxide adopts a rock-salt structure (shown in figure 3.13) with a lattice constant of 4.26 Å and space group Fm_3m. The typical application of CoO is as a blue pigment in ceramics, but it has recently become interesting for the scientific community as a component in DMS due to its ferromagnetism below a temperature of 289 K. [hd95, pc95, sp81, wc74]

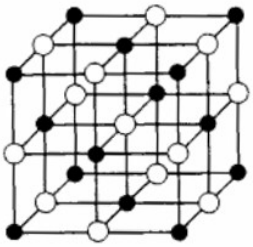

Fig. 3. 13: Model of the rock-salt structure. Black and white spheres represent different species. Image from [ue96].

Like in the case of ZnO, a surface with hexagonal symmetry is apt to evolve, when CoO is grown on top of a Pd(111) substrate. For the shown rock-salt structure, that corresponds to the (111) surface with a lattice constant of 3.01 Å and a step height of 2.46 Å. [wc74]

3.4.2 Thin ZnCoO-films

Like discussed in the introduction, one of the proposed origins of ferromagnetism in ZnCoO-DMS is the formation of Co-rich precipitates in form of nano-crystals. In a recent study for mixed ZnCoO-films on a Ag(111) substrate [mp09] such a segregation could indeed be observed. This investigation is based on the information available for thin ZnO-films on Ag(111), which has been presented in section 3.3.3. The results of the mixed film study reveal the formation of CoO-inclusions within a ZnO-matrix. Both, ZnO and CoO, undergo structural changes: For ZnO, the already discussed relaxation into a planar h-BN structure takes place. The CoO also relaxes from its bulk rock-salt structure into a wurtzite structure. Further collaps into a graphite-like structure, like for ZnO, is energetically unfavourable as a result of the large compression of the unit cell, which would be necessary to obtain this change. This structural difference between the ZnO-matrix and the CoO-inclusions, as shown in figure 3.14, allows easy identification of the materials on the substrate surface. One aim of the thesis at hand has been to clarify if such a separation of materials can also be obtained for ZnCoO-mixed films on a Pd(111)-substrate. [mp09, tp07]

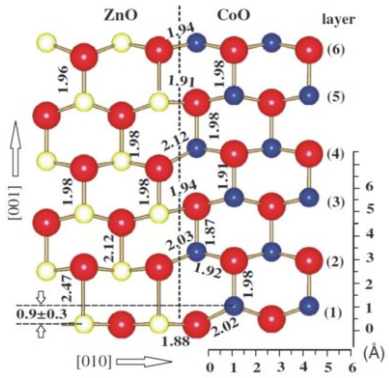

Fig. 3. 14: Different structures of ZnO (left) and CoO (right) on top of a Ag(111) substrate. Whereas ZnO adopts a planar h-BN structure in the lowest layers, which transforms into the bulk wurtzite-structure with increasing coverage, CoO collapses into a wurtzite structure. Thus a region in the low-coverage-regime exists, where the ZnO h-BN structure and the CoO wurtzite-structure coexist. Original picture from [mp09].

With this chapter the introductory part of this thesis is completed. In the next three chapters the results of the experimental and the corresponding theoretical investigations will be presented. The three chapters deal with the structures of PdZn(111)-surface alloys and adjacent Zn-layers (chapter 4), thin ZnO-films on a Pd(111)-substrate (chapter 5) and mixed ZnCoO-films on a Pd(111) support (chapter 6). A summary of the most important findings can be found subsequent to chapter 6.

Chapter 4: Zn on Pd(111)

As already mentioned in the introduction, the formation of a PdZn-alloy phase at the interface between Pd and ZnO is deemed to be responsible for the high catalytic qualities of Pd/ZnO catalysts. Since the PdZn(111) surface is expected to be the most stable one, the interest of the scientific community has been directed towards it [cp03]. PdZn(111) alloy phases have been created by deposition of Zn onto Pd(111), also followed by annealing steps in some cases. There is already data available concerning the electronic structure of such alloys, yet their atomic ordering is still not understood completely. Two models have been proposed favouring either a p(2x1)-PdZn or a p(2x2)-3Zn superstructure on Pd(111) substrates.

This chapter deals with the surface structure of PdZn(111) surface alloys. Experimental data obtained with STM, LEED and TPD will be presented, supplemented by DFT-derived models.

4.1 Growth and morphology of Zn deposited onto Pd(111)

To investigate the growth mode, metallic zinc has been deposited onto a clean Pd(111) surface at 300 K in UHV. From preliminary experiments it was already known that ordered structures can be obtained by this procedure, so no additional annealing step has been performed. The amount of adsorbed zinc has been controlled by temperature adjustment of the evaporator and deposition time, as described in chapter 2.3.2. After each deposition step the sample has been investigated with STM and LEED.

In figure 4.1 the results of this growth experiment are presented, showing large scale STM images and the corresponding LEED patterns. The coverage stated for each picture should be understood as apparent coverage θ_{app}, which is the amount of overlayers as measured in the STM.

Figure 4.1a shows the surface at θ_{app} = 0.5 ML. The Pd(111) is covered by atomically flat islands. Their shape is dentritic what indicates a growth governed by diffusion limited aggregation (DLA). In this mode the atoms diffuse on the surface after condensation until they either desorb or find an appropriate adsorption site. As can be seen in the STM image such suitable sites are either step edges of the substrate or adsorbate nuclei. The form of the islands indicate that there are preferred diffusion directions coinciding with the main directions of the Pd(111) substrate - $\langle 01\bar{1}\rangle, \langle 10\bar{1}\rangle$ and $\langle \bar{1}10\rangle$. The lack of a second layer indicates that the atoms condensed on top of the islands have enough energy left to overcome the Ehrich Schwoebel barrier. The LEED picture shown in the inset displays a p(2x2) pattern. A more detailed analysis of this pattern can be seen in figure 4.2a.

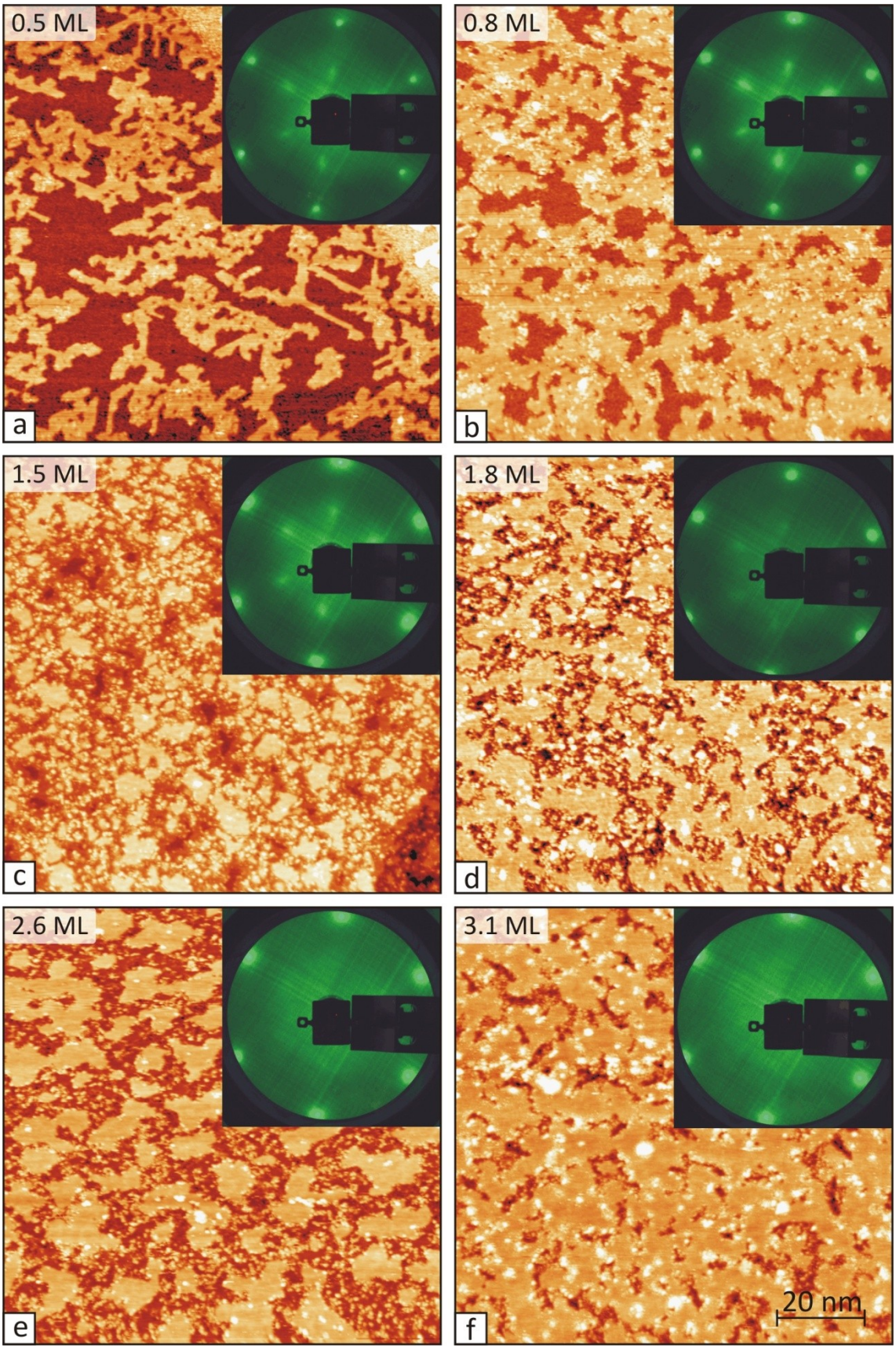

Fig. 4. 1: Growth series for Zn on Pd(111), showing (100×100) nm^2 STM images. In the insets the corresponding LEED patterns are presented. (a) θ_{app} = 0.5 ML; STM: U = +1.0 V, I = 0.4 nA; LEED: E_e = 63.7 eV. (b) θ_{app} = 0.8 ML; STM: U = -1.0 V, I = 0.4 nA; LEED: E_e = 61.6 eV. (c) θ_{app} = 1.5 ML; STM: U = -1.0 V, I = 0.4 nA; LEED: E_e = 56.3 eV. (d) θ_{app} = 1.8 ML; STM: U = 1.0 V, I = 0.4 nA; LEED: E_e = 67.0 eV. (e) θ_{app} = 2.6 ML; STM: U = -1.0 V, I = 0.4 nA; LEED: E_e = 55.7 eV. (f) θ_{app} = 3.1 ML; STM: U = -1.0 V, I = 0.4 nA; LEED: E_e = 55.7 eV.

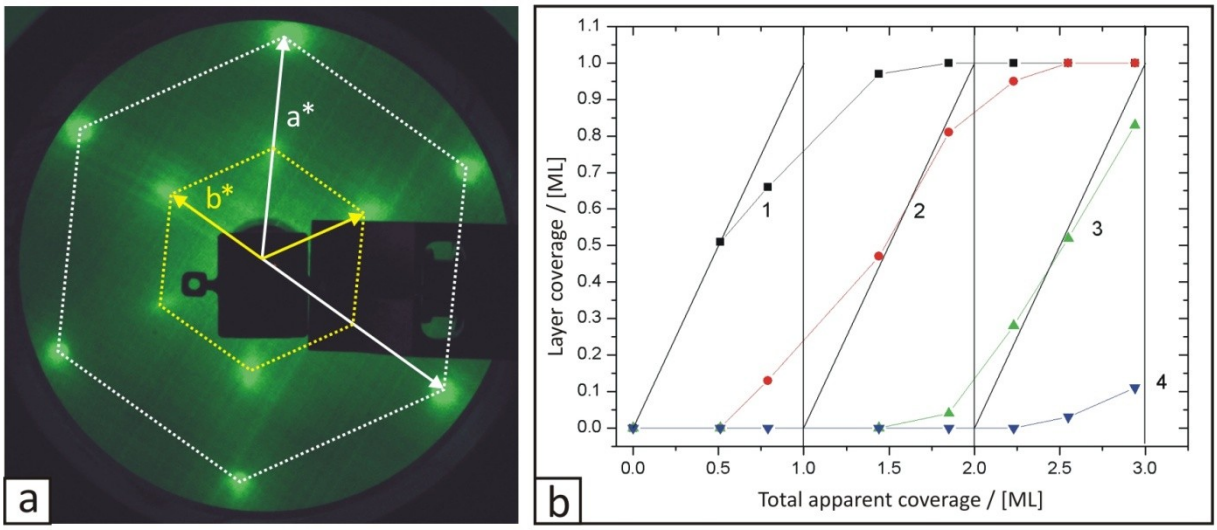

Fig. 4. 2: (a) LEED pattern observed at θ_{app} = 0.8 ML; E_e = 61.1 eV. In the image the reciprocal lattice vectors of the Pd substrate ($\vec{a}^*$) and of the superstructure ($\vec{b}^*$) are shown. With $\vec{a}_2^* = \frac{1}{2}\vec{a}_1^*$ this leads to a p(2×2) superstructure in real space. (b) Layer coverage versus total apparent coverage. The dots show the growth of the 1st (black rectangles), 2nd (red circles), 3rd (green triangles) and 4th layer (blue triangles). For comparison the diagonal solid lines represent perfect Frank van der Merve growth for the first three layers.

From this p(2×2) pattern it can be concluded that the islands already consist of a PdZn alloy, as known from literature [gj06, ss09, bs06, np07]. The LEED thus gives indirect information on the composition of the alloy, since the observed pattern should only occur for a 1:1 ratio of Zn to Pd.

In figure 4.1b θ_{app} has been increased to 0.8 ML. Although there are still some dendritic features visible, the islands expose more general forms now. Preferred orientations are hardly visible any more. Even though DLA might still have some influence on the growth but it definitely is not the major process any more. Also the second layer starts to be filled with clusters while the first layer is not yet completely filled. The p(2×2) pattern has become more intense what can be attributed to the higher coverage.

Figure 4.1c shows a coverage of θ_{app} = 1.5 ML. The clusters in the second layer have formed islands now and the first layer has also grown more dense although there are still some void spaces visible. The third layer is still empty except for a few clusters. The islands do not show any specific shapes now, so a more general nucleation process must be assumed. In contrast to the formation of the first layer, in the second there are a lot of clusters present in the space between the larger islands. This indicates a generally lower diffusion rate of the adsorbed species and a higher density of nucleation centres. In the LEED picture a decrease of intensity for the p(2×2) spots can be observed. This leads to the conclusion that this signal is mainly originating from the first layer.

At an apparent coverage of 1.8 ML (figure 4.1d), this trend is continued. The first layer is almost closed, most of the growth going on in the second layer and also the formation of

clusters in the third layer can be observed. The intensity of the p(2×2) signal has decreased further.

When θ_{app} is increased to 2.6 ML, as shown in figure 4.1e, a new growth pattern evolves. First and second layer are completely closed now. In comparison to figure 4.1c (θ_{app} = 1.5 ML), the formation of larger, more compact, islands is preferred in the third layer. In the LEED the p(2×2) signal has practically vanished, only the (1×1) spots are visible.

In figure 4.1f an apparent coverage of 3.1 ML is shown. Here the third layer is almost closed. Growth already starts in the fourth layer but now in form of small islands instead of clusters. The LEED is still depicting a (1×1) signal solely.

Summarizing these observations, a continuous change in the growth of the different layers is noticeable. For the first layer a DLA governed growth can be stated. In the second layer small clusters are formed first more comparable to a hit-and-stick mode. These clusters coalesce to larger islands. This mechanism is also present in the third layer but now the formation of larger islands is preferred. In the fourth layer no clusters but small islands are formed from the start on.

To get a more general picture of the growth mode it is helpful to plot the coverage of each single layer over the total apparent coverage, as it has been done in figure 4.2b. The boxes mark the borders of the individual layers and the solid diagonal lines represent ideal Frank van der Merve growth (layer-by-layer). The dots are the experimental values obtained for the different layers. For the first layer there is quite some discrepancy between observed and ideal growth. The uptake curve for the second layer is already approaching the ideal form and for the third layer there is quite good agreement between real and ideal line shapes. Even though there is some discrepancy between the observed growth and the ideal layer-by-layer model, the experimental data definitely does not support Vollmer-Weber or Stranski-Krastanov growth modes. So the general conclusion can be drawn that for zinc deposition onto Pd(111) the growth follows a Frank van der Merve line mode.

4.2 Structural analysis of the PdZn alloy

4.2.1 Experimental results

The main questions, regarding the PdZn surface alloy, concern its structure and composition. As described in the previous section a p(2×2) LEED pattern is visible for θ_{app} up to 1.8 ML. The strongest signal has been obtained at θ_{app} = 0.8 ML.

In figure 4.3 small area scans are presented for different apparent coverages of Zn on Pd(111). At an apparent coverage of 0.5 ML (figure 4.3a) a well defined stripe structure can

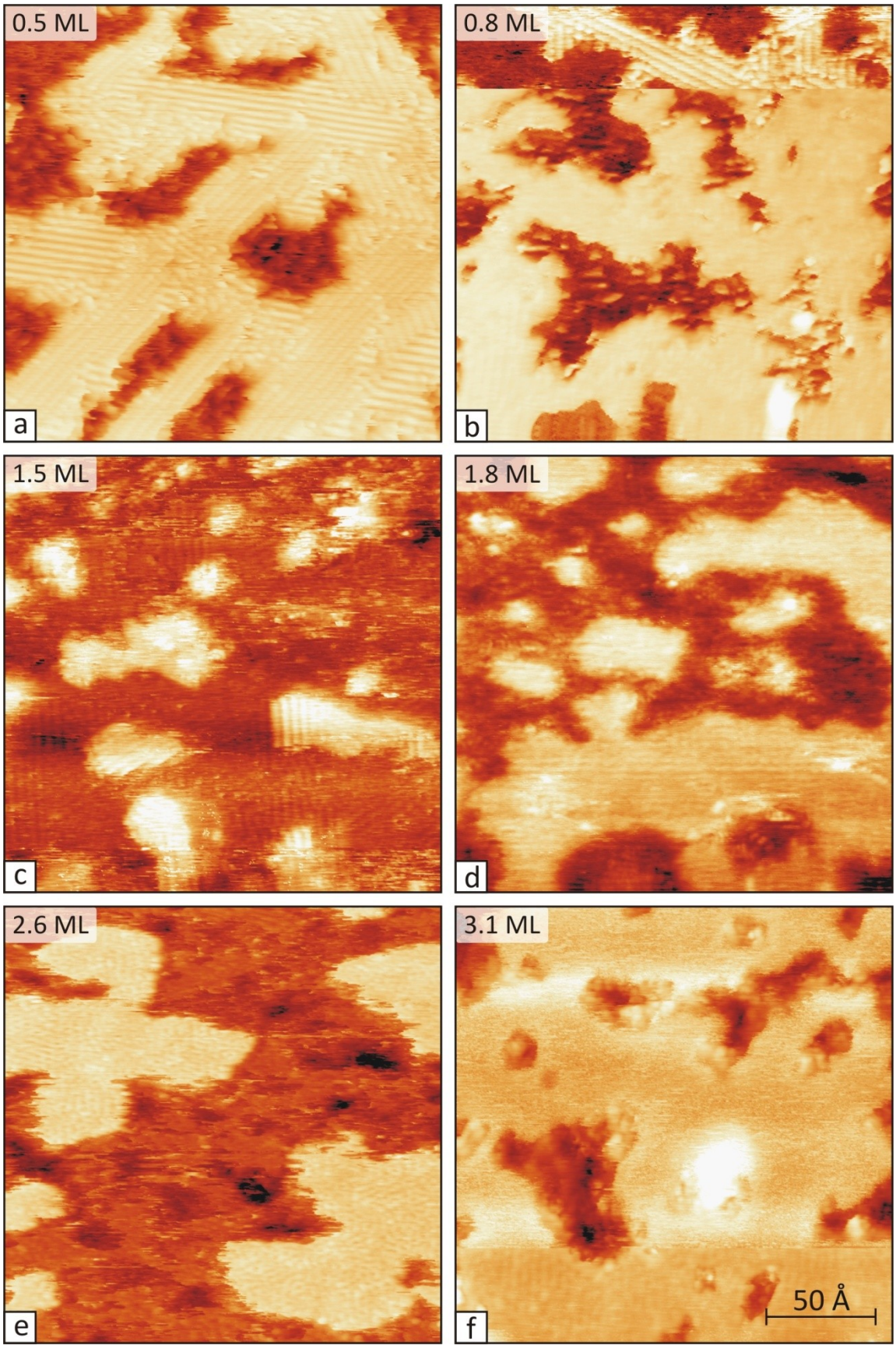

Fig. 4. 3: (20×20) nm^2 scans for different apparent coverage, showing stripes along the three main directions of the Pd(111) substrate - $\langle 01\bar{1}\rangle$, $\langle 10\bar{1}\rangle$ and $\langle \bar{1}10\rangle$. The directions of the stripes may differ between the pictures due to different orientation of the sample in the STM. (a) θ_{app} = 0.5 ML; STM: U = +140.0 mV, I = 2.0 nA. (b) θ_{app} = 0.8 ML; STM: U = -0.3 V, I = 3.0 nA; Inset: U = -30.0 mV, I = 7.5 nA. (c) θ_{app} = 1.5 ML; STM: U = -30.0 mV, I = 15.0 nA. (d) θ_{app} = 1.8 ML; STM: U = -30.0 mV, I = 14.0 nA. (e) θ_{app} = 2.6 ML; STM: U = -0.3 V, I = 3.0 nA. (f) θ_{app} = 3.1 ML; STM: U = -0.3 V, I = 1.0 nA.

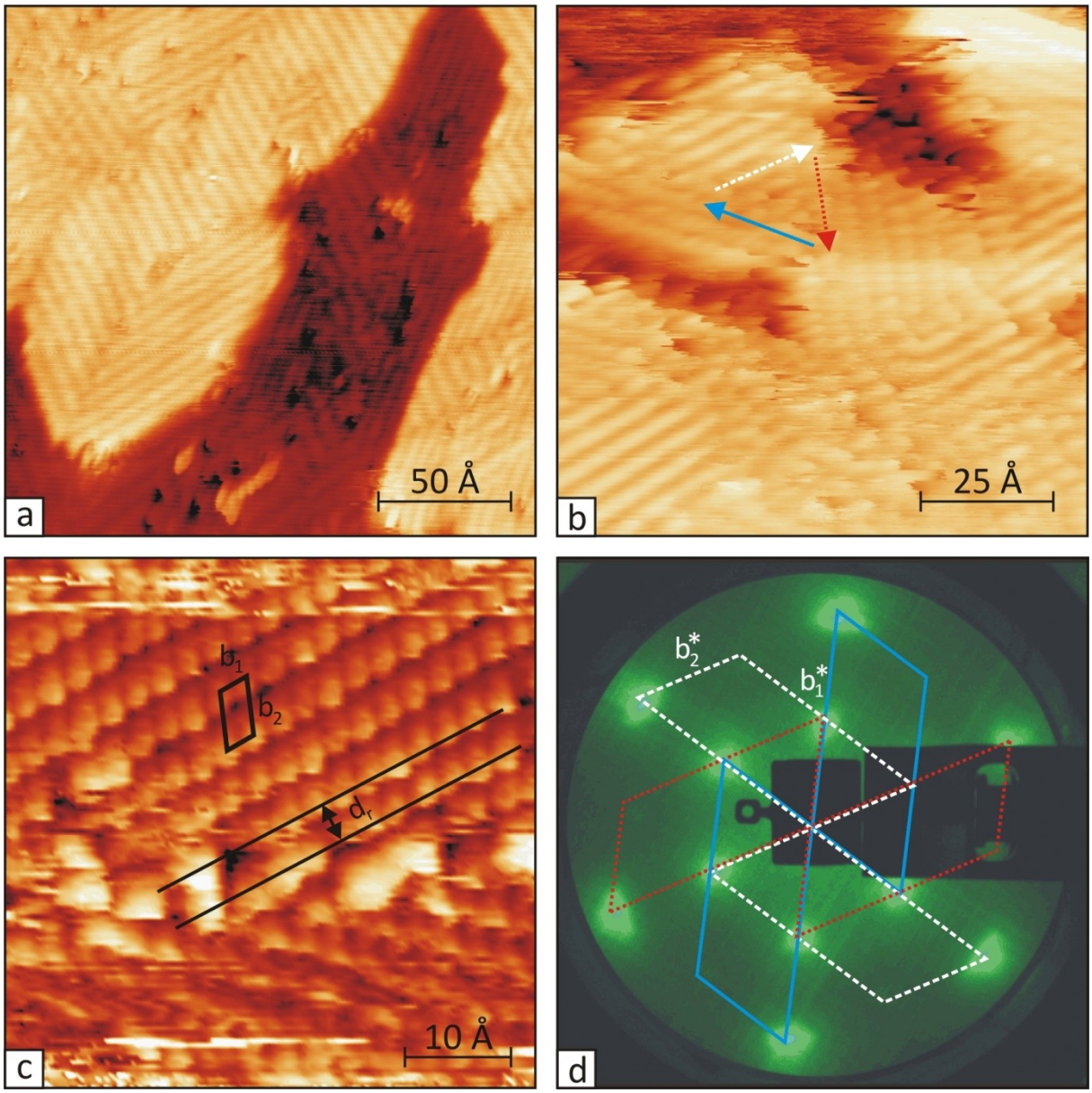

Fig. 4. 4: High resolution STM-scans of the PdZn - p(2×1) structure and the according LEED analysis. (a) p(2×1) stripes with three different orientations visible in two layers ; STM: (20×20) nm^2, U = -750.0 mV, I = 1.5 nA. (b) Stripe structure in the first layer. Domains with three different orientations are visible within the same island; STM: (10×10) nm^2, U = +140.0 mV, I = 2.0 nA. (c) Atomically resolved STM image of rows in two domains. The interrow distance d_r and the unit cell of the p(2×1) superstructure are also plotted; STM: (5×5) nm^2, U = +10.0 mV, I = 20.0 nA. (d) Construction of the p(2×2) LEED pattern with a p(2×1) unit cell along the three main directions of the Pd(111) surface. The outer spots of the superstructure show very low intensity due to interference and other dynamic effects; E_e = 58.5 eV.

be seen, with the rows running along three different substrate directions. They are also strongly pronounced at θ_{app} = 0.8 ML, which can be seen in the inset of figure 4.3b.

Also above one monolayer the stripe phase can still be observed but it becomes less pronounced with increasing amount of deposited zinc, being replaced by a more compact phase (figures 4.3c-f). At an apparent coverage of 2 ML and above, the rows are practically not visible any more. This observation is compatible with the LEED results, where a progressive vanishing of the p(2×1) has been observed.

To gain more information on the stripe phase, high resolution STM scans have been performed. Figure 4.4c shows an atomically resolved image of the stripe phase, also depicting the unit cell and the inter-row distance d_r.

With an experimental value for d_r of (4.4 ± 0.4) Å and

$$b_2 = \frac{d_r}{\sin\left(\frac{\pi}{3}\right)} \tag{6.1}$$

a value of (5.1 ± 0.5) Å can be calculated for the lattice vector b_2. To gain a value for the lattice vector b_1, line scans along the atomically resolved rows have been performed leading to b_1 = (2.7 ± 0.2) Å. Those numbers are in good agreement with the expectation values for a p(2×1) superstructure: $b_{1,exp}$ = 2.75 Å and $b_{2,exp}$ = 5.50 Å. This result also confirms the observations made by Bayer [bs06].

Figures 4.4a and b show islands of the stripe phase in the first and the second layer. These islands exhibit domains with different orientation. Having identified the superstructure to be p(2×1), these orientations coincide with the three main directions of the Pd(111) substrate - $\langle 01\bar{1}\rangle$, $\langle 10\bar{1}\rangle$ and $\langle \bar{1}10\rangle$. The corresponding construction of the observed LEED pattern is shown in figure 4.4d.

Further experimental details, for the height of the different layers and the corrugation normal to the stripes, are listed in table 4.1.

	layer height / [Å]	**corrugation / [Å]**
1st layer	2.2 ± 0.1	0.5 ± 0.2
2nd layer	2.2 ± 0.3	0.2 ± 0.1
3rd layer	2.2 ± 0.2	0.2 ± 0.1

Table 4. 1: Experimental values for Zn deposited on Pd(111), showing height and corrugation of the individual layers.

4.2.2 Computational results and analysis

The experimental data has already revealed some details on the growth of Zn on Pd(111) and of the structure of the PdZn alloy. To gain more insight into these topics DFT calculations have been performed by H. P. Koch [ks10, wj10]. In this section the structure of the PdZn alloy phase for an apparent coverage of up to 1 ML will be discussed.

For the PdZn alloy the p(2×1) structure is shown in figure 4.5a. Calculations for one, two and three alloy layers on a Pd(111) substrate have been carried out – the corresponding results are summarized in table 4.2. For comparison also the values for a stoichiometric bulk alloy are given. The latter are in very good agreement with the calculations performed by Chen [cp03] within the limits of DFT.

For one layer of PdZn on Pd(111) it has been found that the palladium atoms are moved slightly outwards by 0.012 Å, with respect to their equilibrium positions on the Pd(111) surface. The Zn atoms move inward by 0.133 Å, resulting in a total corrugation of the surface of 0.145 Å. This is also depicted graphically in figure 4.5c.

Parameter	1 x PdZn	2 x PdZn	3 x PdZn	PdZn bulk alloy
$\Delta z(Pd^1)$	+0.012	+0.082	+0.040	+0.009
$\Delta z(Zn^1)$	-0.133	-0.180	-0.156	-0.045
$\Delta z(Pd^2)$	-	-0.277	-0.169	-0.127
$\Delta z(Zn^2)$	-	-0.043	-0.112	+0.077
$\Delta z(Pd^3)$	-	-	-0.268	-
$\Delta z(Zn^3)$	-	-	-0.190	-
d^{Pd}_{01}	2.116	1.917	-	2.226
d^{Zn}_{01}	2.277	2.428	-	2.172
d^{Pd}_{12}	-	2.346	2.184	2.080
d^{Zn}_{12}	-	2.074	2.205	2.339
d^{Pd}_{23}	-	-	2.074	-
d^{Zn}_{23}	-	-	2.327	-
γ	1.40	1.22	1.16	1.16

Table 4. 2: Results of the DFT calculations for one, two and three layers of PdZn on a Pd(111) surface. Given are the values for the vertical displacement Δz with respect to the equilibrium position of an atom in pure Pd, the interlayer distances d and the surface energies γ. Upper indices mark the material, lower indices correspond to the concerned PdZn layers, where 0 denotes the topmost layer of the Pd(111) substrate. All distances are given in Å, the surface energies are given in Jm^{-2}. Values for the stoichiometric PdZn-bulk alloy phase are presented for comparison. Table taken from [ks10].

From the values for the interlayer spacing a mean value of 2.2 Å for the height of this layer can be derived, which is practically equivalent to the Pd step height. The surface energy of this layer is 1.40 Jm^{-2}, which is equal to that of the clean Pd(111) surface.

For a bilayer of PdZn the situation is very different. Here a value of 1.22 Jm^{-2} has been found for the surface energy, which makes this configuration more favourable than a single alloy layer. There is also a change in the corrugation: In the second alloy layer the zinc atoms move inward by 0.043 Å, but now the palladium atoms move inwards by 0.277 Å, resulting in a total corrugation of 0.234 Å. Due to the strong inward movement of palladium, the zinc atoms stick out of the surface, as shown in figure 4.5 d.

With a surface energy of 1.16 Jm^{-2} the formation of a third PdZn adlayer is virtually equal to the formation of a stoichiometric bulk alloy. These two configurations show a smaller value for the surface energy than two layers of PdZn, thus they would be more favourable from an energetic point of view. According to the values given in table 4.2, a surface buckling, with the zinc atoms sticking out, would be adopted by the three layer configuration as well as by the bulk alloy. The corrugation would be 0.078 Å for three layers of PdZn and 0.204 Å for the bulk alloy phase.

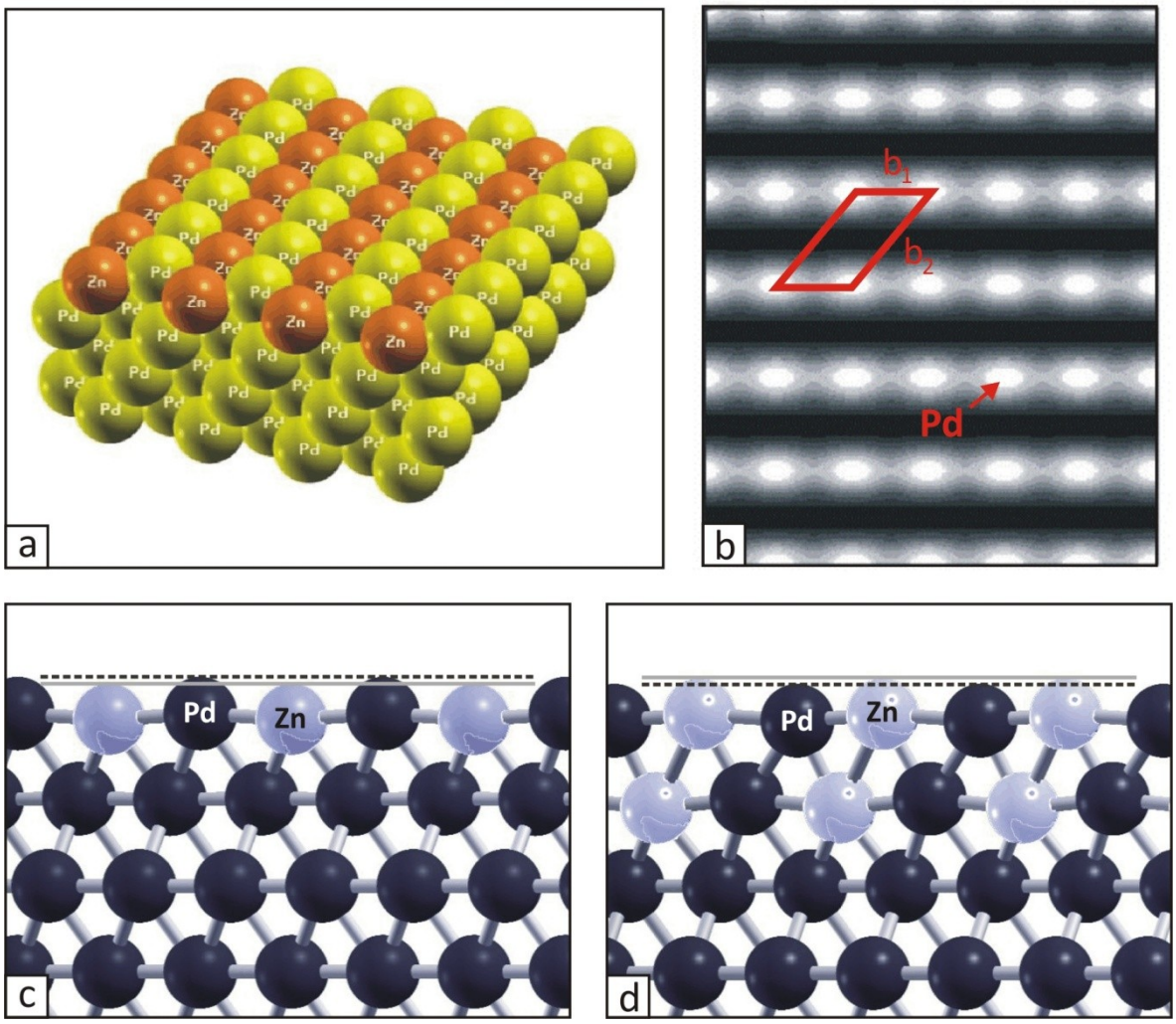

Fig. 4. 5: (a) Slab model for the calculations of the PdZn-alloy phase. (b) Simulated STM image for a PdZn –bilayer, also showing the unit cell; U = +0.5 V. (c) Side view for a single layer PdZn alloy. The dashed and the solid line represent the corrugation of Pd and Zn atoms respectively. (d) Side view for a PdZn - bilayer. The dashed and the solid line represent the corrugation of Pd and Zn atoms respectively. Pictures taken from [ks10].

Now the question is, if the islands observed in STM correspond to 1, 2, 3 or more layers of PdZn. The amount of deposited zinc reveals that bilayer islands are formed under experimental conditions, although 3 or more layers would be energetically more favourable according to the calculations. Some kinetic considerations help to understand, why this is the case.

In figure 4.6 a schematic representation of the PdZn alloy phases is shown. In (a) the case of a bilayer can be seen. To form this bilayer Zn atoms are incorporated into the topmost layer of the Pd(111) surface. The displaced Pd atoms move into the “first adlayer” to form an alloy with the rest of the Zn. According to table 4.2 the effective height, h_{eff}, of the resulting island corresponds to 2.21 Å, the mean value of d^{Pd}_{12} and d^{Zn}_{12}. This value fits very well with the experimental one of (2.1 ± 0.4) Å. In the case of such a bilayer the total Zn coverage would be equal to the apparent coverage seen in STM, which is indeed the case.

For a triple layer several possible configurations exist. Figure 4.6b depicts the easiest case: On top of a bilayer a third PdZn adlayer is formed. The required Pd atoms are taken from the

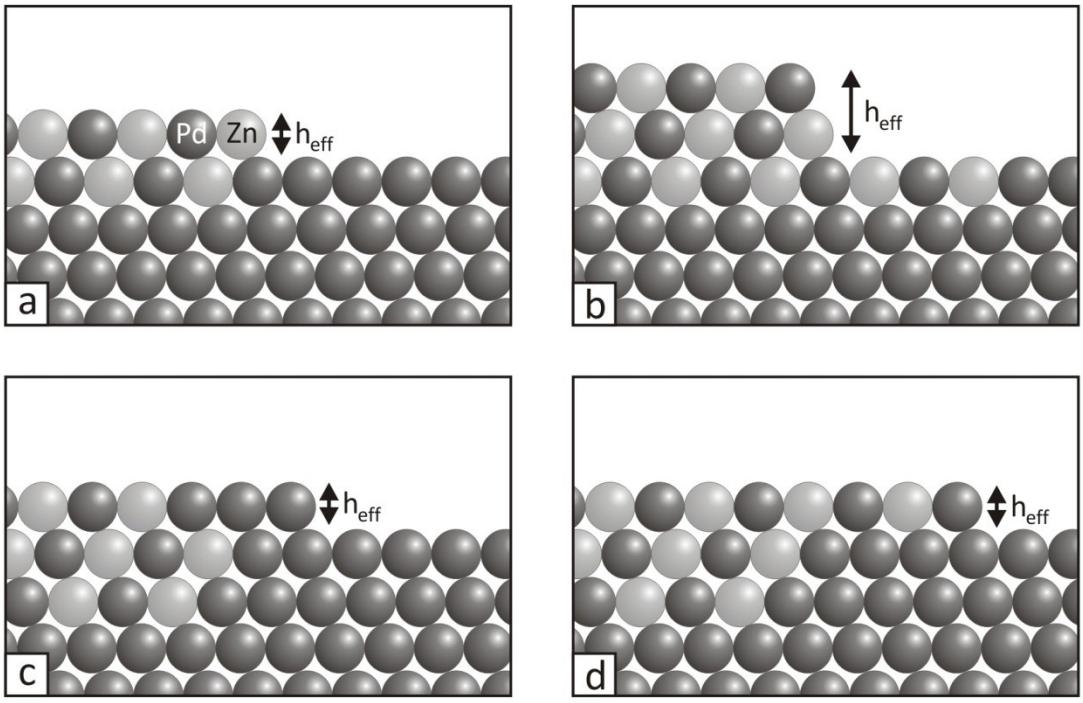

Fig. 4. 6: Different atomic configurations for two (a) or three layers (b,c,d) of an PdZn alloy.

topmost Pd(111) layer and the created holes being filled up with zinc. The so created single layer of PdZn is energetically less favourable than a bilayer, but due to the triple layer island the total surface energy is lowered. But in this configuration h_{eff} would be about 4.4 Å.

To gain an apparent island height of about 2.2 Å, two of the three PdZn layers must be incorporated into the palladium matrix. The displaced Pd atoms can either form a new Pd(111) surface or a single alloy layer – both configurations are equivalent in gained energy.

The case of a freshly formed Pd(111) surface, shown in figure 4.6c, would result either in islands, not showing a p(2×1) structure, or in areas at the perimeter of the alloyed islands without stripes. Both cases do not fit into the experimental data.

The other model with a “sunk-in” triple alloy layer accompanied by a single alloy layer is shown in figure 4.6d. This configuration would suffice the experimental observations. But here the kinetic expenditure needs to be considered. To form such a “mixed” structure an already considerable movement of atoms is necessary. With a melting point of 1825 K for palladium it is questionable if such a process can be actuated at a sample temperature of 300 K, even if the Zn atoms, hitting the surface, have higher thermal and kinetic energy. Similar considerations need to be attended to in the case of a bulk alloy phase.

According to these considerations, the bilayer phase is most favourable because it needs the least rearrangement of atoms. That explains, why bilayer islands are observed with STM. Moreover it shows that the alloy formation is strongly governed by kinetics. Apparently incompatible with the bilayer model is the fact, that a p(2×1) structure has been also been observed for a second adlayer (e.g.: figure 4.4a). Yet this can be easily explained with the

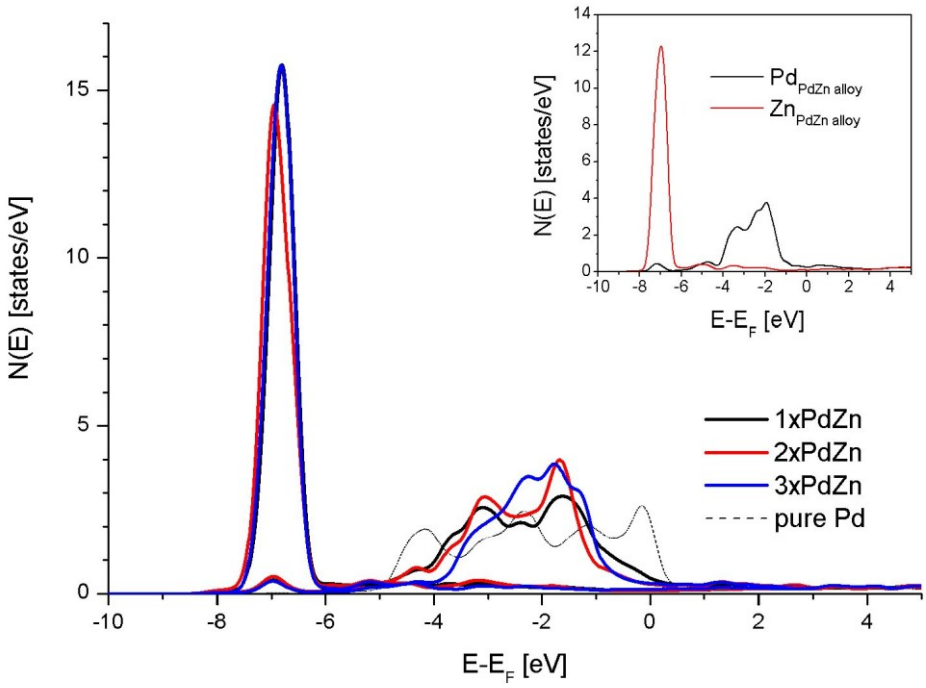

Fig. 4. 7: Calculated LDOS for one, two and three layers of PdZn on a Pd(111) surface. The inset shows the contribution of each species to the total DOS. Picture taken from [ks10].

preference of Zn to adsorb in places with a high Pd-coordination on a PdZn alloy, as described in section 4.3. Thus the p(2×1) structure, observed for the 2nd adlayer, corresponds to Zn, adsorbed on top of a PdZn-bilayer.

Stadlmayr et al. have performed low energy ion scattering (LEIS) experiments on 2 ML of Zn deposited onto Pd(111) at 150 K and annealed to 450 K [ss09]. After annealing, a stable p(2×1) structure could be observed in LEED. The LEIS measurement confirmed a buckling of the PdZn surface with the Zn atoms being at higher position than the Pd atoms in the topmost layer. The measurement also yielded a value of 0.25 Å for the surface corrugation. These results agree with the values, calculated for the bilayer phase, thus confirming the correct modelling of the alloy by the DFT-model.

Layer composition	layer number	Pd	Zn
Pd(111)	1	10.03	-
Pd(111)	2	9.96	-
PdZn(111)	1	10.41	11.64
PdZn(111)	2	10.41	11.53
PdZn surface alloy	Surface	10.23	11.62

Table 4. 3: Calculated Bader charges for the two topmost layers of a Pd(111) surface and a PdZn(111) surface as well as for a PdZn layer on top of a Pd(111) surface. All charge values are given in units of elementary charge e = 1.602 × 10^{-19} C. Standard values for free Pd atoms are 10 e and 12 e for free Zn atoms respectively. Values taken from [ks10].

Since STM essentially yields information about the electronic properties of a surface it is also necessary to take some theoretical insight into this topic to make a proper interpretation of the obtained images possible. As known from literature [np07, nj04, bs06], the electronic structure of PdZn is dominated by a charge transfer from zinc to Pd-4d orbitals resulting in a density of states similar to that of copper. In table 4.3 the Bader charges calculated by H.P. Koch [ks10] for pure palladium adlayers and PdZn adlayers on a Pd(111) surface are presented for one and two layers coverage. When zinc is added to the surface, the value for palladium increases by about 0.23 e in comparison to a free Pd atom. This is a direct result of the charge transfer from zinc to palladium. For zinc the charge decreases by about 0.38 e. The discrepancy can be attributed to interlayer charge transfer.

In figure 4.7 the calculated local density of states (LDOS) for one, two and three layers of PdZn can be seen. The inset shows the contributions of the two atomic species to the spectra. It reveals that around the Fermi edge the palladium states are dominant, creating the bright spot signals in the STM pictures although the Zn atoms are situated higher in the lattice at bilayer coverage. The electronic contrast supersedes the structural one. This fact explains why the theoretical and experimental corrugation values, stated in table 4.1 and 4.2, do not fit together. A simulated STM picture for a PdZn bilayer is presented in figure 4.5b.

The model presented in this chapter is well suited to explain the structure of the PdZn alloy phase for an apparent coverage up to one monolayer. Yet it only poorly describes the situation at higher apparent coverage when the p(2×1) structure becomes less evident in LEED and STM. Additional experimental data makes an analysis of this coverage range easier. This data and the according calculations will be presented in the next section.

4.3 Zinc desorption

More information about the composition of the film at higher apparent coverage could be obtained by zinc desorption analysis. Kratzer et al. have performed temperature programmed desorption (TPD) experiments for different amounts of deposited Zn [wj09]. In those experiments Zn has been deposited onto a Pd(111) sample at 300 K. Subsequently the sample has been heated at a rate of $2Ks^{-1}$. The amount of desorbing zinc has been measured with a quadrupole mass spectrometer, mounted in line of sight of the sample. Additionally two heating series with the same experimental parameters have been performed and analysed using LEED and STM. In these experiments the apparent coverage has been equal or larger than 3 ML. The results for both setups are presented in figures 4.8 and 4.9.

In figure 4.8 the TPD spectra for amounts of deposited Zn of 0.3 ML (a) to 15.7 ML (o) are shown. The inset shows the spectra for up to 3 ML in more detail. Please note that in the large diagram the high temperature peak has been upscaled for better visibility. For an

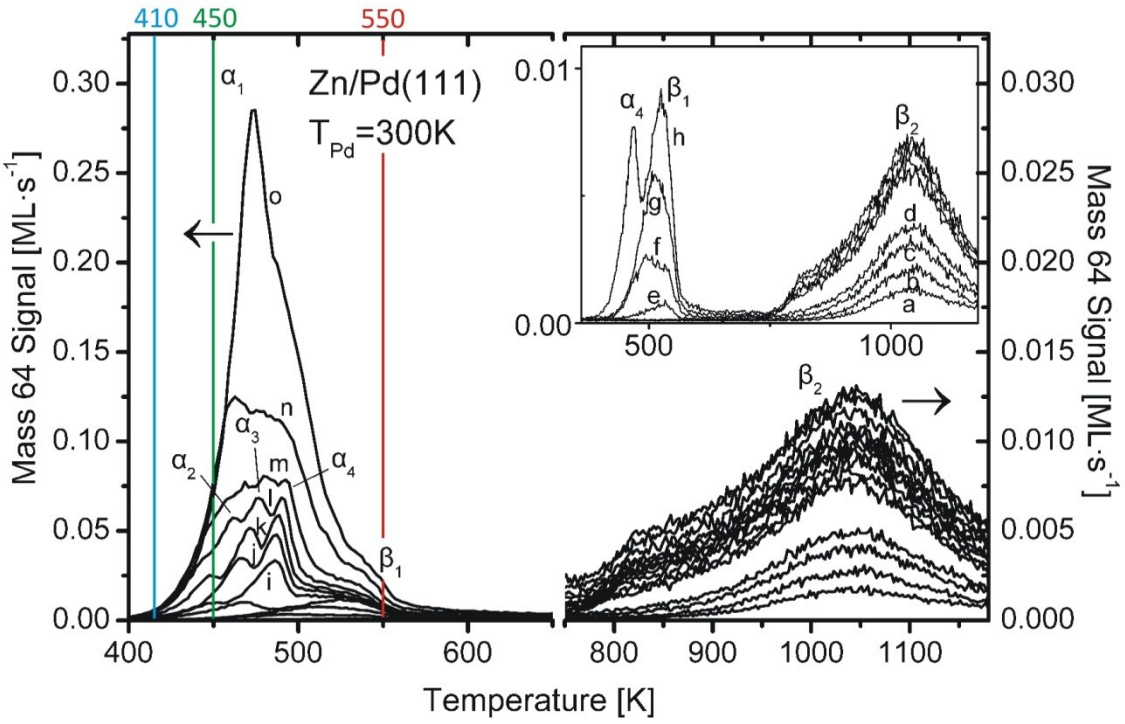

Fig. 4. 8: TPD spectra for different amounts of deposited zinc: (a) 0.3 ML; (b) 0.5 ML; (c) 0.8 ML; (d) 1.0 ML; (e) 1.7 ML; (f) 2.0 ML; (g) 2.5 ML; (h) 3.0 ML; (i) 3.9 ML; (j) 4.6ML; (k) 5.5 ML; (l) 6.6 ML; (m) 8.3 ML; (n) 11.3 ML and (o) 15.7 ML. The inset shows the structures up to 3.0 ML in more detail. The coloured lines show the temperatures for the different stages shown in figure 6.9. Picture taken from [wj09].

amount of deposited Zn, $\theta_{Zn,dep} \leq 1$ ML one peak can be observed, centred at 1040 K. In the spectrum it is denoted β_2. For 1 ML < $\theta_{Zn,dep} \leq 3$ ML a second peak (β_1) evolves, with its centre at 530 K. At $\theta_{Zn,dep} > 3$ ML several new peaks with complicated structure arise in the low temperature region (α_1 - α_4).

In figure 4.9 the representative results of the according STM measurements are shown. (a) depicts the surface at an apparent coverage of 3 ML. In the LEED only the (1×1) signal is visible. The 3rd layer is almost closed, and some islands are already present in the 4th layer. No stripes can be seen in the high resolution scans.

At annealing temperatures between 400 and 420 K a weak p(2×2) signal appears in the LEED (figure 4.9b). Large area STM scans already show quite some loss of material. A lot of clusters are visible on the surface. High resolution images show the emergence of a weak and not so well ordered stripe structure. It can be seen in figure 4.8 that the onset of low temperature α-peaks is situated in this temperature range.

A strong increase of intensity of the p(2×2) signal in the LEED can be observed at annealing temperatures from 420 to 480 K, more deeply in the α-peak range. This situation is depicted in figure 4.9c. The STM images show two visible layers. The upper one consists of medium sized islands, the lower one is just starting to break up. Clusters are less frequent than before and they are mainly situated at the rim of the islands. High resolution images show a well ordered stripe structure in both layers.

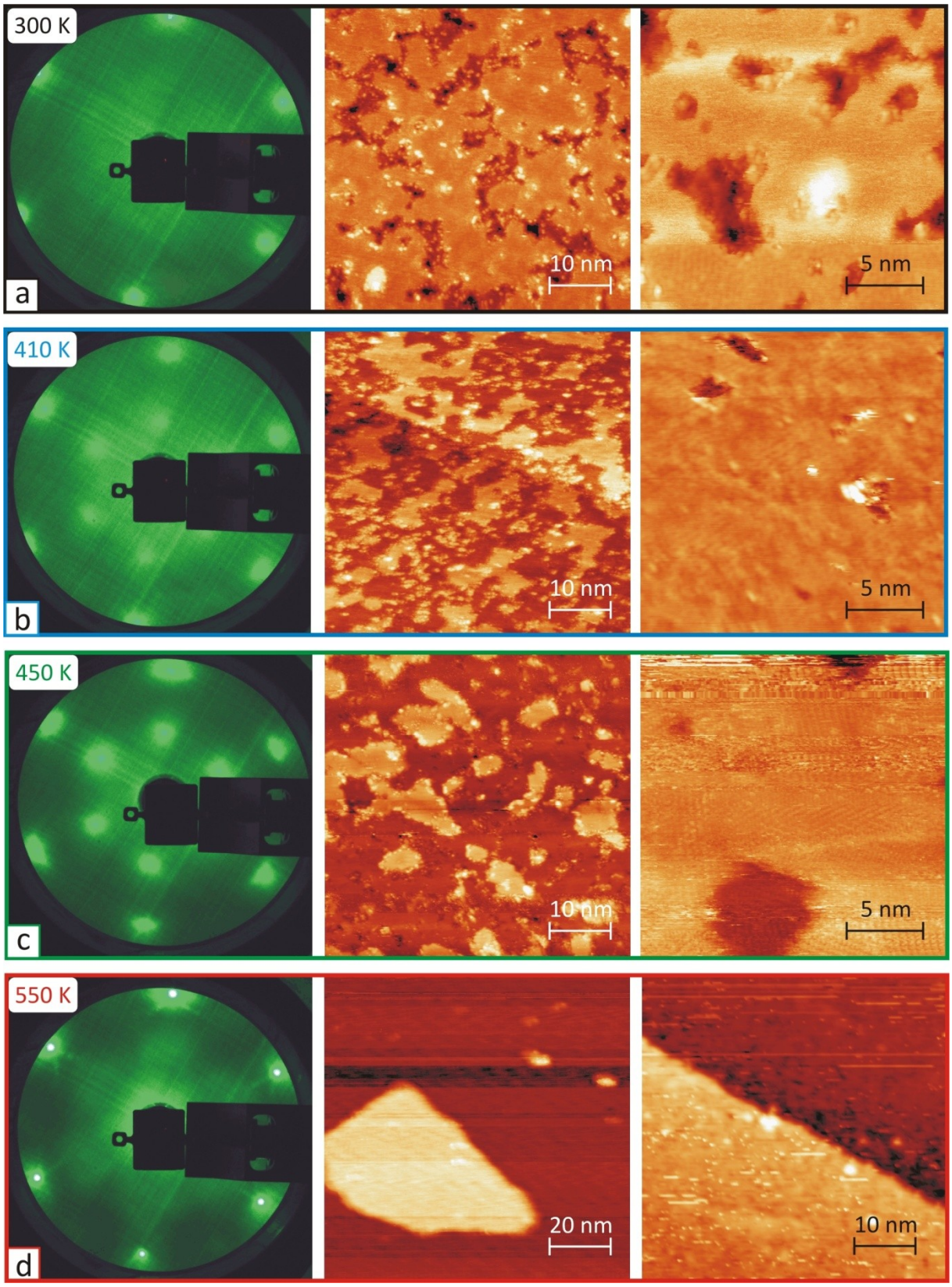

Fig. 4. 9: STM annealing series for an apparent coverage of 3 ML. All LEED pictures have been acquired at E_B = 58.2 eV, the STM pictures in the central column have been measured at U = -1 V and I = 1 nA. For the pictures in the right column varying parameters have been used: (a) U = -300 mV, I = 1.0 nA; (b) U = -30 mV, I = 5.0 nA; (c) U = +10 mV, I = 20 nA, (d) U = +1.0 V, I = 0.4 nA.

After further annealing to temperatures between 530 and 560 K, at the high temperature end of the β_1 peak, the signal of the superstructure has disappeared in the LEED. STM scans

show an empty surface without structure. Sometimes islands can be found on the surface but they expose no special features.

At this point it should be noted that there might be some discrepancies up to 30 K for the temperature values measured during the TPD and STM experiments due to different calibration. Generally the temperatures stated for the TPD measurements are more trustworthy. Still the STM results show a general trend that can be roughly assigned to different peaks in the desorption spectrum.

Additional insight into the situation could be gained by a more profound analysis of the TPD data. The desorption-process can be described using the rate equation:

$$R_{des} = k\, N^{x} \tag{6.2}$$

where R_{des} is the desorption rate, k is the rate constant, N is the surface concentration of the concerned species and x is the desorption order.

For α_1 an x- value equal to zero has been found. This concentration independent process is typical for multilayer desorption. α_2 to α_4 show an order of 0.5, implying a fractional process. That indicates desorption of Zn atoms at the perimeter of islands and clusters. β_1 represents a first order state, classical for simple atomic desorption depending on the concentration. Having common leading edges the peaks could be fitted using a multiple peak least squares algorithm which allowed separation of the individual peaks. Those could be fitted again using a Polany-Wigner simulation and yielded the desorption energies listed in table 4.4. Especially α_1 could be fitted with high accuracy using an Arrhenius -plot method for zero order desorption. Statistical data evaluation also yielded the amount of desorbed zinc per peak which is equal to (1.0 ± 0.2) ML for α_2 to α_4 and β_1.

Peak	Measured desorption energy / [kJmol^{-1}]	Calculated desorption energy / [kJmol^{-1}]
α_1	119 ± 5	-
α_2	122 ± 5	-
α_3	124 ± 5	111.9
α_4	128 ± 5	114.8
β_1	137 ± 5	141.8
β_2	281 ± 5	270.0

Table 4. 4: Desorption energies derived from the TDS spectra shown in figure 6.8 and calculated with DFT. Values taken from [wj09] and [ks10].

The value for the multilayer desorption peak α_1 is very close to the literature value for the heat of evaporation of metallic zinc, which is 115 kJmol^{-1} [wc74]. The desorption-energies for the underlying layers which correspond to the peaks α_2 to α_4 rise slowly but steadily, the closer they are to the substrate. Then, when coming to the next layer, attributed to β_1, there

is a sudden jump in the desorption energy. This implies some more drastic change in the binding energy and thus in the kind of binding.

The high temperature peak β_2 shows characteristics comparable to 1st order desorption and has been analyzed using a Redhead approximation. The resulting value for the desorption-energy is also listed in table 4.4. At higher coverage a shoulder appears in the β_2 peak at 800 K. The amount of desorbing zinc has been determined to be 2 ML. This value contrasts the amount of 1 ML reported by Gabasch [gj06].

The desorption energies found for higher coverage and the absence of p(2×1) structure for these layers lead to the conclusion that they do not consist of a PdZn alloy but of pure zinc instead. Interpretation of the TPD- and STM- measurements result in the following model:

From section 4.2 it is already known that Zn forms an ordered 1:1 alloy phase with p(2×1) structure at an apparent coverage up to 1 ML. This alloy phase most likely exists in bilayer form resulting in a total Zn coverage equal to the apparent coverage in STM. On top of that bilayer already a pure Zn layer forms when the coverage is increased. Due to the stronger interlayer binding to the Zn atoms in the alloy the desorption energy is higher than the one for pure zinc. This results in the desorption-peak β_1. The assumption, that this Zn layer is already formed at a coverage slightly above 1 ML, stems from the TPD-result that β_1 cannot be seen at 1.0 ML of deposited Zn but is already present at 1.7 ML.

On top of this 1st Zn layer a second one is formed with already lowered binding energy resulting in the peak α_4. The 3rd Zn layer produces α_3 and the 4th one α_2. At even higher coverage the conditions of a pure Zn crystal are reached leading to the multilayer desorption peak α_1.

The high desorption energy of the β_2 peak indicates that it originates from a dissociation of the PdZn alloy. Yet the STM pictures reveal that the surface is already empty at temperatures around 550K at the high temperature. From literature it is known that Zn

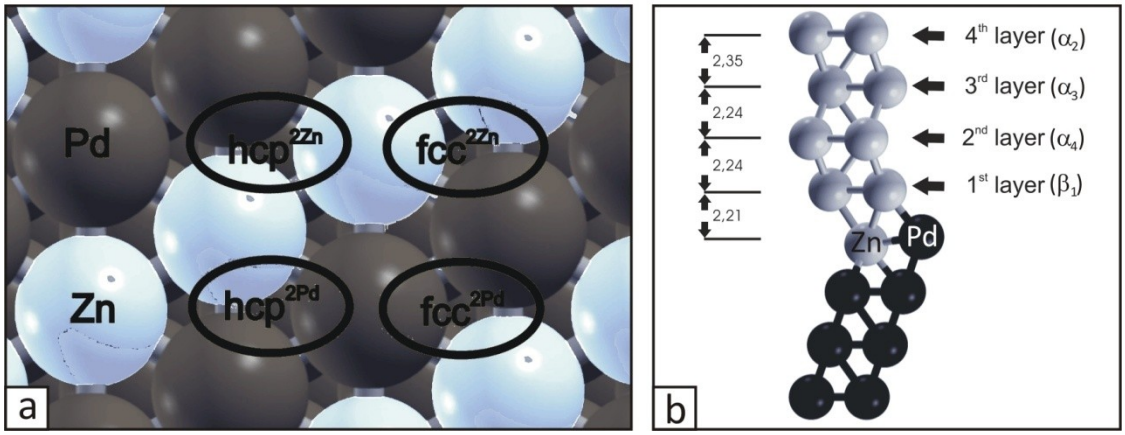

Fig. 4. 10: (a) Highly coordinated adsorption sites on a p(2×1) PdZn alloy. For hcp and fcc sites either two Pd and one Zn atom or two Zn atoms and one Pd atom are acting as nearest neighbours, as marked in the indices. (b) Model for the adsorption of Zn layers on top of a PdZn alloy phase. The corresponding layer heights and the assignment to the observed TPD peaks are also noted. Pictures taken from [ks10].

1st layer Zn on a 2x1 PdZn structure		
adsorption site	Coverage / [ML]	adsorption energy / [eV]
br^{2Pd}	0.25	-1.401
br^{2Zn}	0.25	-0.937
fcc^{2Pd}	0.25	-1.398
fcc^{2Zn}	0.25	-1.018
hcp^{2Pd}	0.25	-1.401
hcp^{2Zn}	0.25	-0.996
top^{Pd}	0.25	-1.015
top^{Zn}	0.25	-0.562
br^{2Pd}	0.50	-1.520
fcc^{2Pd}	0.50	-1.521
hcp^{2Pd}	0.50	-1.520
fcc	1.00	-1.470
hcp	1.00	-1.466
2nd layer Zn on a 2x1 PdZn structure		
fcc	0.25	-0.624
hcp	0.25	-0.564
hcp	0.50	-0.819
fcc	1.00	-1.171
hcp	1.00	-1.188
3rd layer Zn on a 2x1 PdZn structure		
fcc	1.00 ML	-1.131
hcp	1.00 ML	-1.158
4th layer Zn on a 2x1 PdZn structure		
fcc	1.00	-1.087
hcp	1.00	-1.109
Zn on pure Pd		
fcc	0.25	-1.646
hcp	0.25	-1.659
top	0.25	-1.046
fcc	1.00	-1.821
hcp	1.00	-1.816

Table 4. 5: Calculated adsorption energies for Zn on a p(2×1) PdZn surface alloy depending on coverage and adsorption site. Adsorption sites are on top (top), bridge (br), hexagonal close packed hollow (hcp) or face centred cubic hollow (fcc). The index denotes different coordination on the PdZn layer as shown in figure 4.10a. The most stable sites are highlighted. Table taken from [ks10].

tends to diffuse into the bulk at elevated temperatures [ls98, hm69]. Regarding that fact the situation can be explained in the following way: Already at temperatures above 300 K a concentration driven diffusion process of Zn atoms into the Pd bulk sets in. At the high temperature end of β_1 the surface is practically free of Zn leading to a reversal of the concentration gradient. The dissolved Zn starts to diffuse back to the surface and desorbs at

temperatures above 700 K. Due to this process of diffusion and desorption and also due to the fact that the diffusion will result in different PdZn-stoichiometries lead to the particular shape of β_2, especially the pronounced broadening of the peak. Due to this diffusion of Zn into the bulk it is also difficult to assign the amount of desorbed Zn in β_2 to a special layer.

To confirm this model additional DFT calculations have been performed by H. P. Koch, simulating Zn layers on top of a PdZn alloy. The corresponding geometry is shown in figure 4.10b. The layer heights calculated for this model agree very well with the ones measured in STM. Figure 4.10a shows the different coordination for adsorption sites on a p(2×1) PdZn layer. The adsorption energies for different sites are listed in table 4.5.

There is a large jump from the adsorption energies of the Zn atoms directly on the PdZn alloy to those of the layers above. The reason for that is the larger binding energy between Zn and Pd in comparison to two Pd atoms. From table 4.5 it also becomes clear that Zn prefers adsorption sites with a high coordination of Pd atoms, what fits very well into that picture. For comparison also the adsorption energies for Zn directly on a Pd(111) surface are given.

With these numbers the desorption energies of the 1st (β_1), 2nd (α_4) and 3rd Zn-layer (α_3) on the PdZn surface alloy can be calculated. The values are presented in table 4.4. For β_1 the calculated desorption energy is in good agreement with the measured one. For the α-peaks the discrepancy is higher. This can be attributed to the limits of DFT in this case, because the calculations have been performed for a temperature of 0 K. Still the general trend, with a large jump in the desorption energy between β_1 and α_4 and further decrease for α_3, is also reflected in the calculated values, thus confirming the proposed model of Zn layers on top of a PdZn surface alloy.

1 layer Zn		
layer	**Pd**	**Zn**
PdZn layer	10.34	11.62
1st Zn layer		11.86 - 11.93
2 layers Zn		
PdZn layer	10.35	11.62
1st Zn layer		11.85 - 11.92
2nd Zn layer		11.98 - 11.99
3 layers Zn		
PdZn layer	10.35	11.62
1st Zn layer		11.86 - 11.93
2nd Zn layer		12.01 - 12.02
3rd Zn layer		11.97 - 11.99

Table 4. 6: Calculated Bader charges for one layer of PdZn on a Pd(111) substrate and an increasing number of Zn layers over the alloy layer. All charge values are given in units of elementary charge e = 1.602 × 10^{-19} C. Standard values for free Pd atoms are 10 e and 12 e for free Zn atoms respectively. Values taken from [ks10].

Since the high temperature peak β_2 is assigned to desorption of Zn from the alloy, this situation has been simulated by removing Zn from the PdZn layer in the model shown in figure 4.10b. The energy needed to create a Zn-hole in the alloy has been calculated to be 270 $kJmol^{-1}$. Using the same parameters for the Redhead approximation, that have been used for the TPD peak fitting procedure, this results in a desorption peak centred at 990 K. This result is again in good agreement with the experiments. Additionally calculations of the electronic structure have been made for the Zn layers on top of the PdZn alloy. The calculated Bader charges are listed in table 4.6.

These calculations reveal a small charge transfer of 0.07 to 0.15 e from the Zn atoms in the first Zn adlayer to the Pd atoms in the alloy. For the Zn in the higher layers only very small deviations from the charge of pure Zn can be observed. For the density of states, shown in figure 4.11, a change of shape and a decrease of width can be observed with increasing number of adsorbed Zn layers. These changes also correspond to a convergence to the line shape of pure zinc.

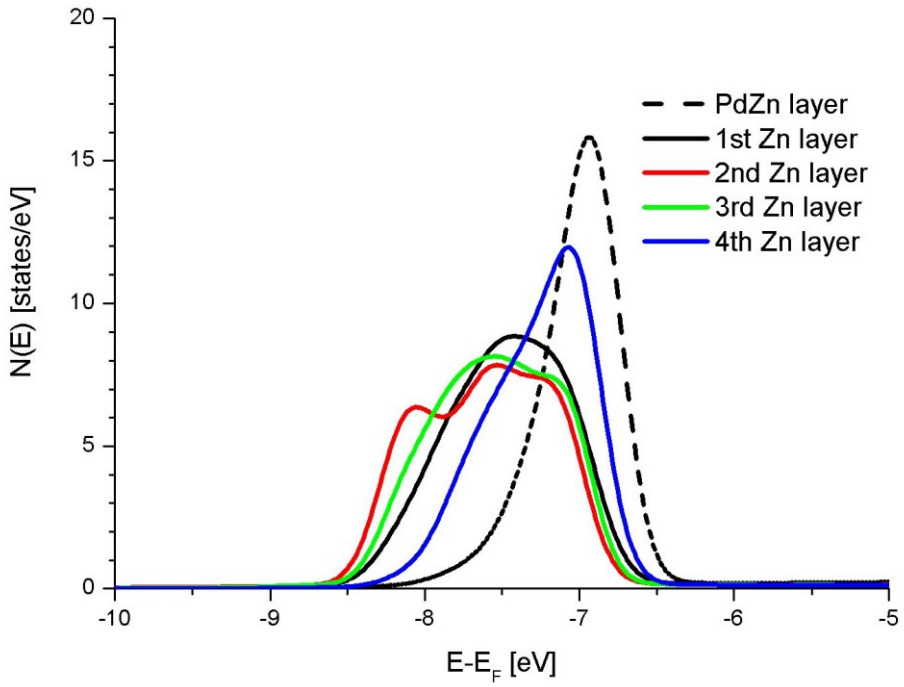

Fig. 4. 11: Density of states calculated for one layer of PdZn on Pd(111) and an increasing number of Zn layers on top of it. Picture taken from [ks10].

4.4 Summary

Adsorption, structure and desorption of Zn on a Pd(111) surface have been investigated using LEED, STM, TPD and DFT. Experimental and theoretical results have been used to build a suitable model for the corresponding layer structures.

Upon desorption of Zn onto a Pd(111) surface, first a PdZn surface alloy is formed with a 1:1 Pd:Zn ratio. The alloy forms a bilayer, with the lower level corresponding to the former Pd(111) surface layer, and shows a distinct p(2×1) superstructure. Along the equivalent substrate directions $\langle 01\bar{1}\rangle, \langle 10\bar{1}\rangle \text{ and } \langle \bar{1}10\rangle$, three domains evolve, giving rise to a p(2×2)-signal in LEED. The lower PdZn layer has a corrugation of 0.145 Å, with the Pd atoms being located higher than the Zn atoms. For the upper PdZn layer a corrugation of 0.234 Å has been found with the Zn atoms located at higher positions than the Pd atoms.

With increasing coverage, layers of pure Zn are formed on the PdZn alloy. The higher the coverage, the less the topmost layer is influenced by the PdZn. Already for the 5th Zn adlayer the situation is the same as in a pure Zn crystal.

Electronically the PdZn alloy is characterized by a charge transfer of about 0.2 to 0.4 e from Zn to Pd 4d. Also a weak interlayer charge transfer takes place. As a result of this transfer the DOS changes significantly, finally resembling the one of copper. Around the Fermi edge, the Pd states are dominant leading to a bright spot signal in STM. For the Zn-layers on top of the alloy a charge transfer has been calculated, which decreases rapidly for further Zn-adlayers. The first Zn-adlayer is more strongly bound, due to the Pd in the alloy phase, the subsequent Zn layers have much lower binding energies. Zn binds to the Pd-atoms on the alloy surface first. As a consequence, the stripe structure is (partly) visible until the 1st Zn-adlayer is completely filled.

The different binding energies of individual layers lead to a characteristic desorption spectrum. Upon heating the outermost Zn-layers desorb first, resulting in one multilayer desorption peak around 480 K (α_1). The 2nd to 4th Zn adlayers produce each a distinct desorption signal according to their binding energies ($\alpha_2 - \alpha_4$). The Zn layer situated directly on top of the alloy phase desorbs at higher temperature due to its tighter binding to the layer beneath (β_1). At the same time Zn already diffuses into the bulk leaving the surface empty. At high temperatures (>700 K) the dissolved Zn diffuses back to the surface and desorbs giving rise to a broad peak in TPD centred at 1040K (β_2).

Chapter 5: ZnO on Pd(111)

As explained in the introduction, real catalysts often consist of small metal particles on top of an oxide substrate. Yet they are difficult to study within the means of charged probe techniques in surface science. Therefore inverse model-catalyst systems are built, consisting of oxide films grown on well defined metal surfaces. Real catalysts work in highly reactive environment, the model catalysts, on contrary, are typically examined in ultrahigh vacuum (UHV). The hence arising differences between models and real catalysts are called “pressure gap” and “materials gap”.

Nonetheless by the study of model catalysts valuable information is gained about the bonding and interaction of the metal- and oxide-components. This information can be used to determine the related values for real catalysts, regardless of pressure- and materials gap. These insights again reveal more about the structure and, even more important, about suitable adsorption sites for the real catalysts, thus providing data for their optimisation. Due to these reasons the investigation of model catalysts is a means, used by default, to model future catalyst systems.

In this chapter the structural characterisation of such a model catalyst consisting of ZnO layers on a Pd(111) surface, will be presented. The results have been obtained with LEED, STM, TPD- and infrared spectroscopy, supported by DFT calculations.

5.1 Growth, morphology and structure of ZnO films

5.1.1 Submonolayer coverages

For this investigation, experiments have been performed using LEED and STM. The ZnO films have been grown freshly for each coverage, using standard conditions. Standard conditions mean that during film preparation a sample temperature of 300 K and an oxygen pressure of 5×10^{-7} mbar have been used with subsequent annealing to 550 K in the same oxygen atmosphere. In a few experiments the oxygen pressure deviated a bit from the standard value - the corresponding parameters will be marked separately for these cases. Preliminary tests have shown, that for this coverage range no significant difference between post oxidation (PO) and reactive evaporation (RE) can be observed. Nevertheless, the PO-procedure has been preferred, since it yields slightly better ordered films. As mentioned in the experimental section, it has not been possible to determine the amount of deposited Zn by using a microbalance. The amount of ZnO on the sample surface has been controlled roughly via temperature adjustment of the evaporator and deposition time, as described in

chapter 2.3. With this procedure a total quantification has not been possible. The deposition process resulted in a rough expectation value for the coverage, which has been compared to the island area, measured with STM. Thus an estimate of the real coverage could be obtained. In this sense all coverage values θ_{ZnO} given in chapters 5 and 6 must be understood as "apparent coverage".

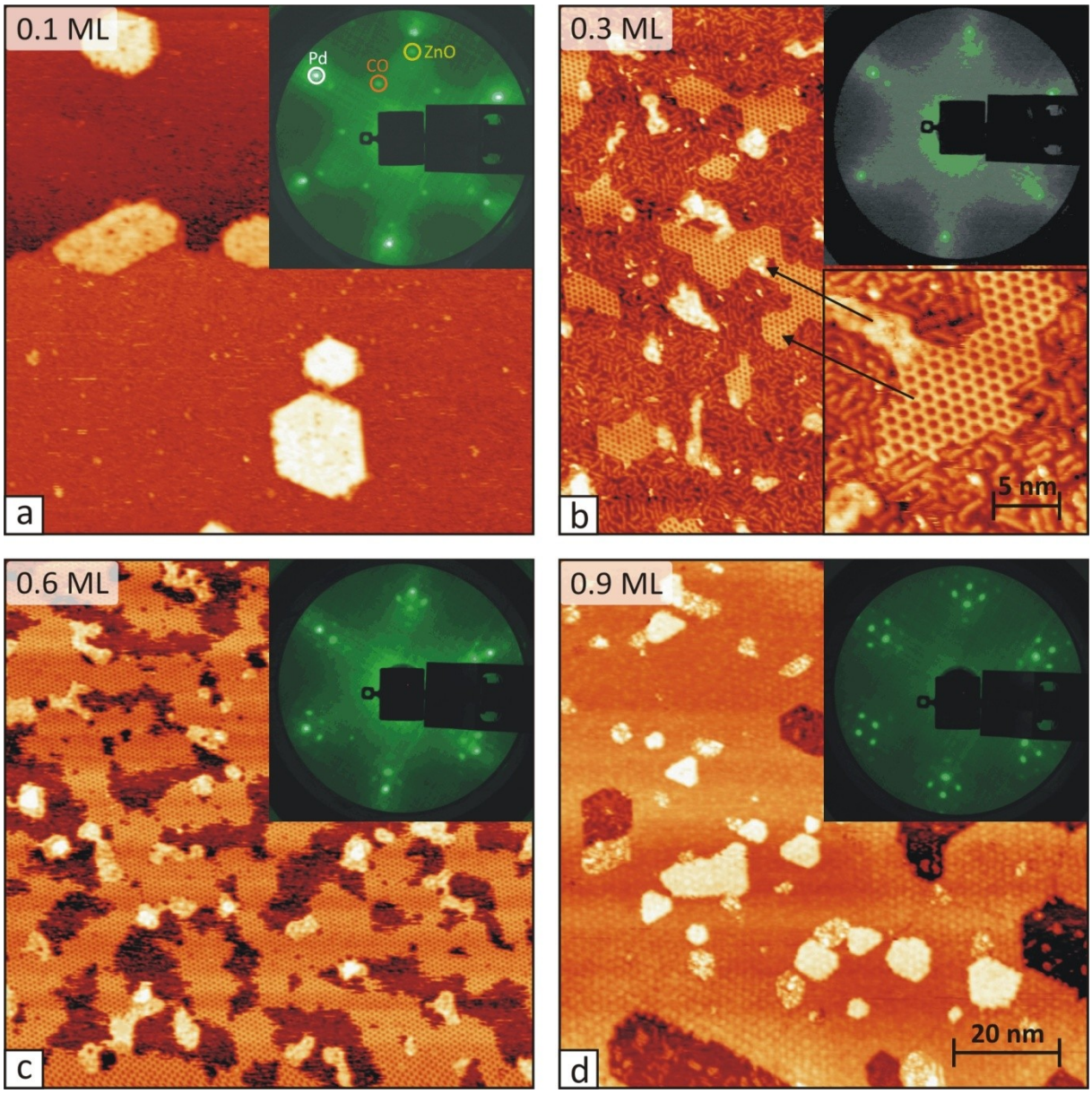

Fig. 5. 1: Growth series for θ_{ZnO} < 1ML. Films shown in (a) and (b) have been prepared at standard conditions, those in (c) and (d) at an oxygen pressure of 1 × 10^{-7} mbar. Within this pressure range the resulting films typically show similar properties. (a) 0.1 ML coverage: On the surface bilayer-islands with hexagonal unit cell can be observed. STM: (100 × 100) nm^2, U = +1.0 V, I = 0.4 nA; LEED: E_B = 63.6 eV. (b) 0.3 ML coverage: Two different kinds of islands can be seen on the surface. One kind is showing an open honeycomb-like appearance, the other one displays a more compact, hexagonal structure. All islands are one monolayer high. STM: (100 × 100) nm^2, U = +1.0 V, I = 0.4 nA; Inset: (20 × 20) nm^2, U = +1.0 V, I = 1.0 nA; LEED: E_B = 72.3 eV. (c) 0.6 ML coverage: Islands with the open structure dominate the surface. Compact islands show traces of a second layer in some places. STM: (100 × 100) nm^2, U = +1.0 V, I = 0.4 nA; LEED: E_B = 71.6 eV. (d) 0.9 ML coverage: only the compact structure can be observed on the surface. Most of the material is situated in the first monolayer, which exposes a moiré structure now. A few islands are present in the second layer. STM: (100 × 100) nm^2, U = +1.0 V, I = 0.4 nA ; LEED: E_B = 69.6 eV.

Figure 5.1 shows the growth and morphology for θ_{ZnO} < 1ML. Large scale STM pictures and the corresponding LEED patterns are presented.

In 5.1a the surface is shown for a coverage of θ_{ZnO} = 0.1 ML. The major part of the Pd-surface is empty, only few ZnO islands could be found. Most of them are situated at or nearby step edges. The islands show strict geometrical shapes, mainly hexagonal, indicating a high degree of structural order. The apparent height of those islands in STM amounts to (4.6 ± 0.6) Å. The corresponding LEED image shows two superstructures: a p($\sqrt{3}$ ×$\sqrt{3}$) R30° that could be attributed to CO on the free Pd surface and a very weak p(6×6) coming from the ZnO.

When the coverage is increased to 0.3 ML, as shown in figure 5.1b, two different phases can be seen. One has an open, honeycomb-like appearance and an apparent height of (1.3 ± 0.3) Å. The other one is more compact, with an apparent height of (1.9 ± 0.3) Å. Both structures do not exhibit specific shapes, but the open structure, which is dominant on the surface, does clearly have some preferential directions, which are influencing the shape of the islands. The compact islands do not show any evidence of preferential directions or of good order. In the spaces between the islands, small, rod-like clusters can be seen. They do not appear directly after the preparation but evolve with time. Scanning over the surface with the STM tip seems to favour this process. In the LEED still a weak p(6×6) can be observed but no other signals are apparent. It is possible to obtain a (4×4)-pattern with LEED which is created by the open honeycomb-structure. But this ZnO-phase is destabilized by the electron beam and disintegrates within a few seconds. As a consequence most of the LEED-images only show the (6×6)-spots, which stem from the compact phase. Yet by appropriate timing it is also possible to record the (4×4)-pattern, as shown in figure 5.5a.

By further increasing the coverage to 0.6 ML, the situation does not change significantly. Both phases are still present, both having gained area on the surface. The increase is stronger pronounced for the open structure. Clusters can still be observed in the areas between islands. The p(6×6)-LEED pattern has become stronger too.

For a coverage of 0.9 ML the situation changes drastically. The open structure has disappeared completely. The compact structure, that is now dominating the surface, appears as a largely closed film and some islands in the second layer. The order has increased significantly – preferential directions are clearly visible and on the film a regular hexagonal pattern with a periodicity of (16 ± 2) Å is visible. In the corresponding LEED image a pronounced p(6 × 6) pattern can be observed.

A closer examination of the observed structures will be presented next, starting with the compact one. In figure 5.2b an atomically resolved STM image of this structure can be seen, displaying hexagonal symmetry. Two periodicities can be observed on the film, a small and a large one. The large periodic structure is the one that could already be observed in the large scale images and stems from the moiré effect, as described in section 1.2.4. The unit cell of this pattern is marked in the picture with the vectors $\vec{b}_{m1}$ and $\vec{b}_{m2}$. Using the moiré formula

(1.11) the lattice constant of the ZnO film can be determined with high accuracy. With $|\vec{b}_{m1}| = |\vec{b}_{m2}| =$ (16 ± 2) Å, as stated before, and $|\vec{a}_{Pd}|$ = 2.75 Å for the underlying Pd(111) substrate a value of (3.3 ± 0.1) Å could be obtained. Direct measurement of the atomic distances gives a lattice constant of (3.1 ± 0.4) Å. Both numbers are in good agreement with the value for a ZnO(0001) surface, which is 3.25 Å.

The observed moiré pattern indicates that the adsorbate forms a coincidence structure. With the lattice constants for Pd and ZnO the following relation can be found: $5 \cdot |\vec{a}_{Pd}| = 6 \cdot |\vec{b}_{ZnO}|$, with a lattice mismatch ε of 20%. The bright spots of the moiré pattern have a periodicity 6 times larger than the one of the Pd substrate. As a consequence the p(6×6) LEED-pattern can be directly linked to this structure. Due to this correlation, the compact oxide-structure is from now on addressed as "6×6"-structure with the lattice vectors $\vec{b}_{6x6,1}$ and $\vec{b}_{6x6,2}$. In figure 5.2a the according analysis of the LEED image is shown, together with the reciprocal lattice vectors of the substrate ($\vec{a}^*$) and the moiré ($\vec{b}_m^*$). All the experimentally obtained values are also summarised in table 5.1.

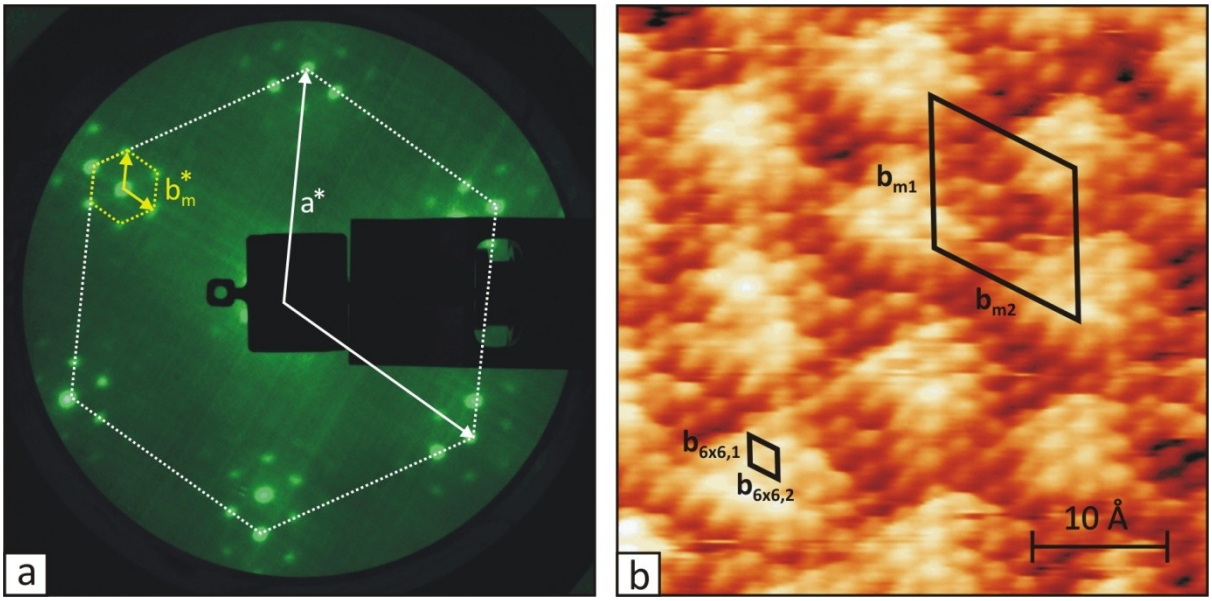

Fig. 5. 2: Analysis of the compact structure. (a) p(6×6) LEED pattern, E_B = 67.9 eV. The reciprocal lattice vectors of the substrate ($\vec{a}^*$) and of the superstructure ($\vec{b}_m^*$) are indicated. (b) High resolution STM image of the compact structure, (50 × 50) Å^2, U = +100 mV, I = 2.0 nA. The unit cells and lattice vectors of the ZnO-film $\vec{b}_{6x6,1,2}$ and of the moiré-pattern $\vec{b}_m$ are depicted in the image.

Neither LEED nor STM pictures show any hints for a rotation of the 6×6-stucture with respect to the substrate. Thus the highly symmetric directions on this film are equal to the main directions of the Pd(111) surface - $\langle 01\bar{1} \rangle$, $\langle 10\bar{1} \rangle$ and $\langle \bar{1}10 \rangle$. High resolution STM pictures proofed that the islands, seen at a coverage of 0.1 ML, also expose a 6×6-structure. The apparent height of (4.6 ± 0.6) Å for these islands is a bit larger than twice the height of a single layer, thus indicating bilayer growth. A more detailed analysis of this growth mode will be presented in section 5.2.

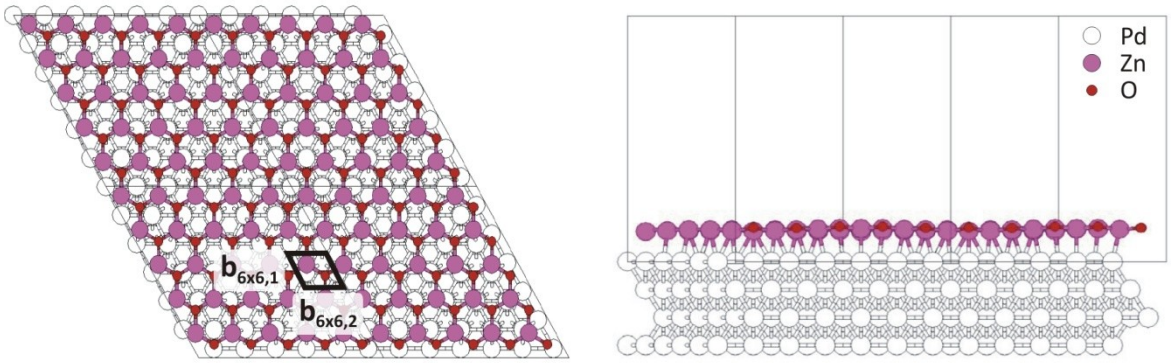

Fig. 5. 3: DFT model of the 6×6-structure. Left: top view, right: side view. During relaxation the ZnO-film adopts a planar h-BN structure instead of the wurtzite structure, which is present in bulk ZnO-crystals. Models made by G. Barcaro and A. Fortunelli.

As already mentioned before, the unit cell of the 6×6-structure has dimensions similar to those of a ZnO(0001) surface. Yet there is a difference too: for the ZnO(0001) surface the layer height would be 2.7 Å, but the 6×6-structure only shows a layer height of about 1.9 Å. To gain more insight into this problem, auxiliary DFT calculations have been performed by G. Barcaro and A. Fortunelli [wj10]. Figure 5.3 shows the result of their work. In the top view the structure looks like the (0001)-surface of the ZnO wurtzite structure, but in the side view a difference is visible. In the simulation the zinc atoms have been fixed, while the oxygen atoms were allowed to relax. In that process the oxygen atoms moved "into" the film. In the side view in figure 5.3 it can be seen, that the oxygen atoms still reside at slightly higher positions than the zinc atoms. Still, in the wurtzite structure the Zn- and O-atoms are separated by 0.63 Å along the [0001] direction [tp07], whereas in the 6×6-structure the two species are coplanar, thus eliminating the surface dipole moment. The total layer height of the simulated film is 2.75 Å, with a lattice constant of 3.2 Å. All values are also listed in table 5.1.

By comparing the structure model with the measured STM-pictures it becomes clear that only one sort of atoms is visible in the STM. To analyse the electronic properties of the 6×6-structure, its local density of electronic states has been calculated. The resulting diagram is displayed in figure 5.4. It becomes clear that oxygen p-states are dominant in the region around the Fermi-level, where the STM-measurements have been performed (marked by the dotted lines in figure 5.4). Thus electrons, tunnelling from or into oxygen states, create

Structure	6×6	4×4
Lattice constant*	3.3 ± 0.1	10.3 ± 0.9
Atomic distance**	3.1 ± 0.4	3.1 ± 0.3
Lattice constant – moiré	16.0 ± 2.0	-
Periodicity determined by LEED	16.2 ± 0.8	10.5 ± 0.3
Apparent film height	1.9 ± 0.3	1.3 ± 0.3

Table 5. 1: Experimentally obtained values for the structures observed for θ_{ZnO} < 1 ML. all values are given in Å. (*) The lattice constant for the 6×6-structure has been derived from the moiré pattern. For the 4×4-structure it has been measured directly in STM. (**) The atomic distances have been obtained by direct measurement in STM for both structures.

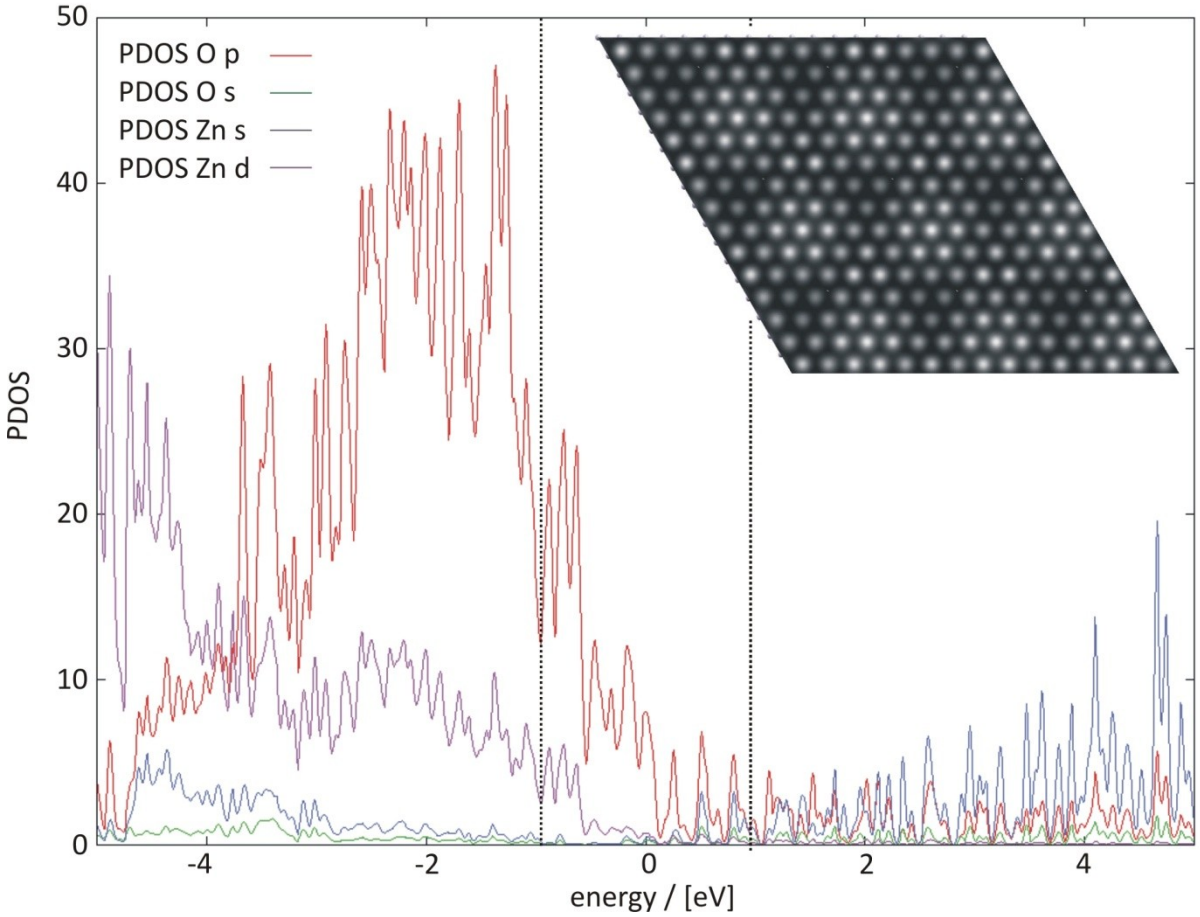

Fig. 5. 4: Projected density of states (PDOS) of the 6×6-structure. The PDOS of oxygen p- and s-states as well as those of Zn d- and s-states are shown. The area between the dashed lines marks the typical energy-range for STM-measurements around the Fermi-level. The fluctuations of the individual lines are due to the limited slab thickness in the DFT-model. Inset: simulated STM-picture at +1.0 V. Calculations made by G. Barcaro and A. Fortunelli.

the bright spot signals in the STM pictures at positive and negative bias respectively. A simulated STM image is shown in the inset of figure 5.4. It is in very good agreement with the experimentally obtained one.

Next the open ZnO-structure will be discussed in more detail. Figure 5.5b shows a high resolution STM scan of this phase. The atoms arrange in a honeycomb-like fashion, thus creating a hexagonal unit cell with a lattice constant of (10.3 ± 0.9) Å. At each side of the hexagons three maxima can be observed. The distance between two of these maxima amounts to (3.1 ± 0.3) Å. This value is similar to the interatomic distance in the 6×6-structure. The average height measured for this structure is (1.3 ± 0.3) Å. The maxima at the corners exhibit a greater apparent height of (1.4 ± 0.1) Å, than those situated in the centre of each side with (1.2 ± 0.1) Å.

A LEED-pattern generated by this structure can be seen in figure 5.5a. Beside the strong p(1×1)-signal from the substrate a weak p(4×4)-pattern emerges. No rotation with respect to the substrate could be observed. Evaluation of the LEED-pattern results in a lattice constant of (10.5 ± 0.3) Å, what is in good agreement with the value obtained by direct measurement in the STM. Since this indicates a unit cell about four times larger than the one of the substrate, this structure is addressed as “4×4” from now on.

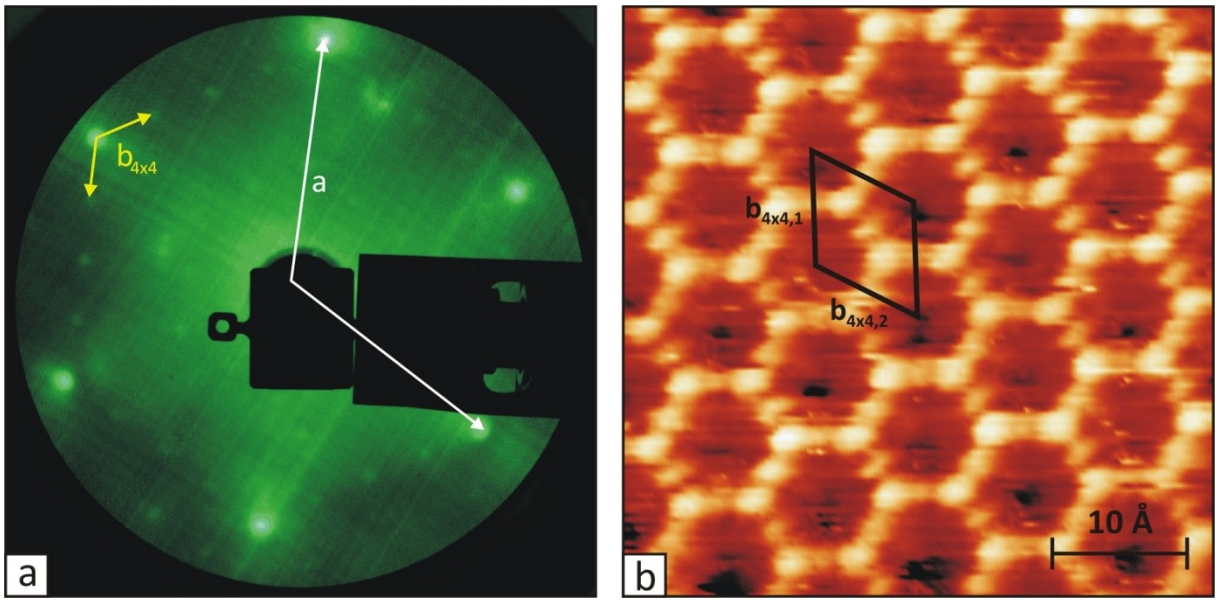

Fig. 5. 5: Experimental results for the compact structure. (a) p(4×4) LEED pattern, E_B = 66.9 eV. The reciprocal lattice vectors of the substrate ($\vec{a}^*$) and of the superstructure ($\vec{b}^*_{4\times4}$) are indicated. (b) High resolution STM image of the open structure, (50 × 50) Å^2, U = +10 mV, I = 3.0 nA. The unit cells with the lattice vectors $\vec{b}_{4\times4,1,2}$ is shown in the picture.

The 4×4-structure is very instable - in the LEED-beam it lasts only few seconds. That is the reason, why a p(6×6) pattern appears in the LEED images, even when the surface is covered mainly by the 4×4-structure. As shown in figure 5.6(a) and (b), the edges of the 4×4-islands are constantly changing. Manipulation with the STM tip often leads to disintegration of the structure, as demonstrated in figure 5.6(c) and (d).

The fast disintegration and the constant change of the island shapes indicate weak binding forces within the 4×4-layer. From the DFT-results for the 6×6-structure, it can be assumed that also for the 4×4 not all atoms are visible in STM. For further investigation DFT-calculations have also been performed for this structure by A. Fortunelli and G. Barcaro. But in this case the modelling of the proper atomic arrangement appeared to be more complicated.

Figure 5.7 shows three different approaches to model the observed structure. In (a) a stoichiometry of 5 zinc atoms and 6 oxygen atoms per unit cell has been used. The Zn atoms have been set to the positions in the unit cell where a bright spot signal has been observed in the STM. Oxygen atoms have been located at bridge sites between the zinc atoms. After relaxation, a planar structure has formed, as shown in figure 5.7a. The STM picture created by this structure shows a starlike shape, which has not been observed in the experiment.

To examine the validity of the stoichiometry, ab-initio thermodynamics have been performed for 550 K and a pressure of 5×10^{-7} mbar. The results have shown that under the applied conditions a Zn_6O_5-stoichiometry is more favourable. The according DFT-model is presented in figure 5.7b. Here the oxygen atoms are situated at places, where a bright spot signal should emerge and the zinc atoms are located at bridge positions. The structure has not yet been allowed to relax. The corresponding STM picture already shows greater similarity with the experimentally obtained one. But in this simulation the maxima at the

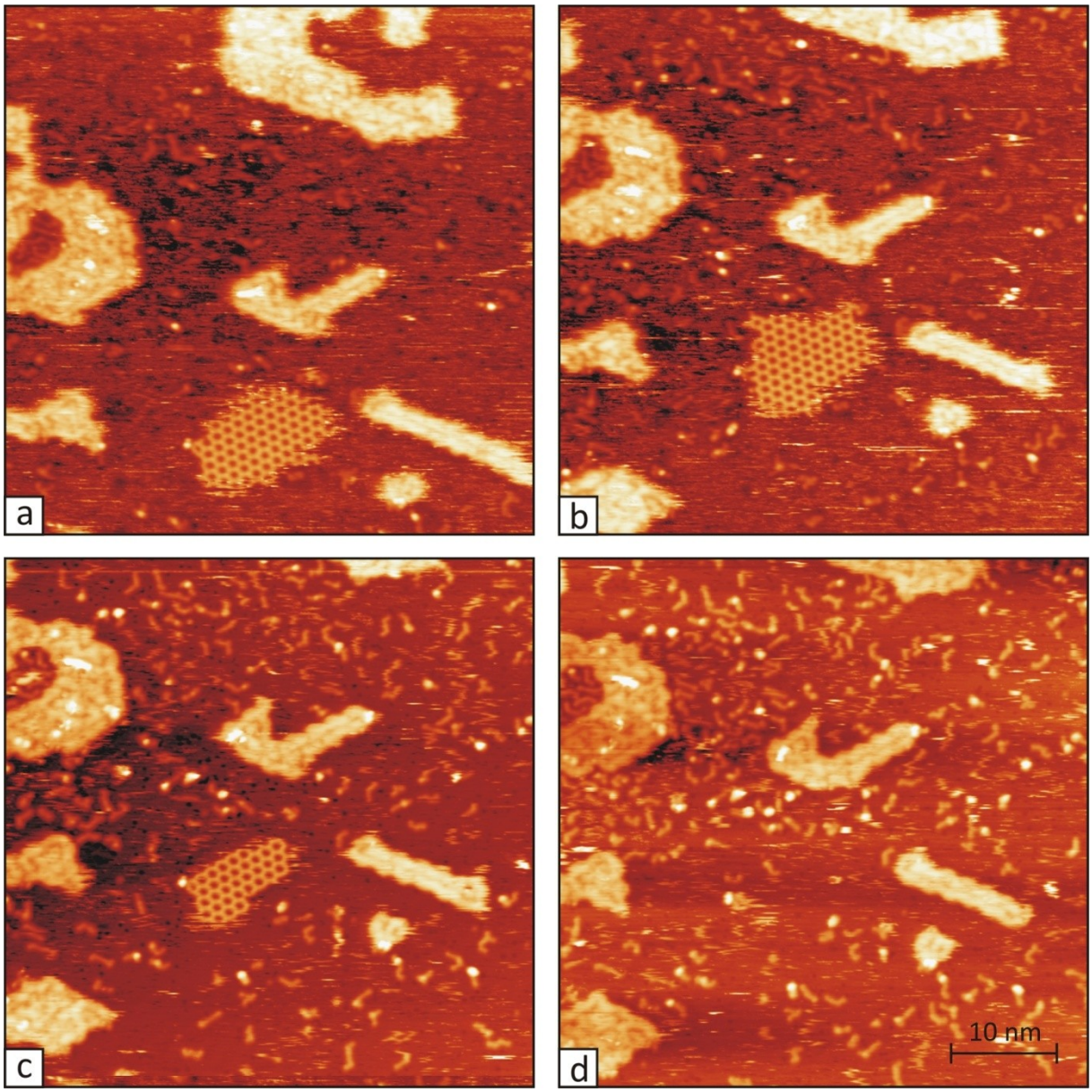

Fig. 5. 6: Change and disintegration of the 4×4-structure. In (a) and (b) the constant changes at the perimeter of the island can be observed. In (c) and (d) the bias has been switched to -1.0 V resulting in disintegration of the island. All STM pictures show an area of (50 × 50) nm^2. (a) and (b): U = +1.0 V, I = 1.0 nA; (c) and (d): U = -1.0 V, I = 1.0 nA;

centre of each side show a greater apparent height than those at the corners, contrary to the real STM pictures. Furthermore this structure is polar, with a dipole moment μ of 9.0×10^{-31} Cm.

When the structure, presented in figure 5.7b, is allowed to relax, it adopts a planar geometry, like shown in figure 5.7c. In this process μ is minimized to a value of 1.3×10^{-31} Cm. Yet the hexagonal shape is lost and the STM simulation does not fit the experimental data any more.

Of all presented STM simulations only the one of the unrelaxed model structure shows a resemblance with the experimental data. Yet due to the nonzero dipole-moment this structure is instable. As mentioned in chapter 3.3.2 one possibility to stabilize a polar surface is adsorption of hydrogen. Since some amount of molecular hydrogen is generally present in

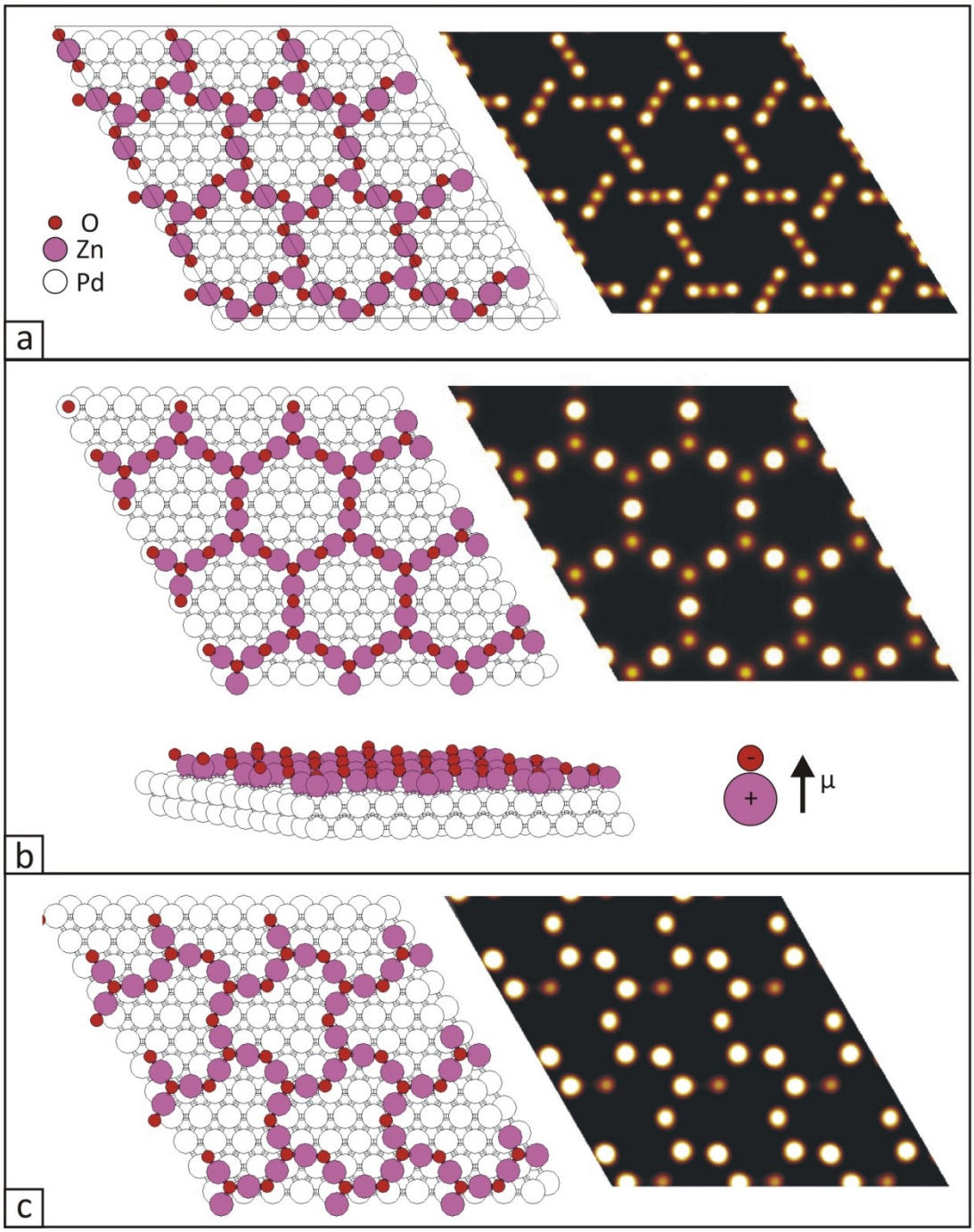

Fig. 5. 7: DFT models and according STM-simulations of the 4×4-structure. (a) Zn_5O_6-stoichiometry with the Zn atoms situated at the corners, relaxed; STM simulation for U = +0.3 V. (b) Zn_6O_5-stoichiometry with the O atoms situated at the corners, not relaxed; STM simulation for U = -0.3 V. (c) Zn_6O_5-stoichiometry with the O atoms situated at the corners, relaxed; STM simulation for U = +0.3 V. Calculations performed by G. Barcaro and A. Fortunelli.

the UHV chamber, the possibility for this mechanism cannot be neglected. In figure 5.8 two models of hydrogen stabilized structures are presented. Unrelaxed Zn_6O_5- and Zn_5O_6-stoichiometries, saturated with hydrogen, have been used as model systems. After relaxation both structures still showed a nonzero dipole moment. Ab-initio thermodynamics, performed with the same parameters as before, showed again that the $Zn_6(OH)_5$-stoichiometry is the favourable one. The according model and simulated STM picture can be seen in figure 5.8b.

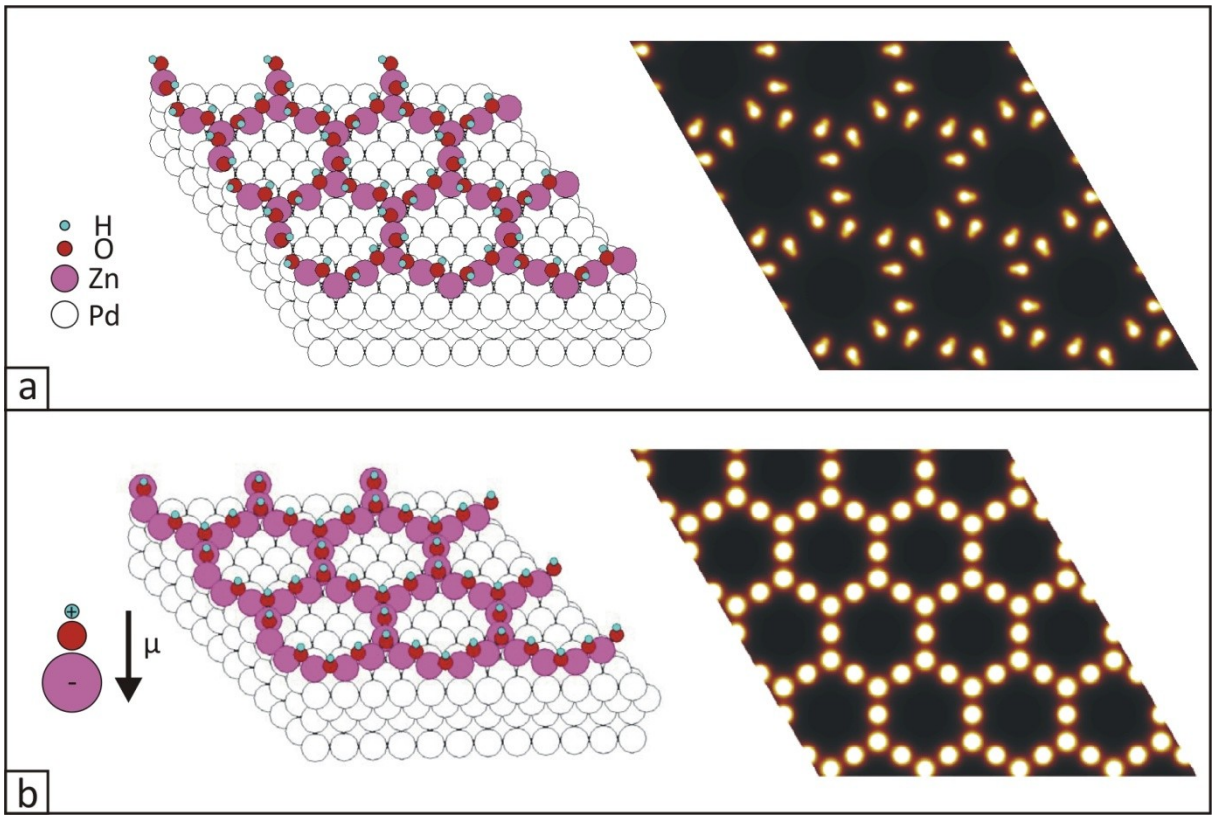

Fig. 5. 8: Models of the hydrogen-stabilized structures for $Zn_5(OH)_6$ (a) and $Zn_6(OH)_5$ (b). Both structures expose a nonzero dipole moment μ. The direction of μ has reversed in comparison to the same structure without hydrogen (figure 5.7b). The STM simulations have been performed for U = +1.0 V. Calculations performed by G. Barcaro and A. Fortunelli.

The simulated STM-picture is in good agreement with the experimentally obtained ones. The observed differences in the apparent heights between the maxima at the corners and the side-centres of the hexagons are not visible in the simulation at 0 K. At higher temperatures, the position at the side-centres allows the OH-groups to flip from one side to the other rapidly. This movement results in a decrease in apparent height as measured with STM. From the model and the simulated STM-image it is clear that the oxygen atoms give rise to the maxima observed in STM, similar to the 6×6-structue. Due to the stabilisation the dipole-moment is not eliminated but the calculations show a reversal of sign as depicted in figure 5.8b. The strength of μ has been calculated to be 1.4×10^{-30} Cm.

At the end of this section a few words should be spend on the third submonolayer-phase of ZnO. Especially in figure 5.1b little rod-like clusters can be seen in the areas between the islands. Those rods are not present on the surface right after preparation, but emerge with increasing age of the film. Scanning over the surface with the STM-tip accelerates the process of formation. High resolution images of this species revealed monoatomic chains with typically one or two kinks of about 60°. The atomic distance along the rods could be determined to be (3.0 ± 0.1) Å, indicating that this structure consists of ZnO-building-units. The origin of this species is not clear yet. Most likely they can be interpreted as decomposition products of a denser ZnO-structure, but it could not be determined, whether the 6×6 or the 4×4, give rise to them. The rods could mainly be observed on the Pd-surface, where they are very mobile and cover the whole area between islands after some time. But

they have also been detected on several islands, which will be described in more detail in the next section.

5.1.2 Structure of 1.5 ML ZnO

Similar structural investigations, as shown in the last section, have been performed for 1.5 ML of ZnO on Pd(111). This time only reactive evaporation has been used during film-preparation, because post-oxidation might have led to undesired alloying effects at the metal-oxide interface.

The situation at a coverage of 1.5 ML has been examined closely because it already reflects the behaviour of thicker ZnO-films. A corresponding surface is shown in figure 5.9. (a) gives a topographical overview, (c) and (d) are high resolution scans exposing the atomic arrangement. (b) shows a height profile, measured along the dotted line in (a).

In the presented case the first ZnO-layer is completely closed. In the figure it is labelled A. The high resolution images expose a 6×6-structure for this layer. Its surface is smooth and the typical moiré pattern can be observed. From additional experiments it is known that the height of A amounts to (1.9 ± 0.3) Å, in accordance with previous measurements of the 6×6-phase.

In the second layer three different kinds of islands could be detected, labelled B, C and D. C and D both expose a 6×6-structure but they differ in several points: the relative apparent height with respect to A, the appearance of the surface at atomic level and, in some cases, the shape of the islands.

The most important point is the relative apparent height. With respect to A the B-islands show a height of (1.6 ±0.2) Å, whereas C-islands exhibit (2.3 ± 0.3) Å. That makes a difference in the apparent height of (0.7 ± 0.3) Å. An overview of the different apparent heights with respect to A is given in the height profile in figure 5.10b.

The difference in the surface appearance can be seen best in figure 5.9d. The B-islands display a larger number of defects, a higher surface roughness, and the surface appears slightly more unordered than the one of C-islands. Both island types display a 6×6-structure and the corresponding moiré pattern. Note that the appearance of the layers A and C is very similar in the high resolution STM-scans, whereas B looks different.

Concerning the shape it can be said that the B-islands seem to form triangular shapes preferentially, whereas the C-islands tend to grow in hexagonal or elongates shapes. Yet this point should be understood more as a trend, than a rule. The form of the islands is strongly influenced by the actual film-growth-conditions. Often both island types expose shapes without special geometries.

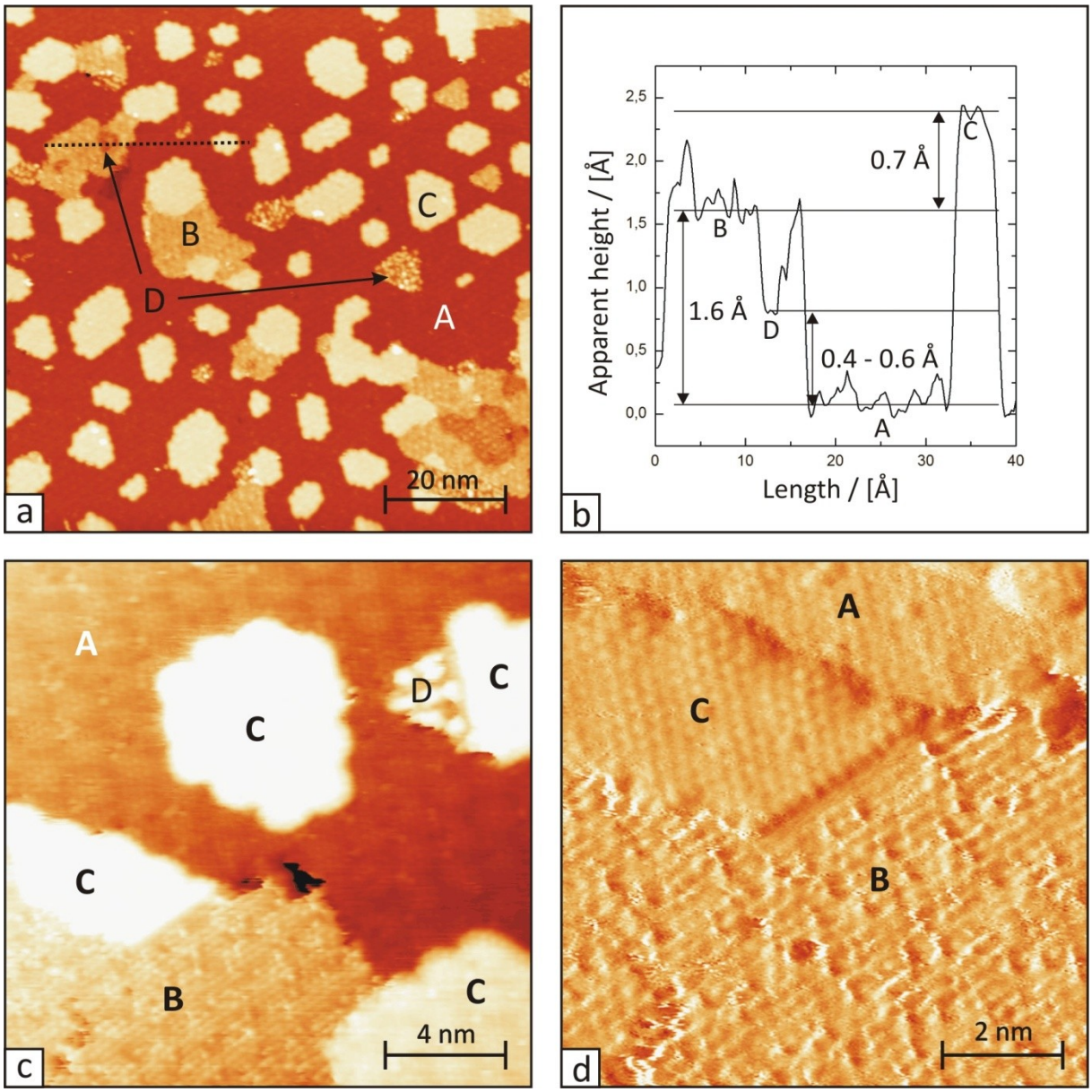

Fig. 5. 9: Analysis of the sample surface for a ZnO film with θ_{ZnO} = 1.5 ML, prepared at standard conditions. Different 6×6-phases can be observed in the second ZnO-layer. Legend: A – 1st ZnO layer, B – 2nd ZnO layer - thin phase, C – 2nd ZnO layer - thick phase, D: metallic islands. (a) (100 × 100) nm^2 STM-scan, U = +1.0 V, I = 0.4 nA. (b) Height profile, measured along the dotted line in (a). (c) (20 × 20) nm^2 STM-scan, U = +0.3 V, I = 2.0 nA. (d) Differential image of a (10 × 10) nm^2 STM-scan, U = +0.3 V, I = 2.0 nA.

The islands labelled D are different from both, B and C. In most cases the surface of these islands is covered by clusters similar to those, observed on the free Pd-surface. It has been possible to obtain a few STM-pictures of partly or fully uncovered D-type islands revealing a surface that appears completely flat in STM -no structure could be observed. The apparent height with respect to A has been difficult to obtain reliably, because of the clusters. The measured values are in the range from 0.4 – 0.6 Å. In further experiments D-type islands could also be observed at lower coverage. That made it possible to measure the apparent height with respect to the Pd-surface, yielding a value of (2.3 ± 0.2) Å. Those measurements have been more precise because the D-islands are covered by fewer clusters at this ZnO-coverage. With an apparent height of 1.9 Å of the first ZnO-layer this results in an apparent height of 0.4 Å, with respect to A.

The completely different appearance of D, in comparison with A, B and C, indicates that those islands do not consist of ZnO. This idea is supported by the results of another test. In this experiment ZnO films with a thickness between 1 and 2 ML have been grown at standard conditions and the surfaces have been characterized with LEED and STM. Then pyridine as a probe molecule has been dosed onto the sample followed by another characterisation. Similar experiments have been performed by Frederik Weber, who investigated the surface with IR-spectroscopy at different substrate temperatures. Originally these tests have been undertaken to show if there is a structural difference between B- and C-surfaces. The structure diagram of pyridine is shown in figure 5.10. It has been chosen as probe molecule, since it is known to chemisorb on Zn-terminated (0001) surface (bonds forming between Zn and the nitrogen in the molecule) and to physisorb on the O-terminated ($000\bar{1}$) surface (bound by van der Waals–forces) of ZnO single crystals [hj00].

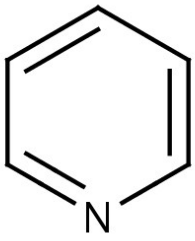

Fig. 5. 10: Structure of pyridine. The molecule belongs to the group of aromatic hydrocarbons, with one carbon atom in the benzol-ring replaced by nitrogen.

The tests in the STM have been performed at room temperature. According to [hj00] only the chemisorbed pyridine stays on the surface under these conditions. As shown in figure 5.11, no molecules could be detected on A, B or C. But the apparent height of D-type islands changed after pyridine dosing. In the example shown in figure 5.11, it increased by (1.1 ± 0.2) Å. Also on the Pd-surface an increasing amount of clusters has been observed. That last point is in accordance with the results, reported in [nc83], where the formation of unordered pyridine adlayers on Pd(111) has been observed at room temperature. The IR-spectroscopy confirmed that pyridine does not bind to ZnO.

These results indicate that D-islands do not consist of ZnO. In fact they show a lot of similarities to the Pd-substrate: Both are covered by rod-like ZnO-clusters, both have been decorated by pyridine and the D-island height of 2.3 Å corresponds to the step height on a Pd(111) surface. Those facts lead to the assumption that D corresponds to Pd-adislands. Their formation is attributed to dynamic processes during the film preparation like alloying of Pd and Zn on the hot surface and subsequent de-alloying due to Zn-oxidation.

Still the question remains open, why the B- and C-islands display different heights with respect to layer A. A structural change from h-BN to the bulk wurtzite structure in the C-islands could be a possible explanation. In the wurtzite lattice the zinc- and oxygen-atoms are located in separated sheets along the [0001] direction. The distance between these

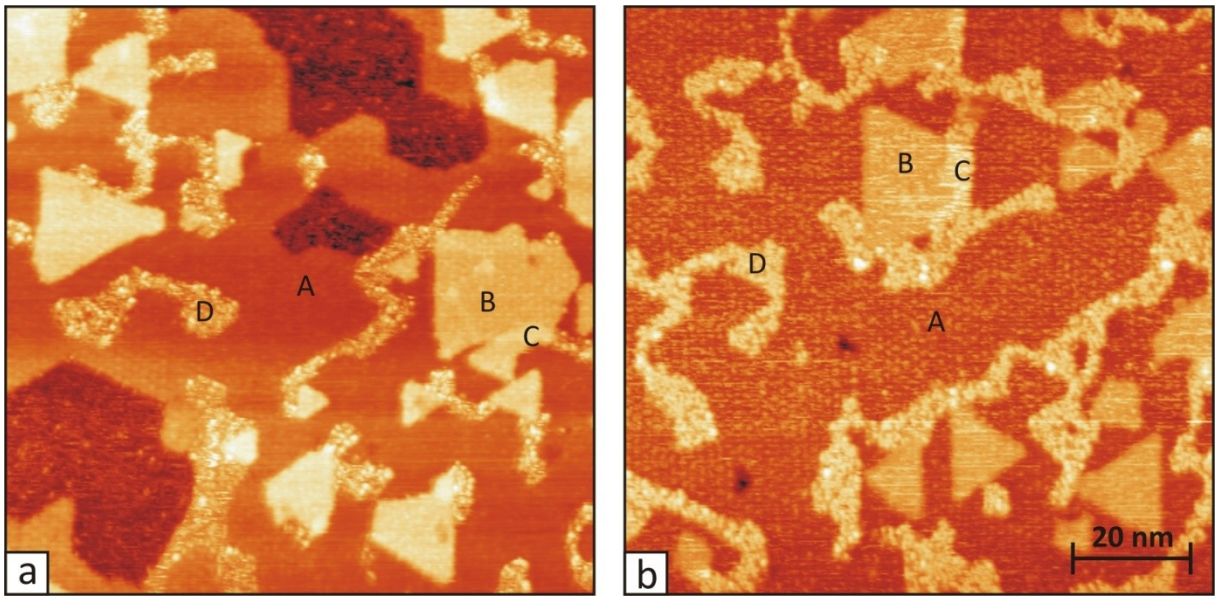

Fig. 5. 11: Pyridine-test, Θ_{ZnO} = 1.2 ML. (a) After preparation, U = +1.0 V, I = 0.4 nA. (b) After dosing 1 L of pyridine, U = +1.0 V, I = 0.4 nA. An increase of molecules can be observed on D-islands but neither on B- nor on C-islands. The dots visible on the first layer A in (b) stem from the moiré structure. They are also visible in (a) but appear less bright due to different contrast-settings in the two pictures.

sheets is 0.63 Å, what would be in accordance with the measured height difference of 0.7 Å between B and C. Yet DFT-calculations performed by A. Fortunelli and G. Barcaro have shown that a transformation to the bulk structure is not favorable under the employed experimental conditions. Instead the simulations showed that first and second ZnO-layer adopt a planar h-BN structure, as shown in figure 5.15b. The experiments performed by Tusche for ZnO on Ag(111) [tp07] also showed a planar structure for the first four layers. Moreover no other experimental evidence could be found for a transformation into the bulk ZnO-structure.

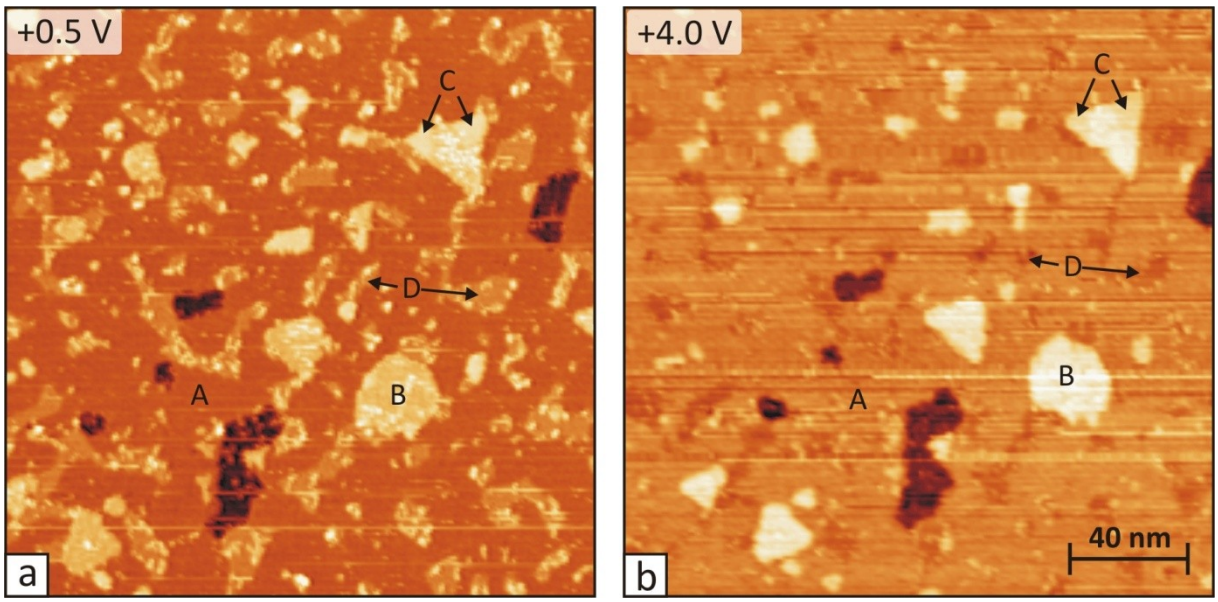

Fig. 5. 12: Bias-dependence of ZnO. The contrast between A and D and between B and C is reversed, when the bias is changed from +0.5 v to +4.0 V. STM-images: (200 × 200) nm^2, θ_{ZnO} = 1.2 ML; (a) U = +0.5 V, I = 1.0 nA; (b) U = +4.0 V, I = 1.0 nA.

At this point it should be noted, that the apparent height of ZnO is bias-dependent. In figure 5.12 the same surface is imaged at +0.5 V (a) and +4.0 V (b). Measurement of the apparent heights shows an increase in apparent height for A and B and a decrease for C and D, when the bias is changed from +0.5 to +4.0 V. The apparent height increases by +(1.6 ± 0.3) Å for A and decreases -(0.7 ± 0.2) Å for D, measured with respect to the Pd-substrate. B shows an increase of +(1.5 ± 0.2) Å and C a decrease of -(0.3 ± 0.2) Å, both measured with respect to A. As a result a contrast change between A - D and B - C can be observed. At a bias of +0.5 V, D appears 0.9 Å higher than A and C appears 0.8 Å higher than B. At +4.0 V however, D appears -1.4 Å lower than A and C appears -1.0 Å lower than B. At negative bias no such changes could be observed.

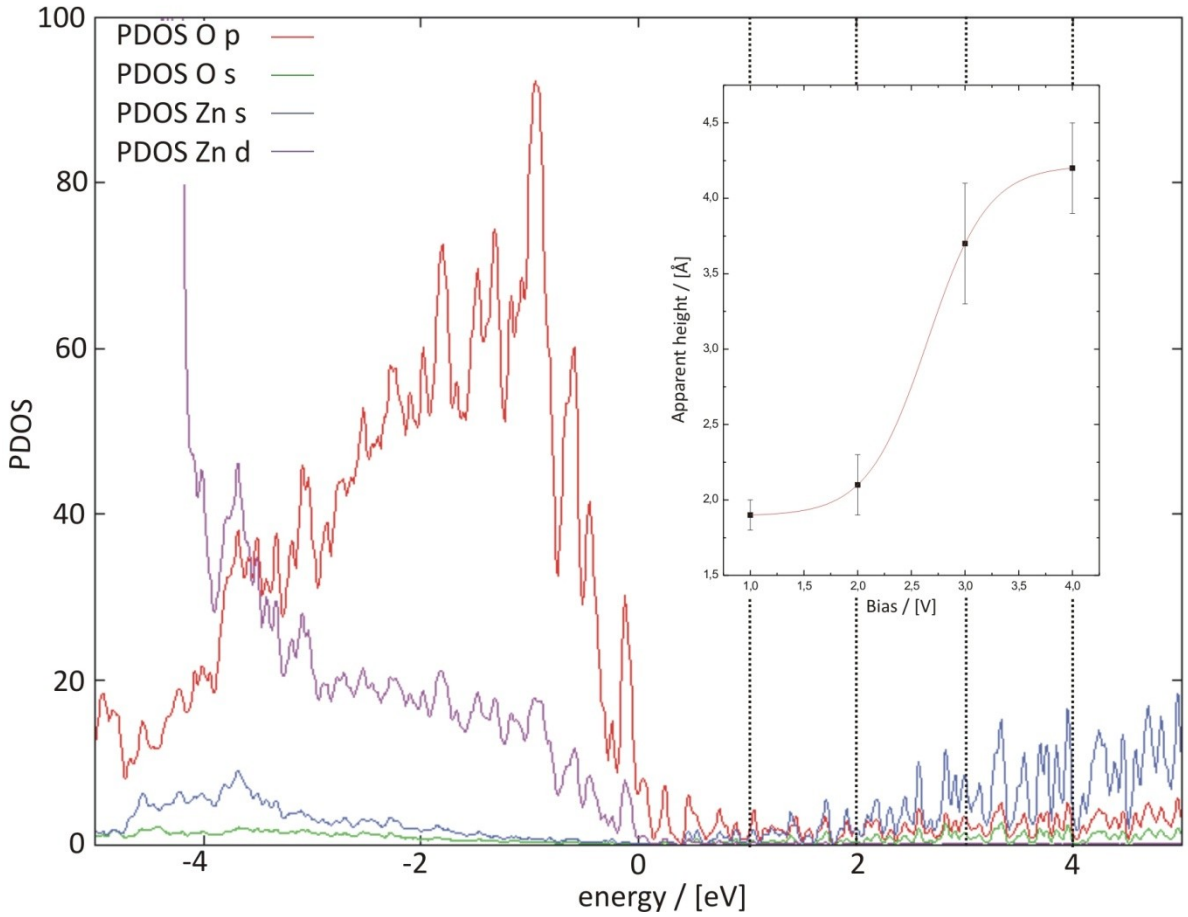

Fig. 5. 13: Calculated PDOS of two layers of ZnO on Pd(111). In this simulation both ZnO-layer adopt a planar h-BN structure, as shown in figure 5.15b. Calculations performed by A. Fortunelli and G. Barcaro. Inset: Evolution of the apparent height of a B-island, as measured in STM.

The change in apparent height is not linear. The inset of figure 5.13 shows the increase in apparent height of B as a function of the bias. The strongest change happens in the region between +2.0 V and +3.0 V. According to the density of states, calculated for 2 layers of ZnO, the final tunnelling state changes from oxygen-p to zinc-s in this bias range, as shown in figure 5.13. A correlation of these two results is possible but it should not be overestimated because at these voltage values also field-emission resonances may come into play which might contribute to the current-signal in STM.

Yet, as a consequence of these observations, throughout this thesis, apparent height measurements of ZnO have been performed at a fixed bias of +1.0 V to guarantee a proper comparison of heights for different experiments.

5.1.3 Thicker ZnO-films

After the structural analysis in the last section, the growth of ZnO has been investigated for higher film coverage. The experimental procedure and conditions have been the same as in the previous section.

Figure 5.14 shows the sample surface covered with 1.5, 2.7, 4.7 and 10 ML ZnO. For 1.5 and 2.7 ML a 6×6-structure could be confirmed for all visible layers by high resolution scans. At 4.7 and 10 ML coverage no structure could be resolved. A 4×4-lattice could not be detected at any of the investigated coverages, indicating that this ZnO phase is only present directly on the Pd(111) surface at submonolayer coverage.

The situation for 1.5 ML has already been discussed in detail and is only sketched shortly here, with emphasis on the growth mode. Figure 5.14a shows the corresponding surface revealing an almost completed first layer and a half filled second layer. B- and C-islands are present on the surface but the latter only represent a minority-phase. The visible moiré structure indicates a high degree of order for both layers, also supported by the clear 6×6-pattern in the LEED-image. No hints of a third ZnO layer are present.

The situation at 2.7 ML coverage is similar to the one at 1.5 ML. 70% of the surface are covered by an almost closed ZnO film with an apparent thickness of (1.7 ± 0.1) Å. This layer is interspersed with elongated islands, which cover 30% of the surface and appear (0.7 ± 0.2) Å higher than the surrounding material. In analogy to the situation at 1.5 ML coverage, these areas are labelled B* and C*. On top of C* a few bright islands can be observed with an apparent height of (1.8 ± 0.2) over C*, covering about 2% of the surface. They have been attributed to the fourth layer of ZnO. The LEED pattern still shows a 6×6 pattern but appears more diffuse than at 1.5 ML. The spot intensity has decreased, especially for the Pd-spots. That can be attributed to the screening of the Pd-surface by the ZnO-layers.

At about 5 ML coverage (figure 5.14c) only a p(1×1)-signal can be detected with LEED. The spot positions correspond to those of ZnO. The Pd-signal and the rest of the p(6×6)-pattern are only visible as a diffuse halo around the remaining spots. This is again a result of the shielding of the substrate from the electron-beam. In the STM-images an increasing roughness of the surface can be observed. The 4^{th} layer appears almost closed but material is already present in the 5^{th}, 6^{th} and 7^{th} layer indicating a change from Frank van der Merve – to Volmer Weber growth. The measured apparent heights are (2.4 ± 0.2) Å for the 5^{th} layer, (2.1 ± 0.2) Å for the 6^{th} layer and (1.8 ± 0.2) Å for the 7^{th} layer. Indications for different B*- or

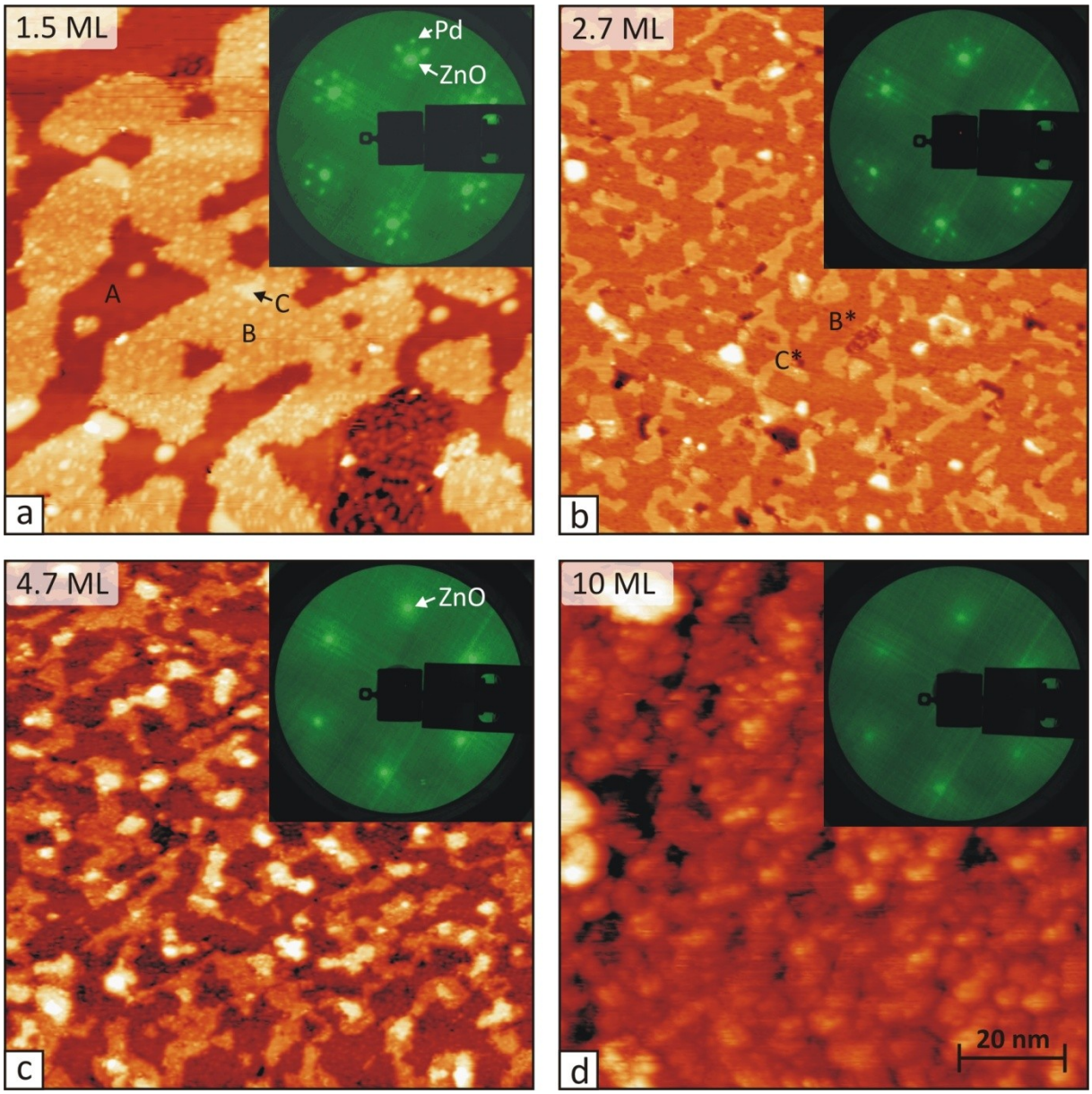

Fig. 5. 14: Growth series, performed at standard conditions, for θ_{ZnO} > 1 ML. A transition from Frank van der Merve- (layer by layer-) growth to Volmer-Weber- (island-) growth can be observed between 3 and 5 ML coverage. STM pictures: (100 × 100) nm^2, U = +1.0 V, I = 0.4 nA. LEED: (a) 67.9 eV, (b)(c)(d) 70.2 eV.

C*-type islands are not visible but the generally high roughness makes a reliable evaluation difficult. Also atomic resolution could not be obtained any more on this surface.

In figure 5.14d finally a coverage of about 10 ML ZnO is shown. The roughness of the surface has still increased. Individual layers are no longer visible, the surface appearance is dominated by grain-like structures. This fact indicates a complete change to the Volmer-Weber growth mode. In the LEED only a diffuse ZnO(1×1)-signal is observable, a continuation of the already mentioned trend.

At the end of this section the theoretical results for coverages up to 4 ML shall be discussed. Since STM and LEED measurements revealed a 6×6-structure for every coverage above 1 ML, the structure, shown in figure 5.3, has been used to model the individual layers. Then the

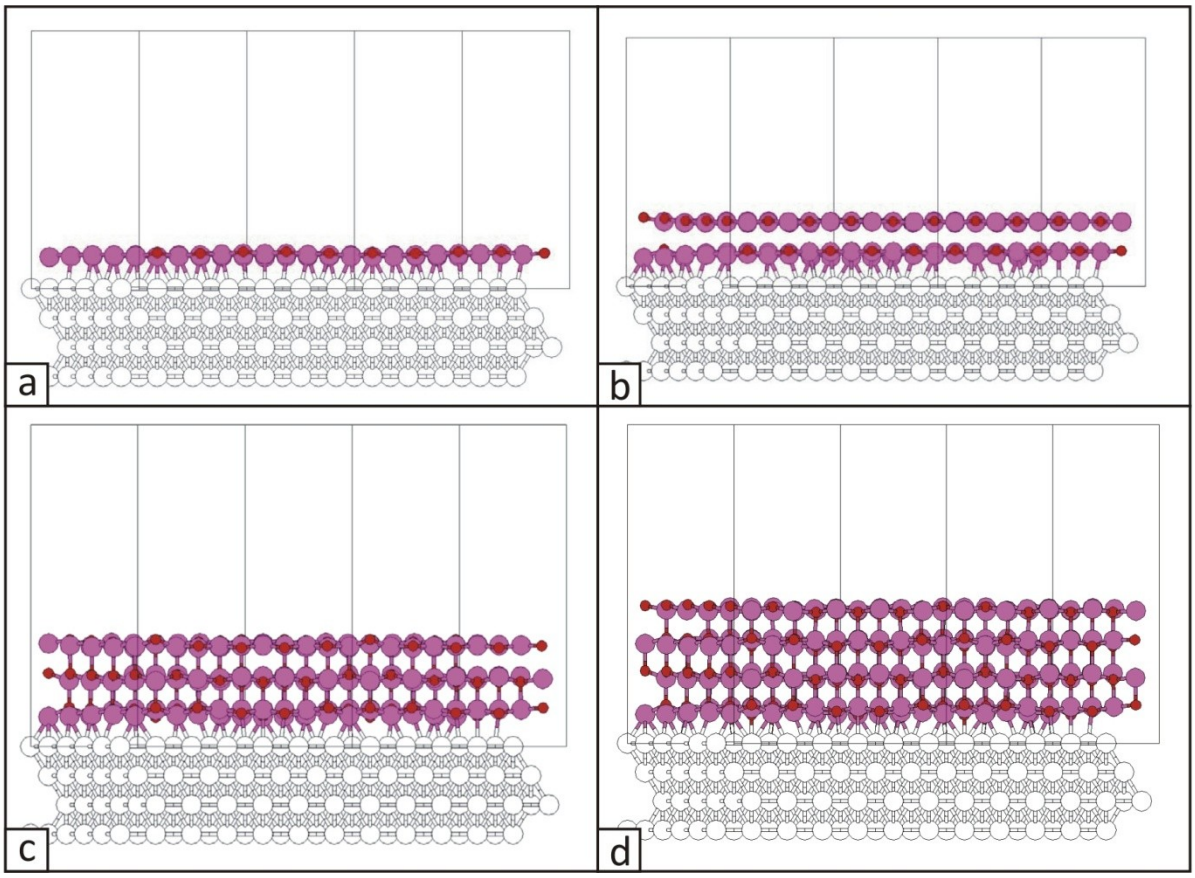

Fig. 5.15: DFT-models for the growth of ZnO up to four layers on a Pd(111)-substrate. All layers exhibit a planar h-BN structure with a unit cell as shown in figure 5.3. Models calculated by G. Barcaro and A. Fortunelli.

Layer #	h_{Zn}	h_O	$\sqrt{(z_{Zn} - \langle z \rangle)^2}$	$\sqrt{(z_O - \langle z \rangle)^2}$
4-layer stack				
1	2.54	2.75	0.24	0.29
2	2.56	2.45	0.22	0.31
3	2.54	2.59	0.24	0.28
4	2.54	2.59	0.10	0.23
Single layer				
1	-	-	0.07	0.08

Table 5. 2: Calculated structural parameters for Zn- and O-atoms in a 4-layer stack and in a single layer. Listed are the calculated values for the layer height h and the square root deviation from the average z-position in each layer, $\sqrt{(z - \langle z \rangle)^2}$. All values are given in Å.

whole system has been allowed to relax. The results of these calculations are shown in figure 5.15. In (a), the situation for the first monolayer is depicted again. After relaxation the vertical distance $z_{Zn\text{-}O}$ between Zn- and O-atoms is reduced to a minimum - the film is practically flat on the atomic level and can be attributed as planar h-BN structure. Figure 5.15b shows that in the second layer too, a planar structure evolves. Note that the corrugation in the first monolayer has also changed a little. At 3 ML coverage (figure 5.15c), the situation has become different. The corrugation of each layer has increased, but it is still much lower than for the bulk wurtzite-structure of ZnO.

This behaviour can also be observed at a coverage of 4 ML. In table 5.2 the square root deviation from the average z-position for each species are given for the case of a 4 layer stack and a single ZnO-layer. The values confirm a larger buckling for all layers in the 4 layer stack in comparison to the single layer. This increase of roughness with increasing coverage can be understood as striving of the system towards the bulk structure.

Concerning the electronic structure of the individual layers there is not much change in comparison with the results of 1 ML coverage. Also the density of states does not change significantly. Representatively the calculated DOS for 3 ML coverage is shown in figure 5.17. Still the oxygen 2s-states are dominant in the region around the Fermi-level where STM-experiments have been carried out. Thus the maxima seen in the STM-pictures still stem from the oxygen-atoms. In figure 5.16 also a simulated STM picture at +1.0 V is shown. Intensity modulations like in this simulation could not be observed in the experiments. Comparable triangular structures sometimes emerged but this effect has proven to be strongly tip-dependent.

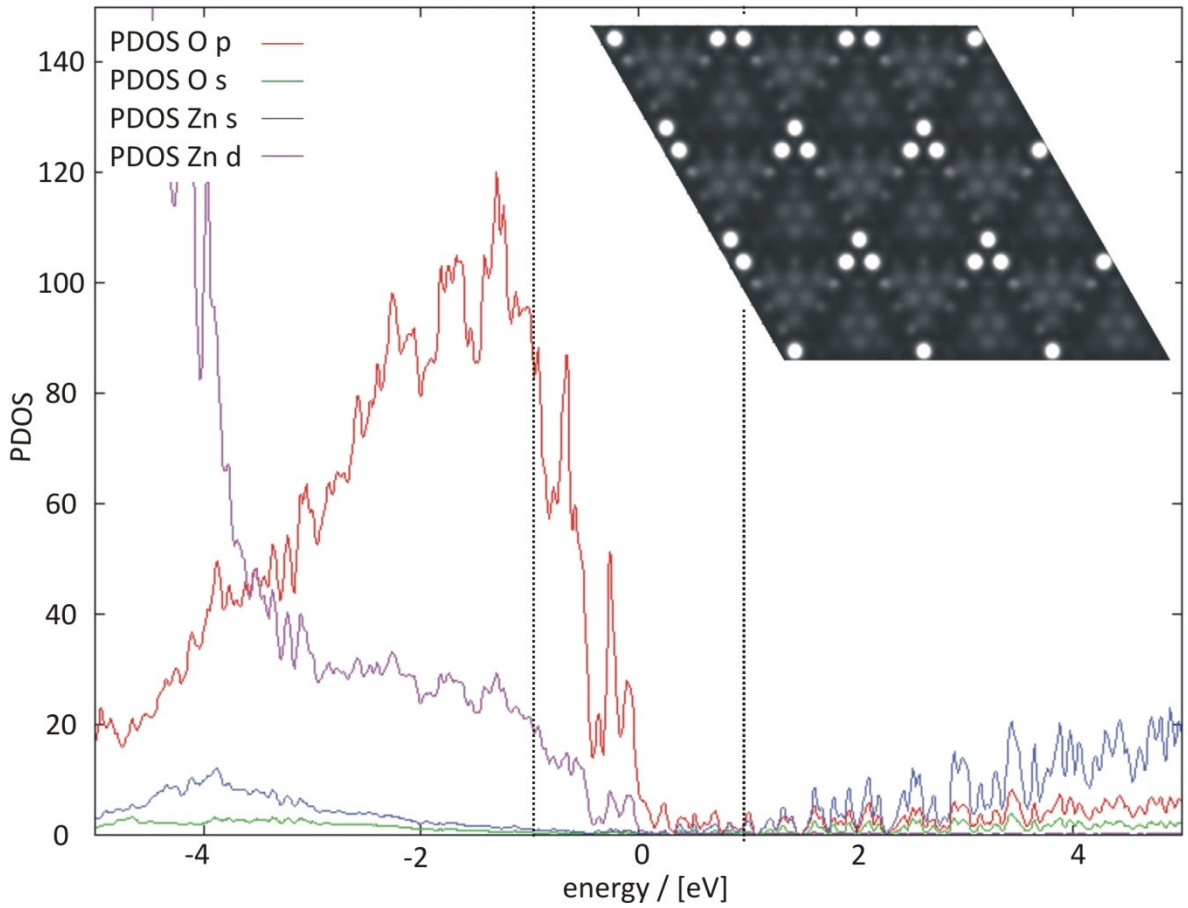

Fig. 5.16: Projected density of states for 3 ML of ZnO. The dashed lines mark the typical energy-range for STM-measurements. The fluctuations of the individual lines are due to limited slab thickness. Inset: simulated STM-picture at +1.0 V. Calculations made by G. Barcaro and A. Fortunelli.

5.2 Influence of the oxygen chemical potential on growth and structure of ZnO

For the methanol reforming reaction, a real catalyst operates in strongly oxidative and reductive environments. These conditions can have a strong influence on the composition of the oxide. To simulate such conditions for the model catalyst, ZnO films have been grown at different oxygen pressures, thus influencing the oxygen chemical potential during growth. To investigate this topic, two sets of experiments have been carried out for three different coverages: 0.7 ML, 1.5 ML and 3.0 ML.

In the first set of experiments ZnO films have been prepared at four different oxygen-pressures for each coverage: 5×10^{-8} mbar, 1×10^{-7} mbar, 1×10^{-6} mbar and 1×10^{-5} mbar. During deposition the sample has been held at room temperature, afterwards it has been annealed to 550 K in oxygen atmosphere. Post-oxidation has been used for 0.7 ML coverage, reactive evaporation for all other coverages. After preparation the surface has been investigated with LEED and STM. For each coverage and each oxygen-pressure a separate preparation has been performed. This procedure ensures complete oxidation of the oxide-overlayers. The drawback is that the coverage shows relatively large deviations due to the problems described in section 2.3. This sometimes complicates the comparison of experimental data and the extraction of general trends.

To gain better control of the coverage, a second set of experiments has been carried out. For that purpose ZnO films with the stated coverages have been grown at a sample temperature of 300 K and an oxygen-pressure of 5×10^{-8} mbar. Like before, post oxidation has been used for 0.7 ML of ZnO and reactive evaporation for the other coverages. After deposition the sample has been annealed to 550 K in oxygen atmosphere and subsequently investigated with LEED and STM. To keep the coverage constant, the film has been reoxidised at oxygen-pressures of 1×10^{-7} mbar, 1×10^{-6} mbar and 1×10^{-5} mbar by annealing at 550 K in oxygen atmosphere. After each oxidation step LEED- and STM-measurements have been performed. This procedure guarantees a constant coverage for each test. The drawback of this method concerns the supply with atomic oxygen. Molecular oxygen is dosed onto the sample during the experiment. The molecules dissociate on metallic palladium or zinc-surfaces, but not on the ZnO-film. At higher coverages most of the surface is covered by the oxide layer. Thus the dissociation rate of molecular oxygen is reduced. This lack of atomic oxygen might lead to variations of the composition within the ZnO-film. Also undesired alloying might take place at the Pd/ZnO-interface. Thus a better comparability is given for each coverage, but the film composition may vary with increasing thickness. Please note that the reoxidation could not be performed in situ. Thus STM pictures of one series do not show the same area on the surface.

Nonetheless, by performing both sets of experiments and careful examination of the results for a large number of measurements, some reliable information about the influence of the

oxygen chemical potential on the structure and growth of ZnO-films could be obtained. Because of the different structural composition of the ZnO-layers below and above 1 ML and different results for the three investigated coverages, those will be presented separately in the next three sections. To make descriptions easier, the different sets of experiments will be denoted as “procedure I” for those where a fresh preparation has been performed for each coverage and oxygen-pressure and “procedure II”, for the reoxidation experiments.

5.2.1 θ_{ZnO} = 0.7 ML

The experimental results, obtained with procedure I, are shown in figure 5.17. The amount of detected ZnO ranges from 0.5 to 0.8 ML in this test.

The situation for an oxygen partial pressure of 5×10^{-8} mbar is depicted in figure 5.17a. In the LEED a clear (6×6)-pattern can be observed. With STM 4×4-, as well as single layer 6×6-islands (labelled A) and a few Pd D-islands can be seen. Most of the surface is covered by the 4×4-structure. Its appearance is like the one obtained at $p_{O2} = 5 \times 10^{-7}$ mbar, described in section 5.1.1, - no structural changes or other deviations could be found.

The 6×6-structure nucleates in quite large, compact islands. In contrast to the 4×4-stucture, definite structural changes can be observed. The 6×6-islands show an increased apparent height of (2.3 ± 0.6) Å. The large error stems from a strong buckling of the surface, which makes a more precise height determination difficult. In figure 7.18a this effect is best seen in comparison to the Pd D-island on the top left, which appears even lower than the 6×6-island labelled A.

On top of the 6×6-islands a network of triangles and pits appears that cannot be seen on films prepared under standard conditions. Figure 5.18a shows the structure in more detail. From the high resolution image in the inset, it can be seen that the ZnO-lattice is not disturbed but modulated along the dark lines of the triangles. The amplitude of this modulation is about (0.6 ± 0.1) Å. The pits on the other hand do not show any maxima within their borders. Taking into account that the maxima in the STM images stem from oxygen states, the obvious conclusion is that the pits represent oxygen-vacancies. The triangles on the other side can be interpreted as a disturbed moiré-structure, created by the strain which has been induced to the film by the, more or less regularly spaced, pits. Similar results have also been obtained for CeO_2 on Rh(111) [ss04]. It might also be possible that the increase in apparent height is connected to the defect-structure.

To test if oxygen vacancies can create the observed pattern on the islands, according DFT-calculations have been performed for a 6×6 h-BN structure with oxygen vacancies, as shown in figure 5.18b. The resulting STM-simulation reproduces the experimental results reasonably well.

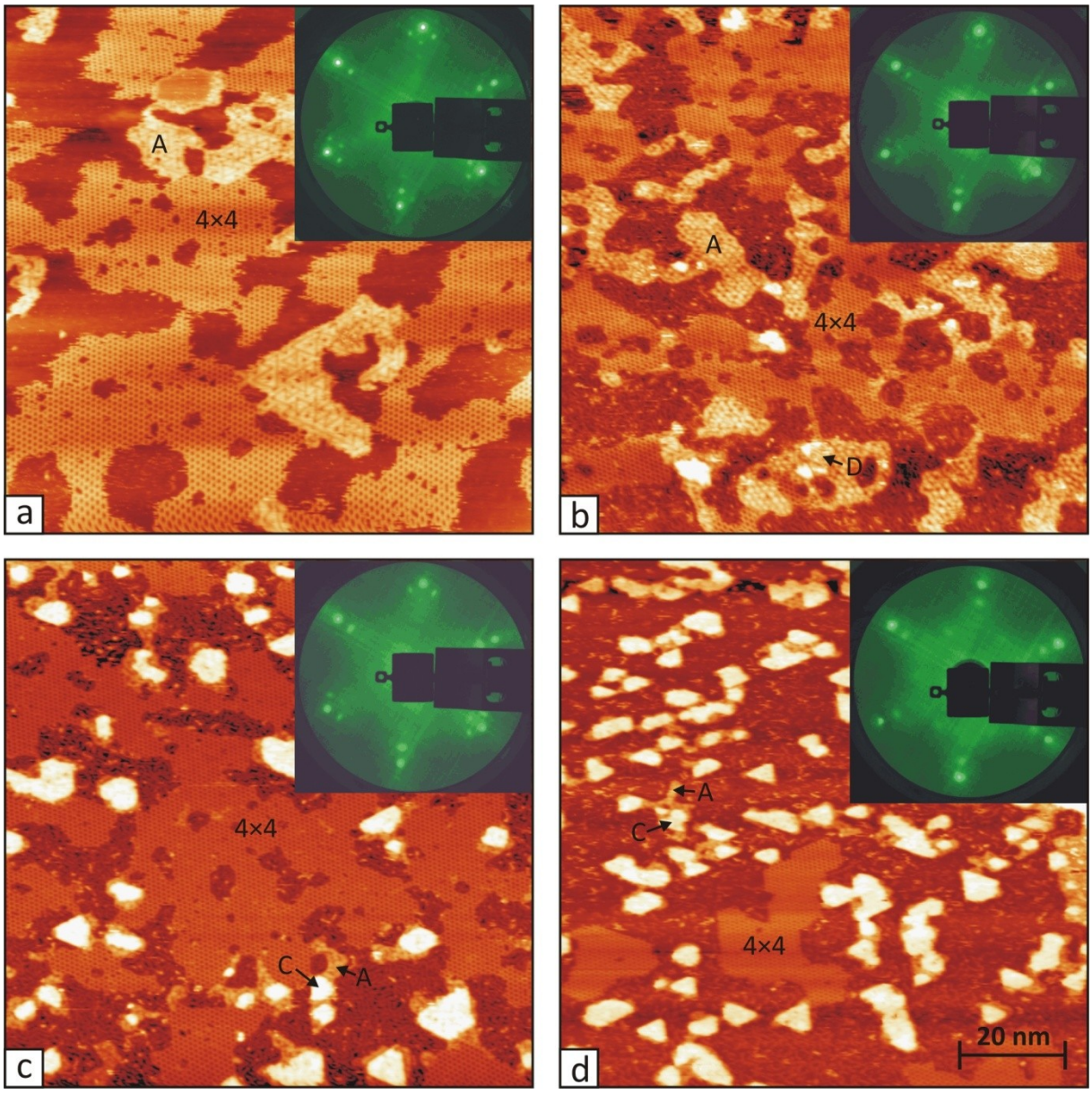

Fig. 5. 17: Variation of the oxygen chemical potential for a mean coverage of 0.7 ML, prepared with procedure I. ZnO 6×6-islands are labelled A, C corresponds to the 2nd ZnO layer, Pd-islands are labelled D. STM-pictures show an area of (100 × 100) nm^2 and have been obtained at U = +1.0 V and I = 0.4 nA. (a) p_{O2} = 5 × 10^{-8} mbar, LEED: E_B = 69.8 eV; (b) p_{O2} = 1 × 10^{-7} mbar, LEED: E_B = 71.3 eV; (c) p_{O2} = 1 × 10^{-6} mbar, LEED: E_B = 72.9 eV; (d) p_{O2} = 1 × 10^{-5} mbar, LEED: E_B = 66.2 eV. The 6×6 islands change most, when the oxygen chemical potential is increased. At the lowest pressure they expose a defect structure, which can be seen in more detail in figure 5.18. At 1 × 10^{-7} mbar this defect structure has vanished. Further increase of the oxygen pressure leads to a structural change resulting in bilayer islands. the 4×4- on the other hand remains unchanged for a large pressure range. Only at the highest oxygen pressure it is restructured into 6×6-bilayer islands.

Both, triangular pits and the moiré-pattern, can be found in the simulation. But there are also differences between theoretical and experimental results: In the simulation the pits are surrounded by a ring of bright maxima, which cannot be observed in experiment. Also the simulated structure would need temperatures of 800 K to become stable. Yet under experimental conditions other stabilisation mechanisms may very well be at work. The good agreement between simulation and experimental data however supports the model of missing oxygen atoms in the 6×6-structure.

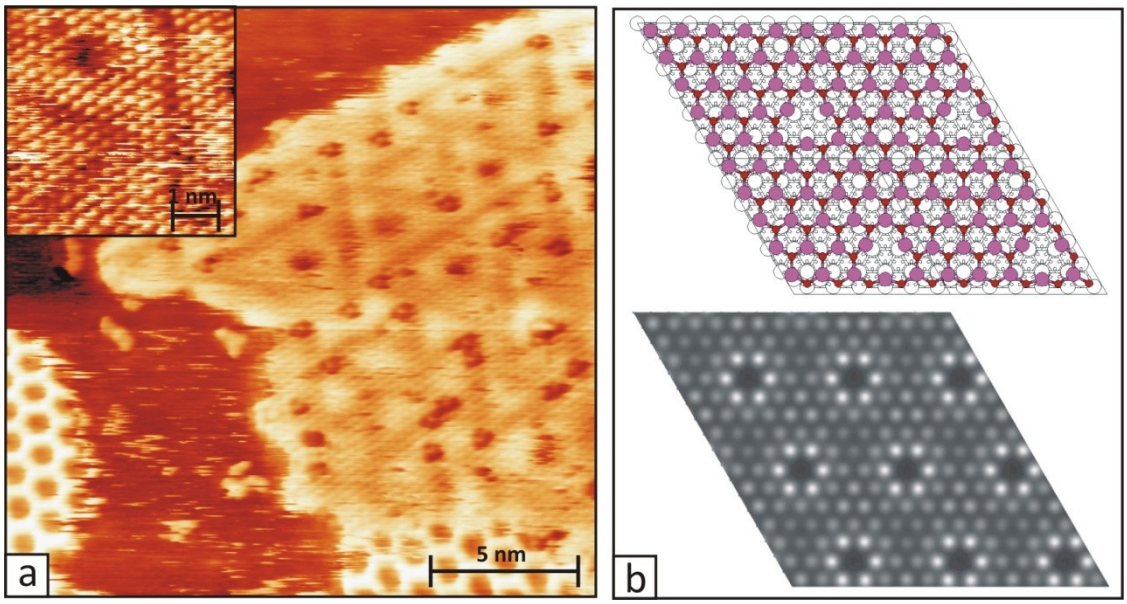

Fig. 5.18: (a) High resolution STM scans of the 6×6-defect-structure at $p_{O2} = 5 \times 10^{-8}$. Both pictures have been obtained at U = +30 mV, I = 1.5 nA. Area of the large picture: (20 × 20) nm^2; area of the inset: (5 × 5) nm^2. (b) DFT-model of the 6×6-structure with oxygen vacancies and the according STM-simulation at +1.0 V. Calculations performed by A. Fortunelli and G. Barcaro.

The defect structure is replaced by the normal moiré pattern when the oxygen pressure is increased to 1×10^{-7} mbar, as shown in figure 5.17b. This change indicates a filling of the oxygen- vacancies at higher oxygen chemical potential. The apparent height of the 6×6-islands comes to a "normal" value of (2.0 ± 0.4) Å. The size of the islands also varies with the trend going to smaller, interconnected shapes. Single layer growth is still predominant but in some places traces of a beginning second layer can be detected. The 4×4 islands do not show any changes due to the increase of the oxygen-pressure. Also a few Pd D-islands could be observed. The LEED pattern remains largely unchanged, it only appears a little bit more blurred.

Upon a further increase of the oxygen pressure to 1×10^{-6} mbar (figure 5.17c) a more drastic rearrangement happens. The 6×6-islands change from single layer to a bilayer growth mode, thus strongly reducing the area covered by this structure. Typical shapes of these bilayer islands expose tetragonal or hexagonal symmetries with alternating side lengths. In most of the observed cases the 1st layer is almost completely covered by the 2nd one. Only in a small stripe at the rim of the islands traces of the first layer could be seen. Yet a few examples exist, where a bit more of the 1st layer is visible, allowing a comparison of 1st and 2nd layer.

Such an example is shown in figure 5.19. The high resolution scans show similar atomic structures with a 6×6 unit cell for both layers. The surface of the 2nd layer appears slightly rougher than the one of the 1st layer. The 1st layer also shows triangular moiré stripes in many cases, as shown in figure 5.19a. The difference to the layers, grown at 5×10^{-8} mbar, is the absence of pits. It should be noted, that these stripes are only observed at low coverage. With increasing amount of deposited ZnO, this effect disappears. It might be that the formation of the 2nd layer produces strain in the 1st one, when the island size is small.

It has been difficult to obtain reliable values for the apparent heights of the two ZnO-layers. Because only a small part of the 1st layer could be seen at the rim of the islands, no definite plateau could be detected in the height profiles of these areas, only a more or less pronounced change in the slope. Thus the choice of the reference points for the height measurement of the 2nd layer has become highly subjective. Also in the few cases, where more area of the 1st layer has been visible in STM, no reliable height information could be extracted from the images. To circumvent these problems, the total apparent island height has been measured, resulting in a mean value of (4.2 ± 0.7) Å. This value is quite high, indicating, that the 2nd layer is present in form of phase C.

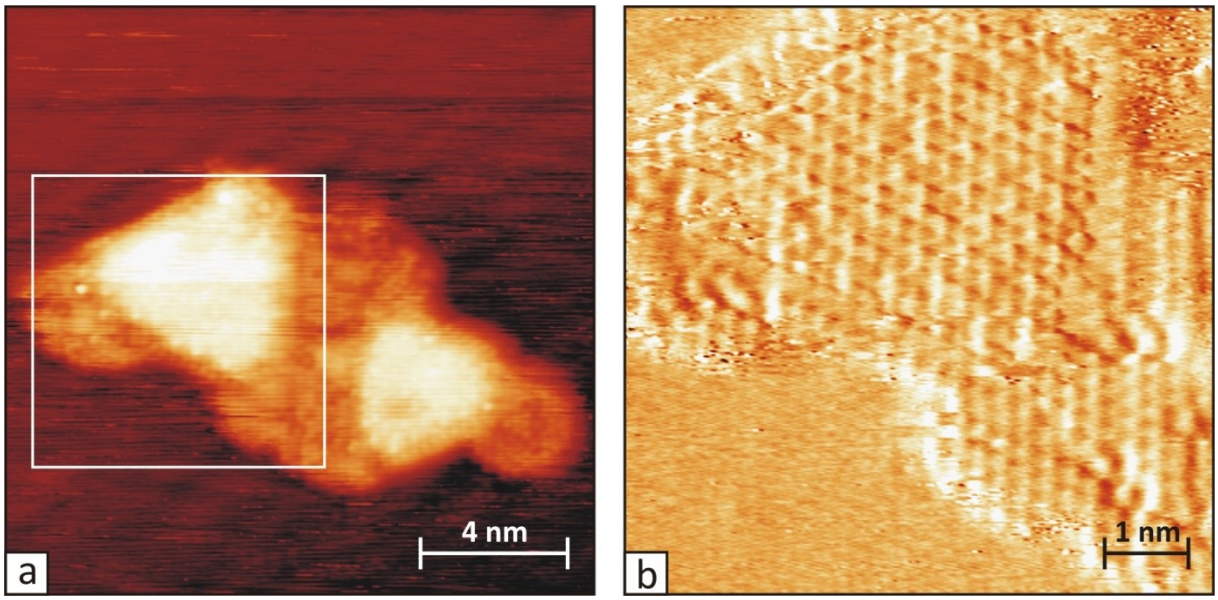

Fig. 5. 19: High resolution scans of bilayer islands grown at p_{O2} = 1 × 10^{-6} mbar. (a) (16 × 16) nm^2 scan taken at U = +200 mV and I = 2.0 nA. (b) (7 × 7) nm^2 differential image corresponding to the area in the white rectangle in (a), U = +30 mV, I = 1.5 nA.

At p_{O2} = 1 × 10^{-6} mbar, the 4×4-structure is very dominant covering almost the whole surface. Structural changes in the 4×4 again could not be observed. Although the 6×6-structure has changed drastically this is not visible in the LEED, which is showing the usual pattern. Pd D-type islands could not be observed.

The trend towards bilayer islands continues for p_{O2} = 1 × 10^{-5} mbar. At this pressure also the 4×4 is affected by the structural change, being radically transformed into 6×6-bilayer islands. Pd D-islands again could not be seen on the surface. In the LEED image an attenuation of the 6×6-signal is observable, caused by the reduced area covered by ZnO. But also $p(\sqrt{3}\times\sqrt{3})$R30-spots can be detected, which can be attributed to CO adsorbed on the free Pd-surface.

The results obtained with procedure II concur with those stated above. They are shown in figure 5.20. In this test the 4×4-structure even disappeared completely at 1 × 10^{-5} mbar O_2. The mean apparent height of the bilayer islands, as shown in figure 5.20d, is (4.0 ± 0.4) Å.

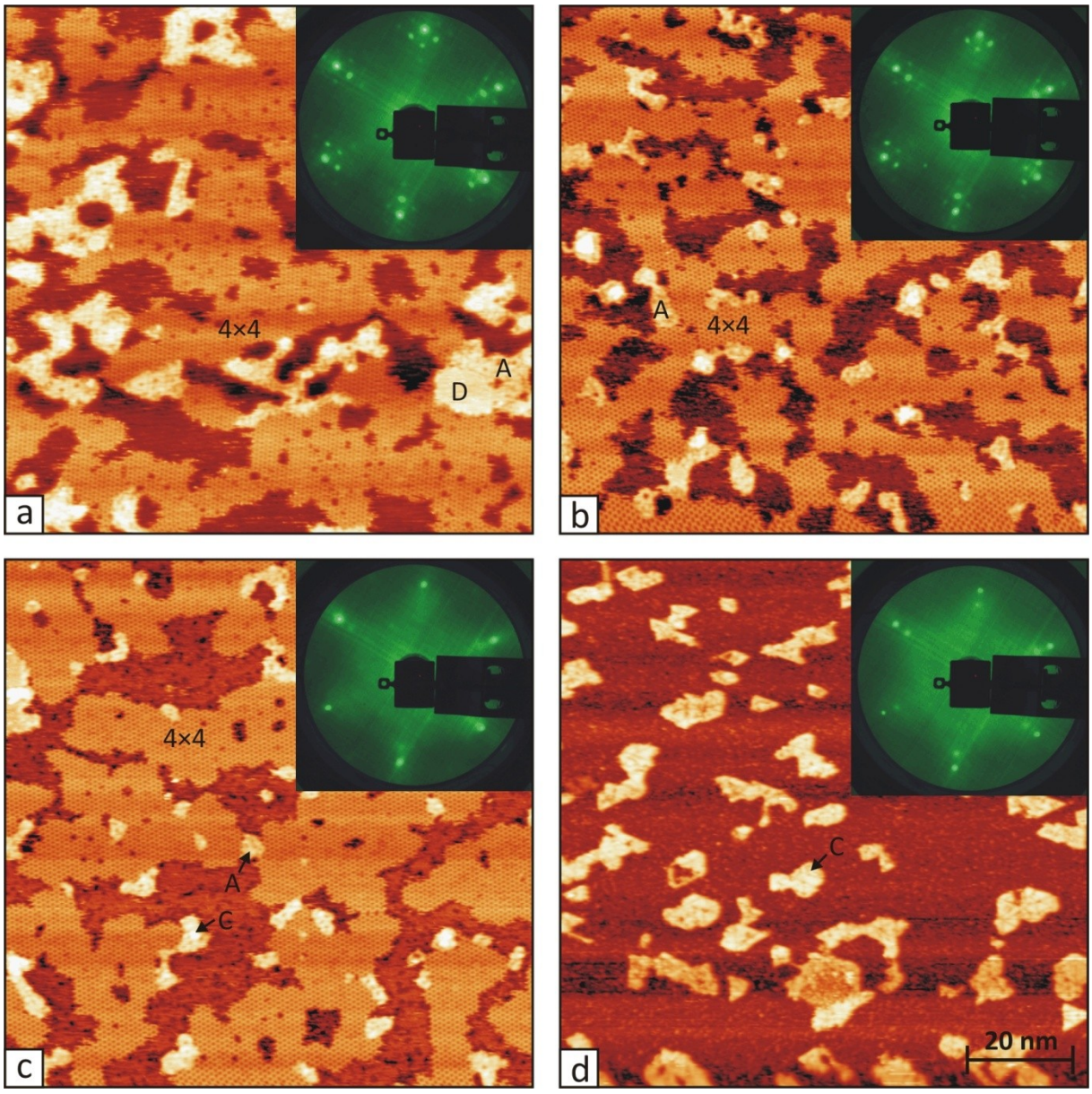

Fig. 5.20: Variation of the oxygen chemical potential for a coverage of 0.7 ML, measured with setup II. The results of this test are in agreement with those obtained by procedure I, which are shown in figure 5.17. Legend: A: 1st ZnO layer, C: 2nd ZnO layer, D: Pd-islands. (a) p_{O2} = 5 × 10^{-8} mbar; (b) p_{O2} = 1 × 10^{-7} mbar; (c) p_{O2} = 1 × 10^{-6} mbar; (d) p_{O2} = 1 × 10^{-5} mbar. STM-pictures have been obtained at U = +1.0 V and I = 0.4 nA and show an area of (100 × 100) nm^2. LEED images have been obtained at E_B = 71.5 eV.

The general trend, which has been observed in these experiments, can be described as minimisation of the Pd-ZnO interface with increasing oxygen chemical potential. This minimisation takes place within the limits of bilayer growth, meaning that the formation of needle-like structures is suppressed. Moreover a structural change seems to take place in the 6×6-phase at low oxygen pressure. For the open 4×4-structure only in 3/8 of the covered area an interface between oxide and substrate is formed. That might explain why this structure remains unchanged over such a large pressure range.

The driving force behind the interface-minimisation must be sought in the surface tension γ. As described in chapter 1.5 the form of an island depends on the balance between γ_s, γ_f, and $\gamma_{s/f}$. Other influences like a change of the oversaturation grade of ZnO can be neglected since

the effect also appears when the film is reoxidised. Thus a change in the growth mode indicates a change in the balance of the contributions to the surface tension, caused by the increase in the oxygen chemical potential. This leads to a change in the free Gibbs energy of the surface ΔG^s.

DFT calculations, performed by A. Fortunelli and G. Barcaro, reveal the mechanism at work. As known from [ls00] oxygen tends to chemisorb in a p(2×2)-structure on top of Pd(111). Calculations show that this process already is favourable at standard conditions (T = 550 K, $p_{O2} = 5 \times 10^{-7}$ mbar) with $\Delta G_{2\times2} = -0.55$ eV. With increasing oxygen pressure and thus increasing oxygen chemical potential, the structure becomes even more stable. The DFT calculations show that upon formation of a 2×2-oxygen chemisorbed phase it is thermodynamically more attractive for the 6×6 ZnO structure to form bilayers. The according gain in free Gibbs energy amounts to $\Delta G^s = -4.26$ eV for the reaction 2 single layers (6×6)+ $\frac{9}{2}O_2 \rightarrow$ bilayer (6×6)+ 9 Pd(111)-O(2×2) [wj10].

Fortunelli and Barcaro mention that the calculated structure is stable up to 800 K in their simulations. That is in disagreement with the experimental results stated in [ls00] where desorption of oxygen from the chemisorbed phase already takes place around 750 K. As source for this discrepancy they name the choice of the oxygen chemical potential as well as an overestimation of the O-bonds due to the chosen xc-functional and the choice of the pseudopotential. Still the results for the behaviour of the ZnO are in accordance with the experimental data. The model is supported by the observation that the transformation to bilayers depends on the amount of free substrate area. As shown in figure 5.1a bilayers can also be formed at lower oxygen pressures if the amount of deposited material is sufficiently small.

5.2.2 θ_{ZnO} = 1.5 ML

At an apparent coverage of 1.5 ML two trends can be observed, when the oxygen chemical potential is varied. Both of them can be seen with procedure I as well with procedure II. The corresponding experimental results are shown in figures 5.21 and 5.22.

The first trend concerns the apparent height of the first ZnO-layer. The corresponding values are listed in table 5.3. At oxygen pressures, ranging from 1×10^{-7} mbar to 1×10^{-5} mbar, the

O_2-pressure / [mbar]	1st ZnO-layer / [Å]
5×10^{-8}	2.3 ± 0.6
1×10^{-7}	2.0 ± 0.4
1×10^{-6}	1.9 ± 0.5
1×10^{-5}	2.0 ± 0.3

Table 5. 3: Apparent heights of the 1st ZnO layer as a function of the oxygen pressure, obtained with procedures I and II.

apparent height of the 1st ZnO layer is in the typical range of 1.9-2.0 Å. At $p_{O2} = 5 \times 10^{-8}$ mbar however, an increase of about 0.3 Å can be observed. This increase in mean apparent height is small, but reproducible. Moreover it is in accordance with the results obtained for 0.7 ML ZnO-coverage. Yet at 1.5 ML coverage the oxygen-defect structure cannot be seen, which has been observed in the submonolayer-regime.

The second trend concerns the apparent heights of the different ZnO-phases in the second layer. As described in section 5.1.2 two ZnO-phases have been observed in the second layer. Phase B has shown an apparent height of (1.6 ± 0.2) Å, phase C displayed an apparent height of (2.3 ± 0.3) Å. Both values have been obtained with respect to the first layer, which has been labelled A.

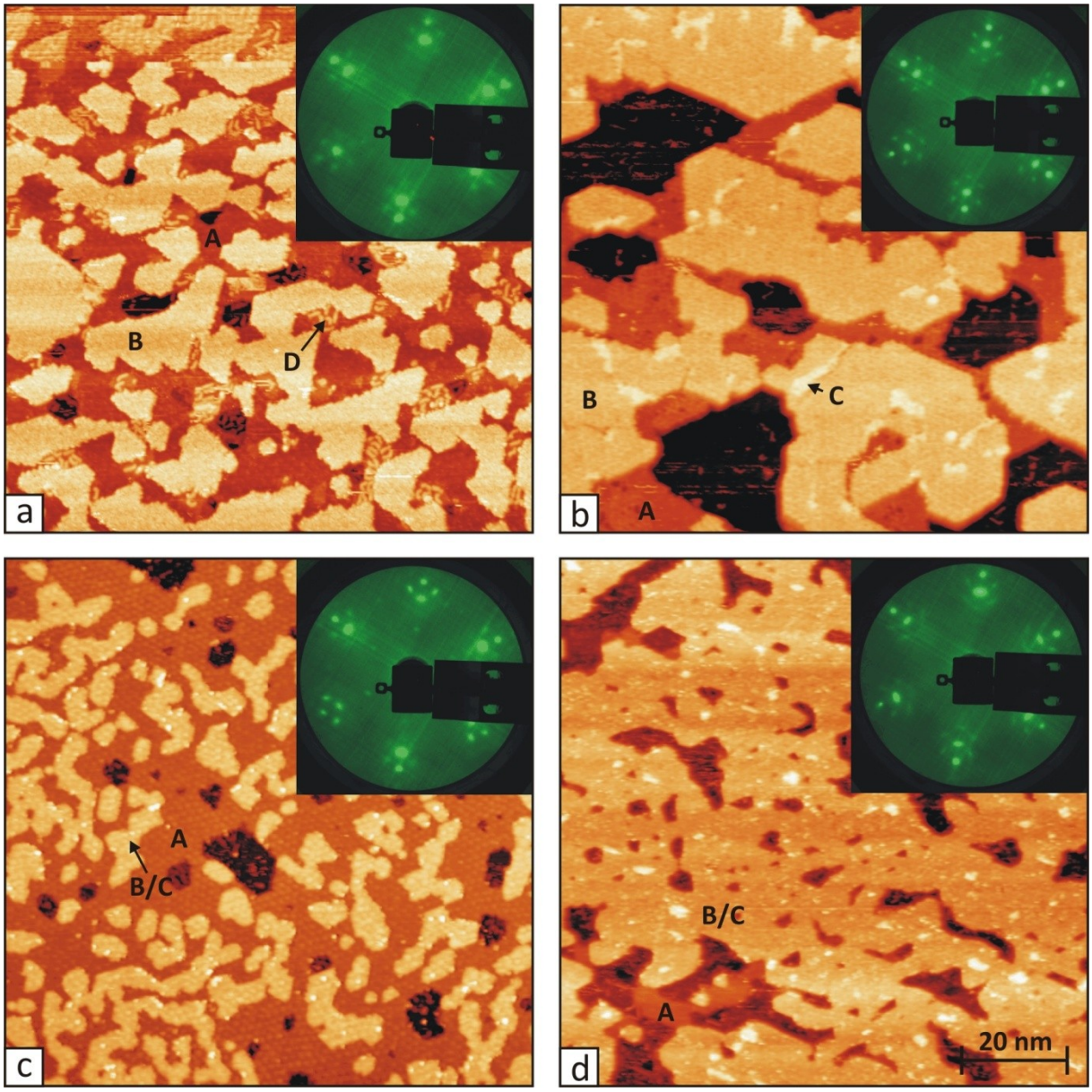

Fig. 5. 21: Variation of the oxygen partial pressure for a mean coverage of 1.5 ML, performed with procedure I. Individual coverages range from 1.4 to 1.7 ML. STM-pictures show an area of (100 × 100) nm². Legend: A: 1st ZnO layer, B: 2nd ZnO layer – thin phase, C: 2nd ZnO layer – thick phase, D: Pd-islands. (a) $p_{O2} = 5 \times 10^{-8}$ mbar; STM: U = +1.0 V, I = 0.4 nA; LEED: E_B = 68.1 eV. (b) $p_{O2} = 1 \times 10^{-7}$ mbar; STM: U = +1.0 V, I = 0.4 nA; LEED: E_B = 64.8 eV. (c) $p_{O2} = 1 \times 10^{-6}$ mbar; STM: U = +1.0 V, I = 0.1 nA; LEED: E_B = 69.1 eV. (d) $p_{O2} = 1 \times 10^{-5}$ mbar; STM: U = +1.0 V, I = 0.4 nA; LEED: E_B = 65.2 eV.

The experiments with different oxygen pressures have shown that these phases react to the change of the oxygen chemical potential. At low oxygen pressures up to 5×10^{-7} mbar both ZnO-phases can be observed. At $p_{O2} \geq 1 \times 10^{-6}$ mbar, typically just one phase can be seen. Yet it has proven astonishingly difficult to identify this single phase as B or C. Values obtained in different experiments vary strongly. Using procedure I a mean value of (1.7 ± 0.3) Å could be obtained in the stated pressure range. Procedure II on the other hand revealed a mean apparent height of (2.5 ± 0.2) Å. Also in some other cases B and C could both be observed at oxygen pressures $\geq 1 \times 10^{-6}$ mbar. A clear-cut decision cannot be made on basis of the height measurements alone. Yet the experiments showed, that with procedure I as well as with procedure II an increase of phase C could be observed with increasing oxygen chemical potential.

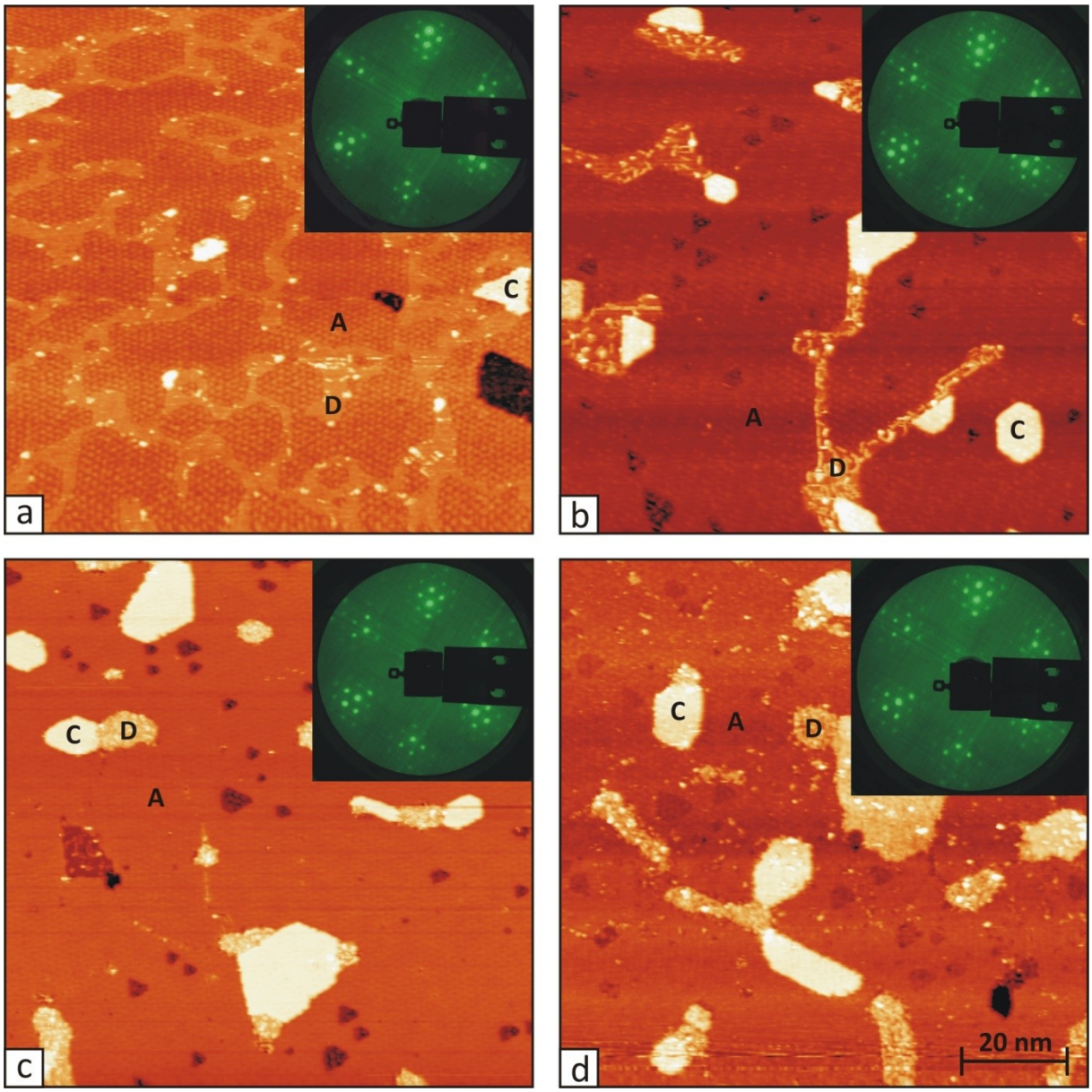

Fig. 5. 22: Variation of the oxygen chemical potential for a coverage of 1.2 ML, performed with procedure II. A: 1st ZnO layer, C: 2nd ZnO layer – thick phase, D: Pd-islands. (a) $p_{O2} = 5 \times 10^{-8}$ mbar; (b) $p_{O2} = 1 \times 10^{-7}$ mbar; (c) $p_{O2} = 1 \times 10^{-6}$ mbar; (d) $p_{O2} = 1 \times 10^{-5}$ mbar. STM-pictures have been obtained at U = +1.0 V and I = 0.4 nA and show an area of (100 × 100) nm^2. LEED images have been obtained at $E_B = 75.9$ eV.

Also the results, obtained in submonolayer coverage-regime, show a tendency towards this phase. In this larger picture of the process it appears like phase C is preferably formed at oxygen pressures of 1×10^{-6} mbar and 1×10^{-5} mbar.

High resolution STM-scans and LEED analysis showed that the surface unit cell of ZnO is not influenced by the changes in the film. At all oxygen pressures a clear 6×6-structure could be observed for 1st and 2nd layer.

5.2.3 θ_{ZnO} = 3.3 ML

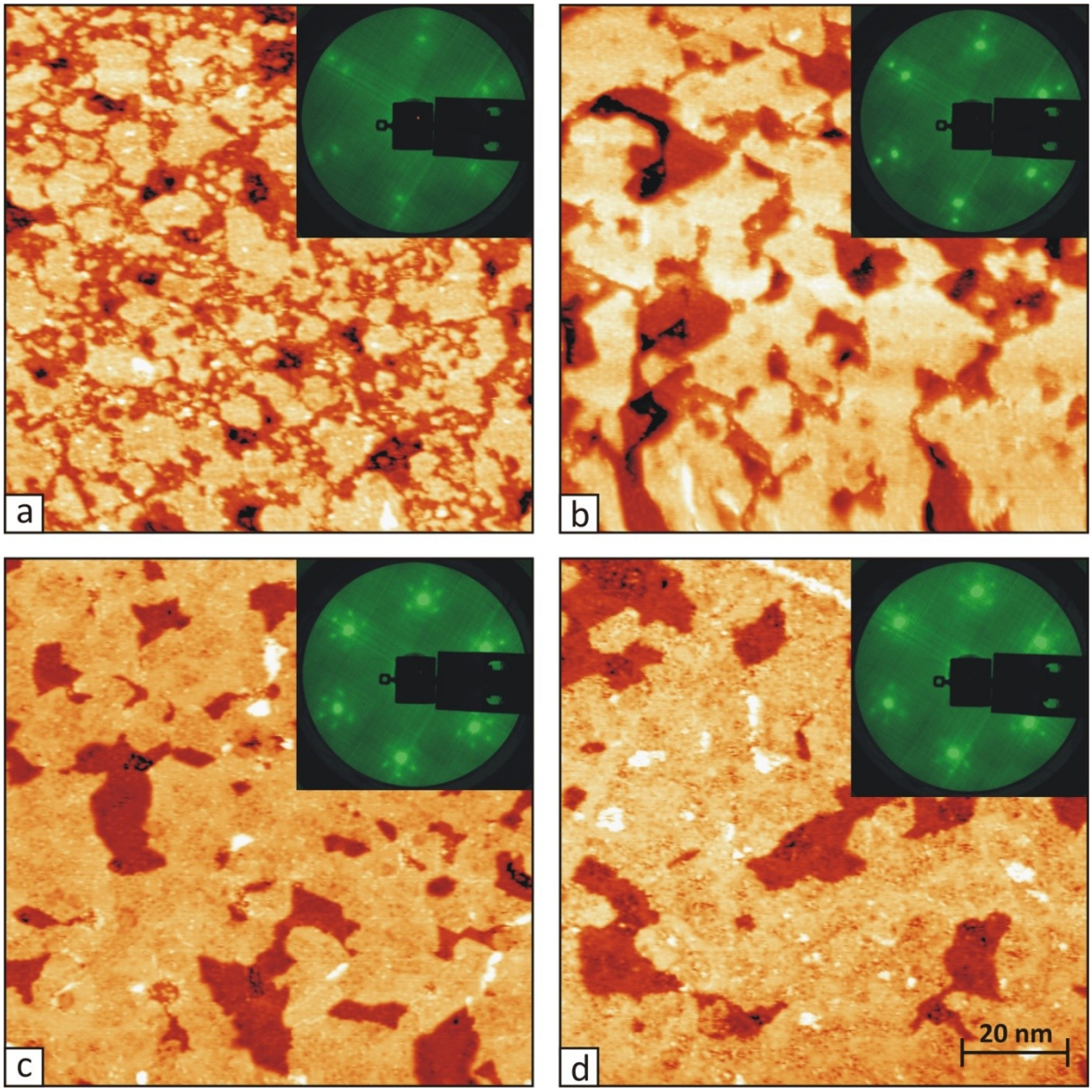

Fig. 5. 23: Variation of the oxygen chemical potential for a coverage of 3.5 ML, measured with setup II. (a) $p_{O2} = 5 \times 10^{-8}$ mbar; (b) $p_{O2} = 1 \times 10^{-7}$ mbar; (c) $p_{O2} = 1 \times 10^{-6}$ mbar; (d) $p_{O2} = 1 \times 10^{-5}$ mbar. Upon reoxidation large structural changes can be observed, accompanied by a roughening of the surface. Since alloying at the Pd/ZnO-interface cannot be excluded, the results of this test have been discarded. STM-pictures have been obtained at U = +1.0 V and I = 0.4 nA and show an area of (100 × 100) nm^2. LEED images have been obtained at E_B = 61.9 eV.

For a coverage of 3.3 ML the measurements, performed with procedure II, are not completely trustworthy. As shown in figure 5.23, large morphological changes take place upon reoxidation, accompanied by a surface roughening. It might be that the heating process leads to dissociation of ZnO at the interface and subsequent alloying, due to insufficient supply of atomic oxygen. Thus the results obtained by this procedure have been discarded.

The images, obtained with procedure I, are shown in figure 5.24. Two kinds of islands can be detected on the surface: C*-islands show an apparent height of (0.6 ± 0.2) Å with respect to their surrounding areas. The apparent height of B*-islands has been determined to be (1.7 ± 0.3) Å with respect to the C* surface of the layer underneath.

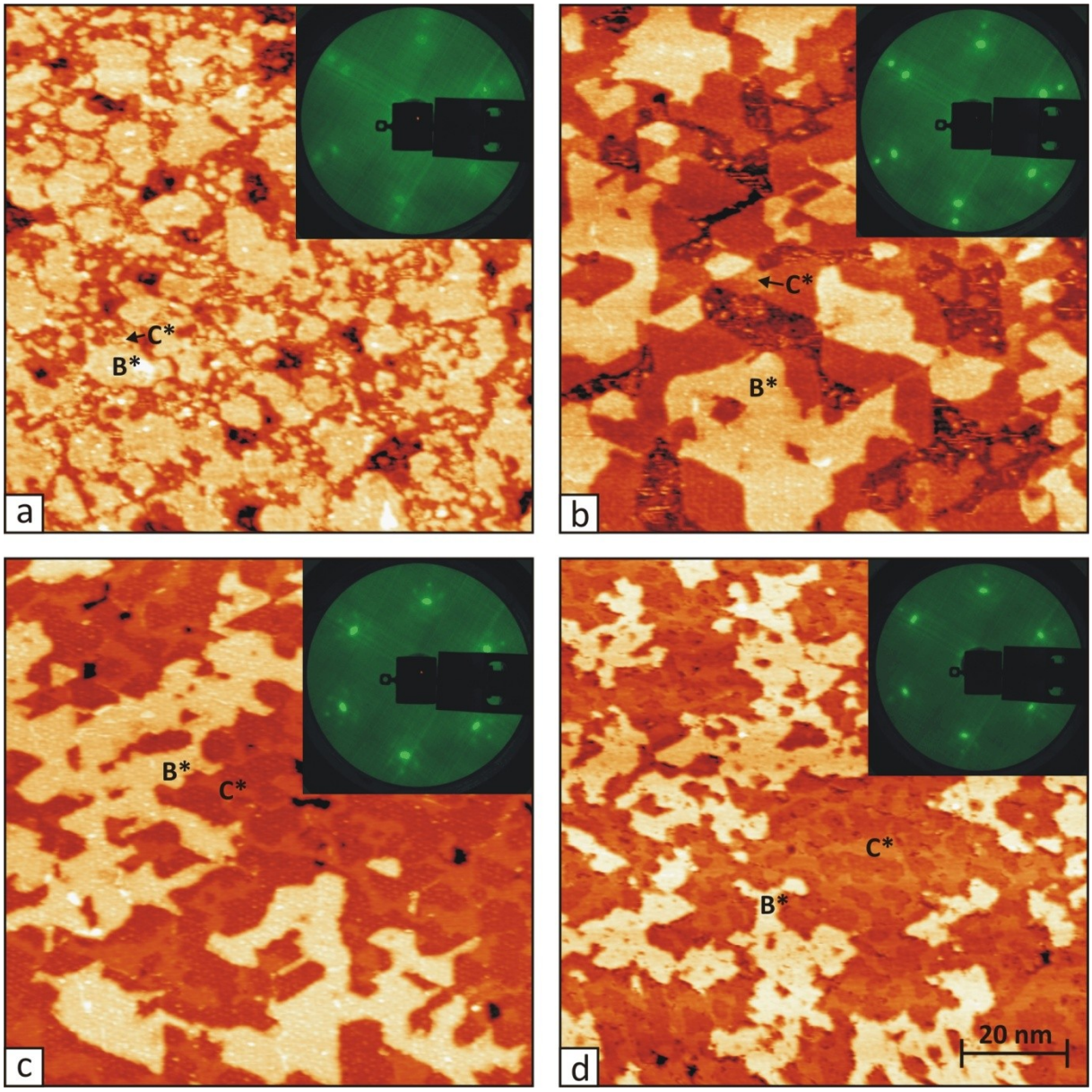

Fig. 5. 24: Variation of the oxygen partial pressure for a mean coverage of 3.3 ML, measured with setup I. STM-pictures have been obtained at U = +1.0 V and I = 0.4 nA and show an area of (100 × 100) nm^2. (a) p_{O2} = 5 × 10^{-8} mbar, LEED: E_B = 61.9 eV. (b) p_{O2} = 1 × 10^{-7} mbar, LEED: E_B = 61.0 eV. (c) p_{O2} = 1 × 10^{-6} mbar, LEED: E_B = 65.3 eV. (d) p_{O2} = 1 × 10^{-5} mbar, LEED: E_B = 63.6 eV. Islands labelled C* show an apparent height which is 0.7 Å larger, than the surrounding area. Islands labelled B* show an apparent height of 1.6 Å with respect to the C*-surface of the layer underneath.

In contrast to the results, presented for 1.5 ML coverage both kinds of islands can be observed on the surface independent of the applied oxygen pressure. Yet with increasing oxygen chemical potential also an increasing amount of C*-islands can be detected on the surface. This observation is in agreement with the trends observed at 0.7 and 1.5 ML coverage.

Again the ZnO 6×6 surface-structure appears not to be influenced by the applied oxygen pressures as LEED and high resolution STM-images show.

5.3 Reduction of ZnO-films

In the methanol steam reforming process, the catalyst is operated at elevated temperatures. This may lead to a thermal reduction of the ZnO-support. Moreover, hydrogen is created during the reaction, which might also reduce the oxide. To test the reaction of ZnO-films to those conditions, the model catalyst system has been subjected to two reduction series, which will be described in this section.

5.3.1 Thermal decomposition

To test the stability of the ZnO-films at elevated temperatures, several heating series have been performed. In those experiments ZnO films with varying thickness have been heated in UHV to different temperatures and then characterized with LEED and STM. The investigated films have been prepared at high oxygen pressures to ensure total oxidation of the deposited Zn. The heating could not be performed in-situ. As a consequence the presented STM-pictures do not show the same area. Nonetheless a clear trend could be observed. In addition to these experiments temperature programmed desorption (TPD) measurements have been performed by Frederik Weber for ZnO films with varying thickness on a Pd(111) template. Two coverage values have been chosen as examples to assist the observed behaviour of the films: 0.7 and 1.6 ML. Next the experimental data of STM- and TDS-measurements will be presented for these two coverages.

In the first example a ZnO film with 0.7 ML coverage has been grown by post-oxidation at 1×10^{-6} mbar O_2. Figure 5.25 shows the surface after annealing at different temperatures. (a) represents the situation after preparation. Most of the surface is covered by a 4×4-structure (dark islands). Bright areas correspond to bilayer 6×6-islands. The LEED shows a distinct (6×6) pattern.

In (b) the surface is shown after annealing to 400 K. Most of the 4×4 has disappeared, instead islands with irregular shapes can be observed on the Pd-surface. Although the 6×6-

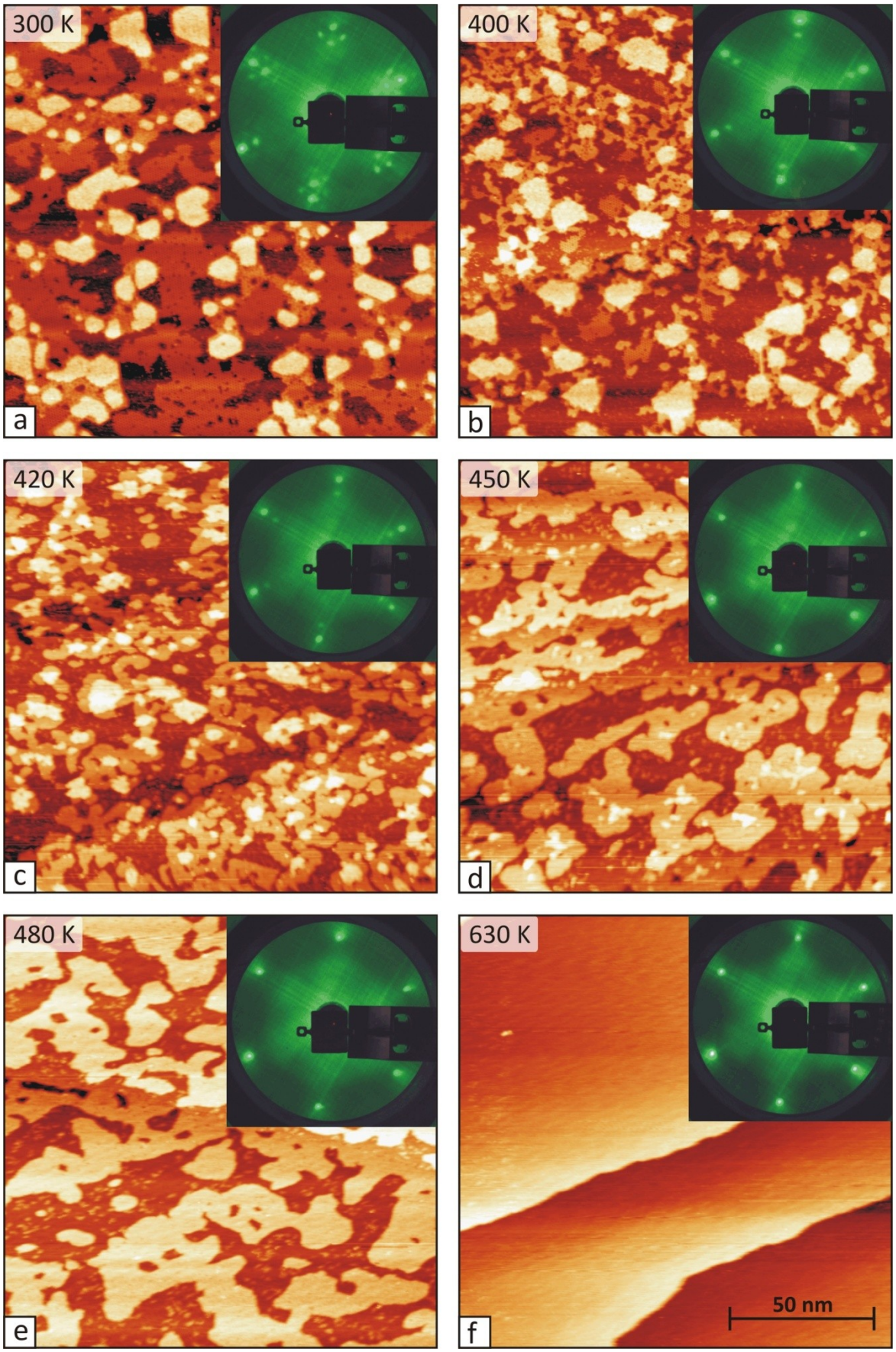

Fig. 5. 25: 0.7 ML ZnO after annealing at different temperatures. (a) after preparation, (b) 400 K, (c) 420 K, (d) 450 K, (e) 480 K, (f) 630 K. STM images show an area of (150 × 150) nm^2 and have been obtained at U = +1.0 V and I = 0.4 nA. LEED images have been recorded at E_B = 66.1 eV. Further descriptions are given in the text.

bilayer islands have not changed upon heating, the (6×6)-pattern in the LEED image has become less pronounced, suggesting a reduction of the surface order.

Further heating to 420 K has lead to an increase of the irregular shaped islands, as shown in (c). The 6×6 bilayer islands have been reduced in area. In the LEED a further attenuation of the (6×6)-signal could be observed. Furthermore a weak 2×2-pattern appeared, indicating a decomposition of ZnO and subsequent alloying of Pd and Zn.

The (6×6) pattern has disappeared completely in the LEED after annealing to 450 K, as depicted in (d). No structure could be resolved with STM but clear p(2×2) spots can be observed with LEED, indicating an ordered PdZn surface-alloy with 2×1-structure. This is an important observation, because it shows that thermal treatment of Pd/ZnO-interface may indeed lead to the formation of a PdZn-interface-alloy, a point which has not yet been clear.

(e) shows the surface after annealing to 480 K. The (2×2)-pattern in the LEED has disappeared, indicating a further reduction of the Zn-concentration in the surface region.

Finally, after annealing to 630 K, only a flat surface has been observed (figure 5.25f). Also the LEED has only displayed a Pd(1×1)-pattern.

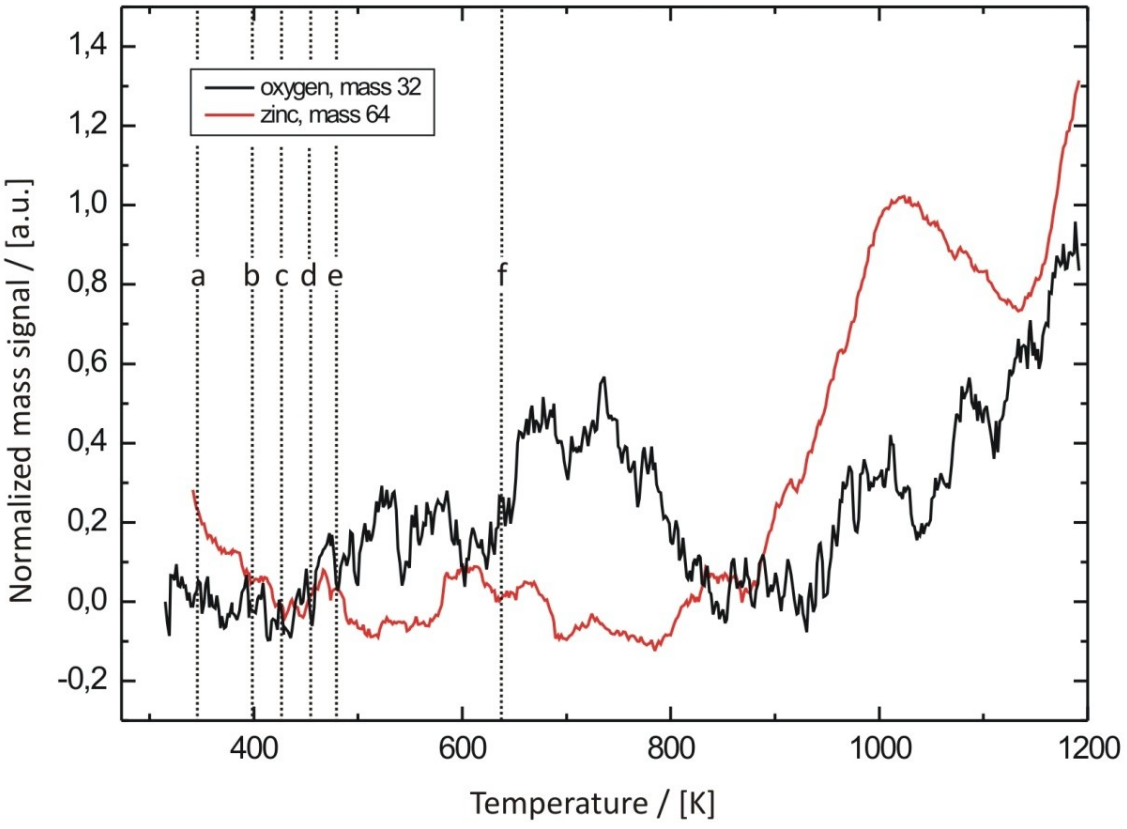

Fig. 5. 26: TPD-spectra of oxygen and zinc for a coverage below 1 ML. The spectra have been smoothed, normalized and submitted to background subtraction for each mass. a – f represent the temperatures applied in the STM experiment, as shown in figure 5.25.

In figure 5.26 TPD-spectra of zinc and oxygen are shown for a comparable ZnO coverage of about 0.5 ML. In this case the peak position is more relevant than the total peak height. Since both signals have been very small in this measurement, the corresponding spectra have been smoothed, normalized and submitted to background subtraction separately for each mass, thus a comparison of the peak height does not make sense.

The oxygen signal shows one clear peak, centred at 720 K. Also for the zinc signal one peak could be detected, centred at 1020 K. Yet, as shown by the dotted lines in figure 5.26, the decomposition of ZnO has been observed at lower temperatures in STM. For the zinc-desorption the explanation is straightforward: It is known, that zinc is easily dissolved in palladium, thus Zn-atoms tend to diffuse into the Pd-bulk. At temperatures around 1000 K the Zn migrates back to the surface and desorbs.

At higher coverage the situation becomes even more difficult. Figure 5.27 shows the TPD-spectra obtained for a coverage of about 1.5 ML. The Zn-spectrum has not changed but for oxygen a second peak has arisen at 890 K in addition to the peak at 720 K. Also a small feature could be detected at 600 K for zinc as well as for oxygen. Related STM-measurements have been performed at annealing temperatures, marked by the dotted lines in figure 5.27. This film has been prepared by post-oxidation at $p_{O2} = 1 \times 10^{-5}$ mbar.

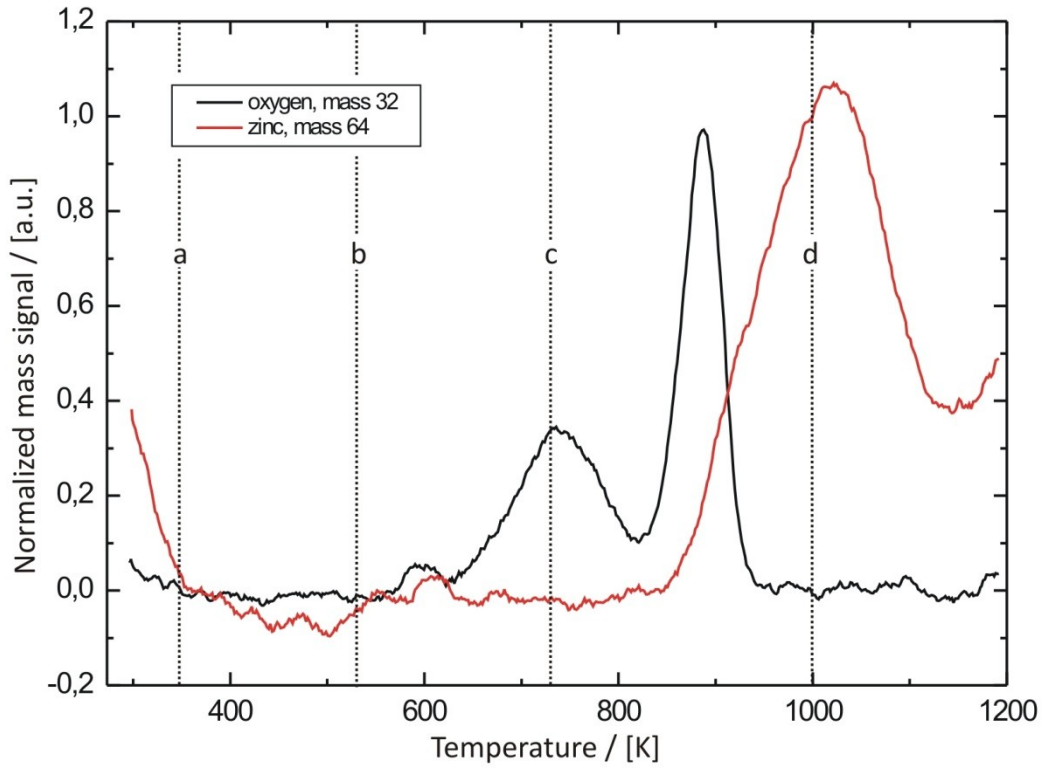

Fig. 5. 27: TPD-spectra of oxygen and zinc at a coverage between 1 and 2 ML. The spectra have been smoothed, normalized and submitted to background subtraction for each mass. a – d represent the temperatures applied in the STM experiment, as shown in figure 5.28.

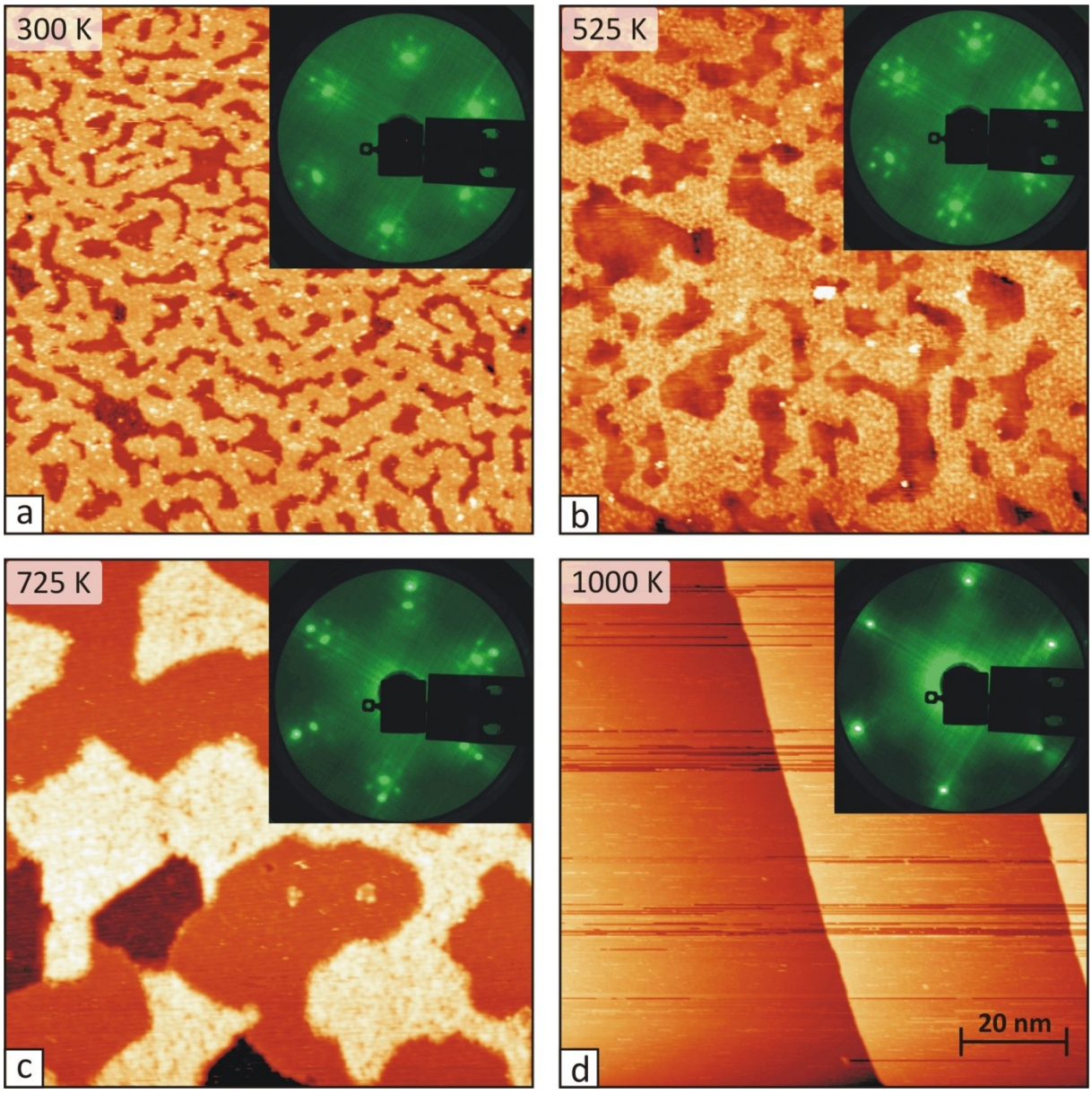

Fig. 5.28: 1.7 ML ZnO, grown at p_{O2} = 1 × 10^{-5} mbar, after annealing to different temperatures. (a) after preparation, (b) 425 K, (c) 725 K, (d) 1000 K. STM images: (100 × 100) nm^2, U = +1.0 V, I = 0.4 nA; LEED images: E_B = 66.1 eV. Further descriptions are given in the text.

Annealing steps have been performed as described above - the results of this investigation are shown in figure 5.28. (a) depicts the situation after preparation. The total Zn-coverage is 1.7 ML. The first ZnO layer is almost closed, in the second layer only one type of islands can be seen. It has been expected that C-type islands would form, but height measurements revealed an apparent height of (1.5 ± 0.1) Å for the 2nd layer. High resolution STM-scans showed a well ordered 6×6-structure with a distinct moiré-pattern. A few clusters are present in the third layer. The corresponding LEED-picture shows a (6×6)-pattern.

This (6×6)-pattern becomes even more pronounced after annealing to 525 K, as shown in (b). The second ZnO layer appears unchanged in STM, for the first one no structural resolution could be obtained.

Further annealing to 725 K shows a definite reduction of the film (figure 5.28c). Islands in the first layer appear metallic, the second layer islands do show some pattern but no atomic resolution could be obtained in STM. The LEED still shows (6×6)-spots, indicating that the 2nd layer islands still consist of ZnO.

Finally, after heating to 1000 K, the surface appears flat, accompanied by a Pd(1×1) LEED pattern.

At this coverage the results obtained with STM and TPD show a better agreement. Decomposition of ZnO may already take place at 525 K but the first desorption peak is observed at 725 K, indicating that this peak is due to oxygen desorbing from the ZnO film. It can be assumed that this is also the case at 0.7 ML coverage. It is not clear why the results of TPD- and STM-measurements do not fit together at this coverage. It should be taken into account, that the coverage in the TPD measurement may have exceeded the one of the STM measurement. The results at 1.7 ML coverage also reflect those obtained for thicker ZnO-films, thus no further discussion of those experiments will be given.

5.3.2 Reduction with hydrogen

Finally the behaviour of ZnO-films in a hydrogen atmosphere will be discussed briefly. For investigation a ZnO film has been grown at 1×10^{-7} mbar O_2 and characterized with STM. Then molecular hydrogen has been led into the chamber while scanning over the surface at room-temperature. To provide dissociation of molecular hydrogen via the Pd-surface a ZnO-coverage of 0.7 ML has been chosen for this test. The results are presented in figure 5.29 and table 5.4.

Figure 5.29a shows the surface after preparation. About 60% are covered with 4×4 islands and 13% with single layer 6×6-islands. The rest of the Pd-surface is uncovered. Dosing of 1 and 3 L of hydrogen has not changed this situation. Only upon dosing an amount of 30 L of hydrogen, a change could be observed in the STM. The data in table 5.4 shows that the area of the 4×4 islands has been reduced by 8.1% at this exposure. But the increase in free Pd-surface only amounts to 3.7%. The missing 4.4% have been covered by newly formed 6×6-islands. Thus the 4×4 has not been reduced but transformed into the denser 6×6-structure.

Hydrogen exposure	Free Pd area	Area covered by 4×4	Area covered by 6×6
0 L	26.5%	61.2%	12.3%
1 L	23.7%	62.3%	14.0%
3 L	25.6%	62.2%	12.2%
30 L	29.3%	54.1%	16.6%

Table 5. 4: Areas of free Pd, 4×4- and 6×6-islands after exposure to different amounts of hydrogen. The presented values are based on the STM pictures, shown in figure 5.29.

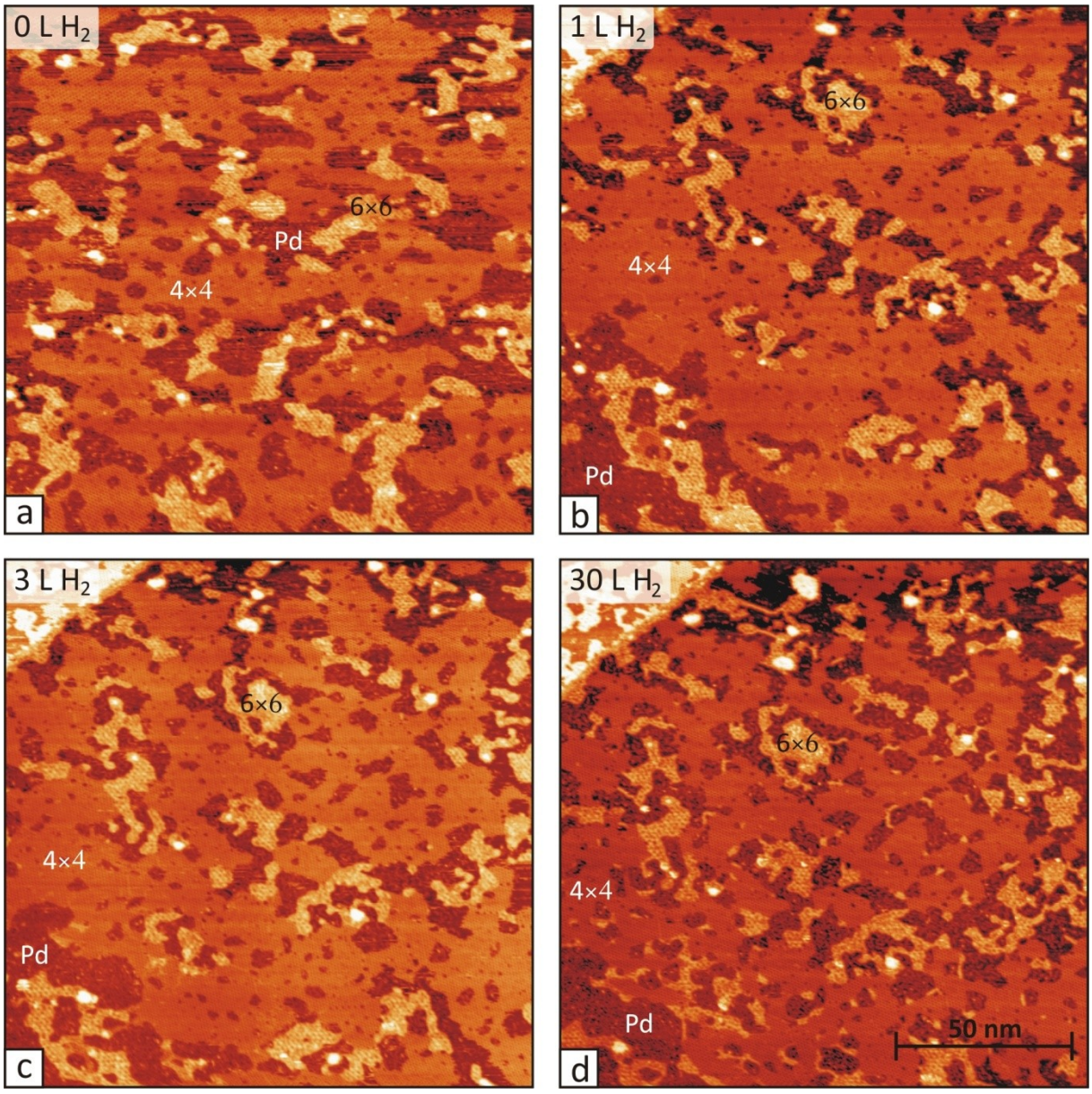

Fig. 5. 29: Reduction of ZnO with hydrogen. (a) after preparation at standard conditions, (b) after dosing 1 L of H_2, (c) after dosing 3 L of H_2, (d) after dosing 30 L of H_2. STM pictures show an area of (150 × 150) nm^2 and have been obtained at U = +1.0 V and I = 0.4 nA. (b), (c) and (d) show the same area on the surface, the area shown in (a) has been pictured at another site of the sample surface. Up to 3 L of hydrogen, no changes can be observed in the ZnO-film. Upon exposure to 30 L of hydrogen a partial transformation of 4×4- into 6×6-islands takes place

The high stability of the ZnO film is not surprising. It has already been shown in section 5.1 that the 4×4 structure is stabilized by hydrogen. Moreover DFT results have also shown that the 6×6-structure can also be decorated by hydrogen without destabilizing the structure. The results presented in this section show, that a change from 4×4- to 6×6-geometry seems favourable at a high chemical potential of hydrogen, but that ZnO does not decompose.

5.4 Discussion

Within the presented investigations of ZnO, one point could not yet be clarified sufficiently: the formation of the two ZnO 6×6-phases with different apparent height in the 2nd layer and in the layers above.

To summarize the information gathered about this feature: In the 2nd layer two different ZnO-phases could be observed. One phase, labelled B, shows an apparent height of (1.6 ±0.2) Å with respect to the 1st ZnO-layer, labelled A. The other phase, labelled C displays a corresponding apparent height of (2.3 ± 0.3) Å, thus it appears 0.7 Å thicker. Moreover B exhibits a greater surface roughness than C (C resembles A in the high resolution STM-images). Such phases could not be observed for the 1st layer A. Further investigation showed that both phases coexist on the surface, when the oxygen pressure during film preparation is the range from 5×10^{-8} mbar to 5×10^{-7} mbar. For higher oxygen pressures of 1×10^{-6} mbar and 1×10^{-5} mbar only one phase could be detected. It has proven difficult to obtain a certain identification which of the two phases is present at these pressure values, yet the observed trends indicate, that it should be phase C.

At a coverage of 3 ML both phases (labelled B* and C*) are present, independent of the oxygen pressure during preparation. But with increasing oxygen pressure also an increasing amount of C* could be observed on the surface. From the STM-images it cannot be deduced if this phase-formation is limited to the surface of the ZnO-film or if the two phases are present in all layers, except the 1st one.

No definite explanation of these phenomena could be obtained up to now. Yet with the help of DFT-calculations it has been possible to gain some more insight into possible processes which might lead to the observed surface appearance. On basis of these calculations a “working-model” is proposed, which yielded the most accurate reproduction of the gained data at the time, when this thesis was written.

The DFT-calculations have shown, that a transformation of the ZnO structure (for example into the bulk wurtzite structure) is unlikely. Instead the planar h-BN structure seems to be stable up to 4 ML coverage (see figure 5.16). This structure alone cannot produce the observed differences in apparent height. As a consequence the material forming one of the two 6×6-phases must be different from ZnO. This is supported by the observation that the contrast between B and C depends on the applied bias voltage in STM (figure 5.13). Since phase C appears similar to the first ZnO layer A in the STM-images, but phase B appears different, it is reasonable to assume that B is formed by some other material, whereas phase C consists of ZnO.

Now on the one hand the material, forming phase B, also adopts the 6×6 surface structure of the underlying ZnO but shows a bit more disorder. On the other hand increasing amount of phase C (or C* for higher coverage), could be observed on the surface, with rising oxygen

chemical potential. On basis of this information the following model has been created: it is assumed, that phase B is formed by metallic zinc on top of a ZnO 6×6-structure, whereas phase C corresponds to a regular ZnO-sheet with h-BN structure. With increasing oxygen chemical potential this zinc-film is more likely to be oxidised, thus increasing the amount of phase C, visible on the surface.

To test if metallic zinc can form stable structures on a ZnO-film with h-BN structure, corresponding calculations have been performed by Alessandro Fortunelli and Giovanni Barcaro [wj10]. Their results have shown that a single layer of zinc is indeed stable on a monolayer of ZnO with 6×6-structure on a Pd(111) surface.

In their simulation, the ZnO-monolayer in the slab includes 36 atoms. For the resulting Zn-adlayer however a minimum in the in Gibbs free energy has been found for 38 adatoms with $\Delta G = -2.56$ eV, in comparison to $\Delta G = -2.11$ eV for 36 Zn-adatoms or $\Delta G = -1.91$ eV for 41 Zn-adatoms. As a consequence, the Zn-film in the model adopts the 6×6 surface-structure but it is slightly compressed with respect to the ZnO-monolayer beneath. The compression leads to a decrease in order, as shown in figure 5.30. This is in good agreement with the results obtained for phase B with STM thus strengthening the impression that B is a Zn-phase indeed.

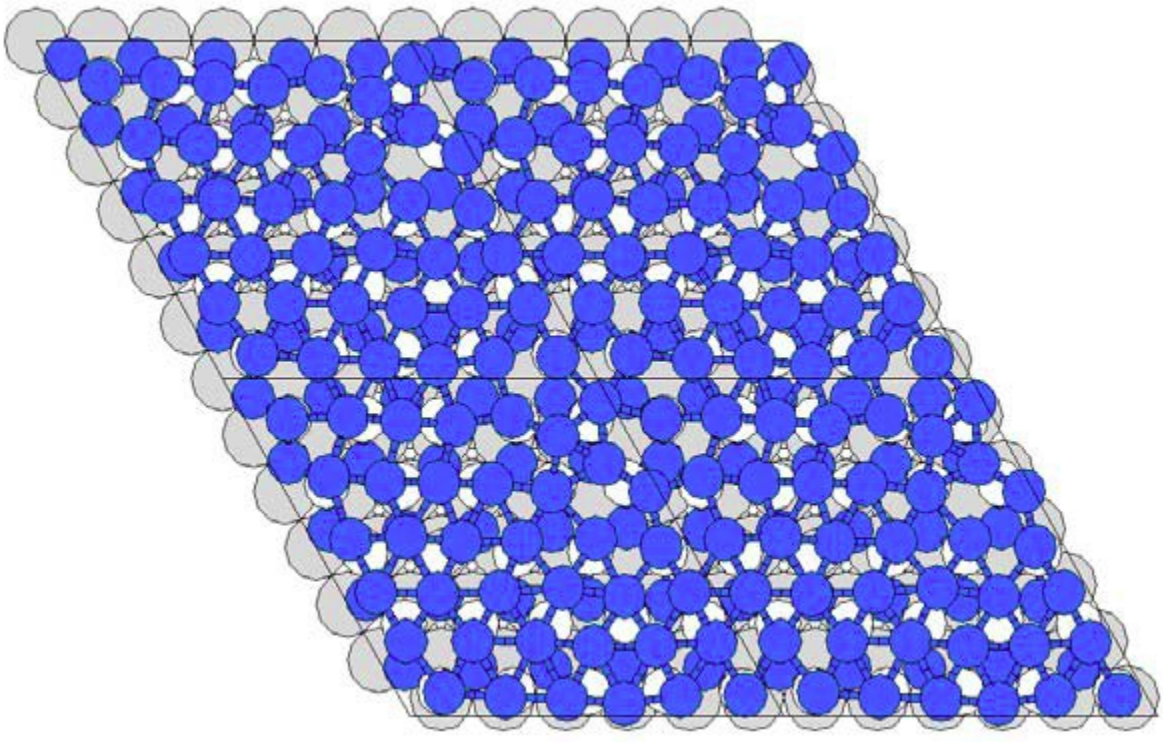

Fig. 5. 30: One monolayer of zinc on top of a single ZnO-layer with h-BN structure on a Pd(111) substrate. Grey spheres represent palladium, blue ones symbolize zinc and white spheres stand for oxygen. In the presented slab, the ZnO layer is made up by 36 atoms arranged in a 6×6-structure. The overlying Zn layer however contains 38 atoms. The resulting compression imposes a small degree of disorder in the Zn-adlayer. Calculations performed by A. Fortunelli and G. Barcaro [wj10].

Although a Zn-adlayer has proven stable in the DFT-simulations, Fortunelli and Barcaro state that it must be stabilized by adsorbates to prevent oxidation, since formation of a regular ZnO-layer is thermodynamically more favourable. This mechanism is assumed to be realistic, since species like hydrogen or carbon-monoxide have been present in the UHV-chamber during the experiments. The composition of this residual gas is a parameter, which cannot be controlled entirely. If this composition however has an influence on the stabilisation of the Zn-adlayers (presumably phase B), it could explain why the experiments at higher oxygen pressures did not yield a unique result to the question if phase B or phase C is present. Yet this is just an assumption.

The presented model reproduces the observed behaviour of the experimentally grown films reasonably well. On the other hand it has not been possible to validate it with the means of STM and LEED. STS measurements on the two phases proved to be too imprecise to allow a distinct characterisation of the corresponding film compositions. Several tests have been performed using pyridine as a probe molecule. In [hj00] it has been stated that pyridine binds more strongly to the Zn-terminated (0001)-surface of a ZnO single crystal, than to the O-terminated $(000\bar{1})$-surface. At room temperature only pyridine on the Zn-terminated surface should be bound strongly enough to be visible in STM, whereas the O-terminated surface should appear void of the probe molecules.

In the experiments performed on the thin ZnO-films however, pyridine did neither bind to B, nor to C. Only an increase of material on Pd could be observed. Although this result does not support the proposed model, it also does not contradict it. Indeed Zn-islands on top of a single layer of ZnO with h-BN structure on top of a Pd crystal have been probed in these experiments. It has already been shown, that the electronic structure of the thin ZnO-films deviates strongly from the one of ZnO-single crystals. Thus it can also be assumed that the electronic structure of the Zn-adatoms has been altered, what might very well result in a different binding of the pyridine molecules.

STM and LEED are well suited to obtain structural information of surfaces, but they cannot yield reliable chemical information. Other methods, sensitive to the composition of the topmost surface layer, like low energy ion scattering (LEIS), should be applied to answer this question. Until such experiments have been performed, the proposed surface construction must be viewed as a “working-model”.

In addition to the process described above, a second mechanism is proposed which might also be at work. As presented in figure 5.9, a few metallic islands could be observed on the surface for coverages up to 1.5 ML, which have been attributed to be Pd-adislands. As shown in figure 5.31, these metallic islands may give rise to a “quasi” phase C, when they are covered by a single layer of ZnO. In STM a distinction between “real” and “quasi” phase C is not possible. The process which gives rise to the metallic islands is not totally clear. Etching or (non-stoichiometric) alloying with zinc are possible pathways which might lead to their emergence. Yet the amount of metallic islands on the surface is typically low and consequently “quasi” C-islands are viewed to form a minority phase only.

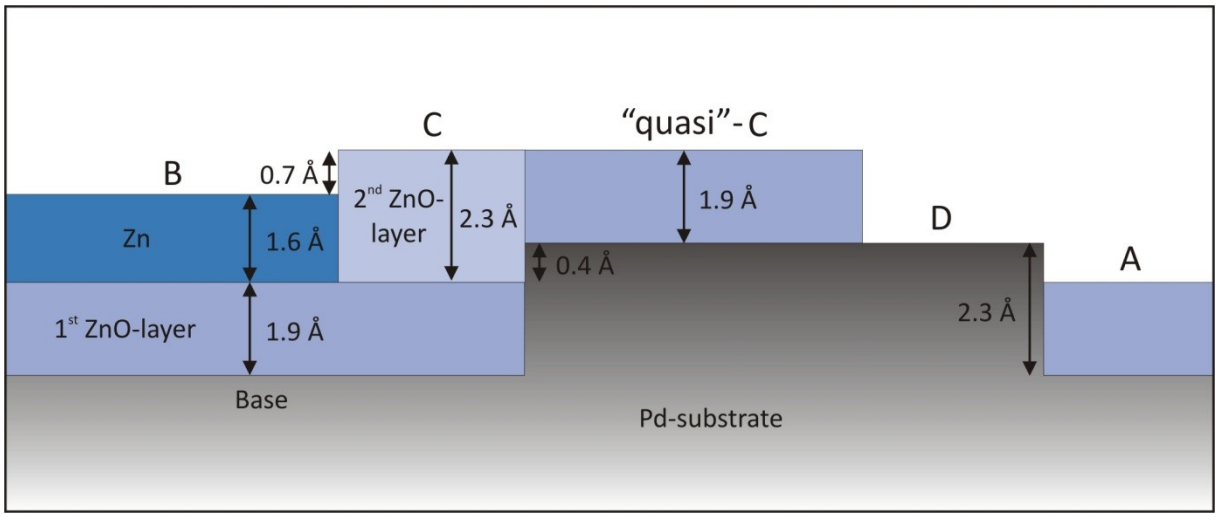

Fig. 5. 31: Formation of "quasi" C-islands by adsorption of a single ZnO-layer on top of a Pd-adisland. Legend: A - 1st ZnO-layer, B – Zn on ZnO, C – 2nd ZnO layer. Since the "real" C-phase has a similar apparent height as the Pd-islands and C shows the same surface appearance as A, a distinction between real and quasi C-islands is not possible with STM.

5.5 Summary

In this chapter, the morphology and structure of thin ZnO-films on a Pd(111) substrate have been investigated, as functions of coverage and oxygen chemical potential. Moreover the thermal decomposition of the resulting films and the reduction with hydrogen have been examined.

To investigate structure and growth, ZnO films have been grown on Pd(111) at an oxygen pressure of 5×10^{-7} mbar and an annealing temperature of 550 K. Post oxidation has typically been used for ZnO-coverages up to 1 ML and reactive evaporation for higher coverages.

In the submonolayer regime ZnO adopts three different phases. The first one is open and forms hexagonal, honeycomb-like unit cells. The lattice constant and apparent height of this structure have been found to be (10.5 ± 0.3) Å and (1.3 ± 0.3) Å respectively. Each side of the hexagons shows three maxima in STM with a distance of (3.1 ± 0.3) Å. DFT calculation revealed, that this structure is stabilized by hydrogen and corresponds to $Zn_6(OH)_5$. Bright spots in the STM are created by oxygen states. Since the lattice constant of this structure is about four times the one of the Pd(111)-substrate, it is addressed as "4×4". The 4×4 structure is quite instable and easily disintegrates in the LEED beam or during STM-scans.

The second phase is much more stable and forms denser islands with a hexagonal surface unit cell. Lattice constant and layer height are (3.3 ± 0.1) Å and (1.9 ± 0.3) Å respectively. This phase forms a coincidence structure on the Pd(111) surface with $6 \cdot |\vec{a}_{Pd}| = 5 \cdot |\vec{b}_{ZnO}|$. This gives rise to a moiré structure with a lattice constant of (16.2 ± 0.8) Å and a p(6×6) LEED-signal. Due to these reasons this structure is addressed as "6×6". DFT calculations revealed that the

ZnO in this phase adopts a planar h-BN structure instead of the bulk wurtzite geometry. Bright spots in STM again stem from oxygen states.

The third phase consists of monoatomic rod-like molecules which fill up the uncovered Pd-surface between islands. These molecules are considered to be a dissociation product of one or both of the other two phases.

For coverages larger than one monolayer only the 6×6 structure can be observed. Up to three monolayers ZnO grow in a Frank-van-der-Merve-like fashion (layer-by-layer). At higher coverage a transition to Volmer-Weber growth (island growth) could be detected.

DFT-calculations predict a planar h-BN structure for the first four ZnO-adlayers on Pd(111). Yet in the coverage-regime between one and two layers, two different kinds of islands could be observed on top of the 1st ZnO-layer, labelled A. C-islands show an apparent height of (2.3 ± 0.3) Å with respect to A and have display a surface similar to the one of the 1st ZnO-layer. These islands are supposed to be the next ZnO-layer. B-islands show a reduced apparent height of (1.6 ± 0.2) Å with respect to A and display a rougher surface with more unordered 6×6-symmetry. It is proposed that these islands correspond to zinc adlayers on top of the 1st ZnO-layer. DFT-calculations have shown that such Zn-monolayers are indeed stable and show a slightly disordered 6×6-structure, due to a small compression. These predictions are in good agreement with the observed data. Calculations however showed that other adsorbates are needed to stabilize the Zn-layer in oxygen atmosphere. Similar observations and interpretations have been made for a coverage of three monolayers of ZnO, where the two phases have been labelled B* and C*.

To test the dependence on the oxygen chemical potential, ZnO films with varying thickness have been prepared at different oxygen pressures: 5×10^{-8} mbar, 1×10^{-7} mbar, 1×10^{-6} mbar and 1×10^{-5} mbar. Two different approaches have been taken for each of the four pressure values: In procedure I a new ZnO-film has been prepared for each pressure and coverage value, in procedure II the ZnO-films have been prepared at the lowest oxygen pressure and reoxidised at the higher values. Results have been obtained by comparison of both methods.

In the submonolayer regime, the 6×6-islands display a distinct defect structure at the lowest oxygen pressure, accompanied by an increase in apparent height to (2.3 ± 0.6) Å. The defect structure is attributed to oxygen vacancies and manifests in the formation of triangular pits and a resulting modification of the moiré-structure. By increasing the oxygen pressure to 1×10^{-7} mbar both, defect structure and increased apparent height, diminish. Further increase to 1×10^{-6} mbar and higher leads to a change in growth mode of the 6×6-islands. At this pressures bilayer islands are formed due to chemisorbed oxygen on the Pd(111)-surface. The 4×4-islands remain stable and unchanged up to an oxygen pressure of 1×10^{-6} mbar. At 1×10^{-5} mbar however a transformation into 6×6-bilayer can be observed.

For higher coverages similar observations can be made. Additionally an increasing amount of C-islands (C*-islands) can be observed, which is attributed to oxidation of the Zn-adlayers (B- and B*-islands).

To study the thermal decomposition, ZnO-films have been prepared at high oxygen pressures (1×10^{-6} mbar and 1×10^{-5} mbar) for two coverages (0.7 ML and 1.5 ML). These films have subsequently been annealed in UHV and characterized with LEED and STM after each annealing step. These investigations have been assisted by temperature programmed desorption (TPD)-experiments, performed by Frederik Weber.

For 0.7 ML ZnO-coverage a decomposition of the 4×4-islands can already be observed at 400 K. At 450 K, the 6×6-islands decompose and a 2×1 PdZn alloy is formed. This alloy also disintegrates upon heating up to 600 K. The corresponding TPD-analysis shows that Zn does not desorb at these temperatures but diffuses into the bulk of the Pd-crystal. Further annealing to 1020 K is needed to remove the zinc from the sample.

At 1.7 ML ZnO-coverage, the decomposition of the oxide proceeds more slowly. Although large morphological changes take place, 6×6-islands can still be found on the surface at 750 K. The corresponding TPD-spectra reveal, that oxygen desorbs from the surface between 600 and 900 K. Zn again diffuses into the bulk and can be removed by annealing to 1020 K.

To investigate the stability of the ZnO films in hydrogen atmosphere, 0.7 ML of ZnO have been deposited onto the Pd(111) surface at an oxygen pressure of 5×10^{-7} mbar and an annealing temperature of 550 K. Afterwards molecular hydrogen has been dosed onto the sample in situ and the corresponding changes have been recorded with STM. A submonolayer coverage has been chosen for this test, to provide enough Pd surface-area to dissociate the molecular hydrogen into its atomic components.

The result of this investigation is that both, 4×4- and 6×6-islands, show a high stability in hydrogen atmosphere. No reduction of the ZnO could be observed, only a partial transformation of 4×4- into 6×6-islands, at 30 L of molecular hydrogen, dosed onto the sample.

Chapter 6: ZnO/CoO-mixed films

Mixed ZnO/CoO films have attracted the interest of the scientific community due to their magnetic properties [oe08, ds00, dp07, dp06, cn05, dn06, mp09]. An important feature, in this context, is the formation of ferromagnetic CoO-nanoclusters within those films. This construct might prove useful for future data-storage-devices. In a recent study by Meyerheim [mp09] it had been shown that CoO forms wurtzite-type nanocrystals within a planar h-BN ZnO matrix on Ag(111). Since ZnO adopts a similar planar structure on Pd(111), experiments have been performed to test if such a formation of CoO-islands can also be observed for this system. The results of this study, obtained with LEED and STM, are presented in this chapter.

6.1 CoO on Pd(111)

Before mixed films could be prepared, the structure of CoO on a Pd(111) substrate had to be investigated. For this purpose thin CoO-films have been grown at different coverages. The preparation of the CoO-films was similar to that of ZnO, by using the post-oxidation method. The experiments showed that CoO orders better if it gets annealed to temperatures around 620 K in oxygen atmosphere, instead of 550 K, as used for ZnO. The characterisation of the films has been performed with LEED and STM.

The results for a coverage of 0.2 ML are presented in figure 6.1. The film has been prepared by post-oxidation at an annealing temperature of 550 K and an oxygen pressure of 1×10^{-6} mbar. The CoO has formed bilayer-islands exposing hexagonal shapes with alternating side lengths. The corresponding layer heights are listed in table 6.1. It should be noted, that this measurement has proven difficult for the 1st layer - a layer height, comparable to those of the other layers, might be more appropriate. The second layer appears better ordered than the first one, displaying a pronounced moiré structure with a periodicity of (22 ± 2) Å. The appearance of the moiré effect indicates, that CoO forms a coincidence structure on Pd(111) with a lattice constant of about 3.1 Å. This value is in good agreement with the one obtained by direct measurement (table 6.1). The visible part of the 1st layer shows a high degree of disorder. Yet the moiré pattern in the 2nd layer implies a better order of the 1st layer underneath. In the LEED-image no distinct CoO-spots could be detected. Only a weak network of lines with hexagonal shape appeared, connecting the Pd(111)-spots.

Figure 6.2 shows the appearance of the CoO-surface in STM at 1.7 ML coverage. In this preparation post oxidation has been used at an annealing temperature of 650 K and an oxygen pressure of 1×10^{-6} mbar.

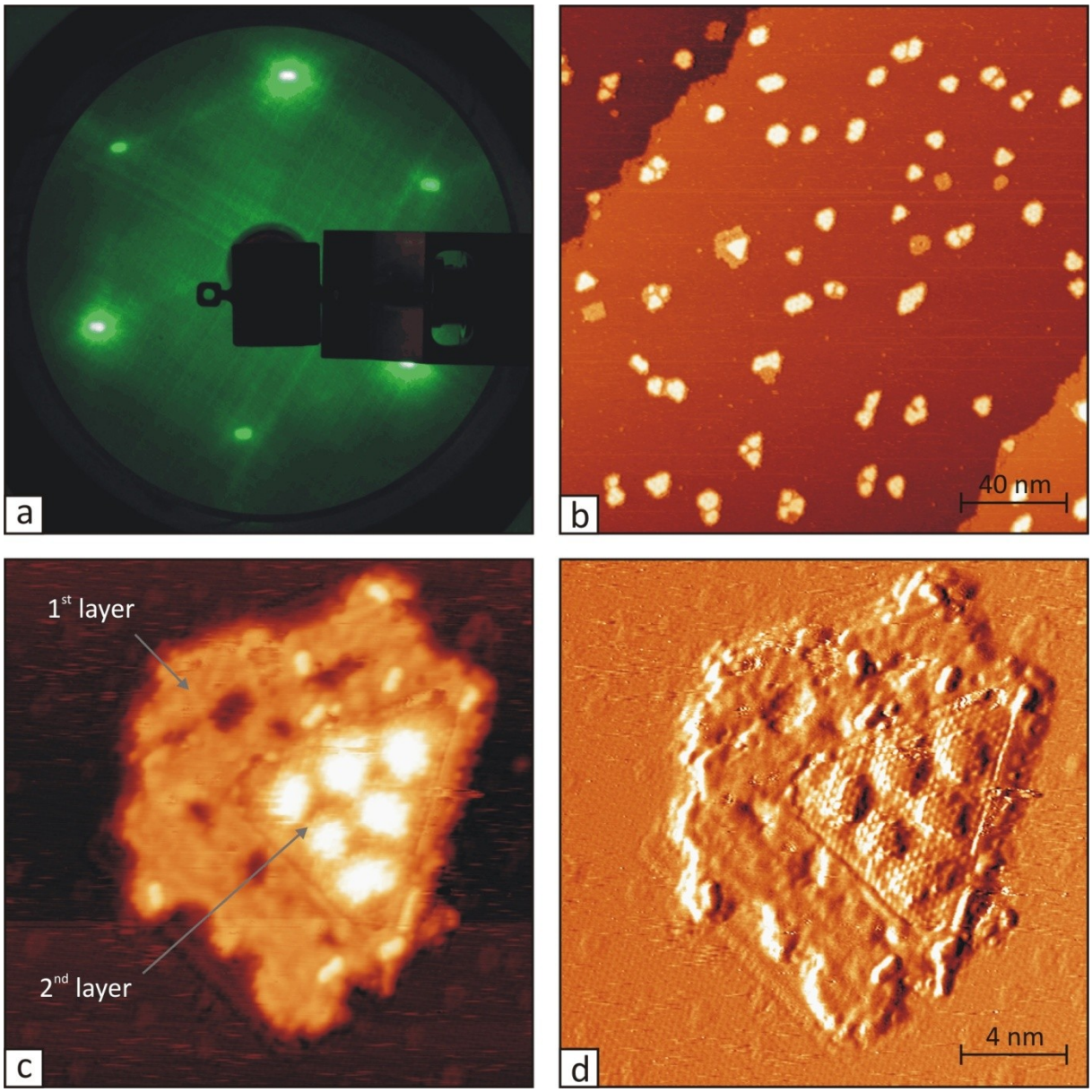

Fig. 6. 1: Results for 0.2 ML of CoO on Pd(111). Bilayer islands emerge, showing hexagonal shapes with alternating side-lengths. The visible part of the 1st layer appears unordered, whereas the 2nd layer shows a high degree of order, including the formation moiré pattern with large contrast. (a) LEED image, taken at E_B =85.6 eV; (b) (200 × 200) nm^2 STM-scan, U = +1.0 V, I = 0.1 nA; (c) (20 × 20) nm^2 STM-scan, U = +0.25 V, I = 1.0 nA; (d) Differential image of (c).

	Apparent height	Moiré constant	Calc. lattice constant	Meas. lattice constant
1st layer	2.2 ± 0.3	-	-	2.7 ± 0.2
2nd layer	2.6 ± 0.2	22 ± 2	3.1 ± 0.1	3.3 ± 0.3
3rd layer	2.6 ± 0.2	26 ± 1	3.1 ± 0.1	2.6 ± 0.4
4th layer	2.6 ± 0.2	-	-	-

Table 6. 1: Experimentally obtained values for CoO. The calculated lattice constants have been derived from the corresponding moiré constants. The measured lattice constants have been obtained directly via high resolution-STM. All values are given in Å. For comparison: the bulk lattice constant of CoO(111) amounts to 3.01 Å.

The 1st monolayer is completely closed, the 2nd layer is half-filled. 3rd-layer islands are visible and in some places already traces of the 4th layer can be found. The corresponding layer heights are again listed in table 6.1. In the LEED-image the network of lines has gained in intensity. In the 1st layer two CoO phases can be detected. Most of the layer exposes a

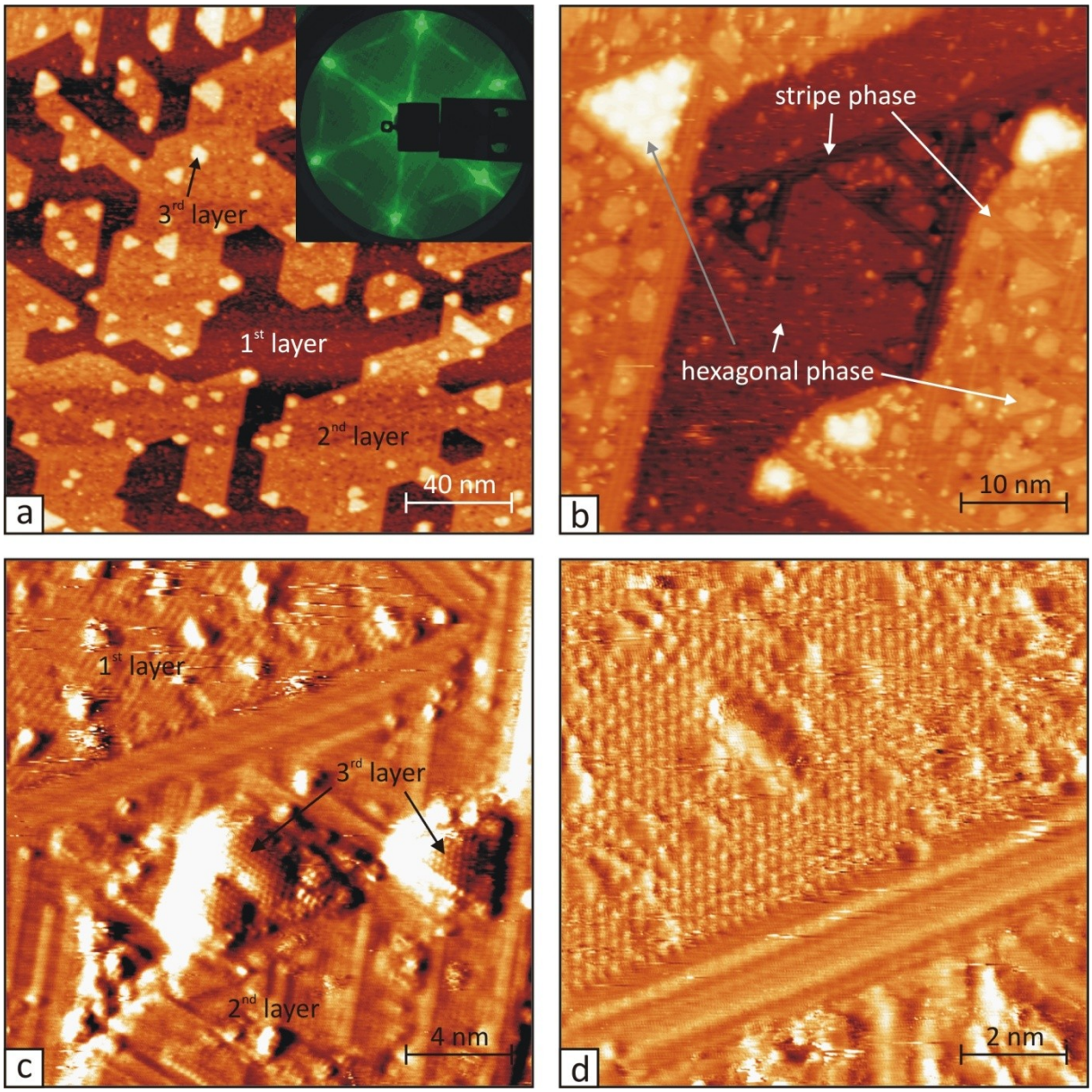

Fig. 6. 2: Results for 1.7 ML of CoO on Pd(111). Two phases can be detected on the surface: a hexagonal phase and a stripe phase. In the 1st layer the hexagonal phase is dominant, interspersed by domains showing the stripe phase. In the 2nd layer the stripe phase is dominant. 3rd layer islands only expose the hexagonal phase. (a) (200 × 200) nm² STM-scan showing the morphology of the surface; U = +1.0 V, I = 0.1 nA ; inset: LEED image, taken at E_B =66.5 eV. (b) (50 × 50) nm² STM-scan, resolving the two different CoO-phases; U = +1.0 V, I = 0.1 nA. (c)) (20 × 20) nm² differential STM-image showing both phases in more detail; Upper half: 1st layer, lower half: 2nd layer and a 3rd-layer island; U = +0.3 V, I = 2.0 nA. (d) (10 × 10) nm² differential STM-image of the 1st layer revealing the atomic structures of the two phases; U = +0.1 V, I = 2.0 nA.

hexagonal structure, comparable to the one seen for the 2nd layer at 0.2 ML coverage. Direct measurement of the lattice constant produces a value of (2.7 ± 0.2) Å. Yet doubt arises, concerning the accuracy of this number: in the third layer a moiré pattern with 26 Å-periodicity can be observed, yielding a lattice constant of 3.1 Å, whereas direct measurement of the same lattice constant gives a value of 2.6 Å. Since the moiré-measurement is the more reliable method, the values obtained by direct measurement must be regarded with some caution.

The areas, showing the hexagonal structure, in the first layer do not show any moiré-pattern. But these areas also do not appear homogeneous – they are strewn with clusters and vacancies, which might prevent the formation of a regular moiré pattern.

The second observable phase is a stripe-structure running along the main directions of the substrate and separating areas with hexagonal structure. The stripes appear lower than the other phase by (0.9 ± 0.3) Å. The normal distance between the stripes could be determined to be (3.1 ± 0.6) Å.

Both phases are also observable in the 2nd layer, but there the stripe-phase is the dominant one, as shown in figure 6.2b. Areas with hexagonal structure appear as islands with hexagonal shapes, close to triangles, which are slightly higher than the stripes by (1.2 ± 0.2) Å. The layer heights, listed in table 6.1, have all been measured between the hexagonal phases of different layers.

Third-layer-islands only show the hexagonal structure, with a clear moiré pattern. The shapes of those islands correspond again to hexagons with alternating side-lengths. The same is true for fourth-layer-islands.

Since the amount of CoO in the mixed films is generally low, the results, obtained for 0.2 ML coverage, are more important for the experiments, which will be presented in the next section.

6.2 Zn(1-x)Co(x)O-mixed films

Several experiments have been performed to produce and characterize mixed ZnO/CoO-films. The aim of those experiment has been to clarify if CoO-islands can separate from the ZnO-matrix on a Pd(111) surface, as suggested in [mp09]. If a separation of these two materials takes place, it should be possible to identify CoO-islands with STM, due to their characteristic structure. The lattice constants of CoO and ZnO are not well suited, to distinguish between the two oxides, since they show almost similar values.

Three approaches have been taken to prepare such a phase-separated film: ZnO-deposition followed by addition of CoO, co-deposition of the two oxides and CoO-deposition followed by addition of ZnO. Additionally, the preparation parameters like annealing-temperature, oxygen-pressure and Zn- and Co-concentration have been varied.

In case of the first two approaches, no distinct CoO-islands could be found within the ZnO matrix. In figure 6.3 an example for such a preparation is given. In this case the ZnO-film has been grown first (figures 6.3a and b), then Co has been deposited onto this film (figures 6.3c and d) and finally the sample has been annealed in oxygen atmosphere (figures 6.3e and f). Although the Co-clusters could be easily recognized after the second preparation-step, the ZnO- and CoO-phases could not be distinguished any more after oxidation. LEED-pattern,

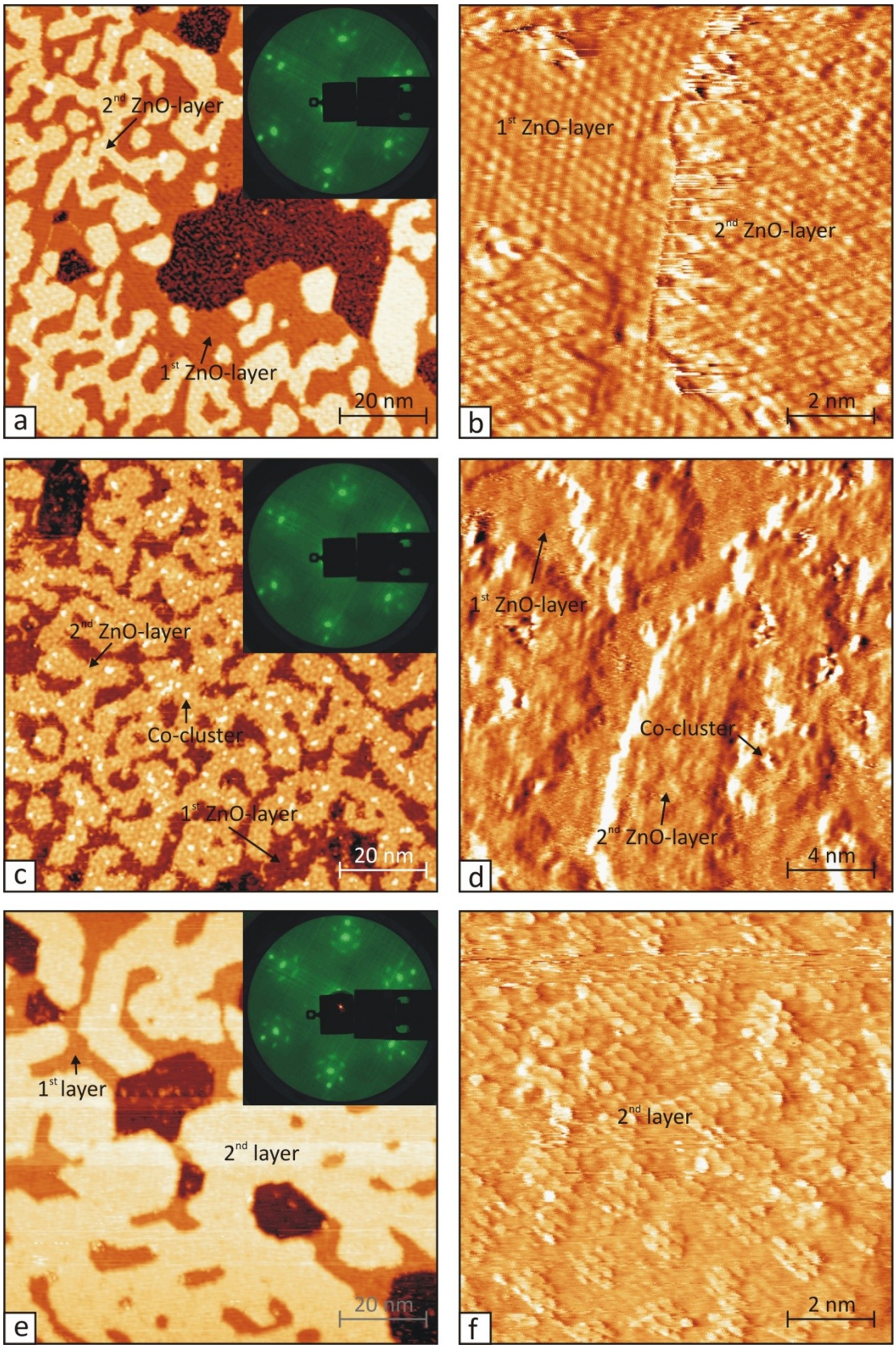

Fig. 6. 3: Preparation of a mixed ZnO/CoO-film with 1.7 ML coverage by deposition of Co onto ZnO. (a) and (b): 1.4 ML ZnO, prepared by post oxidation at 550K and 1 × 10^{-7} mbar O_2; (c) and (d): 0.3 ML Co on top of the ZnO-film; (e) and (f): mixed surface after annealing to 620 K at 5 × 10^{-7} mbar O_2. The sample has first been annealed to 550 K at the same oxygen pressure, which yielded a similar result as shown in (e) and (f). (a), (c) and (e): (100 × 100) nm^2 STM-scans, U = +1.0 V, I = 0.1 nA, insets: LEED images, taken at E_B =63.4 eV; (b): (10 × 10) nm^2 differential STM-image, U = +0.3 V, I = 1.0 nA; (d) (20 × 20) nm^2 differential STM-image, U = +0.3 V, I = 3.0 nA; (f) (10 × 10) nm^2 differential STM-image, U = +0.1 V, I = 5.0 nA.

morphology and atomic structure of the resulting film have been similar to those of ZnO. No unambiguous traces of a CoO-phase could be found. Variation of the preparation parameters and co-deposition of the two materials lead to similar results.

The third approach however produced the desired result. This time CoO-island have been grown on the Pd(111)-surface first, then the ZnO-matrix has been added. The results are presented in figure 6.4. (a) and (b) show the Pd(111)-surface with 0.3 ML of CoO, prepared by post-oxidation at an oxygen pressure of 1×10^{-6} mbar and an annealing temperature of 620 K. The CoO shows the typical appearance: bilayer islands, exposing hexagonal shapes with alternating side lengths. The 2nd layer is highly ordered, showing traces of a moiré-pattern. The visible part of the 1st layer appears badly ordered. The apparent heights are (2.5 ± 0.2) Å for the 1st layer and (2.6 ± 0.2) Å for the 2nd layer, resulting in a total island height of (5.1 ± 0.4) Å. From high resolution STM-scans a lattice constant of (3.4 ± 0.2) Å could be extracted for the 2nd layer. In the LEED only Pd(111)-spots are visible.

In the second preparation step, zinc has been deposited onto the sample surface in UHV and oxidized at 550 K and 5×10^{-7} mbar O_2. The corresponding results are shown in figures 6.4c and d. Around the CoO-islands a well ordered ZnO-film has formed. The total apparent coverage amounts to 1.5 ML (20% CoO in the film). Most of the ZnO is located in the 1st layer, which covers 96% of the surface. An apparent height of (1.7 ± 0.2) Å and a lattice constant of (3.3 ± 0.1) Å could be determined for this ZnO-layer. On top of it some 2nd layer ZnO-islands have formed. The largest of them are situated around CoO-islands, an indication that the CoO forms nucleation centres for the ZnO. The parameters for the 2nd ZnO-layer are an apparent height of (1.7 ± 0.1) Å and a lattice constant of (3.4 ± 0.1) Å. The total height of both ZnO layers is 3.4 Å, which is 1.7 Å lower than the height of the CoO-islands. That allows an easy identification of CoO. The measured height difference between the 2nd layers of ZnO and CoO is (1.6 ± 0.2) Å. The CoO-islands themselves appear unchanged, showing the typical shapes and layer height.

According to [mp09], the pronounced height difference between ZnO and CoO can be interpreted in a way that ZnO adopts a planar h-BN structure whereas CoO crystallizes in a wurtzite structure with a comparable surface unit cell. Yet from the information, gained with STM and LEED, it cannot be decided with certainty if CoO really adopts a wurtzite-structure or crystallizes in its NaCl-bulk-structure. In some places an additional layer could be found on top of CoO-islands with an apparent height of (2.0 ± 0.4) Å and a lattice constant of (3.4 ± 0.1) Å. Since ZnO and CoO have not mixed, the additional layer can be attributed to a ZnO-layer on top of a CoO-bilayer-island. In the LEED a p(6×6)-pattern could be observed.

In a final step the sample has been annealed at 620 K at an oxygen pressure of 5×10^{-7} mbar. The corresponding images are shown in figures 6.4e and f. The film has changed considerably. Generally a higher degree of order can be observed resulting in islands with hexagonal geometry. But it cannot be distinguished between ZnO and CoO any more. Three layers can be found with STM. The 1st layer has an apparent height of (2.6 ± 0.2) Å and a lattice constant of (3.3 ± 0.3) Å, the 2nd layer shows an apparent height of (2.1 ± 0.2) Å and a

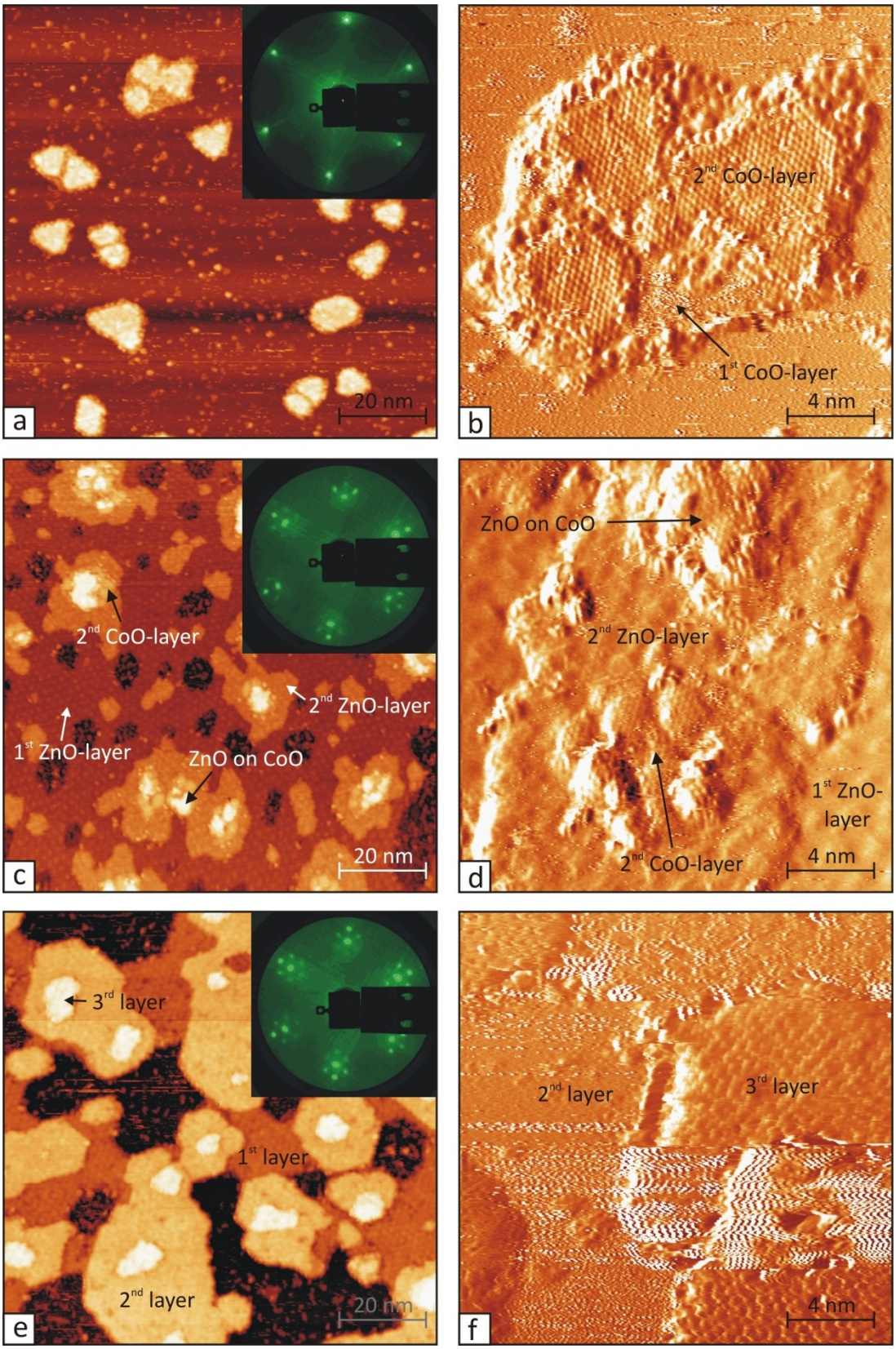

Fig. 6. 4: Preparation of a mixed ZnO/CoO-film with 1.5 ML coverage by deposition of ZnO onto CoO. (a) and (b): 0.3 ML CoO on Pd(111), prepared at 620 K and 1 × 10^{-6} mbar O_2; (c) and (d): addition of 1.2 ML ZnO, oxidized at 550 K and 5 × 10^{-7} mbar O_2; (e) and (f): mixed surface, annealed at 650 K and 5 × 10^{-7} mbar O_2. (a), (c) and (e): (100 × 100) nm^2 STM-scans, U = +1.0 V, I = 0.1 nA, insets: LEED images, taken at E_B =66.8 eV; (b): (20 × 20) nm^2 differential STM-image, U = +0.3 V, I = 1.5 nA; (d) (20 × 20) nm^2 differential STM-image, U = +1.0 V, I = 1.0 nA; (f) (20 × 20) nm^2 differential STM-image, U = +0.3 V, I = 1.0 nA.

lattice constant of (3.3 ± 0.3) Å. For the 3rd layer only the height could be determined with a value of (2.1 ± 0.3) Å. The third layer is scarcely populated, with a layer-coverage of only 5%. It is assumed that the positions of the 3rd layer islands correspond to those of the former CoO-islands. In the LEED a p(6×6)-pattern can be observed. The change in layer heights and the uniform appearance of the layers indicate that a mixing of ZnO and CoO has taken place at the applied annealing temperature. Thus the film can be considered to be Zn(0.8)Co(0.2)O.

6.3 Summary

In this chapter the preparation of ZnO/CoO-mixed films has been discussed. The aim of the investigation has been to clarify if separated CoO-islands can be formed within a ZnO-matrix on Pd(111).

In the first part of the chapter, the behaviour of pure CoO on Pd(111) has been examined. A tendency to form bilayer-islands has been observed at low coverage. The islands developed characteristic hexagonal shapes with alternating side lengths. Apparent layer heights of 2.6 Å and a surface lattice constant of 3.1 Å could be extracted from the available data. At higher coverage a tendency towards Volmer-Weber- or Stranski-Krastanov-like growth could be observed. Different phases of CoO emerged, showing either a compact hexagonal appearance with a lattice constant of 3.1 Å or the formation of stripes along the main substrate directions. The stripe phase appeared to be about 1 Å lower than the hexagonal phase.

Three methods have been used to prepare ZnO/CoO the films: Deposition of ZnO followed by addition of CoO, deposition of CoO followed by addition of ZnO and simultaneous deposition of both materials. The first and the last method resulted in films, where partial or total mixing of the oxides occurred.

Deposition of CoO onto Pd(111) with subsequent addition of ZnO, on the other hand, produced the required result at annealing temperatures of 550 K during Zn-oxidation. Distinct CoO-islands could be observed, surrounded by ZnO. The observed surface unit cells and lattice constants have been similar for both materials, yet CoO adopted a different structure than ZnO, resulting in larger apparent layer-heights of 2.6 Å. These result are comparable to those for ZnO/CoO-mixed layers on Ag(111) [mp09].

Higher annealing temperatures of 620 K, during Zn-oxidation, however lead to a mixing of the two materials. The resulting Zn(1-x)Co(x)O-layers show a 6×6-coincidence structure, like ZnO, but expose a 20% larger layer thickness than the one of undoped zinc-oxide.

Summary

The motivation for this thesis was the good catalytic performance of Pd-ZnO surfaces in methanol steam reforming for hydrogen generation. The formation of a PdZn alloy at the metal-oxide interface has been identified to play a major role in this context. To investigate the structural properties of this system, reverse model catalysts are built, consisting of thin ZnO-layers on a Pd(111) surface and of PdZn(111) surface alloys on a Pd(111) support, respectively. These model systems allow the analysis with surface science techniques, which provide valuable data about the structural composition in the catalytic active interface region. The (111)-surfaces are of special interest, since they show high probability to appear in technical catalysts. Nonetheless the surface structures of PdZn(111) surface alloys and of ZnO-films on Pd(111) have not yet been determined in detail. In the case of the bimetallic alloy, the formation of a p(2×1) or a p(2×2)-3Zn structures has been proposed. For ZnO on Pd(111) no structural data has been available. Yet this very surface is of special interest, because ZnO is likely to exhibit one of its polar surfaces due to symmetry matching reasons. That allows the study of the polarity-compensation mechanisms in the finite thin-film system. Moreover doping the thin ZnO films with Co opens the door to the field of diluted magnetic semiconductors, which are of importance for spintronic devices. In this context the possible formation of ferromagnetic CoO-islands within a nonmagnetic ZnO-matrix was of special interest. Thus the three subjects, treated within this thesis, are the structure of PdZn(111) surface-alloys and adjacent Zn-layers, the structure of ZnO-films grown on Pd(111) and the phase separation in ZnCoO mixed films. The corresponding surface-analysis has been performed by a combination of scanning tunnelling microscopy (STM) and low energy electron diffraction (LEED), assisted by density functional theory (DFT) calculations which have been performed by co-workers. [ia95, ib98, wp01, tp07, mp09, kp06]

The PdZn(111) surface alloy has been created by Zn-deposition onto a Pd(111) substrate. It has been observed, that a stable 1:1 surface-alloy of the two metals forms already at room temperature (or slightly higher temperature, due to the thermal energy of the deposited Zn-atoms). The investigation with STM revealed the formation of a p(2×1) structure, consisting of alternating rows of Zn- and Pd-atoms. The alloy phase adopts a bilayer-structure with dentritic island-shapes. The observed (2×2)-signal in LEED emerges due to three domains with the stripes running along the equivalent surface directions of the Pd(111)-substrate - $\langle 01\bar{1}\rangle$, $\langle 10\bar{1}\rangle$ and $\langle \bar{1}10\rangle$. Further deposition of Zn has led to the formation of (1×1) Zn-adlayers on top of the PdZn-bilayer. DFT-calculations revealed that the binding energy of the first Zn-adlayer differs greatly from those of the rest due to the presence of Pd in the alloy underneath [wj09, ks10]. This leads to a characteristic desorption spectrum, as measured with temperature programmed desorption (TPD)-experiments [wj09]. Accompanied by auxiliary experiments with LEED and STM, it could also be shown that Zn tends to diffuse into the bulk of the Pd-single crystal, thus further complicating the desorption spectrum.

Removal of the Zn from the bulk is not possible until annealing temperatures around 1000 K are reached [wj09].

To prepare ZnO-layers on Pd(111), post-oxidation and reactive evaporation have been employed at standard conditions of $p_{O2} = 5 \times 10^{-7}$ mbar and $T_{anneal.} = 550$ K. Post-oxidation has been used for submonolayer coverage, and reactive evaporation for higher film-thickness. In the coverage regime below 1 ML, two distinct structures have been identified. The first one is an open, honeycomb-like mesh corresponding to p(4×4)-superstructure, with a lattice constant of (10.5 ± 0.9) Å and an apparent height of (1.3 ± 0.3) Å at U = +1.0 V. The DFT-calculations revealed, that this structure is hydrogen-stabilized, forming a polar $Zn_6(OH)_5$-complex. The 4×4-stucture exhibits a low binding energy, which is expressed by fast disintegration in the LEED electron beam and easy manipulation in the STM-experiments. The second phase forms a 5/6-coincidence structure on top of the Pd(111)-surface, with a lattice constant of (3.3 ± 0.1) Å and an apparent height of (1.9 ± 0.3) Å at U = +1.0 V. The lattice mismatch between this structure and underlying Pd(111)-substrate amounts to 20%. The coincidence structure gives rise to a moiré-pattern with a periodicity of (16.2 ± 0.8) Å, which is responsible for the observation of a p(6×6)-pattern in LEED. As a consequence, this structure is labelled “6×6”. The surface geometry of the 6×6-structure corresponds to the one of ZnO(0001) or ZnO(000$\bar{1}$), which are both polar. The polarity is caused by an arrangement of zinc- and oxygen-atoms in discrete planes, which are separated by a distance of 0.63 Å along the [0001]-direction. DFT-calculations for the observed 6×6-structure however showed, that the ZnO relaxes, forming a planar h-BN structure. Thus the surface dipole-moment is eliminated. The DFT-calculations revealed further, that oxygen states are imaged in STM at the applied bias voltages ≤ +1.0 V of for both structures.

To test the influence of the oxygen-chemical potential, ZnO-films have also been prepared at oxygen pressures of 5×10^{-8} mbar, 1×10^{-7} mbar, 1×10^{-6} mbar and 1×10^{-5} mbar. In the low pressure regime (5×10^{-8} mbar and 1×10^{-7} mbar), the 4×4- and 6×6- single layer structures coexist. At the lowest oxygen pressure of 5×10^{-8} mbar a distinct defect structure could be observed, created by oxygen vacancies, which is accompanied by an increase in apparent height to (2.3 ± 0.6) Å. In the high pressure regime (1×10^{-6} mbar and 1×10^{-5} mbar) an explicit structural change takes place. At these oxygen pressures the 6×6-structure tends to form bilayer-islands with an apparent height of (4.2 ± 0.7) Å at U = +1.0 V. At the highest chemical potential also the 4×4-structure transforms into these 6×6-bilayers. The DFT-calculations revealed that the reason for this behaviour is the formation of chemisorbed oxygen on the Pd(111)-surface, thus making the formation of the 6×6-bilayer-islands energetically favourable.

In the coverage regime above 1 ML only the 6×6-structure can be observed in LEED but STM reveals two different phases: one with an apparent height of (1.6 ± 0.2) Å, labelled $B^{(*)}$, and one with an apparent height of (2.3 ± 0.3) Å, labelled $C^{(*)}$, measured at U = +1.0 V. Both phases exhibit the typical unit cell of the 6×6-structure, yet $B^{(*)}$ shows a higher surface-roughness and a poorer structural order. Change of the oxygen pressure during preparation

showed, that $B^{(*)}$ is dominating the surface in the low pressure regime (5×10^{-8} mbar and 1×10^{-7} mbar), whereas $C^{(*)}$ is dominant in the high pressure regime (1×10^{-6} mbar and 1×10^{-5} mbar). DFT-calculations have shown that metallic zinc can form stable adlayers on top of a 6×6-ZnO-film and this structure has been ascribed to the $B^{(*)}$ phase. In the DFT model the Zn-adlayer adopts the unit cell of the 6×6-structure but appears a bit more disordered due to slight compression. For the first four layers DFT also predicts that ZnO adopts the planar h-BN structure over a large oxygen chemical potential range. This structure has been attributed to the C(*) phase, which grows in a layer-by-layer (Frank van der Merve) manner. At higher coverage a transition to Volmer Weber (island-) growth has been observed.

For application in catalysis also the stability of the model catalyst at elevated temperatures and in hydrogen atmosphere is relevant. Two sets of experiments have been performed to test the stability of ZnO-layers on Pd(111). In the first set, the thermal decomposition of thin ZnO-layers has been investigated. The ZnO layers have been prepared at elevated oxygen pressures (1×10^{-6} mbar and 1×10^{-5} mbar) and subsequently annealed in UHV. These experiments have been accompanied by corresponding TPD-experiments. In the submonolayer regime a decomposition of the 4×4-structure could be observed already at 400 K, followed by the decomposition of the 6×6-structure at 600 K. At 1.5 ML coverage the ZnO-film has been stable up to 750 K. The TPD-measurements showed that oxygen desorbs from the sample between 600 and 900 K. The most important result of this investigation was the observation of a 1:1 PdZn alloy forming during the thermal decomposition of ZnO, as proved by the characteristic (2×2) LEED-pattern. For the stability-test in hydrogen atmosphere a submonolayer ZnO-film has been grown at an oxygen pressure of 1×10^{-7} mbar and subsequently exposed to increasing amounts of hydrogen up to 30 L. The test showed that 4×4- and 6×6-structure both show a high resistivity against reduction by hydrogen. The only reaction of the system was a partial transformation of 4×4 into 6×6 at an exposure of 30 L.

For the investigation of the mixed films, preliminary experiments have been conducted to gain information on the structure of CoO on Pd(111). The CoO-films have been grown by the same procedure as ZnO at an oxygen pressure of 1×10^{-6} mbar. Well-ordered films could be obtained by increasing the annealing temperature from 550 K to 620 K. For a layer-thicknesses of 1.7 ML, CoO exposed two different phases. The first phase shows a hexagonal structure, with a lattice constant of (3.1 ± 0.1) Å, which is in good agreement with the value of 3.01 Å of CoO(111). The apparent height of this phase amounts to (2.6 ± 0.2) Å at U = +1.0 V. Since the step height on a CoO(111)-surface is 2.46 Å it cannot be deduced if the CoO thin film adopts the rock-salt structure or relaxes into a wurtzite-structure as proposed in [mp09]. The second phase forms stripes separated by a distance of (3.1 ± 0.6) Å and appears (0.9 ± 0.3) Å lower than the hexagonal phase. In the submonolayer coverage regime, only the hexagonal CoO-phase appears and forms hexagonal bilayer islands with alternating side-lengths. The visible part of the first CoO-layer exposes poor order, but the second layer is highly ordered with a distinct moiré structure {periodicity: (22 ± 2) Å}.

Several different attempts have been undertaken to create CoO-islands within a ZnO matrix. In most cases complete mixing of the two materials occurred, yet one preparation procedure produced the desired result. In this preparation method CoO-islands are first prepared at an oxygen pressure of 1×10^{-6} mbar and an annealing temperature of 620 K. Then ZnO is added at an oxygen pressure of 5×10^{-7} mbar and an annealing temperature of 550 K. In the resulting mixed film, ZnO adopts the 6×6 planar h-BN structure, whereas CoO forms the described bilayer-islands. Although some of these islands are covered by an additional ZnO-layer, discrimination of the two materials is simple due to the different apparent heights and the characteristic shape and moiré-structure of the CoO-islands. Further annealing of this film at 650 K at an oxygen pressure of 1×10^{-6} mbar, destroys this phase separation. A mixed Zn(1-x)Co(x)O-film is formed, which exposes the ZnO 6×6-structure with a 20%-increased apparent layer height compared to undoped ZnO-films.

The hereby presented study on ZnO-layers on Pd(111) may just mark the beginning of a more profound research. More information on the bonding and electronic structure, especially in the interface region, is needed. Thus progressive XPS- and UPS- measurements would be desirable. Also the confirmation of the DFT-models with another method, for example LEIS, would bring the research of this system one step further. In any way the material combination of palladium and zinc-oxide forms the basis for a fascinating class of materials, which allows a great variety of research for the technological sector as well as for the investigation of basic principles.

Acknowledgements

This thesis would not have come into being without the help of a lot of people. First of all I would like to thank my supervisors, Zarko Surnev and Robert Schennach for their support and guidance in the last three years. A great thanks also goes to all my co-workers: Markus Kratzer, Anton Tamtögl, Jörg Killmann and Adolf Winkler, who did the TPD-measurements on PdZn-alloys; Frederik Weber, who measured the TPD- and IR- spectra of ZnO-films on Pd(111) and Giovanni Barcaro, Alessandro Fortunelli, Imre Bako and Hans Peter Koch, who made the DFT-calculations. For funding the project in which this thesis is embedded, my regards go the the FWF, the scientific fund of Austria. I also want to thank all the members of the surface science groups of the Karl-Franzens-University of Graz and the Technical University of Graz for all the nice, funny and informative conversations, the readiness to help when it is needed, the comfortable working climate and the nice evenings, spent together. My thanks also go to Daniela Gaar and Gabriele Zirkl from the Karl-Franzens-University and to Astrid Wischgala from the Technical University who helped me with all the formalities. Last but not least I want to thank my family and my friends whose invaluable support kept me on the way, in hard times, as well as in good ones.

List of abbreviations

bcc	body centred cubic
br	bridge-position
Co	cobalt
CoO	cobalt-oxide
DFT	density functional theory
DLA	diffusion limited aggregation
DMS	diluted magnetic semiconductors
DOS	density of states
fcc	face centred cubic
h-BN	hexagonal boron-nitride structure
hcp	hexagonal close packed
HREELS	high resolution electron energy loss spectroscopy
IR	infrared
ITO	indium tin oxide
LDOS	local density of states
LEED	low energy electron diffraction
LEIS	low energy ion scattering
ML	monolayer
MSR	methanol steam reforming
Pd	palladium
PO	post-oxidation
Pt/Ir	platinum-iridium
PVD	physical vapour deposition
RE	reactive evaporation
STM	scanning tunnelling microscopy
STS	scanning tunnelling spectroscopy
TCO	transparent conductive oxide
TDS	temperature desorption spectroscopy
top	position on top of a substrate-atom
TPD	temperature programmed desorption
UHV	ultrahigh vacuum
UPS	ultraviolet photoelectron spectroscopy
W	tungsten
WKB	Wenzel-Kramers-Brillouin approximation
XPS	x-ray photoelectron spectroscopy
Zn	zinc
ZnCoO	mixed ZnO/CoO
ZnO	zinc-oxide

List of figures

List of tables

Reference list

Note on the index system: the index of each reference consists of two letters and two ciphers which are determined according to the following scheme: *[initial letter of the 1st authors family- name, first letter of the publishing journal, last two ciphers of the year of publication]*. Exceptions: In case of [mp06] and [ss04], the first letter stems from the family-name of the 2nd author to avoid double indexing. For each reference a maximum of three authors is listed.

[ac07] J.E. Ayers; Heteroepitaxy of semiconductors: theory, growth, and characterization; CRC (2007) ISBN 0-849-37195-3

[ah76] N.W. Ashcroft, N.D. Mermin; Solid state physics; Harcourt, Saunders (1976) ISBN 0-030-83993-9

[ak00] I. Amidror; The theory of the moiré phenomenon; Kluwer (2000) ISBN 0-792-35949-6

[ba04] B. Meyer, D. Marx, Ch. Wöll; Partial dissociation of water leads to stable superstructures on the surface of zinc oxide; Angew. Chemie-Int.Ed. 43 (2004) 6642

[bc96] L.I. Berger; Semiconductor Materials (Physical sciences references); CRC (1996) ISBN 0-849-38912-7

[bd05] L. Bergmann, C. Schaefer, R. Kassing; Lehrbuch der Experimentalphysik, Band 6 – Festkörper; de Gruyter (2005) ISBN 3-11-017485-5

[bi01] L.F. Brown; A comparative study of fuels for on-board hydrogen production for fuel-cell-powered automobiles; Int. J. Hydrogen Energy 26 (2001) 381

[bp04] B. Meyer; First-principles study of the polar O-terminated ZnO surface in thermodynamic equilibrium with oxygen and hydrogen; Phys. Rev. B 69 (2004) 045416

[bs00] C. Bai; Scanning tunneling microscopy and its applications; Springer (2000) ISBN 3-540-65715-0

[bs01] T. Becker, S. Hövel, Ch. Wöll; Interaction of hydrogen with metal oxides: the case of the polar ZnO(0001) surface; Surf. Sci- 486 (2001) L502, Erratum Surf. Sci. 511 (2002) 463

[bs06] A. Bayer, K. Flechtner, N. Rösch; Electronic properties of thin Zn layers on Pd(1 1 1) during growth and alloying; Surf. Sci. 600 (2006) 78

[bs73] S. Bloom, J. Ortenburger; Pseudopotential Band Structure of ZnO; Status Solidi (B) 58 (1973) 561

[cc02] Y.H. Chin, R. Dagle, J. Hu; Steam reforming of methanol over highly active Pd/ZnO catalysts; Catalysis today 77 (2002) 79

[cj05] F. Claeyssens, C.L. Freeman, J.H. Harding; Growth of ZnO thin films—experiment and theory; J. Mater. Chem. 15 (2005) 139

[cn05] J.M.D. Coey, M. Venkatesan,C.B. Fitzgerald; Donor impurity band exchange in dilute ferromagnetic oxides; Nature Mater. 4 (2005) 173

[co93] C.J. Chen; Introduction to scanning tunneling microscopy; Oxford (1993) ISBN 0-195-07150-6

[cp03] Z.X. Chen, K.M. Neyman, N. Rösch; Surface structure and stability of PdZn and PtZn alloys: Density-functional slab model studies; Phys. Rev. B 68 (2003) 075417

[cp06] F. Claeyssens, C.L. Freeman, J.H. Harding; Graphitic Nanofilms as Precursors to Wurtzite Films: Theory; Phys. Rev. Lett. 96 (2006) 066102

[cs04] Z.X. Chen, K.M. Neyman, N. Rösch; Theoretical study of segregation of Zn and Pd in Pd–Zn alloys; Surf. Sci. 548 (2004) 291

[cs93] M.F. Crommie, C.P. Lutz, D.M. Eigler; Confinement of electrons to quantum corrals on a metal surface; Science 262 (1993) 218

[dn06] T. Dietl; Self-organized growth controlled by charge states of magnetic impurities; Nature Mater. 5 (2006) 673

[dp03] O. Dulub, U. Diebold, G. Kresse; Novel Stabilization Mechanism on Polar Surfaces: ZnO(0001)-Zn; Phys. Rev. Lett. 90 (2003) 016102

[dp06] T. Dietl; Origin of ferromagnetism and nano-scale phase separations in diluted magnetic semiconductors; Physica E 35 (2006) 293

[dp07] T. Dietl, T. Andrearczyk, A. Lipińska; Origin of ferromagnetism in $Zn_{1-x}Co_xO$ from magnetization and spin-dependent magnetoresistance measurements; Phys.Rev. B 76 (2007) 155312

[ds00] T. Dietl, H. Ohno, F. Matsukura; Zener Model Description of Ferromagnetism in Zinc-Blende Magnetic Semiconductors; Science 287 (2000) 1019

[ds02] O. Dulub, L.A. Boatner, U. Diebold; STM study of the geometric and electronic structure of ZnO(0001)-Zn, (000-1)-O, (10-10), and (11-20) surfaces; Surf. Sci. 519 (2002) 201.

[ds05] A. Dadgar, A. Krtschil, F. Bertram; ZnO MOVPE growth: From local impurity incorporation towards p-type doping; Superlattices and Microstructures 38 (2005)245

[ev85] G. Ertl, J. Küppers; Low energy electrons and surface chemistry, VCH (1985) ISBN 3-527-26056-0

[fp06] C.L. Freeman, F. Claeyssens, J.H. Harding; Graphitic Nanofilms as Precursors to Wurtzite Films: Theory; Phys. Rev. Lett. 96 (2006) 066102

[fp82] A. Fasana, I. Abbati, L. Braicovich; Photoemission evidence of surface segregation at liquid-nitrogen temperature in Zn-Pd system; Phys. Rev. B 26 (1982) 4749

[gj06] H. Gabasch, A. Knop-Gericke, B. Klötzer; Zn Adsorption on Pd(111): ZnO and PdZn Alloy Formation; J. Phys. Chem. B 110 (2006) 11391

[gp04] J. Goniakowski, C. Noguera, L. Giordano; Using Polarity for Engineering Oxide Nanostructures: Structural Phase Diagram in Free and Supported MgO(111) Ultrathin Films; Phys. Rev. Lett. 93 (2004) 215702

[gr08] J. Goniakowski, F. Finocchi, C. Noguera; Polarity of oxide surfaces and nanostructures; Rep. Prog. Phys. 71 (2008) 016501

[gs80] W. Göpel, R.S. Bauer, G. Hansson; Ultraviolet photoemission studies of chemisorption and point defect formation on ZnO nonpolar surfaces; Surf. Sci. 99 (1980) 138

[gs92] H.J. Güntherodt, R. Wiesendanger; Scanning tunneling microscopy I; Springer (1992) ISBN 3-540-54308-2

[hc04] J.D. Holladay, Y. Wang, E. Jones; Review of Developments in Portable Hydrogen Production Using Microreactor Technology; Chem. Rev. 104 (2004) 4767

[hd95] A.F. Holleman, E. Wiberg; Lehrbuch der Anorganischen Chemie; de Gruyter (1995) ISBN 3-110-12641-9

[hj00] St. Hövel, C. Kolczewski, Ch. Wöll; Pyridine adsorption on the polar ZnO□0001□ surface: Zn termination versus O termination; J. Chem. Phys. 112 (2000) 3909

[hm69] M.F. Hansen; Constitution of binary alloys; McGraw-Hill (1969) 2nd edition

[hr07] I. Horcas, R. Fernández, A.M. Baro; WSXM: A software for scanning probe microscopy and a tool for nanotechnology; Rev. Sci. Instrum. 78 (2007) 013705

[hs09] E. Hornbogen, B. Skrotzki; Mikro- und Nanoskopie der Werkstoffe, 3. Auflage; Springer (2009) ISBN 3-540-89945-6

[ia95] N. Iwasa, S. Masuda, N. Takezawa; Steam reforming of methanol over Pd/ZnO: Effect of the formation of PdZn alloys upon the reaction; Appl. Catal. A. 125 (1995) 14

[ib98] N. Iwasa, N. Ogawa, N. Takezawa; Selective PdZn Alloy Formation in the Reduction of Pd/ZnO Catalysts; Bull. Chem. Soc. Jpn. 71 (1998) 1451

[ic93] N. Iwasa, S. Kudo, N. Takezawa; Highly selective supported Pd catalysts for steam reforming of methanol; Catal. Lett. 19 (1993) 211

[ij91] N. Iwasa, O. Yamamoto, N. Takezawa; Dehydrogenation of methanol to methyl formate over palladium/zinc oxide catalysts; J. Chem. Soc. Chem. Commun. 18 (1991) 1322

[ir00] N. Iwasa, T. Mayanagi, N. Takezawa; Steam Reforming of Methanol Over Pd-Zn Catalysts; React. Kinet. Catal. Lett. 69 (2000) 355.

[it03] N. Iwasa, N. Takezawa; New Supported Pd and Pt Alloy Catalysts for Steam Reforming and Dehydrogenation of Methanol; Top. Catal. 22 (2003) 215

[js07] E. Jeroro, V. Lebarbier, J.M. Vohs; Interaction of CO with surface PdZn alloys; Surf. Sci. 601 (2007) 5546

[jw75] J.D. Jackson; Classical electrodynamics; Wiley (1975) ISBN 0-471-43132-X

[ka05] M. Kurtz, J. Strunk, Ch. Wöll; Active sites on oxide surfaces: ZnO-catalyzed synthesis of methanol from CO and H_2; Angew. Chemie-Int. Ed. 44 (2005) 2790

[ka09] M.F. Kratzer, A. Tamtögl, J. Killmann; Preparation and calibration of ultrathin Zn layers on Pd(111); Appl. Surf. Sci. 255 (2009) 5755

[kj03] M. Kunat, S.G. Girol, Ch. Wöll; The Interaction of Water with the Oxygen-Terminated, Polar Surface of ZnO; J. Phys. Chem. B 107 (2003) 14350

[kj06] A. Karim, T. Conant, A. Datye; The role of PdZn-formation and particle size on the selectivity for steam reforming of methanol; J. Cat. 243 (2006) 420

[kn04] R. Kling, C. Kirchner, A. Waag; Analysis of ZnO and ZnMgO nanopillars grown by self-organization; Nanotechnology 15 (2004) 1043

[kp02] M. Kunat, S.G. Girol, Ch. Wöll; Stability of the polar surfaces of ZnO: A reinvestigation using He-atom scattering; Phys. Rev. B 66 (2002) 081402 (R)

[kp03] G. Kresse, O. Dulub, U. Diebold; Competing stabilization mechanism for the polar ZnO(0001)-Zn surface; Phys. Rev. B 68 (2003) 245409

[kp06] C. Klingshirn, M. Grundmann, A. Waag; Zinkoxid - ein alter, neuer Halbleiter; Physik Journal 5 (2006) 33

[kp83] S.D. Kevan; Evidence for a New Broadening Mechanism in Angle-Resolved Photoemission from Cu(111); Phys. Rev. Lett. 50 (1983) 526

[kp97] J. Kraft, M.G. Ramsey, F.P. Netzer; Surface reconstructions of In on Si(111); Phys. Rev. B 55 (1997) 5384

[ks05] C.F. Klingshirn, Semiconductor Optics (Advanced Texts in Physics), 2nd edition; Springer (2005) ISBN 3-540-21328-7

[ks08] S.T. King, S.S. Parihar, P.F. Lyman; Observation of a (√3 × √3)R30° reconstruction on O-polar ZnO surfaces; Surf. Sci. Lett. 602 (2008) L131

[ks10] H.P. Koch, I. Bako, G. Weirum; A theoretical study of Zn adsorption and desorption on a Pd(111) substrate; Surf. Sci. 604 (2010) 926

[kz71] C. Klingshirn, Zur Diffusion lichtelektrisch angeregter Elektronen und über dendc-Effekt an ZnO-Kristallen; Z. Phys. 248 (1971) 433

[lp70] N.D. Lang, W. Kohn; Theory of Metal Surfaces: Charge Density and Surface Energy; Phys. Rev. B1 (1970) 4555

[ls00] F.P. Leisenberg, G. Koller, S. Surnev; Surface and subsurface oxygen on Pd(111) Surf. Sci. 445 (2000) 380

[ls05] D.C. Look; Electrical and optical properties of p-type ZnO; Semicond. Sci. Tech. 20 (2005) S55

[ls93] H. Lüth; Surfaces and interfaces of solids; Springer (1993) ISBN 3-540-52681-1

[ls98] H. Landolt, R. Börnstein, B. Predel; Phase equilibria, crystallographic and thermodynamic data of binary alloys; Springer (1998) ISBN 3-540-61712-4

[mp03] B. Meyer, D. Marx; Density-functional study of the structure and stability of ZnO surfaces; Phys. Rev. B 67 (2003) 035403

[mp06] M. Kunat, B. Meyer, Ch. Wöll; Structure and dynamics of CO overlayers on a hydroxylated metal oxide: The polar ZnO(000-1) surface; Phys. Chem. Chem. Phys. 8 (2006) 1499

[mp09] H.L. Meyerheim, C. Tusche, J. Kirschner; Wurtzite-type CoO nanocrystals in ultrathin ZnCoO films; Phys. Rev. Lett 102 (2009) 156102

[ms82] O. Madelung, M. Schulz, H. Weiss; "Landolt-Börnstein Group III Volume 17, Subvolume B, II-VI and I-VI Compounds; Semimagnetic Compounds"; Springer (1982) ISBN 0-387-11308-8

[mz69] E. Mollwo, G. Pensl, Lichtelektrische Leitung und Polarisation durch Laserstrahlung im Volumen von ZnO-Kristallen; Z. Phys. 228 (1969) 193

[nc83] F.P. Netzer, J.U. Mack; Angle resolved ultraviolet photoemission of pyridine adsorbed on Pd(111); Chem. Phys. Lett. 95 (1983) 492

[nj00] C. Noguera; Polar oxide surfaces; J. Phys.: Condens. Matter 12 (2000) R367

[nj04] K.M. Neyman; R. Sahnoun, N. Rösch; Computational Study of Model Pd-Zn Nanoclusters and Their Adsorption Complexes with CO Molecules; J. Phys. Chem. B 108 (2004) 5424

[nn04] T. Nobis, E.M. Kaidashev, M. Grundmann; Spatially Inhomogeneous Impurity Distribution in ZnO Micropillars; Nano Letters 4 (2004) 797

[np07] K.M. Neyman, K.H. Lim, N. Rösch; Microscopic models of PdZn alloy catalysts: structure and reactivity in methanol decomposition; Phys. Chem. Chem. Phys. 9 (2007) 3470

[oe08] M. Opel, K.W. Nielsen, S. Bauer; Nanosized superparamagnetic precipitates in cobalt-doped ZnO; Eur. Phys. J. B 63 (2008) 437

[öj05] Ü. Özgür, Y.I. Alivov, C. Liu; A comprehensive review of ZnO materials and devices; J. Appl. Phys. 98 (2005) 041301

[op08] F. Ostendorf, S. Torbrügge, M. Reichling; Atomic scale evidence for faceting stabilization of a polar oxide surface; Phys. Rev. B 77 (2008) 041405 (R)

[pa03] W.I. Park, G.C. Yi, S.J. Pennycook; Quantum Confinement Observed in ZnO/ZnMgO Nanorod Heterostructures; Advanced Mat.15 (2003) 526

[pa99] B.A. Peppley, J.C. Amphlett, L.M. Kearns; Methanol-steam reforming on Cu/ZnO/Al2O3. Part 1: the reaction network; Applied Catalysis A 179 (1999) 21

[pc95] D.L. Perry, S.L. Phillips; Handbook of Inorganic Compounds; CRC (1995) ISBN 0-849-38671-3

[ps96] B.N.J Persson, E. Tosatti, Ch. Wöll; Physics of Sliding Friction; Springer (1996) ISBN 0-792-33935-5

[rj94] J.A. Rodriguez; Interactions in Bimetallic Bonding: Electronic and Chemical Properties of PdZn Surfaces; J. Phys. Chem. 89 (1994) 5758

[sp03] V.A. Staemmler, K. Fink, Ch. Wöll; Stabiliation of polar ZnO-surfaces: validating microscopic models by using CO as a probe molecule; Phys. Rev. Lett. 90 (2003) 106102

[sp08] N. Sakaguchi, Y. Suzuki, H. Ichinose; A HRTEM and EELS study of Pd/ZnO polar interfaces; Philos. Mag.88 (2008) 1493

[sp81] P.S. Silinsky, M.S. Seehra; Principal magnetic susceptibilities and uniaxial stress experiments in CoO; Phys. Rev. B 24 (1981) 419

[ss04] C. Castellarin-Cudia, S. Surnev, F.P. Netzer; Strain-induced formation of arrays of catalytically active sites at the metal–oxide interface; Surf. Sci. 554 (2004) L120

[ss09] W. Stadlmayr, S. Penner, B. Klötzer; Growth, thermal stability and structure of ultrathin Zn-layers on Pd(111); Surf. Sci. 603 (2009) 251.

[su89] A. Stemmer, A. Hefti; A.M. Engel; Scanning tunnelling and transmission electron microscopy on identical areas of biological specimens; Ultramicroscopy 30 (1989) 263

[tc01] D.L. Trimm, Z.I. Önsan; Onboard fuell conversion for hydrogen-fuel-cell-driven vehicles; Catal. Rev. Sci. Eng. 43 (2001) 31

[tc97] N. Takezawa, N. Iwasa; Steam reforming and dehydrogenation of methanol: Difference in the catalytic functions of copper and group VIII metals; Catal. Today 36 (1997) 45.

[tj79] P.W. Tasker; The stability of ionic crystal surfaces; J. Phys. C 12 (1979) 4977

[tp07] C. Tusche, H.L. Meyerheim, J. Kirschner; Observation of Depolarized ZnO(0001) Monolayers: Formation of Unreconstructed Planar Sheets; Phys. Rev. Lett. 99 (2007) 026102

[tw06] R.J.D. Tilley; Crystals and Crystal Structures; Wiley (2006) ISBN 0-470-01821-6

[ue96] W.N. Unertl, N.V. Richardson, S. Holloway; Handbook of surface science - volume I: Physical structure; Elsevir (1996) ISBN 0-444-89036-X

[wa91] Ch. Wöll; Phonons on surfaces: the importance of structure and adsorbates; Applied Physics A 53 (1991) 377

[wc74] R.C. Weast; Handbook of chemistry and physics; CRC (1974) ISBN 0-878-19454-1

[wc94] R. Wiesendanger; Scanning probe microscopy and spectroscopy; Cambridge (1994) ISBN 0-521-42847-5

[wj09] G. Weirum, M. Kratzer, H.P. Koch; Growth and Desorption Kinetics of Ultrathin Zn Layers on Pd(111); J. Phys. Chem. C 113 (2009) 9788

[wj10] G. Weirum; S. Surnev, R. Schennach; Growth and surface structure of Zn oxide layers on a Pd(111) surface; submitted to J. Phys. Chem. (2010)

[wp01] A. Wander, F. Schedin, P. Steadman; Stability of polar oxide surfaces; Phys. Rev. Lett. 86 (2001) 3811

[wp06] K. Fink; Ab initio cluster calculations on the electronic structure of oxygen vacancies at the polar ZnO(0001) surface and on the adsorption of H2, CO, and CO2 at these sites; Phys. Chem. Chem. Phys. 8 (2006) 1482

[wp07] Ch. Wöll; The chemistry and physics of zinc oxide surfaces; Prog. Surf. Sci. 82 (2007) 55

[ws04] M. Wegener; Extreme Nonlinear Optics: An Introduction (Advanced Texts in Physics); Springer (2004) ISBN 3-540-22291-X

[ws98] J. Wrzesinski, D. Fröhlich; Determination of electronic parameters of ZnO by nonlinear spectroscopy; Sol. State Commun. 105 (1998) 301

[zp04] A. Zaoui; Energetic stabilities and the bonding mechanism of ZnO{0001}/Pd(111) interfaces; Phys. Rev. B 69 (2004) 115403

[zp05] M. Zacharias, P. Werner; Das Wachstum von Nanodrähten; Physik Journal 5 (2005) 29

Deutsche Fassung:
Beschluss der Curricula-Kommission für Bachelor-, Master- und Diplomstudien vom 10.11.2008
Genehmigung des Senates am 1.12.2008

EIDESSTATTLICHE ERKLÄRUNG

Ich erkläre an Eides statt, dass ich die vorliegende Arbeit selbstständig verfasst, andere als die angegebenen Quellen/Hilfsmittel nicht benutzt, und die den benutzten Quellen wörtlich und inhaltlich entnommene Stellen als solche kenntlich gemacht habe.

Graz, am ……. ……..
(Unterschrift)

Englische Fassung:

STATUTORY DECLARATION

I declare that I have authored this thesis independently, that I have not used other than the declared sources / resources, and that I have explicitly marked all material which has been quoted either literally or by content from the used sources.

……. ……..
date (signature)